Design and topology optimization of heat sinks for the cooling of electronic devices with multiple heat sources

Yijun Li

COLLEGE DOCTORAL PAYS DE LA LOIRE
SCIENCES DE L'INGENIERIE ET DES SYSTEMES

Nantes Université

THESE DE DOCTORAT

NANTES UNIVERSITE

ECOLE DOCTORALE N° 602
Sciences de l'Ingénierie et des Systèmes
Spécialité : *Energétique - Thermique - Combustion*

Par
Yijun LI

Conception et optimisation topologique des dissipateurs thermiques pour le refroidissement de dispositifs électroniques avec plusieurs sources de chaleur

Thèse présentée et soutenue à Nantes, le 07/03/2023
Unité de recherche : Laboratoire de Thermique et Energie de Nantes (CNRS UMR 6607)

Rapporteurs avant soutenance :

Charbel HABCHI — Associate professor (HDR), IMSIA, UMR 9219
Raphaël BOICHOT — Maître de conférences des universités (HDR), INP, Grenoble, SIMAP UMR 5266

Composition du Jury :

Présidente : Lingai LUO — Directrice de recherche, CNRS, LTeN, Nantes Université

Examinateurs : Eva DORIGNAC — Professeur des universités, Institut P' UPR CNRS, Université de POITIERS
Lounès TADRIST — Professeur des universités, IUSTI, Aix-Marseille Université, Marseille

Directeur de thèse : Yilin FAN — Chargé de recherche, CNRS (HDR), LTeN, Nantes Université
Co-directrice de thèse : Cathy CASTELAIN — Directrice de recherche, CNRS, LTeN, Nantes Université
Co-encadrant de thèse : Stéphane ROUX — Maître de conférences des universités, LTeN, Nantes Université

CONTENTS

ACKNOWLEDGEMENTS

First and foremost, I would like to express my sincere gratitude to my supervisor Yilin FAN, for his unwavering support, guidance, and encouragement throughout my Ph.D. journey. His invaluable insights, constructive criticism, and patience have been instrumental in shaping the direction of my research and in pushing me to achieve my academic goals.

I am also deeply grateful to my co-supervisors Cathy Castelain and Stephane Roux, and supporting Lingai LUO for their expertise and advice, which have greatly enriched my work. Their critical feedback and encouragement have been indispensable in helping me navigate the challenges of my research.

I would like to extend my thanks to the members of my thesis committee, Charbel Habchi, Raphael Boichot, Eva Dorignac and Lounes Tadrist, for their valuable, constructive feedback and suggestions, which have greatly improved the quality of my thesis.

I am grateful to the staff, faculty, and lab services (technical, secretory, IT, etc.) of LTeN, for providing me with access to the resources including the calculation resources, experiment instruments and measurement platforms and opportunities to pursue my research. Especially, the calculation resource and helps of the staff from CCIPL: Le centre de calcul intensif des Pays de la Loire. Their support and encouragement have been invaluable and indispensable in helping me overcome the challenges of my PhD journey.

I would like to acknowledge the contributions of my research participants: Gwenael Biotteau, El Mehdi Gouda, Yuchao Hua, Bruno Storti and Julien Aubril whose willingness to share their experiences and insights has been essential to the success of my research. I am also grateful to my colleagues, Hao Cheng, Yiyi Li, Thomas Naudin, Sourour Traouli, Rafic NADER, Rita Moussallem, Antonio della Volpe, Rodrigo Andres Olaya Gomez, Marie Lamard, Elia Missi, and Mosbah Kiwan, and my dear friends, Mickael Kerfant, Li He who have provided me with professional suggestions in the practice of presentation, and a supportive and stimulating academic community.

I would like to express my heartfelt gratitude to my family, for their unwavering love and support throughout my PhD journey. Their belief in me has been a constant source of motivation and inspiration, and I could not have achieved this milestone without their encouragement and support.

Finally, I would like to give my gratitude to the Chinese Scholarship Council (CSC) for supporting this PhD project financially.

ABSTRACT

The heat-generating surface with multiple heat sources is frequently encountered in modern power electronic devices. Efficient cooling techniques are especially needed to prevent the overheating of these devices, so as to avoid consequences like performance deterioration, failure rate increase, reduced lifetime and safety threats. The main objective of this PhD thesis is to design and optimize the structure of heat sinks for single-phase convective cooling of a heat-generating surface under multiple-peak heat flux. Two optimization methods have been developed and applied in this study: one is the size optimization of channel inlets for tailoring the fluid flow distribution in straight channel heat sinks and another is the topology optimization of the global flow channel configuration based on the genetic algorithm (GATO). The impacts of design and operation parameters on the effectiveness of both optimization methods are numerically evaluated, with performance comparison to reference parallel straight channel heat sinks. After that, experimental validations of the proposed optimization approaches have been done by testing different heat sink prototypes using PIV and infrared thermography. Both the numerical and experimental results indicate that the GATO heat sink shows the best cooling performance under the tested conditions. Finally, different objective functions have been tested with the GATO method and the obtained results are further compared and discussed to showcase its effectiveness and robustness.

RESUME

Les dispositifs électroniques génèrent souvent de la chaleur en différents points. Sans un refroidissement efficace, les points chauds et la surchauffe entraînent une augmentation du taux de défaillance, une détérioration des performances et des menaces pour la sécurité des composants électroniques. L'objectif principal de cette thèse est de concevoir et d'optimiser la structure des dissipateurs de chaleur par convection monophasique en minimisant la température maximale pour apporter une solution innovante à ces problèmes. Deux méthodes d'optimisation ont été développées et appliquées : l'optimisation de la taille des entrées de chaque canaux enfin de distribuer de façon optimum les fluide dans le dissipateur de chaleur à canal droit d'une part, et l'optimisation topologique de la configuration sur l'ensemble des canaux d'écoulement basée sur l'algorithme génétique (GATO). L'influence des paramètres, tels que les valeurs des pics de flux de chaleur, la vitesse d'entrée, la résolution matricielle d'un domaine de conception et la fraction de fluide a été étudiée numériquement. Ensuite, les approches d'optimisation proposées ont été validées expérimentalement en testant un dissipateur thermique à canal droit de référence (RSC), un dissipateur thermique à canal droit optimisé (OSC) et un dissipateur thermique GATO. En outre, les indicateurs de performance complets obtenus à partir des modèles validés expérimentalement des trois dissipateurs thermiques ont été comparés. Enfin, l'influence de différents objectifs d'optimisation pour la méthode GATO a été étudiée.

SYNTHESE DE THESE (EN FRANCAIS)

Cette thèse, financée par le CSC (Chinese Scholarship Council) et menée au sein du Laboratoire de Thermique et Energie de Nantes (LTeN) se concentre sur le problème du refroidissement des dispositifs électroniques surchauffés, en particulier de dispositifs ayant un volume compact et soumis à plusieurs sources de chaleur causées par une densité de puissance élevée. Il est important de noter que la surchauffe de ces dispositifs peut entraîner la détérioration de leur efficacité de fonctionnement, la diminution de leur durée de vie ou d'autres dommages irréversibles.

Différentes techniques ont été développées et utilisées pour la gestion thermique de l'électronique. Elles peuvent être simplement classées en deux catégories : (1) refroidissement direct et (2) refroidissement indirect. L'une des approches les plus largement utilisées pour la gestion thermique est le refroidissement convectif à liquide monophasique, en raison de sa structure simple et compacte, de sa sécurité d'utilisation et de son efficacité. Un dispositif de refroidissement convectif à liquide monophasique est appelé un dissipateur thermique. Il contient une ou plusieurs entrées, la zone de conception principale située au milieu (où la convection de chaleur se produit principalement), et une ou plusieurs sorties.

Pour améliorer les performances d'un dissipateur de chaleur, de nombreux articles de recherche se concentrent sur la conception et l'optimisation de sa géométrie, qui est une composante décisive dans l'amélioration du transfert de chaleur. L'approche de base pour l'amélioration des performances du dissipateur de chaleur (ou de l'échangeur de chaleur) consiste à optimiser l'écoulement de fluide couplé et le transfert de chaleur. Trois niveaux d'optimisation sont considérés : l'optimisation de taille, l'optimisation de forme et l'optimisation de topologie (TO). Pour l'optimisation de taille d'un dissipateur de chaleur, les diamètres des canaux ou des ailettes sont les variables à ajuster ou à définir. Avec une forme prédéfinie, l'optimisation de taille est l'approche la plus simple car elle nécessite moins de variables de conception. Cependant, elle ne permet d'obtenir les géométries optimales avec des formes plus complexes. L'optimisation de forme d'un dissipateur de chaleur consiste à optimiser la forme des canaux ou des ailettes du dissipateur, qui peuvent être circulaires, rectangulaires ou irrégulières, etc. Cette approche est plus flexible que l'optimisation de taille car son espace de solution comprend l'espace de solution de l'optimisation de taille, bien que les procédures soient plus compliquées. L'optimisation de topologie (TO) d'un dissipateur de chaleur n'a pas de géométrie prédéfinie requise. Diverses tailles et formes de vides peuvent être créées dans le domaine de conception pour générer différentes géométries TO. La solution de l'espace TO comprend l'espace de solution de l'optimisation de taille et de forme. Par conséquent, c'est l'optimisation avec le plus grand degré de liberté mais aussi la plus grande complexité.

La première partie de ce travail propose une revue détaillée de la littérature sur la gestion thermique des dispositifs électroniques confrontés à des problèmes de chauffage

inégal et de surchauffe. Une attention particulière est accordée à la conception et à l'optimisation structurelle des dissipateurs de chaleur pour le refroidissement efficace à un seul liquide de phase. Dans un premier temps, nous mettons en évidence la présence courante et les conséquences néfastes de la surchauffe des appareils électroniques en raison de sources de chaleur multiples, à travers divers exemples illustratifs. Ensuite, nous présentons brièvement les principales technologies de gestion thermique pour les appareils électroniques, en mettant l'accent sur l'amélioration du transfert de chaleur dans les dissipateurs de chaleur à micro/mini-canaux. Nous analysons ensuite plusieurs études sur la conception et l'optimisation des dissipateurs de chaleur, qui sont classées en quatre catégories : (1) Uniformisation ou contrôle de la distribution du flux pour les dissipateurs de chaleur à canaux droits parallèles ; (2) Optimisation de la forme de la section transversale du canal ; (3) Optimisation de la forme et de l'arrangement des ailettes ; et (4) Optimisation de la topologie de la configuration globale de l'écoulement dans le dissipateur de chaleur. Enfin, nous examinons les études existantes sur les tests expérimentaux de dissipateurs de chaleur optimisés topologiquement, qui sont une étape indispensable pour la validation des résultats de simulation et d'optimisation.

La littérature actuelle met moins l'accent sur la gestion thermique des dispositifs électroniques confrontés à des problèmes de chauffage inégal et de surchauffe dus à des sources de chaleur multiples, qui sont pourtant courants dans l'électronique moderne, que sur le chauffage uniforme ou à pic unique. Cette situation met en évidence des lacunes dans la recherche sur divers aspects de la gestion de ce problème, tels que (1) l'optimisation de la distribution de flux dans les dissipateurs de chaleur à canaux droits parallèles ; (2) les approches sans gradient pour l'optimisation de la topologie de la configuration globale de l'écoulement de canal ; (3) la caractérisation expérimentale fine des comportements fluides et thermiques locaux des dissipateurs de chaleur optimisés topologiquement ; (4) la comparaison de performance entre les dissipateurs de chaleur optimisés par différentes méthodes ou sous différents critères/contraintes d'optimisation.

La deuxième partie de notre thèse concerne le travail d'optimisation de taille pour un dissipateur de chaleur à canaux droits. Nous y abordons l'optimisation de la distribution de l'écoulement de fluide dans des dissipateurs de chaleur à mini-canaux parallèles, soumis à un flux de chaleur à multiples pics non uniforme, afin d'éliminer les points chauds de température. Un dissipateur de chaleur 3D comprenant 16 mini-canaux droits parallèles est utilisé comme modèle pour l'étude, chaque mini-canal ayant une dimension de 1 mm de largeur, 2 mm de hauteur et 34 mm de longueur. Dans cette perspective, un algorithme d'optimisation de taille/forme original est développé pour ajuster les entrées de ces mini-canaux en fonction de la distribution de température sur la surface de la base chauffante. Grâce à cette adaptation, la distribution de l'écoulement de fluide est améliorée, ce qui permet de réduire le pic de température sur la surface de chauffe. L'efficacité et la robustesse de l'algorithme d'optimisation sont testées et discutées dans cette étude.

En utilisant la méthode d'optimisation proposée, des résultats encourageants ont été obtenus montrant une réduction de la température maximale respectivement de 10 K et 7 K pour les cas de flux de chaleur à deux et cinq pics. La configuration du dissipateur de chaleur avec des entrées de canal optimisées a démontré une résistance thermique plus faible que celle de la configuration à entrées de canal égales, même dans des conditions de flux de chaleur moyen ou de débit massique total différents. De plus, il a été constaté que l'adaptation de la distribution de l'écoulement du fluide de refroidissement est plus efficace pour réduire la résistance thermique que simplement augmenter le débit massique du liquide de refroidissement, à la même perte de pression. Cette méthode d'optimisation, simple et facile à mettre en œuvre, pourrait être généralisée en tant que technologie efficace de gestion thermique pour le refroidissement électronique.

Pour atteindre le plus haut degré de liberté dans la conception des dissipateurs thermiques, nous proposons une méthode d'optimisation de topologie basée sur un algorithme génétique (GATO) pour le refroidissement par convection d'une surface de chauffe soumise à un flux de chaleur à pics multiples. La zone centrale du dissipateur thermique recevant le flux de chaleur est traitée comme domaine de conception et représentée sous forme d'une matrice binaire. Chaque élément de la matrice est considéré soit comme fluide, soit comme solide, et leur allocation est optimisée pour minimiser la température maximale (Tpic) à la surface de chauffe du dissipateur thermique sous la contrainte d'un volume de vide constant pour le domaine fluide entièrement connecté. À chaque étape d'optimisation, les caractéristiques d'écoulement et de température du fluide sont obtenues par simulation CFD en utilisant OpenFoam et les opérations de GA (sélection, croisement, mutation, etc.) sont appliquées. Les impacts des paramètres de conception et d'opération sur la configuration du canal d'écoulement optimisé sont évalués, notamment la forme du flux de chaleur, la fraction de vide du fluide, la vitesse d'entrée et la résolution du domaine de conception. Les performances de refroidissement du dissipateur thermique GATO sont également comparées à celles du dissipateur thermique à canaux droits de référence (RSC) dans les mêmes conditions.

Les résultats obtenus montrent que (1) la méthode GATO proposée peut déterminer avec succès la configuration optimale du canal d'écoulement du dissipateur thermique, réduisant ainsi la Tpic à la surface de chauffe ; (2) La configuration optimisée du canal d'écoulement dépend des paramètres de conception et d'exploitation, l'efficacité et la robustesse de la méthode GATO étant clairement démontrées ; (3) Comparé au dissipateur thermique RSC conventionnel, le dissipateur thermique GATO offre de meilleures performances de refroidissement, avec une augmentation raisonnable de la perte de charge.

Après avoir effectué les deux optimisations numériques, la validation expérimentale est indispensable. Par conséquent, le travail suivant présente une évaluation et une comparaison des performances de différents dissipateurs de chaleur sous plusieurs sources de chaleur, en utilisant à la fois des méthodes expérimentales et numériques. Différents prototypes de dissipateurs de chaleur sont optimisés, usinés, instrumentés et testés, notamment un

dissipateur de chaleur à canaux droits uniforme (dissipateur de chaleur RSC), un dissipateur de chaleur à canaux droits optimisé (dissipateur de chaleur OSC) et un dissipateur de chaleur optimisé par une méthode d'optimisation de topologie basée sur un algorithme génétique (dissipateur de chaleur GATO). La méthode PIV a été utilisée pour mesurer le champ de vitesse du dissipateur de chaleur RSC, tandis que la thermographie IR a été appliquée pour mesurer les champs de température du fluide de refroidissement dans les trois dissipateurs de chaleur. Les résultats de visualisation obtenus sont comparés avec le calcul CFD, montrant de bons accords entre eux.

Une étude numérique systématique a ensuite été effectuée pour tester les trois dissipateurs de chaleur dans un large spectre de conditions de fonctionnement. Les résultats numériques ont montré que le dissipateur de chaleur GATO peut toujours atteindre les meilleures performances hydrodynamiques et thermiques parmi les trois dissipateurs de chaleur. L'efficacité et la robustesse de l'approche GATO pour l'optimisation des dissipateurs de chaleur ont ensuite été prouvées.

Pour étendre les études d'optimisation précédentes qui ne concernaient que la performance thermique dans une fonction objective, la dernière partie de ce travail explorera l'influence de différentes fonctions objectives qui concernent à la fois la performance hydrodynamique et thermique sur les configurations de cheminement de flux optimales obtenues par notre approche GATO. En particulier, trois objectifs différents seront égaminés, à savoir (1) l'écart-type des températures à la surface de chauffe (RMSD), (2) le rapport entre le nombre de Poiseuille global et le nombre de Nusselt du dissipateur thermique, et (3) la fonction de somme pondérée de la température maximale à la surface de chauffe et de la chute de pression globale. Nous présenterons alors l'évolution de la géométrie du dissipateur thermique, de la configuration du canal de flux et des distributions de température à la surface de chauffe pour trois optimisations différentes. Les résultats des dissipateurs thermiques optimaux seront comparés et évalués en termes d'indicateurs de performance différents. Les résultats montrent que la méthode GATO proposée est efficace et robuste pour gérer des fonctions objectives complexes. Cependant, la minimisation d'indicateurs de performance globaux tels que RMSD ou Po/Nu ne conduit pas nécessairement à des températures de crête ou à des chutes de pression plus basses. La minimisation de la fonction objective de somme pondérée qui prend en compte à la fois la température de crête et la chute de pression permet non seulement d'obtenir des températures de crête et des chutes de pression plus basses, mais également des nombres de Nusselt plus élevés et des nombres de Poiseuille plus bas que les autres fonctions objectives.

Les résultats obtenus dans cette étude ont ouvert plusieurs perspectives intéressantes. Dans un avenir proche, l'étude de paramètres pour GA pourrait être envisagée pour améliorer l'efficacité de l'algorithme. Le lissage pourrait être appliqué à un dissipateur thermique GATO pour améliorer l'interface fluide-solide et faciliter sa fabrication. L'ensemble du processus pourrait être automatisé en effectuant les calculs de GA et de CFD sur la même infrastructure informatique à haute performance (HPC). La contrainte de fraction de vide constante pourrait

être abandonnée pour offrir plus de liberté dans l'optimisation. À plus long terme, l'extension de la conception en trois dimensions et la conception d'un échangeur de chaleur à deux fluides par GATO pourraient être explorées si le temps de calcul n'est pas une contrainte forte. Pour une proposition de conception plus pratique et efficace, l'étude de l'apprentissage automatique combiné à GATO pourrait être envisagée. Enfin, une comparaison entre l'approche basée sur le gradient de TO et celle non basée sur le gradient de TO pourrait être réalisée à travers une enquête expérimentale.

Nomenclature

Abbreviations

AM	Additive Manufacturing
C	Constraint
CCIPL	Le Centre de Calcul Intensif des Pays de la Loire
CCPC	Crossed Compound Parabolic Concentrator
CFD	Computational Fluid Dynamics
CMOS	Complementary Metal–Oxide–Semiconductor
CPU	Central Processing Unit
CPV	Concentrator Photovoltaics
CSP	Concentrating Solar Power
DI	Deionized
DOD	Depth of Discharge
EA	Evolutionary Algorithm
FEM	Finite Element Method
FFT	Fast Fourier Transform
FVM	Finite Volume Method
GA	Genetic Algorithm
GATO	Genetic Algorithm-based Topology Optimization
HCPVs	High Concentrator Photovoltaics
HF	Heat Flux
HGS	Hollow Glass Sphere
HPC	High-Performance Computing
IGA	Isogeometric Analysis
IGBT	Insulated-Gate Bipolar Transistor and diodes
IHS	Integrated Heat Spreader
IR	InfraRed
LBM	Lattice Boltzmann Method
LED	Light-emitting Diode
MCMs	Multi-Chip Modules
MOEA	Multi-Objective Evolutionary Algorithm

MTTF	Mean Time To Failure
NSGA-II	Non-dominated Sorting Genetic Algorithm-II
NURBS	Non-uniform Rational B-splines
O	Objective
OSC	Optimized Straight Channel
PEC	Performance Evaluation Criteria
PEs	Power Electronics
PIV	Particle Image Velocimetry
RSA	Response Surface Analysis
RSC	Reference Straight Channel
SCMs	Single-Chip Modules
STD	Standard Deviation
TIM	Thermal Interface Material
TO	Topology Optimization
UCPV	Ultra-high Concentrator Photovoltaics
VFDs	Variable-Frequency Drives

Latin symbols

A	Surface area of the base wall [m^2]
B	Constant of heat flux formula [$W \cdot cm^{-2}$]
C	Specific heat [$J \cdot kg^{-1} \cdot K^{-1}$]
D	Hydraulic diameter [m]
E	Energy [J]
e	The thickness of heat sink fluid domain [m]
F	External force [N]
f	Darcy friction factor
g	Gravitational acceleration [$m \cdot s^{-2}$]
H	Specific enthalpy [$J \cdot kg^{-1}$]
h	Heat transfer coefficient
L	Length [m]
Lg	Distance between the inlet and outlet [m]
m	Mass flow rate [$kg \cdot s^{-1}$]
M	Matrix

m^*	Non-dimensional mass flow rate [-]
MF_T^{max}	Non-uniformity of maximum temperatures [-]
N	Number of heat peaks [-]
n	Total number of cell/point in CFD mesh or index of pixel in images from experimental data
Nu	Nusselt number [-]
p	Pressure [Pa]
Pix	Index of cell/point in CFD mesh or index of pixel in images from experimental data
P^*	Normalized pressure drop [-]
Po	Poiseuille number [-]
Q	Heating power [W]
q	Heat flux [$\mathrm{W \cdot cm^{-2}}$]
Re	Reynolds number [-]
R_{th}	Thermal resistance [$\mathrm{K \cdot W^{-1}}$]
S_h	Volumetric heat source [$\mathrm{J \cdot K^{-1} \cdot m^{-3}}$]
STD^*	Normalized standard deviation [-]
T	Temperature [K]
t	Time [s]
T^*	Normalized temperature [-]
T^*_{avg}	Normalized area-weighted-temperature [-]
v	Flow velocity [$\mathrm{m \cdot s^{-1}}$]
v^*	Normalized velocity [-]
w	Width [m]
w^*	Non-dimensional width [-]
x, y, z	Axis

Greek symbols

γ	Adjusting factor [-]
ΔP	Pressure drop [Pa]
σ	Spatial spread of the heat peak [mm]
λ	Thermal conductivity [$\mathrm{W \cdot m^{-1} \cdot K^{-1}}$]
μ	Dynamic viscosity [$\mathrm{kg \cdot m^{-1} \cdot s^{-1}}$]
ρ	Density [$\mathrm{kg \cdot m^{-3}}$]
τ	Shear stress [$\mathrm{N \cdot m^{-2}}$]

Φ	Void fraction [%]

Subscript

0	Reference value
avg	Average value
base	Heat sink base wall
c	Column of matrix
ch	Channel
col	Collector
design	Design domain
dis	Distributor
eff	Effective
element	Elements in a binary matrix
f	Fluid
i	Channel number index
ih	Index of heat flux peak
in	Inlet
k	Iteration step number
max	Maximum value
min	Minimum value
out	Outlet
peak	Peak value
r	Row of matrix
s	Solid part of heat sink material
sa	Sapphire
sw	Solid wall
T	Temperature
tot	Total
w	Wall
we	Wetted

Superscript

min	Minimum value
max	Maximum value
median	Median value

Chapter 1: General introduction

1.1 Context

In modern society, electronics are indispensable to individuals, industries, and public organizations. To meet the requirements of higher work efficiency, less occupied space, and more compact geometry, the working components usually would be enclosed in a small volume. According to Moore's law, the number of transistors in a dense Integrated Circuit (IC) doubles about every two years [1]. However, those high-power density electronics could not fully use the electricity energy during operation, and some of the input energy would be transformed into extra heat. The more compact the electronics, the higher the power density (heat flux). Consequently, overheating will occur, causing the deterioration of normal working efficiency, a shorter lifespan, and irreversible damage.

In most situations, the heating surface of electronics is considered uniform heating for simplification. Nevertheless, most electronics have multiple heat sources, for example, array arrangement of Lithium-ion battery cells in a pack, multiple heat sources of multi-chip modules (MCMs), etc. Under this circumstance, the overheating would become more severe than the previous uniform heating hypothesis because of the generation of extremely high local temperature hot spots (uneven heating). Therefore, it is essential to maintain the temperature of electronics under an acceptable range by thermal management (efficient cooling).

Various techniques have been developed and used for the thermal management of electronics. They can be simply classified by: (1) direct cooling and (2) indirect cooling [2]. One of the most widely used approaches for thermal management is single-phase liquid convective cooling, due to its simple, compact structure, safety of usage, and efficiency. A device for single-phase liquid convective cooling is called a heat sink. It contains one/several inlet(s), the main design area located in the middle where heat convection mostly happens, and one/several outlet(s).

To improve a heat sink performance, plenty of research papers work on the design and optimization of a heat sink geometry which is a decisive reason for the enhancement of heat transfer. The basic approach for heat sink (or heat exchanger) performance improvement is the optimization of coupled fluid flow and heat transfer. Regarding the optimization methods, there are three levels of optimization: *size optimization, shape optimization, and topology optimization (TO)*, as illustrated in Figure 1.1 [3]. For the size optimization of a heat sink, the diameters of a channel or pin-fin are the variables to be adjusted or defined. With a predefined shape, size optimization is the simplest approach because it needs fewer design variables, and also because of this, it cannot obtain the optimal geometry with a more complicated shape. The design variable of a heat sink shape optimization is the shape of a channel or pin-fin of a heat sink, which could be a circle, rectangular or irregular, etc. It is more flexible than a size optimization since its solution space includes the solution space of size optimization, while the

procedures are more complicated than those of a size optimization. There is no required predefined geometry for a heat sink TO approach. Various sizes and shapes of voids can be created in the design domain to generate different TO geometries. The solution of TO space includes the solution space of size and shape optimization. Therefore, it is the optimization with the highest degree of freedom and the maximum complexity of the process. Based on the optimization study on a heat sink, it can be categorized into (1) flow distribution optimization/investigation on a parallel straight channel; (2) heat sink flow cross-section optimization; (3) fin-shape and structure optimization; (4) heat sink global flow configuration optimization.

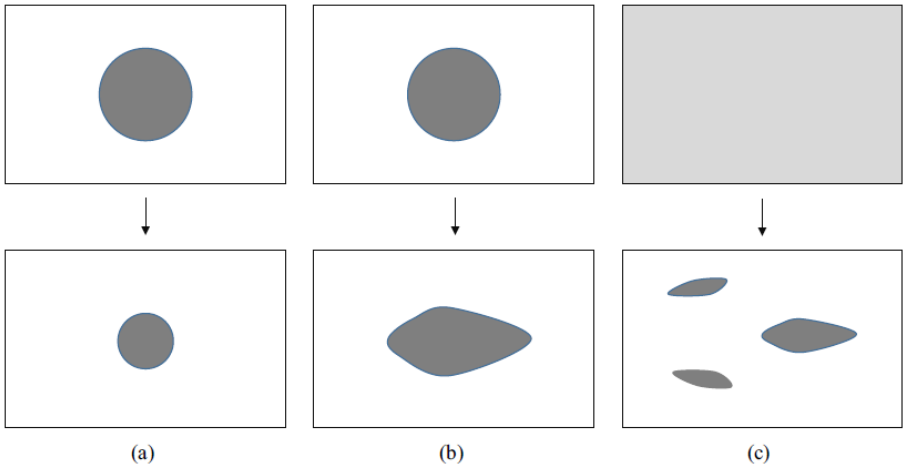

Figure 1.1 Basic principle for size (a), shape (b), and topology (c) optimizations [3].

1.2 Research gaps in the literature

The most important is that they consider the heating condition uniform, which is not the case in reality. To maximize the freedom degree of design, a topology optimization (TO) approach would be chosen for a heat sink global flow configuration optimization. Moreover, without the experimental validation of the optimal heat sink model, under a rough mesh during the optimization process, its accuracy and performance are difficult to be ensured.

The following research gaps still exist in the design and optimization of heat sinks：

- Most heat sink optimizations in the literature are still performed under the uniform heating condition without sufficient awareness of the uneven heating surface with temperature hot spots caused by multiple heat sources for electronics in reality;

- For the conventional parallel straight channel heat sink most research articles focus on the investigation of the inlet/outlet positions, the shape of distributors and collectors, etc., for the achievement of uniform flow distribution;

- As a powerful geometric optimization method, most TO approaches are gradient-based methods, they are easily trapped into local optimum and have difficulties defining the solid-fluid interface. The development of non-gradient based TO approaches is still needed;

- The experimental characterization of optimized heat sink models is always required. However, for TO heat sinks, the validations of numerical models by experiments are inadequate.

- The comparison of different objective functions for the TO approach is still lacking.

1.3 Main research objectives

The main objective of this thesis is the design and optimization of high-performance heat sinks for effective convective cooling of heat-generating surfaces with multiple-peak heat flux by the development and implementation of different optimization methods. The performance of different optimized heat sinks should be tested and compared using both numerical and experimental approaches. Furthermore, the choice of optimization objective on the performance of heat sinks should be investigated.

1.4 Methodology

Two optimization methods are developed and implemented for this purpose, including size optimization and TO.

The size optimization of straight-channel heat sinks aims to tailor the flow distribution in channels based on the temperature distribution of the heated surface with multiple-peak heat flux. The method follows the previous work of Min WEI (2012-2015) in LTeN, which has been developed to realize a target flow distribution [4] and for the cooling of an uneven heating surface of a tubular solar receiver [5].

The genetic algorithm based TO (GATO) is dedicated to allocating fluid and solid elements in the design domain of a heat sink to minimize the peak temperature. This approach is inspired by the pioneering work of Raphaël BOICHOT et al. [6,7] on the pure heat conduction problem.

Optical-based visualization methods are applied for the performance characterization of heat sinks and the validation of numerical simulations. Especially PIV and IR techniques are applied for in-house fabricated prototypes, which are LTeN's historical strengths.

1.5 Thesis outline

The rest of this thesis dissertation is organized into the following chapters:

Chapter 2

This chapter states the overheating issue of electronics with multiple heat sources by listing real examples. An illustration of the structures of those electronics shows how the multiple heat fluxes generated, the allowable working temperature, and the damaging

consequences without efficient cooling. To tackle this issue, various thermal management approaches are introduced. Furthermore, the literature on the design and optimization of single-phase liquid-cooled heat sinks is presented from different design and optimization perspectives. Among them, it presents research gaps for a conventional straight channel heat sink, TO heat sink, and the experimental studies of TO heat sinks.

Chapter 3

In this chapter, a CFD-based size optimization method for parallel straight channel heat sink under a multiple-peak heat flux to vanish the temperature hot spots has been developed. Two optimization cases are studied under two heat flux peaks and five heat flux peaks heating conditions. After the attainment of the optimized heat sinks, a comparison concerning thermal and hydrodynamic performances between the straight channel heat sink and optimized straight channel heat sink is performed. Finally, a robustness study on both heat sinks under various working conditions is investigated.

Chapter 4

This Chapter studies a GATO approach applied the heat sink optimization. Various design and operating parameters of the GATO method are investigated, e.g, the different heat flux peaks, inlet velocities, the fluid void fraction, and matrix resolution of the design domain. Meanwhile, the performances of all the optimal heat sink are compared with those of straight channel heat sink under the same conditions to highlight the performance improvement.

Chapter 5

This chapter numerically and experimentally studies a reference straight channel (RSC) heat sink, an optimized straight channel (OSC) heat sink, and a genetic algorithm-based topology optimized (GATO) heat sink. Experimental results are used to compare with the simulations for numerical model validation. After that, the thermal and hydraulic performances of three heat sinks are compared under a wide range of operating conditions.

Chapter 6

This chapter introduces different objective functions in the GATO approach, including root mean square deviation (RMSD), the ratio of Poiseuille number and Nusselt number, and the weighted sum of peak temperature and pressure drop. The optimal geometries of heat sinks under different objective functions are presented and analyzed. Their performances are evaluated and compared in several aspects.

Chapter 7

This chapter summarizes the main conclusions from the previous chapters and some perspectives for future explorations.

Chapter 2: Design and optimization of heat sink for the thermal management of electronics with multiple heat sources: a literature review

Chapter Summary

This chapter presents a detailed literature review on the thermal management issue for electronic devices facing uneven heating and overheating problems. Special focus is given to the design and structural optimization of heat sinks for efficient single-phase liquid cooling. Firstly, the common presence and harmful consequences of electronics overheating due to multiple heat sources are put in evidence with various illustrative examples. Then, main thermal management technologies for electronics are briefly introduced while more attention is given to the enhancement of heat transfer in micro/mini channel heat sinks. Various studies on the design and optimization of heat sinks are analyzed and classified into four categories: (1). Flow distribution uniformization or control for parallel straight channel heat sinks; (2). Channel cross-section shape optimization; (3). Pin-fin-shape and arrangement optimization; and (4). Topology optimization of global flow configuration in the heat sink. Finally, the existing studies on the experimental testing of topologically-optimized heat sinks, an indispensable step for the validation of simulation and optimization results, are surveyed and compared.

It can be discovered that the uneven and overheating due to multiple heat sources, a problem commonly shown in modern electronics, is currently far less addressed in the literature than uniform or single-peak heating. Research gap exists in various aspects to handle this multiple-peak heat flux issue, including (1). Lack of optimization method to manage the flow distribution in parallel straight channel heat sinks; (2) Lack of gradient-free approaches for the topology optimization of global flow channel configuration; (3) Lack of fine experimental characterization on the local fluid-thermal behaviors of topologically-optimized heat sinks; (4) Lack of performance comparison between heat sinks optimized by different methods or under different optimization criteria/constraints. These identified literature gaps motivate us to perform the research by using different numerical and experimental approaches, to be presented in the following chapters of this thesis.

Keywords of the Chapter:

Electronic overheating; Thermal management; Multiple-peak heat flux; Heat sink; Heat transfer enhancement; Flow distribution; Topology optimization; Experimental verification

2.1 Introduction

Thermal management is vital for modern electronics facing more and more serious overheating problems due to the ever-increasing heat flux generated. In particular, the multiple-peak shape of heat flux occurs due to the compact packaging, such that several functional elements (heat sources) are usually concentrated in a small volume of the package or array arranged on a panel, resulting in the uneven heating of the electronic devices which is quite common in real life. This uneven heating with multiple-peak heat flux, compared to the uniform heating surface, raises higher requirements on the effectiveness of the associated thermal management device to prevent harmful consequences such as reduced lifetime, material damage, or thermal runaway.

In this chapter, we will first list the harmful consequences of electronics overheating due to multiple heat sources in chapter 2.2, through some illustrative examples. The main thermal management techniques of interest and their shortcomings are then briefly introduced in chapter 2.3. Among them, forced-convention cooling using a micro/mini heat sink consists of a widely accepted technique owing to its compact structure, easy integration, and high cooling capacity. Abundant studies on the design and optimization of heat sinks have been reported in the literature, with the aim of performance enhancement. They are classified into four categories and reviewed in detail in chapter 2.4. In particular, a short literature survey on the experimental studies of TO heat sinks is presented in chapter 2.5. Finally, a summary is given in chapter 2.6 to identify the remaining research gaps to fill on this topic.

2.2 Overheating problem of electronics under multiple peak heat flux

In this part, the cases of the electronics generating multiple-peak heat flux are introduced, with an explanation of their packing/arranging structure and generated heat flux shape. Examples include Lithium-ion battery packs for electric vehicles, multiple light-emitting diodes (LED) arrays, power electronics (Insulated-gate bipolar transistor and diodes: IGBT), multi-chip modules (MCMs), multi-junction high concentrator photovoltaics (HCPVs), etc. Usually, there is an acceptable temperature range for each device to work under normal conditions. Nevertheless, uneven heat generation will more likely cause the overheating problem of the devices, leading to lowered working efficiency, components irreversible deterioration, thermal runaway, and shortened lifetimes.

2.2.1 Lithium-ion battery packs

As an energy storage unit, Li-ion batteries are widely used in electric vehicles due to their lightweight and large capacity. According to the shape of the battery cell, the Li-ion battery package can be classified into cylindrical type (Figure 2.1 (a)) and prismatic type (Figure 2.1 (b)). For both packaging types, several battery cells are arranged in an array layout to achieve the required storage capacity, i.e., the maximum endurance mileage for electric vehicles.

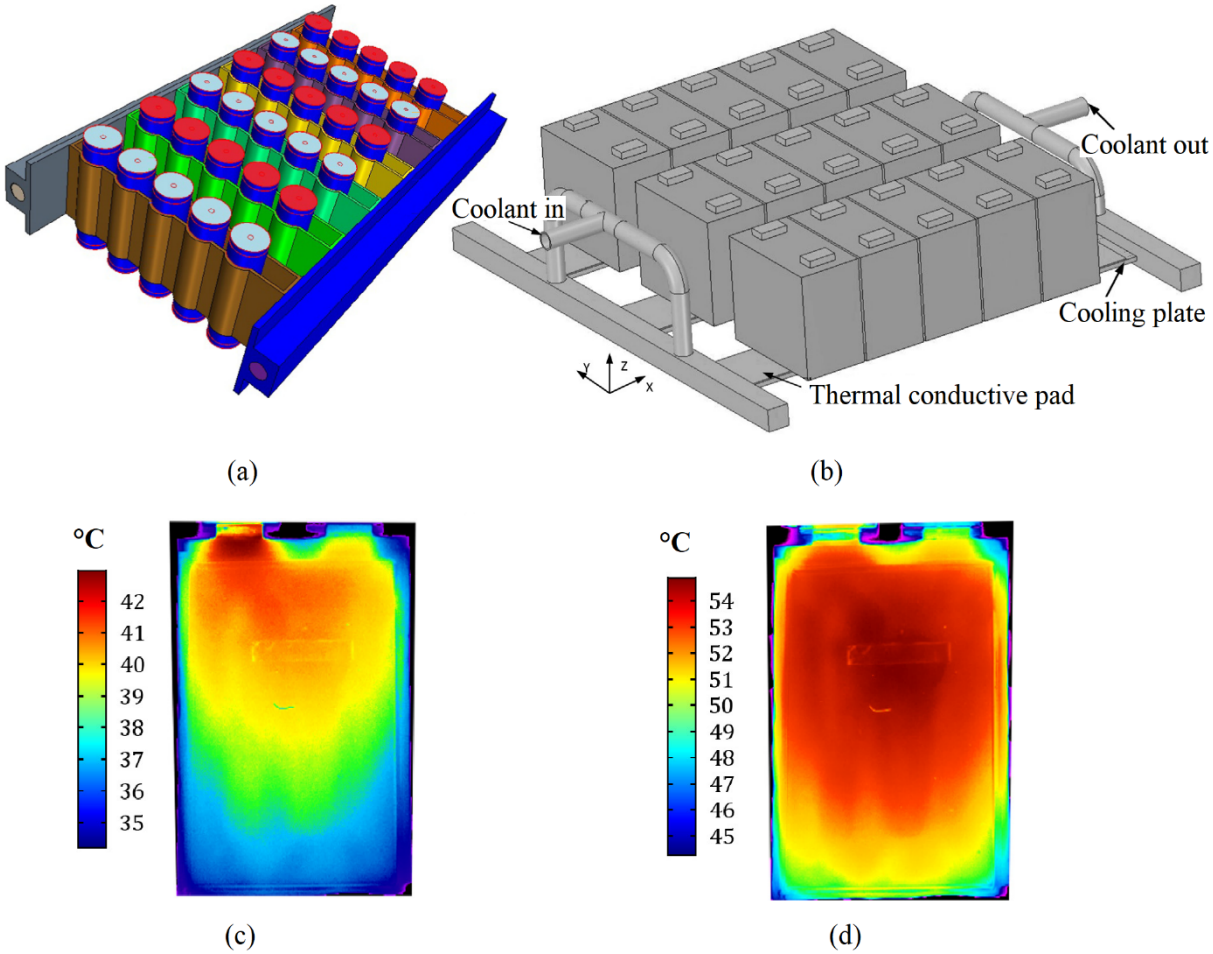

Figure 2.1 Lithium-ion battery package with array arrangement of battery cells. (a) cylindrical type [8]; (b) prismatic type [9]; camera-measured temperature contours of the single battery cell (c) at the initial stage of discharging: t=250s and (d) at the end of discharging t=667s under a constant current [10].

Figures 2.1 (c) and (d) show measured temperature contours of a prismatic battery cell at its initial stage and final stage of discharging, respectively. Clear temperature gradients between the upside (hotspot) and the downside at the initial stage of discharging, and between the middle upside (hotspot) and the bottom at the final stage of discharging can be observed. The multiple peak heat flux shape then occurs for the battery package due to the array arrangement of the unit cells. This uneven heating surface with multiple hotspots would be more complicated to handle than a uniform heating surface, by the associated thermal management technique (e.g., thermal conductive pad shown in Figure 2.1(b)).

Lithium-ion batteries could work normally under the acceptable temperature range of -20 °C - 60 °C [11], and their capacity during normal charge and discharge is very sensitive to temperature. An experimental study [12] on the capacity fade due to thermal impact reported that by keeping the other parameters (such as materials: C/LiMn2O4, depth of discharge (DOD) range: 4.2-2.5 V, cycle rate: C/1 and cycle number: 500) constant, the capacity fades increased from 28.0% to 51.0% when the battery temperature increased from 294 K to 318 K. Moreover, when overheating happens due to insufficient cooling, the chemical components inside are at

the risk of decomposing and undergoing a series of exothermic reactions that can generate excessive heat and gaseous products [13], triggering thermal runaway [14] or even explosion [15].

2.2.2 Multiple LED arrays

LED packages are widely used in different industrial and residential sectors [16] owing to the advantages of low energy consumption, high photoelectric efficiency, high luminous flux, and long lifetime. The unit LED chips are usually arranged into an array configuration (Figure 2.2 (a)), connected to the silicon die by Au-Si bonding, and then bonded to the copper heat spreader Figure 2.2 (b)).

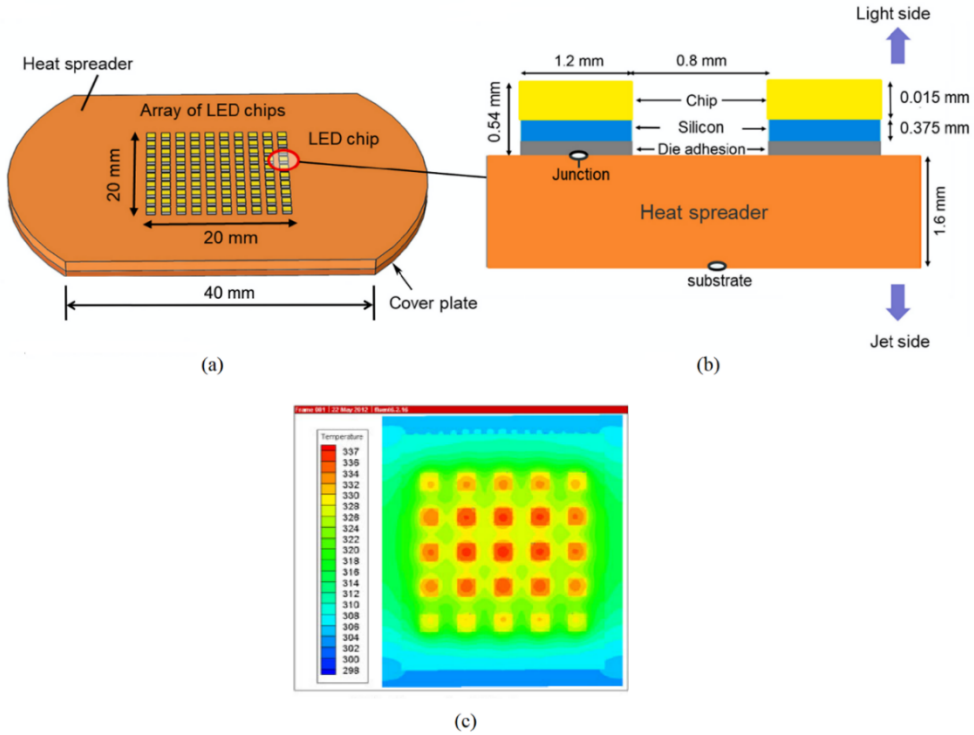

Figure 2.2 LED package. (a) Array arrangement of LED chips; (b) LED layer structure [17]; (c) Temperature distribution on the surface of the microchannel heat sink [18].

While there would be 60% - 70% of the power of the compact package is transferred into extra heat, which brings about the delamination in the electronics packages and causes the blocking of the thermal pass, extremely harmful to its normal use [19]. Even if the LED package is cooled by a liquid cooling microchannel heat sink, temperature hot spots may still exist as shown in the numerical results in Figure 2 (c). This makes the package overheating even worse, i.e., the local temperature may approach the upper limit (85 °C [20]).

2.2.3 Power electronics (Insulated-gate bipolar transistor and diodes)

An insulated-gate bipolar transistor (IGBT) is a three-terminal power semiconductor device primarily used as an electronic switch for high-power applications, such as variable-

frequency drives (VFDs), electric cars, trains, variable-speed refrigerators, lamp ballasts, arc-welding machines, and air-conditioners [21].

Figure 2.3 (a) shows a real example of an IGBT module (Infineon FF225R17ME4) consisting of three sub-modules where diode chips and IGET chips are arranged diagonally. The heat generated by these chips should be timely evacuated by an air-cooling heat sink for example, in between them exist several intermediate layers (different materials) as shown in Figure 2.3 (c). The temperature limit for an IGBT module ranges from 125 °C to 150 °C depending on the rated voltage [22]

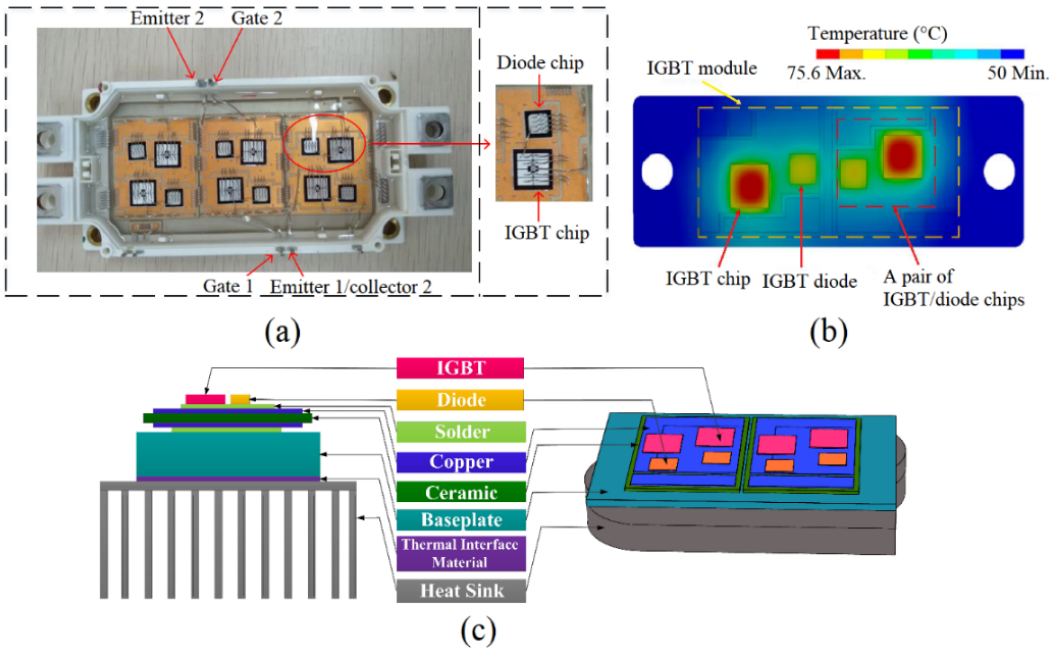

Figure 2.3 Thermal management for IGBT module. (a) A real opened IGBT module [23]; (b) Simulated temperature distribution of IGBT module [24]; (c) Air-cooling of IGBT module through a heat sink [25].

Advances in power electronics (PEs) have led to the need for the manufacturing of highly compact IGBTs, associated with non-uniform and high heat flux generation [25]. Figure.2.3 (b) illustrates a simulated temperature contour of the IGBT module based on the power loss of the IGBT diode chips with a heat sink simplified as an aluminum block. Temperature hotspots at the location of the chip can be seen, the temperature difference reaching up to 25.6 K, which is already quite high. What is even worse is that this temperature gradient due to uneven heating could be much higher for densely packaged powerful IGBT modules with hundreds of chips. According to Choi et al. [26], 34% (the highest proportion in all failure causes) of failures in the power converter systems of IGBT modules are due to the semiconductor. Among them, solder failures induced by high temperatures by nearly 60% [27].

2.2.4 Single-chip modules (SCMs) and multi-chip modules (MCMs)

CPU chips are indispensable elements for modern computing technologies. Based on the number of chips integrated, they can be classified into single-chip models (SCMs) and multi-chip modules (MCMs). A SCM commonly consists of a substrate, a CPU chip (a die), one thermal interface material (TIM-1) between the integrated heat spreader (IHS) and chip, and another TIM-2 between the heat sink and the IHS, as shown in Figure 2.4 (a). An MCM mainly includes several chips in a package (Figure 2.4 (b) for example), of which the arrangement could be a 3D stack or multiple 3D stacks.

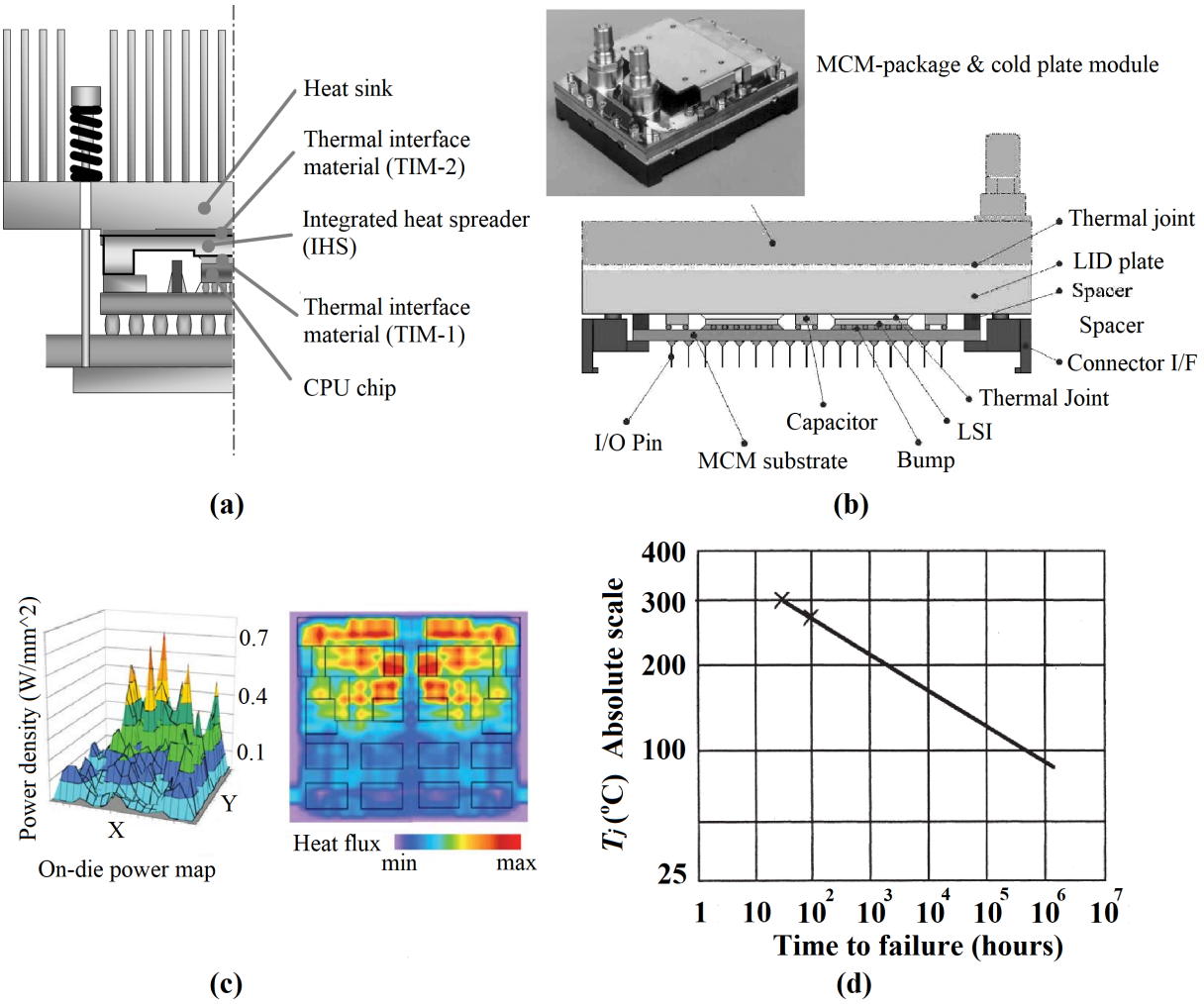

Figure 2.4 Thermal management issue for CPU chips. (a) A SCM with an air-cooled heat sink; (b) A MCM with a liquid-cooled heat sink [28]; (c) Multiple-peak heat generation by a SCM [29,30]; (d) The Arrhenius plot of mean time to failure (MTTF) vs. junction temperature[31].

According to Moore's law, the number of transistors in a dense Integrated Circuit (IC) doubles about every two years [1]. With the increasing demand for performance and the compactness of new-generation processors, the power density generated by the chip would grow higher and higher, causing more severe overheating problems. Meanwhile, SCMs and MCMs have their normal working temperature which ensures their normal working efficiency, security, and lifetime. Most CPUs should operate at thermals that aren't higher than 85-90 °C.

When it comes to CPU idle temperature, it shouldn't go over 50 °C. For example, a Core i5-12600K processor cooled by a decent dual heatsink air CPU cooler with the setup housed inside a case with solid airflow, the thermals shouldn't go much over 70 °C [32]. While every 10 °C rises of the junction temperature, the device failure rate doubles [33], which could be well explained in Figure 2.4 (d) that The decline of junction temperature greatly affects the lifetime of an electronic device. Once the junction temperature exceeds the upper limit (105 – 110 °C) [34] for a long time, the device would choose to shut down for self-protection, to avoid the problems like material damage or shortened lifetime.

When under workload, both SCMs and MCMs could generate multiple-peak shape heat flux. This is due to the different locations of transistors in a SCM (cf. Figure 2.4 (c)), and the presence of multiple chips in an MCM. Again, this multiple-peak heat flux caused overheating problems and could result in the consequences mentioned above, more serious and more difficult to handle than uniform heating conditions, raising higher demand for effective cooling techniques.

2.2.5 Multi-junction high concentrator photovoltaics (HCPVs)

Recently, the use of the solar photovoltaic system has been largely boosted for renewable electricity generation facing global warming [35]. Conventional single-junction solar cell suffers the problem of low maximum theoretical efficiency (the Shockley - Queisser limit of 32% - 33%,) of sunlight conversion [36]. In contrast, high-efficiency multi-junction solar cells (HCPVs) can greatly increase the theoretical conversion efficiency by up to 45% by stacking several solar cells [37] and by increasing the band gaps to exploit a larger part of the solar spectrum and reduce the transmission and thermalization losses [38]. Nevertheless, the concentration of sunlight unavoidably brings higher cell temperature, requiring more efficient thermal management.

Figure 2.5 (a) describes how an HCPV works. Incident sunlight is reflected by the non-imaging dish concentrator to the crossed compound parabolic concentrator (CCPC) lens array which is made up of 8×10 CPV cells. The detailed structure of a single CCPC lens can be observed in the right part of Figure 2.5 (a). The CPV module was attached to the water-cooled heat sink via Artic Silver Adhesive.

Shown in Figure 2.5 (b) is the solar flux contour on this 8×10 CPV cells array. The flux map has multiple peaks with a maximum value of up to 2.940×10^6 $W \cdot m^{-2}$. This uneven solar flux distribution will inevitably cause heterogeneous heat generation and thereby the temperature gradient on the board. Many researchers have reported the consequences of the CPV cells illuminated under a high and non-uniform solar concentration ratio. For instance, open circuit voltage is inversely proportional to the CPV cell temperature and thus deteriorates the power conversion efficiency [39]. The effects of high temperature are considered to be non-negligible at concentration levels approaching 1000 suns even as short as a few milliseconds [39]. A single-cell CPV could reach an extremely high temperature of about 1200 °C without

any heat sink under 400 suns [40], which the current CSP (concentrating solar power) apparatus (maximum 1000 °C [41]) can generally not afford.

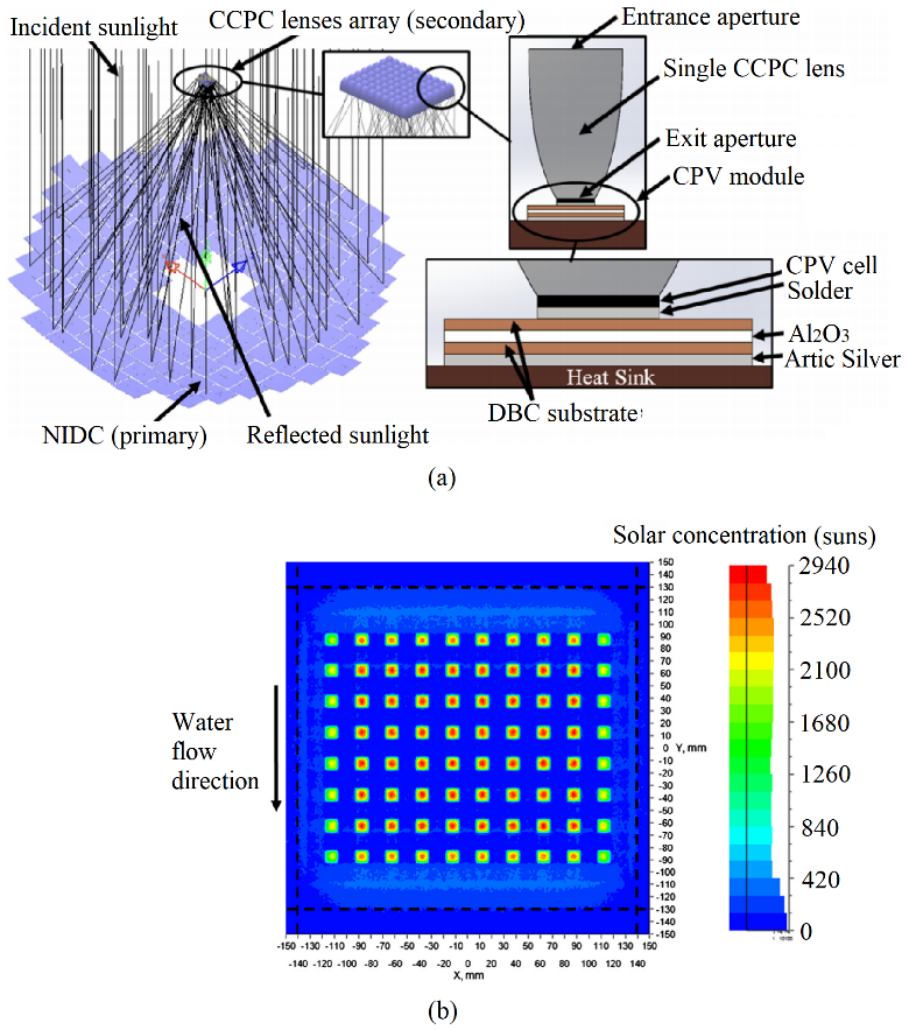

Figure 2.5 Ultra-high concentrator photovoltaics (UCPV) system cooled by a water-cooled multiple-channel heat sink. (a), Schematic diagram and working principle [42]; (b) Power map of an array of CPV cell modules [42].

2.2.6 Summary

From the illustrative examples introduced above, it can be seen that most modern electronic devices have their proper normal operating temperature and maximum temperature limit. The former makes sure that the nominal working performance is ensured within a guaranteed device lifetime whereas the latter prevents them from a shutdown, material damage, or even thermal runaway. Nevertheless, the demand for smaller, multifunctional, faster, and more powerful electronics provokes an ever-increasing heat generation, the increasing power density leading to the more and more frequently encountered overheating problem.

Moreover, the pursuit of higher capacity and performance stimulates the fast development of electronic packages or boards with a higher level of integration. The array or stacking

arrangement of unit functional elements in the integrated package will inevitably result in the uneven heat generation of multiple-peak shapes. Compared to the uniform heating or single heat source cases, this multiple-peak heat flux shape could result in a higher temperature gradient. If not properly cooled, the peak temperature exceeds the electronics' normal working temperature, even reaching the upper limit. Therefore, the development of more efficient thermal management technologies is especially required for this overheating and uneven heating of the electronics under multiple peak heat flux, an essential problem that is still insufficiently addressed in the current literature.

2.3 Thermal management techniques

Various techniques have been developed and used for the thermal management of electronics. They could be generally classified into direct cooling and indirect cooling [2] as presented in Figure 2.6. The difference between them is whether the coolant touches directly the heat-generating objects. Examples of direct cooling are air cooling, jet cooling, spray cooling, immersion cooling, etc.; For indirect cooling, a compact intermediate component is needed for the heat transfer between the heat-generating objects and the coolant, which is usually a "heat sink". Indirect cooling techniques usually contain single-phase liquid cooling, phase change cooling, evaporate cooling, heat pipe, thermal materials, etc. More details about these cooling techniques, their principles, and applied fields are briefly introduced as follows.

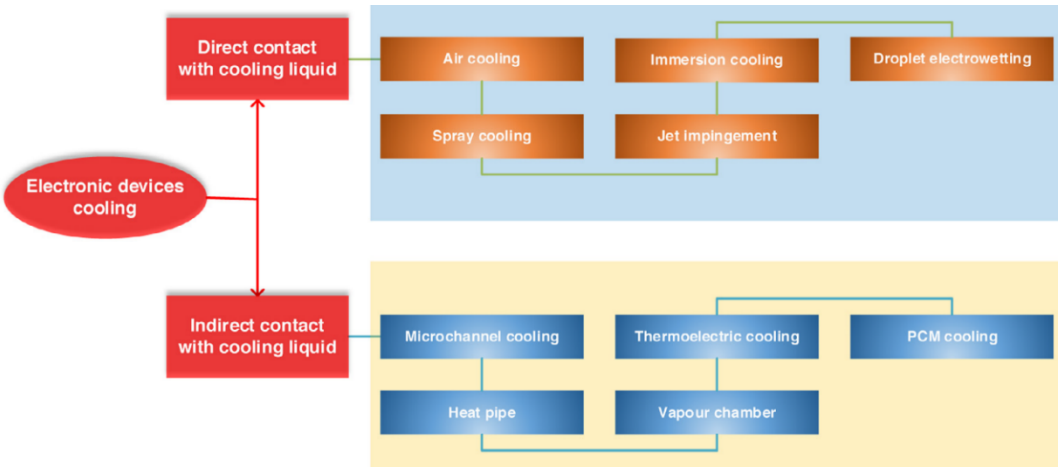

Figure 2.6 Classification of thermal management techniques [2].

2.3.1 Direct cooling

- Direct air cooling: a fan

A fan (ventilator) is commonly used for direct air cooling by forced convection, which uses external mechanical forces to generate the airflow motion around the heating objects. This technique is rather simple, easy to implement, and fast-acting, avoiding the use of accessories and coolant leakage The disadvantages exist in that firstly, it is not efficient when the ambient temperature is high; secondly, the deposition of dust and dirt in critical components in the

equipment can cause short-circuits and even failure; moreover, when encountering the multiple heat sources conditions, it may be not capable of cooling down the surface uniformly.

- Jet implementation cooling

Jet implementation cooling is to cool miniature devices with a liquid/air jet. There are three device implementation schemes of jet impingement cooling [43]: (i) using a free jet, (ii) a submerged jet and (iii) a confined by the device surfaces jet as shown in Figure 2.7 (a). The coolant is applied directly on the heating hot spot often with a speed of around 10m/s for a miniature device at the direction of either normal to the surface or at an angle within 45° [43]. While the shortcoming is that coolant directly in contact with the heated surface may cause damage to the components, and parameters of jet implementation cooling play a significant role in the heat transfer of cooling. However, it is currently not possible to create a general model of the cooling process and singly systematize experimental data [44]. Jet cooling is broadly applied in large-scale industrial systems such as gas turbine cooling, rocket launcher cooling, and high-density electrical equipment cooling [45] to deal with local hot spot problems due to the small effective cooling area.

- Spray cooling

The main working principle of spray is presented in Figure 2.7 (b). An atomizer is used to break down the liquid coolant into numerous tiny droplets by high pressure, and those droplets reach then the heated surface to absorb the heat by evaporation [46]. The whole cooling process includes three stages: single-phase regime, two-phase regime, and constant heat flux regime. Spray cooling is featured by high heat transfer rate, uniformity of heat removal, small fluid inventory, low droplet impact velocity, and no temperature overshoot [46]. However, the sizable investment in the ongoing maintenance of spray cooling equipment could be high due to some technical issues like clogged nozzles and corroded rotary disk atomizers caused by the small size of fluid passages. Spray cooling is frequently used for rapid cooling of a heated surface at high temperature, such as the cooling of medium-thick plates and thin strips in the hot rolling steel mill, glass tempering in the auto industry, and electronic chip cooling in the computer manufacturing industry [47].

- Immersion cooling

Immersion cooling (Figure 2.7 (d)) is another type of direct cooling in which the heat-generating object is directly immersed into a dielectric fluid or coolant having good thermal conductivity but very poor electric conductivity. It is a very effective cooling method. Immersion fluids can increase heat transfer by up to 10000 times compared to air [48]. This direct contact with the cooled surfaces further reduces the thermal contact resistances experienced in indirect cooling systems [49]. Immersion cooling simplifies the system design and reduces the system's complexity [50]. But some disadvantages still exist, including the process of condensing evaporated vapor can be more complex and costly, and it

may also result in higher pumping losses when dealing with high-viscosity fluids. The fluid itself may be expensive, and there may be issues with its compatibility with certain materials. Additionally, using this fluid may add extra weight [48].

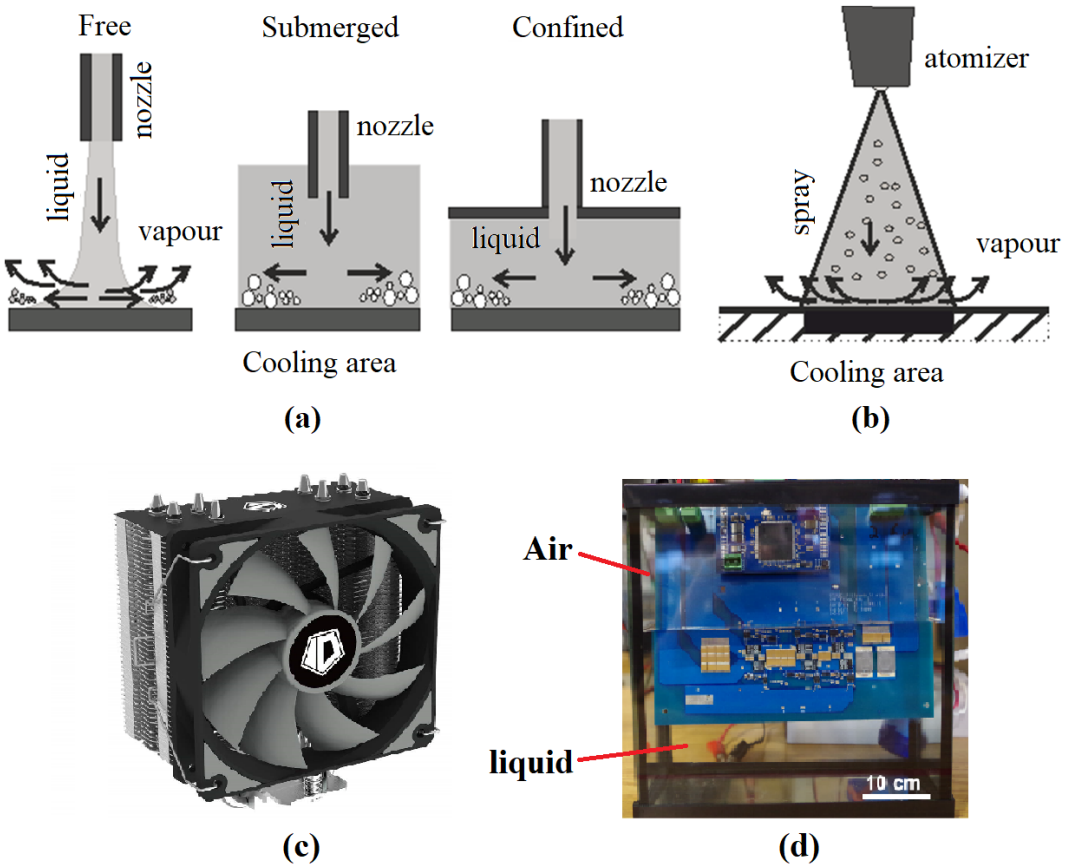

Figure 2.7 Direct cooling techniques. (a) jet cooling [43]; (b) spray cooling [43], (c) air cooling by fan [51]; (d) Immersion cooling for electronics [2].

2.3.2 Indirect cooling

- Air cooling through a pin-fin heat sink

A pin-fin type heat sink (Figure 2.8 (c)) usually made of high thermal conductivity material is an example of indirect air cooling. Its base surface attached to the heat-generating object absorbs the heat and boosts the temperature, pins are extended from its base to increase the heat transfer surface area. The air near the metal is heated, which causes the flow motion (natural convection) brought by density difference due to the temperature difference of air near the heat sink and the ambient. It can easily be combined with a fan to take advantage of forced air convection for better cooling performance.

- Phase change cooling

A phase change cooling system is a heat pump consisting of a compressor, a condenser, an expansion valve, and an evaporator, as depicted in Figure 2.8 (a). The phase change process

happens in the evaporator (cooling section) and the condenser. The evaporator is attached to the heat-generating object, the coolant absorbing a large amount of heat during phase change from liquid to vapor. It is employed for the cooling of computing equipment [52]. But it is less stable, more difficult to control, and with higher cost compared to single-phase liquid cooling which will be introduced below.

- Single-phase liquid cooling

Single-phase liquid cooling is a relatively simple method for indirect cooling a heat-generating surface via a heat sink. Unlike the pin-fin structure for indirect air cooling (Figure 2.8 (c)), the heat sink for liquid cooling usually has confined channels, the liquid coolant flowing inside to bring out the generated heat by forced convection (without phase change). It is usually composed of inlet(s), outlet(s), and the main body (design domain) where the heat dissipation mostly happens. The main body of the liquid-cooling heat sink could have many designs and geometries, which will be introduced in detail in the later sub-section. As a simple and easy-to-implement cooling technique, single-phase liquid cooling by forced convection is broadly applied to various industries. Compared to natural convection, the heat transfer capacity is much higher owing to liquid forced convection. Compared to jet or spray cooling, the effective cooling surface area is much larger with a lower cost of the device. And compared to phase-change cooling, liquid cooling using a heat sink also has many advantages, including higher compactness and hardware reliability, lower system complexity and cost, etc. [53].

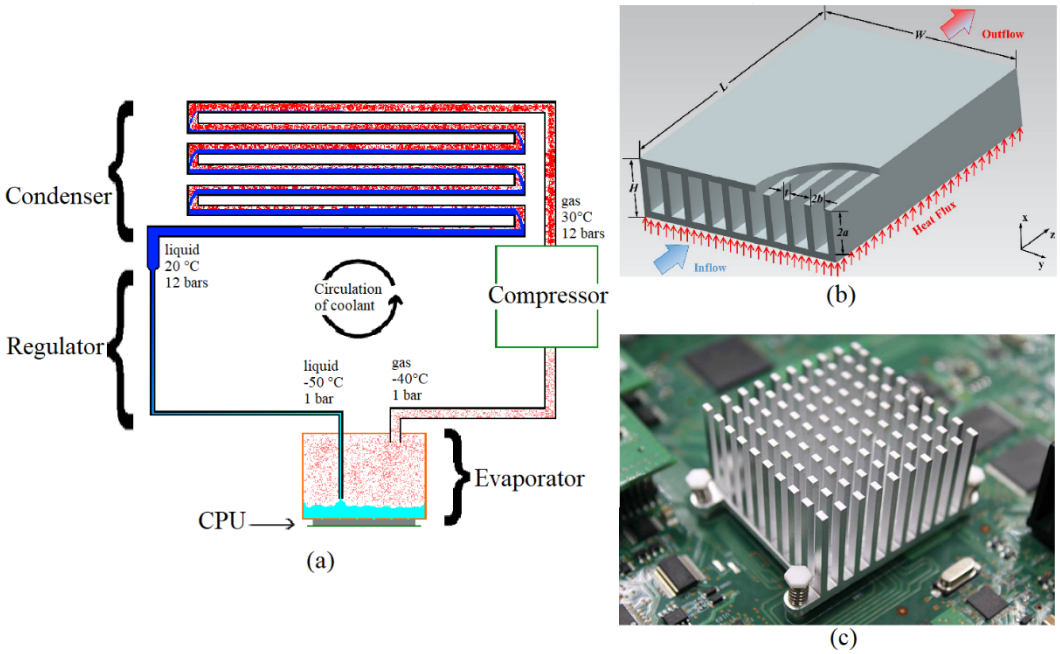

Figure 2.8 Indirect cooling techniques. (a), Principle of phase-change cooling [52]; (b) Single-phase liquid cooling using a straight channel heat sink [54]; (c) a pin-fin structure heat sink for indirect air cooling [55]

In the following of this thesis, we will only focus on the heat sinks for the single-phase liquid cooling system, especially their design and structural optimization. Many research

studies [56–59], reported that the performances of a heat sink depend strongly on the flow channel geometries/topologies, i.e., how the fluid flow paths are arranged and organized. These aspects will be introduced in detail in the following chapter 2.4.

2.4 Heat sink design and optimization

According to the channel structure of the main fluid domain, heat sinks for liquid cooling can be classified into several basic types, including parallel straight channels, pin-fin structures, and complex structures. Some variants also exist, as shown in Figure 2.9.

A parallel straight channel heat sink is one of the most common and conventional structures of which the main fluid domain is constructed by several parallel straight channels (Figure 2.9 (a)), with a thin solid separating wall between two channels. For electronic cooling, the channel characteristic dimension is usually at the micro or millimeter scale to take the high heat dissipation ability and the compact size. A usual variant in this category is the wavy/serpent channel shape (instead of straight channels) as displayed in Figure 2.9 (b). Such channel geometry aids to enhance heat transfer by creating secondary flows and recirculation zones [60]. Moreover, cavities channels are also proposed with obstacles in the middle of the channel, creating the split-recombine flow patterns (Figure 2.9 (d)). Similarly, ribs can be attached to the interior wall of the straight channels (Figure 2.9 (e)), helping to create local vortices and recirculation. Compared to the basic parallel straight channel type, higher thermal performance could be achieved by these variants, but always at the cost of a higher pressure drop (pumping power). Many researches have been published on the size and/or shape optimization of the unit enhancement elements (e.g., a rig, a cavity, etc.). Readers are invited to refer to the review paper [61] [62] for more details. For these parallel channel-type heat sinks, another factor that greatly influences their thermal and hydraulic performances is the flow (mal)distribution, which is in close relation to the inlet/outlet position (s) and the shape of the distributor and collector [63] [64]. While the uniform flow distribution is often the target to achieve for cooling an evenly heating surface, the uneven heating surface with multiple heat sources changes and complicates the rule. Research on this topic will be further reviewed and analyzed in the following section 2.4.1. Moreover, the channel cross-sectional shape can also be subjected to optimization; some relevant work will be summarized in section 2.4.2.

A pin-fin heat sink (Figure 2.9 (c)) is another typical category for which the flow domain is generally a cavity filled with an array of fins usually having the same height. The fin shape could be rectangular, triangular, circular, or others. The shape, the spacing, and the arrangement of fins all have influences on the performances of the heat sink, thereby being subjected to optimization. More studies on the pin fin structure optimization in the literature are reviewed in section 2.4.3.

The last category of the heat sink combines two or more above-mentioned enhancement structures, for instance, cavity, rib, and parallel straight channel as shown in Figure 2.9 (f), or a porous medium (metal foam) structure in general. Again the penalty on the pressure drop

should be specially considered despite the usually better thermal performance. Worth noting for this category is a new trend that recently emerged but rapidly becomes the focus of attention. For these complex heat sinks, their flow channel is not based on some pre-defined geometries (parallel channel, pin-fin, etc.), but is usually a result of topology optimization. Some real examples may be found in Table 2.1 and more discussion on this topic will be given in section 2.4.4.

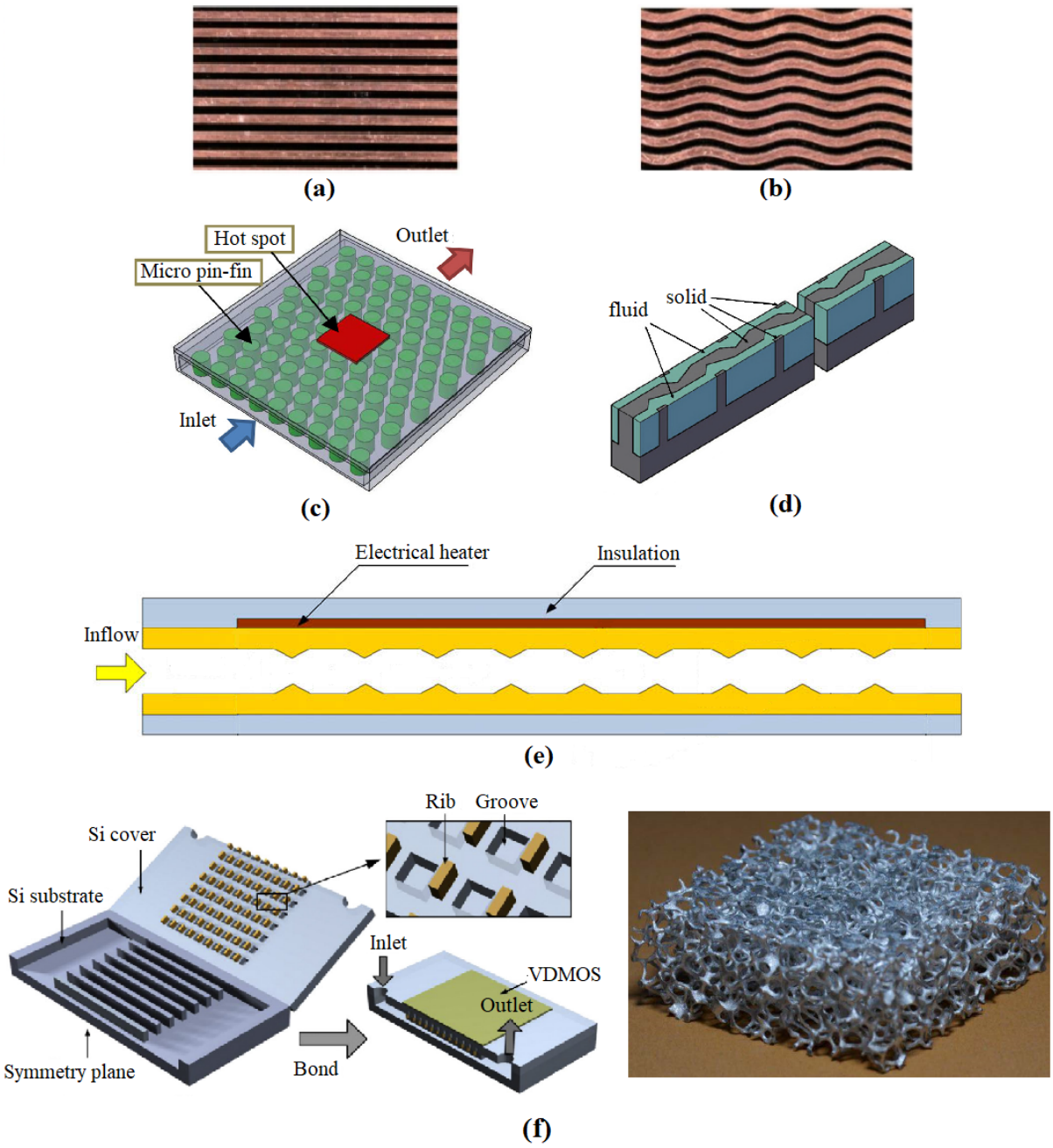

Figure 2.9 Different categories and variants of heat sink for liquid cooling. (a) Parallel straight channel[60]; (b) Parallel wavy channel [60]; (c) Pin-fin structure [65]; (d) Straight channel with cavities [66]; (e) Straight channel with ribs [67]; (f) Complex (hybrid) structure [68,69].

2.4.1 Flow distribution optimization/investigation on parallel straight channel

Among various structures of heat sinks for electronic cooling, the parallel straight micro/mini channel configuration is the most widely used because of its simple geometry, high cooling performance, cost-effective fabrication, and easy implementation [70]. It usually comprises single inlet and outlet ports, inlet/outlet manifolds, and a multitude of micro/mini-channels in the middle. Due to their geometric specificity, the presence of the coolant flow mal-distribution may result in the thermal performance deterioration of the heat sink and the formation of localized temperature hot spots in the electronic device [71]. Therefore, one important issue that attracts great attention is how to properly deliver and distribute the cooling fluid across the parallel micro/mini channels to ensure optimal cooling performance. Plenty of research has been devoted to achieving uniform flow distribution in parallel channel heat sinks under the assumption of an even heating surface. These researches can mainly be classified into three categories: (1) arrangement of heat sink inlet/outlet positions or the injecting angle (Figure 2.10); (2) design and structuration of the manifolds (headers); (3) shape modification of the parallel channels.

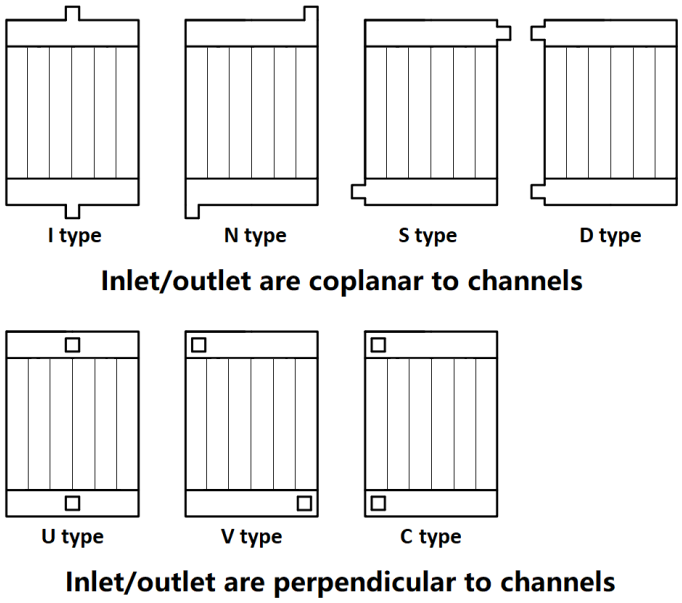

Figure 2.10 Different arrangements of global inlet-outlet position for parallel straight channel heat sinks [72].

Kumar and Singh [73] numerically tested the effect of the flow inlet angle between the inlet port and the parallel channels (theta = 90°, 105°, and 120°) on the flow distribution non-uniformity and the thermal performance of a mini channel heat sink. It was found that the inlet angle of 105° provided the best flow uniformity and the best thermal performance under uniform heating conditions. Manikanda Kumaran et al. [74] experimentally and numerically studied the locations of inlet/outlet (U, C, V, S, and D types as shown in Figure 2.10 on the flow distribution non-uniformity. Their results showed that the main reasons for non-uniform flow distribution were the presence of secondary flow, flow separation, and re-circulation in the manifolds. Among the tested heat sink types, the C-type arrangement exhibited the best

flow distribution uniformity whereas the V-type heat sink had the poorest. Similarly, the effect of inlet/outlet arrangement was numerically studied by Chein and Chen [75]. They found that the velocity distribution is less uniform for the heat sinks with coplanar inlet/outlet tube and parallel channels (I, N, D, and S type in Figure 2.10) than those with vertical fluid supply and collection (U and V type; i.e. inlet/outlet tubes are perpendicular to the parallel channels). Kumar and Singh [71] investigated different types of flow arrangement, and their numerical results showed that I-type flow arrangement could provide better thermal performance for uniform heating than D-type heat sink having a more uniform flow distribution. Chen et al. [76] investigated various positions of the inlet region and the outlet region of an air-cooled battery thermal management system (BTMS), The results showed that the symmetrical BTMS with the inlet and outlet located in the middle of the plenums achieved high cooling efficiency.

Manikanda Kumaran et al. [74] also numerically and experimentally tested different header shapes (rectangular, triangular, and trapezoidal) and header sizes. Their results showed that the triangular inlet header and the trapezoidal outlet header provided better flow uniformity than others. Many other novel header designs [74,77–80] have also been proposed and tested, as summarized in the review paper by Ghani et al. [81]. Different from the studies on the inlet header shapes, Song et al. [82] proposed adding a staggered pin-fin array in the inlet header of the water-cooled heat sink (Figure 2.11 (a)). The influences of different pin-fin arrangements in trapezoidal or rectangular inlet headers on the flow distribution uniformity among the mini-channels were numerically assessed. Liu and Yu [83] proposed a non-uniform-sized mini-inlet baffle to artificially control the mass flow rate of the working fluid in the mini-channels (Figure 2.11 (b)). Hou et al. [84] proposed a built-in spiral baffle in the inlet manifold of a mini channel heat sink to achieve the uniform distribution of flow. In the study [85], Fatahian inserted thin layers of porous media at the inlet of distribution tubes to address the flow mal-distribution in a parallel-flow heat exchanger. A parametric study was conducted to evaluate the effect of porous media geometrical parameters (Figure 2.11 (c)). Gilmore et al. [86] optimized compact and adaptable manifold configurations for achieving uniform flow distribution with minimal pressure drop. Their numerical results showed that both the flow distribution uniformity and the temperature uniformity at the heating base wall could be improved by using the appropriate baffle. Nevertheless, no optimization procedure has been proposed to determine the best baffle or obstacle geometries.

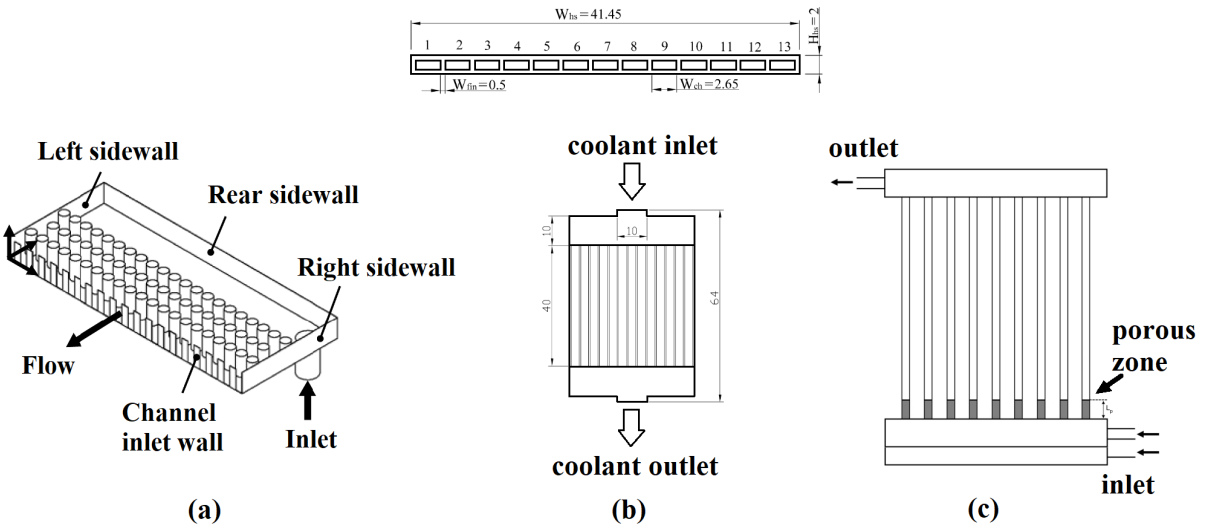

Figure 2.11 Design and structuration of the manifolds (headers) by (a) pin-fin structure [82] **(b) baffle** [83] **and (c) porous structure** [85]**.**

The geometry of the heat sink channel is also considered a design parameter in many studies to adjust the flow distribution. Dhahad et al. [87] showed a decreased flow non-uniformity with decreasing header/channel area ratio. Mu et al. [88] proposed parallel channel water-cooled heat sinks with variable channel height. Their results showed that the temperature non-uniformity (T_{max}-T_{min}) could be reduced from 4.7 K to 0.97 K and the thermal resistance decreased from 0.03 $K \cdot W^{-1}$ to 0.028 $K \cdot W^{-1}$ by replacing the conventional channels with the variable height channels. Hao et al. [89] numerically investigated the effect of geometry parameters (number of channels, channel width, and channel length) of the fluid-cooled heat sink. Optimal values were determined for both flow distribution uniformity and maximum temperature reduction, using the orthogonal experiment design method. The effects of different channel dimensions (parameters) on the reduction of thermal resistance were numerically examined by Mitra and Ghosh [90], and the optimum dimensions of the water-cooled mini-channel heat sink modeled as fins on a substrate have been determined. To achieve the target flow distribution, the Design of Experiments (DOE) along with response surface optimization was used by Sogunuru et al. [91] to arrive at desired flow by introducing suitable orifices obtained by applying Multi-Objective Genetic Algorithm (MOGA). The study [92] developed a new predictive tool for quantitatively assessing flow mal-distribution in parallel channels based on the parametric effect. Their results showed that the magnitude of the relative influence of each variable on flow mal-distribution could be expressed in the following order: header length > channel height > connection tube diameter > total volumetric flow rate > channel width. Narendran et al. [93] evaluated the potential of ribs and inertial-based spillway channels to overcome the flow mal-distribution issue. They found that The ribbed inclined channel was found to perform better than other types and developed a 33 % lower center channel velocity than the normal channel.

All the above-mentioned studies aimed at *achieving uniform flow distribution under the assumption of uniform heat flux* at the base wall of the heat sink. But in reality, the heat flux profile generated by the electronic devices is not uniform, instead, it has multiple heat sources

and presents multiple-peak heat flux just as we presented in section 2.2. Under these circumstances, the intentional flow non-uniform distribution may be a better option to be adopted to decrease the local maximum temperature, as pointed out by Kumar and Singh [71]. This is actually in line with some observations reported in the literature [94–96] in that the optimal flow distribution is usually not uniform but obeys certain trends subjected to a defined optimization objective and constraints. In this regard, Kumar and Singh [71] indicated that the flow arrangement and the actual flow distribution should fit the heat flux shape to achieve a better thermal performance, i.e., lower maximum temperature and thermal resistance. *y*et, no optimization method has been developed so far to determine the optimal flow distribution profile.

The above literature survey indicates that systematic and quantitative studies addressing flow and temperature distribution characteristics in the parallel micro/mini channels heat sink under non-uniform and multiple-peak heat flux conditions are still lacking. In particular, the relation between the optimal flow distribution of cooling fluid and the non-uniform heat flux shape is unclear. Moreover, investigations on the development of effective methods to determine and realize the most adapted flow distribution in parallel channel heat sinks are needed.

2.4.2 Channel cross-section optimization

For parallel straight channel heat sinks, a channel cross-section shape is also an optimization object. Note that the difference between the flow distribution optimization and the channel cross-section shape optimization is that the former targets adjusting the amount of mass flow in every channel whereas the latter focuses on the cross-section shape of a single channel or the shape of the entire heat sink cross-section. An identical cross-section shape is then extruded along the flow direction to form the whole channel length. According to the design parametrizations, the works in this domain could be classified into three classes as presented in Figure 2.12 (a). Single channel cross-section geometrical parameters optimization based on a predefined simple geometry [97–107]; Figure 2.12 (b). Single channel cross-section shape optimization [108,109]; and Figure 2.12 (c) Heat sink entire cross-section topology optimization [110]. The key step for optimization is to build the relationship between the design variables and the objective function, either by direct physics analysis or by constructing a surrogate function.

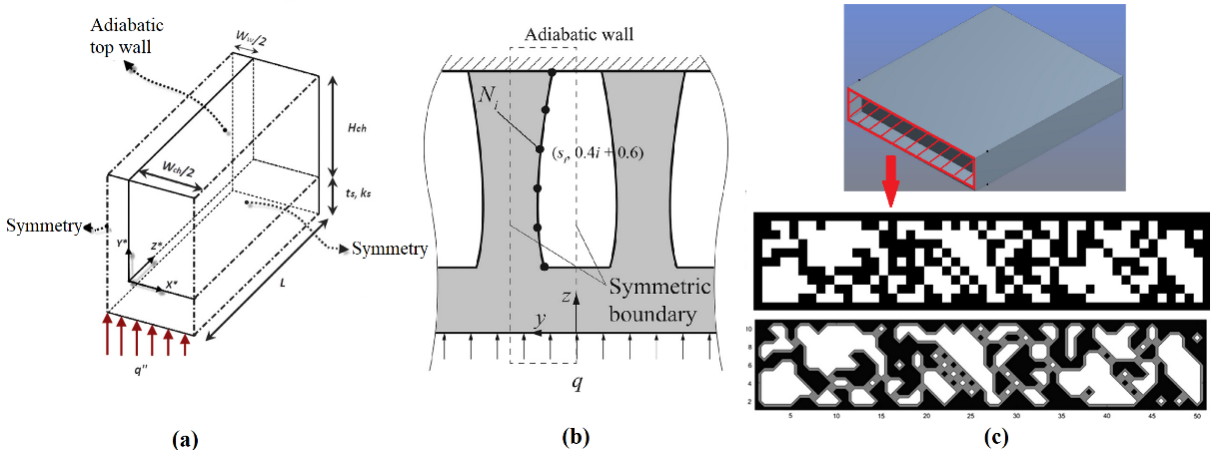

Figure 2.12 Different types of heat sink cross-section optimization: (a) Single channel cross-section geometrical parameters optimization [101], (b) Single channel cross-section shape optimization [109], and (c) entire cross-section topology optimization [110].

Owing to its predefined and simple geometry, the size/parameter optimization of channel cross-section is the only class possible to establish explicit analytical relations between the design variables and the objective function based on some physical models. For example, Shao et al. [97] optimized the number, width, and height of microchannels, as well as the thickness of the solid separating walls for a conventional parallel straight microchannel heat sink. A genetic algorithm (GA) has been applied based on the analytical relations between these variables and objectives (both thermal resistance and pressure drop). Other studies in this line have also been performed [111], usually assuming fully developed laminar flow and simplified heating boundary (e.g., constant Nusselt number). But for more complex heat sink geometries or real operating conditions, the surrogate function has to be built. One of the approaches frequently applied for this purpose is the response surface analysis (RSA) [98,112,113]. For example, Karathanassis et al. [98] used GA to optimize the channel width and solid wall thickness to minimize both the thermal resistance and the pressure drop. The conjugate-gradient method is often used for channel cross-section optimization [102–105]. The number of channels, the channel aspect ratio, and the channel-to-pitch ratio are usually considered design variables, and the total thermal resistance is considered as the (single) objective criterion under the constraint(s) of fixed pressure drop or pumping power. GA method is usually used for multi-objective optimization. For example, Salma Halelfadl et al. [100] used an elitist non-dominated sorting genetic algorithm (NSGA-II) to optimize the channel aspect ratio and wall aspect ratio. Lin et al. [101] employed the CFD-based (COMSOL) GA method to design and optimize the channel aspect ratio and the ratio of the channel width to pitch, with the objectives of minimizing the thermal resistance and the weight of the heat sink. Similar CFD-based GA approach may also be found in study [114]. More recently, Rao et al. [106] proposed a novel algorithm named ‘Jaya’ which relates the design variables and obtained by the RSA in the form of a polynomial expression. They compared the optimization result of the Jaya algorithm with the results obtained by the TLBO algorithm and a hybrid multi-objective evolutionary algorithm (MOEA) and numerical analysis, and it turns out to be better than the result obtained by the Jaya algorithm. To minimize the thermal resistance and pressure drop of a straight square/circle microchannel heat sink, a non-dominated sorting genetic algorithm (NSGA-II) was applied by

Ghazali-Mohd et al. [99]. The Colburn factor and Fanning factor which are the main difficulties for the expression of the objective function (unit entropy production) were calculated by multiple regression analysis of the numerical simulation by *y*in et al. [107].

Relatively fewer studies are focused on the shape optimization of the channel cross-section. In the study of Foli et al., [108] the shape of the separator in the heat exchanger was represented by two non-uniform Rational B-splines (NURBS) [115] as the design parameters. A CFD-based MOGA method has been used considering both the heat transfer and the pressure drop. Similarly, the optimization method used by Ge et al. [109], by describing the cross-sectional shape of a straight mini-channel heat sink was by six variables. Their results indicate that the pumping power could be effectively reduced without significantly increasing the thermal resistance by modifying the rectangular cross-section shape to a curvy boundary shape (Figure 2.12 (b)).

There are two papers have been performed on the topology optimization of the heat sink cross-section (Figure 2.12 (c)) to the best of our knowledge. The one [110]. presented in Figure 2.12 (c)) discretizes a heat sink cross-section into a grid space, and a micro-genetic algorithm is applied to produce optimum shapes for liquid-cooled heat sinks represented as bit arrays based on the system entropy generation rate. In the other research article [116], Gilho Lee et al. propose a topology optimization method for maximizing the thermal performance of a heat sink with an axially uniform cross-section cooled by forced convection under the constraint of fixed pumping power. It is shown that the proposed topology optimization method can be used to design lighter heat sinks with higher thermal performance for practical applications. It should be noticed that this approach differs from the topology optimization of the flow channel configuration to be discussed later, since once optimized, the same cross-section topology is kept all along the channel length direction. It optimizes actually the mass flow distribution inside the heat sink without the parallel channel presetting, providing thereby the same prospects as tailoring the flow distribution to address the multiple-peak heat flux cases.

2.4.3 Fin-shape and arrangement optimization for pin-fin heat sinks

Pin fin structure is commonly used for heat sinks due to its large solid and fluid heat transfer surface area. Conventional pin-fin heat sinks usually have simple, regular, and uniform fin shapes (e.g., cuboid, cylinder, etc.), and the space between them in the structure is also uniform. To further improve their thermal/hydraulic performances, many studies have been devoted to the optimization of a pin-fin geometrical structure. Some of them are focused on size optimization while others optimize the pin shape and/or arrangement based on a predefined pin geometry or through mathematical parametrization. Except for that, it is found that TO is also applied in pin-fin optimization.

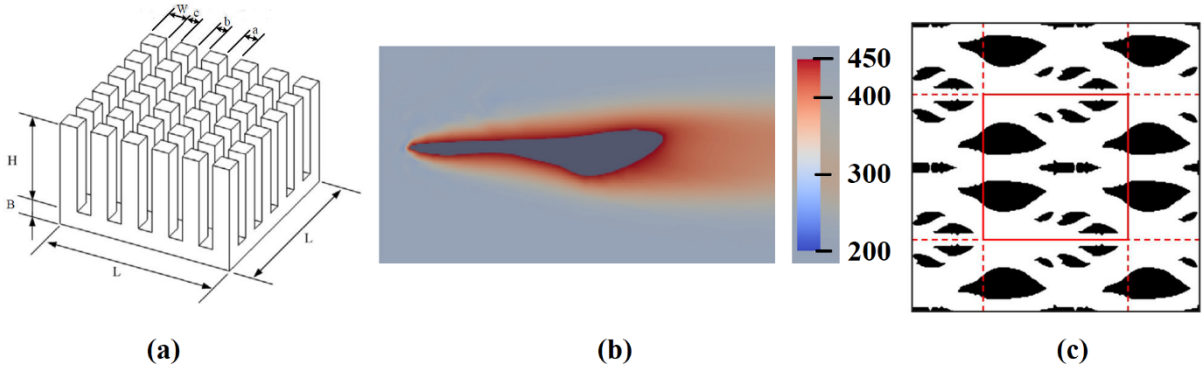

Figure 2.13 Heat sink (a) pin-fins size and spacing arrangement [117], (b) fin-shape [118], and (3) fin TO optimization [119].

The size optimization of the pin-fin structure is relatively simple. It is usually based on simple pin geometry (cuboid or cylinder), and this basic geometry does not change during optimization. The design variables could involve the number, the height, the width/length (or diameter), or the spacing/pitch of pins [120], while the optimization objective(s) could consider both thermal and hydraulic performance indicators of the heat sink. Different optimization methods have also been used for this purpose, either based on simplified physical models or assisted by CFD simulation. For example, the Levenberg Marquardt Method design algorithm was used by Huang et al. [121] to optimize the heights and widths of non-uniform fins, and the thermal resistance decreased by 10.53% compared with a uniform pin-fin structure. A similar study has been performed by Yang et al. using the Taguchi method [117] (Figure 2.13 (a)) or using the GA coupled with RSA [122]. Chen et al. [123] applied the direction-based GA to search the optimal fin design variables for lower entropy generation and material cost. Slightly different pin geometrical design variables (pin-fin porosity and pin-fin located angle) were considered in the study of *Z*hao et al. [124], using the proposed geometry optimizing method The kriging method was employed by Nemati et al. [125] to generate the response surface for the output parameters, and a MOGA approach was used to perform the multi-objective optimization (entropy generation, pressure loss). Polat et al. [126] optimized the arrangement (porosity) of pins with different shapes (circular, square, and diamond) to minimize the pressure drop and maximize the Nusselt number, using the MOGA method. The formula of the objective functions (the time constant of the solid matter's response time when there are external heat disturbances and the pressure drop of pin-fin heat sink) design variables (inner spaces of pin-fins) had been formed by the mathematical model by physical relations, and the real-coded genetic algorithm with a novel direction-based crossover operator was applied to achieve minimize the minimum time constant and pressure drop by Wang et al. [127]. All the above-mentioned studies are based on uniform heating surface. One exception is the study of *y*ang etc. [128], who optimized both the pin arrangement and pin geometry with localized heat sources, using a CFD-assisted GA method.

The shape optimization of a pin-fin heat sink modifies the boundary of a predefined or non-predefined pin geometry using certain optimization methods. For example, Ismayilov et al. [129] utilized the CFD-assisted MOGA to vary the hydrofoil pin-fin shape through flexible parametrization utilizing an ellipse and polynomials. Their results showed that with the novel

pin fin shape, the heat transfer enhancement would dominate over the pressure drop increase at higher Reynolds numbers. Recently, Keramati et al. [118] used a similar approach by defining the geometry with a composite Bézier curve parameterized by control points (Figure 2.13 (b)). the proximal policy optimization with deep neural network and CFD was applied to maximize heat transfer and minimize pressure drop. Results showed that a 30% improvement in overall heat transfer and a 60% reduction of pressure drop compared to the rectangle reference geometry could be achieved. Huang et al. [130] proposed a novel method to extract the wake flow contours in the channels as the geometry contours of the pin fin to enhance the thermal and hydraulic performances of the micro-pin-fin heat sink. The pin convection performance of the novel bream fin could be up to 34% higher than that of the original circular fin.

There is only one study [119] on the TO of a pin-fin heat sink (Figure 2.13(c)). Ghasem et al. developed a multi-objective topology optimization approach to optimize sink geometries to minimize thermal resistance and pressure loss. A dedicated pseudo-3D conjugate heat transfer model is utilized, by assuming periodic flow and fin design pattern. A pseudo-spectral scheme is used for the flow solution and the finite element method for the non-periodic conjugate heat transfer model. They found that the optimized topologies demonstrated superior cooling performances at lower costs of pressure losses compared to conventional (circular) in-line and staggered fins, and confirmed the supremacy of topology over pure sizing optimization.

However, due to the simulation and optimization complexity, these works on the pin-fin shape optimization are usually focused on a single pin shape, or at best one slice along the flow direction. The study addressing the cooling of a whole heat-generating surface in this regard seems still rare to the best of our knowledge by pin-fin shape and TO optimization. Fin optimization without a predefined shape only focuses on single-fin design. Moreover, the relatively simple geometry and array arrangement of the pin-fin structure may restrict the freedom to morph for the heat sink design, less flexible and diversified than the TO of the global flow channel configuration.

2.4.4 Topology optimization (TO) of global flow configuration in the heat sink

The TO of global flow channel configuration optimization allows organizing and arranging both the fluid and solid domains freely, i.e., creating solid islands or flow paths without any geometry presetting. Holding the highest design degrees of freedom, it has attracted enormous attention from both the academic and industrial communities and is regarded as a ground-breaking technique to obtain innovative designs of heat sinks (or heat exchangers in a general sense) with greatly improved effectiveness.

The TO process could generally include four basic stages [131]: (1) design parametrization, (2) heat transfer modeling, (3) optimization process, and (4) final realization. Based on the design parametrization, the TO for single-phase heat sinks may be classified into three types: density-based, level-set, and direct explicit. They differ from one another by different representations of optimization variables determining the design configurations that

establish the relationship between the design variables and the physical properties, e.g., the density distribution describing the flow paths in the density-based method [132]. Once parametrized, the design variables are mapped, interpolated, and updated iteratively to approach the optimum configuration. It involves the modeling of heat transfer (in fluid and solid phases) coupled with fluid flow to compute the distribution of state variables (pressure, velocity, and temperature) in each optimization iteration. Various solvers were implemented in decades, mainly including the finite element method (FEM), the finite volume method (FVM), and the lattice Boltzmann method (LBM), usually under the assumption of laminar, incompressible, and steady-state flow [133–135]. As for the optimizer, both gradient-based and non-gradient-based approaches can be used. Among them, the gradient method relates the design variables and objective function by a function and calculates the objective function's gradient and its stagnant point, generally using the adjoint method [136]. A combination of the density-based method, the FEM, and the gradient-based optimizer is the mainstream in the TO of heat sinks (or heat exchangers in general) [131]. It has shown good efficiency in handling optimization problems with a high number of design variables [137]. More information about these methods and relevant studies are presented and reviewed in the paper [131]. Some optimized examples in this line, and laboratory prototypes realized and tested can be found in Table 2.1. Nevertheless, such a TO strategy has some difficulties in handling numerical artifacts or descriptions of clear solid-fluid interfaces, and more importantly, it can be easily trapped into the local optimum [138]. On the contrary, some novel, gradient-free approaches, like genetic algorithm (GA) and Bayesian optimization, could overcome these deficiencies and converges towards a global optimum [139]. Moreover, the majority of the above-mentioned TO studies deal with the simplified 2D design domain (e.g., [140]). For those studies with 3D parametrization (e.g., [141],[142]), most of them are performed under uniform heating, with only several exceptions [143] addressing more complex (but more realistic) heating boundaries with multiple heat sources.

There are barely a few attempts on performing TO of global flow channel configuration in heat sinks using the non-gradient approach, mainly due to the complexity of modeling conjugate heat transfer and fluid flow, the difficulty in formulating the optimizer, and the high computational cost. Among them, Yoshimura et al. [144] proposed a Kriging surrogate model-assisted GA method on single-/multi-objective TO of cooling flow channel configurations. Later, the NSGA-II method has been coupled with the Kriging surrogate model to search for better designs of lattice-structured heat sinks regarding thermal performance and material cost [145]. Mekki et al. [146,147] developed and tested a GA-based TO method for thermo-fluid equipment in aerospace applications, but only the elementary fin shapes have been focused on using voxel representation. More recently, Yaji et al. [148] proposed a hybrid data-driven multi-fidelity topology design (MFTD) combining both density-based methods for the low-fidelity TO and NSGA-II to select the optimal Pareto front.

2.5 Experimental studies on the topologically optimized (TO) heat sinks

As an essential step from theory to practice, heat sinks with TO geometries should be realized and experimentally tested to validate the numerical model and algorithms on one hand, and to showcase the superior performances compared to conventional designs. However, due to its geometry complexity and irregularity, the fabrication would be more difficult and costly than a conventional heat sink with or without enhancement units. Therefore, only a few researchers have realized their TO structures, even with the rapid development of additive manufacturing (AM) techniques. Proper post-treatments on the TO-derived structures are often needed and some engineering simplified versions are tested in practice.

Table 2.1 presents a complete list of the manufactured and tested TO heat sinks reported in the open literature for single-phase forced convection cooling. The obtained and tested geometries shown in Table 2.1 are distinct from one another due to different objective functions and boundary settings, but usually involve the splitting and recombining of flow channels enclosing some solid islands. The prototypes are realized either by conventional manufacturing (e.g., CNC milling, laser cutting, etc.) or by Additive Manufacturing (AM). Conductive metal (e.g., aluminum, copper) is usually used to build a heat sink (solid part) while water is usually used as the coolant. Most of the tests are realized under ambient temperature and pressure and laminar flow condition, with only some exceptions [149–151] being extended to the transitional/turbulent flow regime. Worth noting is the fact that although uneven heating (multiple heat sources) has been addressed by some TO studies [152] by numerical simulation, it has never been configured in practice to the best of our knowledge: all the TO heat sinks are tested under uniform heating conditions.

Table 2.1 A summary of experimental studies on TO heat sink for single-phase forced convective cooling.

Paper ID	Photo of prototype and TO geometry	Optimization objective(s)/Constraint(s)	Fabrication method & heat sink material	Heating boundary/Input power	Thermal measuring method and locations	Coolant type and operation conditions	Main findings
Dede et al. (2013) [149]	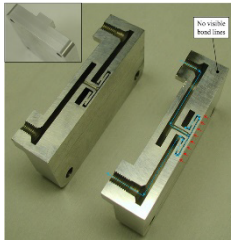	Not mentioned.	Micro-machining; Aluminum;	Uniform heat flux; Input power: 37.5 - 75 37 $W \cdot cm^{-2}$.	Heat sink base; near the heater; 2 K-thermocouples	50/50 ethylene-glycol/water mix. Inlet Re: 1270-6370; Inlet fluid temperature: >40 °C; Ambient temperature: 24.9 °C	Favorable cooling performance of TO-geometry with a lower unit thermal resistance (0.34 cm^2 K/W) and pressure drop (19.5 kPa at 1 L/min) for high-power-density (of order 100 $W \cdot cm^{-2}$) applications.
Zeng et al. (2018) [3]		Pressure drop (O); heat transfer performance (C)	CNC machining; Aluminum alloy 6061-T6	Uniform heat flux; heat flux density: 0.185, 0.37 $W \cdot cm^{-2}$.	Heat sink base temperature; 8 T-type thermocouples	Air. Inlet Re: 150-2850; Inlet fluid temperature: 20 °C	At 40 W heating power, the junction temperature of the TO heat sink is 5.5 K lower than that of RSC under the same pumping power of 0.065 W.

Li et al. (2019) [153]		Combination of heat exchange and total pressure drop (O)	CNC milling; Aluminum 6061	Uniform heat flux; Input power: 2.7 $W \cdot cm^{-2}$.	The top (cover) surface of the heat sink; Infrared thermal imager.	DI water; Inlet Re: 200-2200; Inlet fluid temperature: 20 °C	The maximum surface temperature of TO-geometry is 11.7% lower than that of RSC
Zeng et al. (2019) [152]		Pressure drop (O); average junction temperature (C)	CNC machining; Copper;	Uniform heat flux; Input power: 360 W (32mm×45mm×25 $W \cdot cm^{-2}$).	Heat sink base; T-type thermocouples.	DI water; Inlet Re: 187-1311; Inlet fluid temperature: 25 °C	>50% of pumping power saving for the same cooling requirements by TO-geometry compared to RSC.
Qian et al. (2021) [154]		Root mean square of the temperature in the design domain and the pumping power (O)	CNC milling; Heat sink material: not mentioned.	Uniform heat flux; Input power: not mentioned.	Top (cover) surface of the heat sink; Thermal Infrared Imager.	Water. Inlet Re: 30-100; Inlet fluid temperature: 20 °C; Ambient temperature: 20 °C	Temperature-dependent fluid physical properties have non-negligible effects on the TO conjugate heat transfer problem

Mo et al. (2021) [155]		The average temperature of the cooling plate surface and the pumping power dissipation (O)	3D printing technology; AlSi10Mg;	Uniform heat flux; Input power: 0.7 $W \cdot cm^{-2}$.	The top wall of the cooling plate; 9 K-type thermocouples.	DI water; Inlet Re: 256, 277; Inlet fluid temperature: 20 °C	47.9% lower pressure drop of TO-geometry compared to the traditional straight channel heat sink; The T_{max} of the TO-optimized cooling plate is at most 7.4 °C lower than that of the traditional straight channel heat sink.
Li et al. (2021) [150]	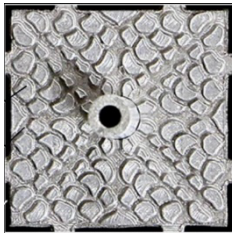	Average temperature (O); fluid void fraction and pressure drop (C).	Micro milling; Aluminum;	Uniform heat flux; Input power: 125 $W \cdot cm^{-2}$ (surface: 20 mm × 20 mm)	Bottom of the cold plate; 4 thermocouples.	Water; Inlet Re > 2300; Inlet fluid temperature: 25 °C Ambient temperature: 24 °C	Compared with the FEA-based TO method, the IGA (isogeometric analysis)-based approach achieves better results with higher calculation accuracy.

Lee et al. (2021) [151]	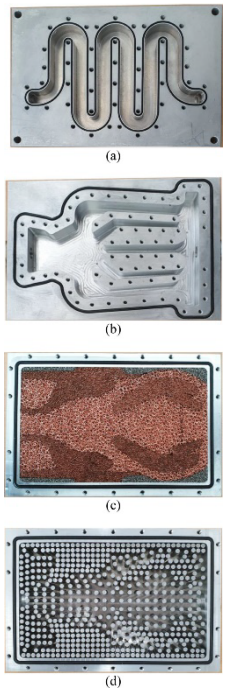 (a) (b) (c) (d)	Combination of pumping power dissipation and the average solid temperature. (O)	Laser cutting technique; Aluminum, copper;	Uniform heat flux; Input power: not mentioned.	Top (cover) surface of the heat sink; 3 K-type thermocouples.	Water. Inlet Re: 4000; Inlet fluid temperature: 50 °C	The pressure drop of the cylindrical pin fin model with a varying pitch based on the TO optimized results was reduced by 24% and the average temperature decreased by 9%, compared to the baseline model (the first model).
Han et al. (2021) [156]		1. Combination of temperature difference of substrate and pressure drop (O); 2. Combination of average temperature and pressure drop (O)	3D printing technology; Aluminum;	Uniform heat flux; Input power: 20 $W \cdot cm^{-2}$.	Substrate temperature (0.75 mm deep from the film resistors); 4 K-type thermocouples.	Water. Inlet Re:1000-2100; Inlet fluid temperature: 20 °C	The substrate temperature difference can be decreased by 57.35% by the TO-geometry compared to the reference spider web flow channel.

Zhou et al. (2022) [157]		1. Combination of temperature difference of the heat sink and pressure drop (O); 2. Combination of average temperature and pressure drop (O)	3D printing technology; Aluminum;	Uniform heat flux; Input power: 40 $W \cdot cm^{-2}$.	Wall of substrate temperature (0.5 mm deep from the film resistors); 4 K-type thermocouples.	Water. Inlet Re: 800-1280; Inlet fluid; Temperature: 20 °C	Up to 42.48% reduction in the temperature difference for the TO-geometry compared to the RSC heat sink
Zhou et al. (2022) [158]		The average temperature of the design domain (O); pressure drop (C).	Micro milling; Copper;	Uniform heat flux; Input power: 18-45 $W \cdot cm^{-2}$. (surface: 26 mm×30 mm).	Bottom of the flow channels; 3 K-type thermocouples.	DI water; Inlet Re: 171-1715; Inlet fluid temperature: 20 °C	7.1–15.2% reduction in the thermal entropy generation rate for the TO-geometry compared to CEBTO-generated MCHS (microchannel heat sink).
Chen et al. (2022) [159]		The average temperature of solid (O)	NC machining; Al5083	Uniform heat flux; heat flux density =1 $W \cdot cm^{-2}$.	Upper cover of the heat sink; Infrared thermal imager	DI Water; Inlet Re: 300-2100; Inlet fluid temperature: 20 °C	The better cooling effect of TO geometry than that of the straight channel heat sink. T_{peak} at plate surface reduces at most about 5 K under max. inlet *Re*.

Commonly the coolant flow rate, the overall pressure drop, the fluid inlet, and outlet temperatures, and the temperatures at specific locations of solid walls are measured to characterize the global thermal and hydraulic performances of the TO heat sink. Some more words on the measurement technique of temperature (field) of the solid part, which can be classified into direct and indirect methods. For the direct method, several thermocouples are installed at the specific locations of the heat sink, usually close to the heat source. Nevertheless, only a limited number of points can be recorded by the thermocouples [155], but usually insufficient to correctly reconstruct or represent the temperature field of a certain surface (e.g., heating surface, fluid channel wall, etc.). To overcome this drawback, an Infrared thermal imager has been adopted by some researchers [153,154,159] as an indirect method to measure and record the temperature field of a target surface. However, only the upper cover of the heat sink has been measured due to technical difficulties. This measuring surface is far away from the heating surface, with a smaller temperature difference, and thus cannot reflect the situation of the locations of interest. It should be noted that the local flow and temperature distributions of the cooling fluid in the TO heat sinks, which are of great interest in understanding the optimized geometries and their performances, *have never been characterized by experiments to the best of our knowledge*.

Regarding the global performance of the tested TO-heat sinks, some of the experimental studies (cf. Table 2.1) include a reference prototype (usually parallel-straight channel heat sink) for comparison, while others focus on the improvement of the TO geometry itself or the proposition of a new treatment.

2.6 Conclusion

In this chapter, an extensive literature review has been presented on the design and optimization of heat sinks for the cooling of a heating surface with multiple heat sources. The main conclusions can be summarized as follows:

- **Non-uniform heating with multiple heat sources** commonly appears in electronic devices due to the stacking/array arrangement of functional units for higher power or capacity. Such multiple-peak heat flux condition, compared to uniform heating or single-peak heating, is more likely to cause the overheating problem of electronics, bringing about serious issues like reduced working efficiency, device shut-down, reduced lifetime, irreversibly component deterioration, or even thermal runaway.
- Consequently, an efficient thermal management approach is essential for cooling the non-uniform heating surface with multiple heat sources. Plenty of solutions exist for the thermal management of electronics. Among the above methods, **single-phase cooling** based on forced convection is found to be an efficient, compact, simple, low-cost, and safer technique for this purpose.
- Conventional heat sinks for single-phase cooling can be classified into parallel channel, pin-fin, and complex types, with different variants having been proposed and developed for heat transfer enhancement. In particular, the thermal and hydraulic performances of

heat sinks can be further improved by adopting size, shape, or topology optimization methods. Research efforts have been made on (1) flow distribution uniformization or control for parallel straight channel heat sinks; (2) channel cross-section shape optimization; (3) pin-fin shape and arrangement optimization; and (4) TO of global flow configuration in the heat sink.

- The TO of global flow channel configuration involves reallocating organizing and arranging both the fluid and solid domains without a predefined geometry. Currently, the most popular TO method is a combination of the density-based design parametrization, the FEM for heat transfer modeling, and the gradient-based optimization algorithm. While this type of TO strategy is fast and straightforward, it also suffers from some problems like local optimum trapping, vague fluid-solid boundary, conjugate heat transfer modeling inaccuracy, etc.
- Experiment testing of TO heat sinks is an essential step to validate the numerical modeling and optimization method. Only a few TO geometries have been manufactured and tested in practice. Thermocouples are often used to measure the solid temperature near the heaters while an IR camera is also employed but only to measure the temperature distribution on the top cover surface of the heat sink. The global thermal and hydraulic performances of the TO heat sink are often compared with those of a reference (straight channel) heat sink to showcase the design advantages.
- The parameters usually chosen to measure for a single-phase heat sink experiment are inlet flow rate, inlet/outlet temperature, pressure drop, and temperature on the heat sink surface. No research papers on heat sink experimental studies measure the detailed **temperature or velocity fields inside the fluid** domain **under the uneven heating condition of multiple heat sources**. Almost no research paper on the experiment of topology optimization heat sink compares a benchmark straight channel heat sink and its size optimization with topology optimization.

Various research gaps can be identified facing this multiple-peak heat flux issue, a problem commonly existing in modern electronics, but insufficiently addressed in the literature:

(1) Lack of optimization method to tailor the fluid flow distribution for conventional parallel straight channel heat sinks under multiple-peak heat flux;

(2) Lack of gradient-free approaches (e.g., GA) for the TO of global flow channel configuration for forced convection problem with coupled fluid flow and heat transfer;

(3) Lack of fine experimental characterization of TO heat sinks under uneven heating with multiple heat sources, especially the local flow and temperature characteristics of cooling fluid;

(4) Lack of performance comparison between heat sinks optimized by different methods or under different optimization criteria/constraints.

These identified literature gaps are strong motivations for us to perform the research of this Ph.D. thesis by using different numerical and experimental approaches, to be presented in the following chapter.

Chapter 3: Tailoring the fluid flow distribution in a parallel mini-channel heat sink under multiple-peak heat flux

Chapter Summary

This chapter addresses the optimization of fluid flow distribution in parallel mini-channel heat sinks subjected to a non-uniform multiple-peak heat flux to eliminate the temperature hotspots. A 3D heat sink comprising 16 parallel straight mini-channels is used as a model for the study, each mini-channel having the dimension of 1 mm in width, 2 mm in height and 34 mm in length. In particular, an original size/shape optimization algorithm is developed to adjust the inlets of these mini-channels according to the temperature distribution on the heating base surface. The fluid flow distribution is thereby tailored, leading to the reduced peak temperature on the heating surface. The effectiveness and robustness of the optimization algorithm are tested and discussed.

Results obtained show that the maximum temperature can be reduced by 10 K and 7 K for two-peak and five-peak heat flux cases, respectively, by using the proposed optimization method. The heat sink configuration with optimized channel inlets could always provide smaller thermal resistance than that of the equal channel inlet configuration under different average heat flux or total mass flow-rate conditions. At the same pressure drop, tailoring the flow distribution of the cooling fluid is more effective in reducing the thermal resistance than simply increasing the mass flow rate of the cooling liquid. This optimization method, simple and straightforward to implement as it is, could also be generalized as an efficient thermal management technology for electronic cooling.

Keywords of the Chapter:

Mini-channel heat sink; Fluid flow distribution; Temperature hot spots; Multiple-peak heat flux; Thermal management; Size/shape optimization.

3.1 Introduction

Being a conventional structure, parallel micro/mini-channel heat sinks are widely and commonly used for the efficient cooling of electronic devices. The cooling fluid is usually injected into the single inlet port, divided and distributed into parallel straight channels, and finally collected from the single outlet port. Due to such geometric specificity, the flow distribution among the parallel channels is naturally an essential characteristic that determines the cooling performance: the coolant maldistribution may result in the thermal performance deterioration of the heat sink and the formation of localized temperature hotspots [73,81]. In chapter 2.4.1 it has been shown that almost all the studies on this issue in the literature target achieving a uniform flow distribution among channels based on the assumption of uniform heat flux generated by electronics. Unfortunately, this assumption is not accurate for many real devices especially with high integration levels and array arrangement, as has been reviewed in detail in chapter 2.2). The only exception is the study of Kumar & Singe [71] which addressed the uneven heating condition and proposed that the flow arrangement and the actual flow distribution should fit the (non-uniform) heat flux shape to achieve a better heat sink thermal performance. *y*et no optimization method has been developed so far to determine the optimal flow distribution profile. A systematic and quantitative exploration of the optimal flow distribution under non-uniform and multiple-peak heat flux conditions is still lacking.

In this chapter, we seek to fill this research gap by tailoring the flow distribution of the cooling fluid in parallel mini-channel heat sinks subjected to non-uniform multiple-peak heat flux, to minimize the peak temperature on the heating surface. For this purpose, a 3D heat sink comprising 16 parallel straight mini-channels is used as a model for the study. Non-uniform heat flux with multiple Gaussian peaks is set to the base heating surface of the heat sink to represent the real hot spots generated by the electronic devices. An original optimization algorithm is developed to adjust the channel inlets of the mini-channels according to the temperature distribution on the base surface. Consequently, the fluid flow distribution among the mini-channels is tailored step by step, reducing the peak temperature (global thermal resistance) of the heat sink. The effectiveness of the optimization algorithm will be illustrated and discussed through various numerical examples.

It should be noted that acting on the channel inlets (also called perforated baffle in some studies) to regulate the flow distribution among parallel channels or tubes is not new but has been proposed and proven to be effective by many researchers [83,160–162]. But most of them use homogeneous or non-homogeneous insertion baffle as a convenient way to improve the flow uniformity. In an earlier study of our research group (Ph.D. thesis of Dr. Min WEI, 2015) [163], the baffle geometry has been optimized to generate non-uniform flow distributions for absorbing heat in a high-temperature solar receiver. But the heat flux considered is a single-peak Gaussian shape and the targeted flow distribution profile is predefined. The current study goes a step further by addressing the multiple peak heat flux condition, with a necessary extension of the previous optimization algorithm developed in-house [96,161]. The peak

temperature of the heating surface is minimized by directly adjusting the widths of the channel inlets; the resulting flow distribution profile is thus consequential and adapted.

3.2 Methodology

In this section, the heat sink model and optimization algorithm are first presented. Then the computational fluid dynamics (CFD) parameters for numerical testing and the performance indicators are introduced.

3.2.1 Heat sink model

Figure 3.1 shows the geometry and dimensions of the heat sink model used in this study. The core part of the heat sink is a cuboid solid monoblock, with overall dimensions of 54 mm in length (*x*-direction), 54 mm in width (*y*-direction), and 6 mm in height (*z*-direction). It has a U-type flow arrangement (cf. Figure 2.10), with a single inlet and outlet tube (i.d.: 5 mm) aligned with the central line, perpendicular to the heating surface (and the cooling parallel channels). The length of the global inlet/outlet tubes is 18 mm and the distance between their centers is 45 mm. Between the global inlet and the outlet tubes, the fluid domain consists of three sections: the inlet distributing manifold, 16 parallel straight channels, and the outlet collecting manifold. Both the inlet and outlet fluid manifolds have a rectangular shape of 50 mm in length, 8 mm in width, and 2 mm in height. Mini channels with a rectangular cross-section of 1 mm in width and 2 mm in height are arranged in parallel, connecting the inlet manifold and the outlet manifold. The distance between the axes of two neighboring channels is 3 mm and the total length of the straight mini-channels is equal to 34 mm. For the convenience of description, these channels are indexed by *i* from 1 to 16 along the *x*-direction. The inlet of the mini-channels (2 mm in length) is subject to enlarging or narrowing by the optimization algorithm to adjust the mass flow rate of the cooling fluid flowing inside.

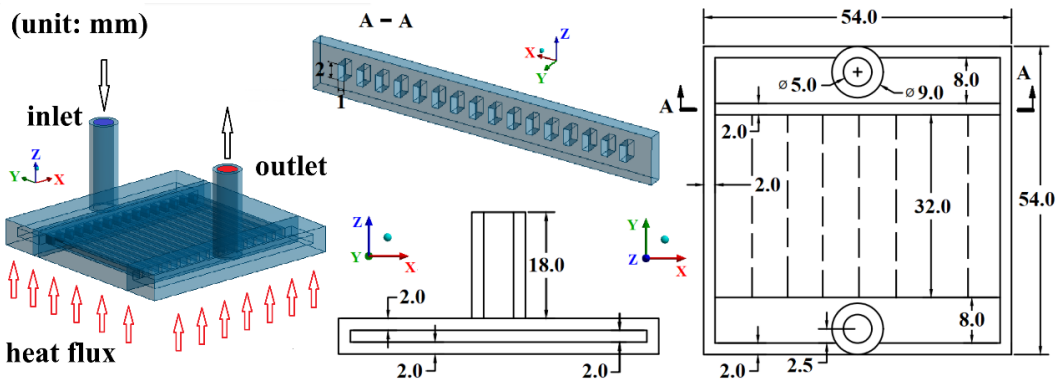

Figure 3.1. Schematic view and dimensions of the heat sink model (unit: mm)

The wall thickness of the solid envelope that encloses the fluid domain is equal to 2 mm. The base wall of the heat sink is a flat square surface (54×54 mm^2), receiving non-uniform multiple-peak heat flux generated by the electronic device. The heat will be firstly transferred by conduction in the solid part, and then by convection to the cooling fluid.

3.2.2 Optimization algorithm

This sub-section presents the basic principles of the optimization algorithm for tailoring the cooling fluid flow distribution in the parallel straight-channel heat sink. The following assumptions and simplifications have been made for this study:

- Steady-state, incompressible Newtonian fluid flow;
- Negligible viscous heating effect;
- Negligible radiation heat transfer; negligible heat loss to the environment;
- No phase change of the cooling fluid.

Based on the mass and energy conservation, the following equations could be written:

$$m_{tot} = m_{in} = \sum_{i=1}^{16} m_i = m_{out} \tag{3.1}$$

$$Q_{tot} = \iint q dA = m_{tot}(Cp_{tot}T_{tot} - Cp_{in}T_{in}) \tag{3.2}$$

Where m_{tot}, m_{in}, m_i *and* m_{out} are the total, inlet, *i*th mini-channel, and outlet mass flow rate of the cooling fluid, respectively. Q_{tot} is the total heating power; q is the heat flux at the heating surface of the heat sink; Cp_{out} and Cp_{in} are the specific heat of the outlet and inlet fluid and T_{out} *and* T_{in} are the inlet and outlet fluid temperature, respectively. Different from many earlier relevant studies, the heat flux q treated here is no longer uniform but shows a multiple-peak form (as shown in Figure 3.3 for example).

The optimization algorithm is developed to determine the optimal inlet sizes of the parallel mini-channels to minimize the maximum temperature of the heating surface (and also the thermal resistance, cf. Eq. (3.24)) via tailoring the flow distribution of the cooling fluid. The method developed is deterministic, i.e. the width distribution of the channel inlets was optimized (adjusted) in a way of evolution, but not arbitrarily imposed or randomly generated in most of the existing studies in the literature. For this purpose, the heating surface of the heat sink was hypothetically divided into 16 monitoring planes corresponding to every mini channel, as schematically shown in Figure 3.2.

T_i^{max} is defined as the maximum temperature of the *i*th plane, the indexing being marked in Figure 3.2. The objective of optimization may be written as:

$$T_i^{max} = \bar{T}^{max} \ (i=1, 2,\ldots,16) \tag{3.3}$$

Where $\bar{T}^{max}$ is the mean temperature of all 16 T_i^{max} (i=1, 2,…,16).

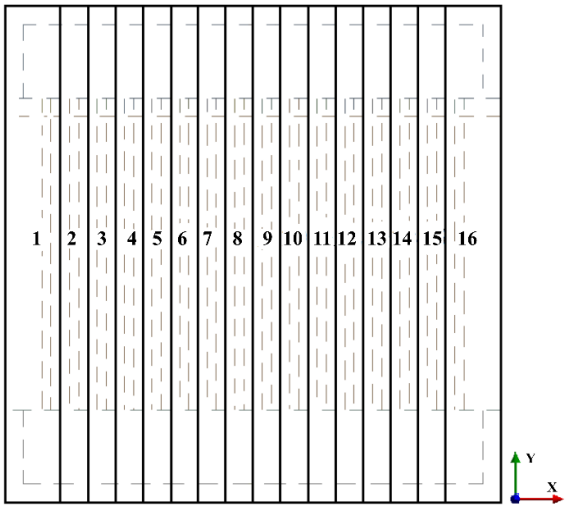

Figure 3.2. The base wall (heating surface) divided into 16 hypothetical planes

Practically, the relative standard deviation (it is also called coefficient of variation) of the maximum temperatures of the 16 monitoring planes ($MF_{T^{max}}$) is monitored, written as:

$$MF_{T^{max}} = \sqrt{\frac{1}{15}\sum_{i=1}^{16}\left(\frac{T_i^{max}-\bar{T}^{max}}{\bar{T}^{max}}\right)^2} \tag{3.4}$$

Given the constant total mass flow rate (m_{tot}) of the cooling fluid, the mass flow rate in each mini-channel is intended to be managed by adjusting the corresponding channel inlet width according to the temperature difference between $T_i^{\max}$ and $\overline{T}_i^{\max}$. In more detail, if $T_i^{\max}$ is higher than $\overline{T}_i^{\max}$, the higher mass flow rate is required for enhancing the cooling, thus the corresponding channel inlet width of the *i*th mini-channel should be enlarged. And vice-versa, if $T_i^{\max}$ is lower than $\overline{T}_i^{\max}$, the mass flow rate could be reduced by narrowing the channel inlet. This variation rule is written in Eq. (3.5).

$$w_{k+1,i} = w_{k,i} + \gamma\left(T_{k,i}^{max} - \bar{T}_k^{max}\right) \tag{3.5}$$

Where $w_{k,i}$ is the width of the i^{th} channel inlet for the step k iteration. γ is the adjusting factor deciding the variation amplitude of each iteration. The value of γ for each iteration was selected considering the geometric constraints in that all the channel inlets should not be smaller than zero ($w_i \geq 0$, i = 1, 2, ..., 16) and two adjacent channel inlets should not overlap ($w_i + w_{i+1} \leq 3$, i = 1, 2, ..., 15):

$$\gamma \leq \frac{3-w_{k,i}}{T_{k,i}^{max}-\bar{T}_k^{max}} \tag{3.6}$$

$$\gamma \leq \frac{w_{k,i}}{\bar{T}_k^{max}-T_{k,i}^{max}} \tag{3.7}$$

With the variation rule shown in Eq. (3.5), the passage ratio of the channel inlets (defined as the ratio between the total width of the channel inlets and the width of the distributing manifold) remains constant (29.6%) during iteration, as indicated by Eq. (3.8).

$$\sum_{i=1}^{16}\left(w_{k+1,i}-w_{k,i}\right)=\gamma\sum_{i=1}^{16}\left(T_{k,i}^{max}-\bar{T}_{k}^{max}\right)=\gamma\left(\sum_{i=1}^{16}T_{k,i}^{max}-16\times\bar{T}_{k}^{max}\right)=\gamma\left(\sum_{i=1}^{16}T_{k,i}^{max}-16\times\frac{\sum_{i=1}^{16}T_{k,i}^{max}}{16}\right)=0 \tag{3.8}$$

The optimization is started with the equal width of all the channel inlets, representing a conventional heat sink configuration with parallel straight channels. The optimization is considered to be completed when $MF_{T_k^{max}}$ (Eq. 3.4) is smaller than 0.003. Under the value of 0.003, the variation of T_k^{max} is very small.

The main steps of the optimization procedure are explained below and the flow chart of the whole procedure is presented in Appendix 3.A:

(1) Input the initial geometrical parameters of the heat sink and the channel inlet width distribution (equal channel inlets at step 0);
(2) Generate the geometry and mesh of the heat sink;
(3) Calculate the temperature and fluid flow characteristics by CFD simulation under designed working conditions and simulation setup; compute the $T_{k,i}^{max}$ and $MF_{T^{max}}$ of the heat sink in step k;
(4) If $MF_{T^{max}} < 0.003$, then export the optimal geometry of the channel inlets and end the procedure; if $MF_{T^{max}} > 0.003$, update the new geometry according to Eq. (3.5), and go back to step (2) for iteration.

3.2.3 CFD simulation parameters

The flow and temperature fields of the heat sink at each iteration step are calculated using CFD simulation. Governing equations under steady-state are shown as follows:

Continuity equation:

$$\nabla\cdot(\rho\vec{v})=0 \tag{3.9}$$

Momentum conservation equation:

$$\nabla\cdot(\rho\vec{v}\vec{v})=-\nabla p+\nabla\cdot(\bar{\bar{\tau}})+\rho\vec{g}+\vec{F} \tag{3.10}$$

Where p is the static pressure; $\bar{\bar{\tau}}$ is the stress tensor; $\rho\vec{g}$ and $\vec{F}$ are the gravitational body force and external body force.

Energy equation:

$$\nabla \cdot \left(\vec{v}(\rho E + p)\right) = \nabla \cdot \left(\lambda_{eff} \nabla T - \sum_j H_j \overrightarrow{J_j} + \left(\bar{\bar{\tau}}_{eff} \cdot \vec{v}\right)\right) \quad (3.11)$$

Where λ_{eff} is the effective conductivity; H is the sensible enthalpy; $\bar{\bar{\tau}}_{eff}$ is the effective shear stress. To predict turbulent flow patterns, an additional turbulence model should be employed.

For the solid zone, the energy transport equation is:

$$\nabla \cdot (\lambda_s \nabla T) + S_{hs} = 0 \quad (3.12)$$

Where S_{hs} is the heat source within the solid.

In this study, geometries and meshes were generated using different modules of Ansys Workbench 18.2. Hexahedral elements and the multi-zone method were applied for meshing fluid and solid domains. Inflation and sizing meshing methods were adopted at the solid-fluid interface and the corners of the fluid domain to capture the boundary layer region of the fluid flow.

Water was used as the cooling fluid and aluminum was chosen as the solid material of the heat sink body. Their temperature-dependent or constant thermophysical properties are expressed by the equations listed in Table 3.1.

Table 3.1. Thermal-physical properties of solid and fluid used for simulation [164–166]

Property		Fitting correlation (temperature range: 293K - 360K)
Water	Density (kg·m^{-3})	$\rho_f = -2.604 \times 10^{-8}T^4 + 4.719 \times 10^{-5}T^3 - 3.279 \times 10^{-2}T^2 + 9.469T + 43.486$ (3.13)
	Dynamic viscosity (kg·m^{-1}·s^{-1})	$\mu = 2.414 \times 10^{-5} \times 10^{\frac{247.8}{T-140}}$ (3.14)
	Thermal conductivity (W·m^{-1}·K^{-1})	$\lambda_f = -8.356 \times 10^{-6}T^2 + 6.530 \times 10^{-3}T - 0.598$ (3.15)
	Specific heat (J·kg^{-1}·K^{-1})	$Cp_f = 4182$ (3.16)
Aluminum	Specific heat (J·kg^{-1}·K^{-1})	$Cp_s = -3.973 \times 10^{-6}T^3 - 5.667 \times 10^{-3}T^2 + 3.069T + 380.170$ (3.17)
	Thermal conductivity (W·m^{-1}·K^{-1})	$\lambda_s = 202.4$ (3.18)
	Density (kg·m-3)	$\rho_s = 2719$ (3.19)

For the fluid zone, the velocity inlet normal to the inlet boundary surface was set, with a temperature of 293 K. The inlet velocity was set to be constant and equal to 0.5 m·s^{-1}, 0.55 m·s^{-1}, 0.6 m·s^{-1}, 0.65 m·s^{-1} and 0.7 m·s^{-1} (with inlet *Re* number (Eq. 3.26): 2488, 2737, 2986, 3234 and 3483, respectively, the corresponding mean channel *Re* number (Eq. 3.27): 406, 447, 487, 528 and 569, respectively) in different cases. The pressure outlet boundary was set for the outlet surface with the gauge pressure value being zero. All the walls for channels were defined as non-slip conditions. For the solid zone, all walls were considered adiabatic except the heating surface (base wall). For the latter, two-peak and five-peak heat flux were defined and tested, respectively, as shown in Figure 3.3. Their 2D surface heat flux Gaussian repartitions are given by Eq. 3.20.

$$q(x,y) = \sum_{ih=1}^{N} q_{ih}(x,y) = \sum_{ih=1}^{N} B_{ih} e^{-\frac{(x-x_{ih})^2+(y-y_{ih})^2}{2\sigma_{ih}^2}} \tag{3.20}$$

where N represents the number of heat peaks (2 or 5), a peak located at $x = x_{ih}, y = y_{ih}$ presents a maximum local heat flux; B_{ih}, σ_{ih} represents the spatial spread of the peak. The total heat Q_{ih} generated by a peak (if the plate had an infinite extent) can be computed by:

$$Q_{ih} = \iint_{\mathbb{R}^2} q_{ih}(x,y)dx\,dy = 2\pi B_{ih}\sigma_{ih}^2 \tag{3.21}$$

The different values of x_{ih}, y_{ih}, B_{ih}, σ_{ih} and Q_{ih} are summarized in Table 3.2.

Table 3.2. The values of constants used for two-peak and five-peak heat flux cases

Two peak heat flux case: N = 2					
i	x_{ih} (mm)	y_{ih} (mm)	B_{ih} (W·cm^{-2})	σ_{ih} (mm)	Q_{ih} (W)
1	−13.5	16	130	10	817
2	13.5	24	70	10	440
Five peak heat flux case: N = 5					
1	−16	28	120	7.2	391
2	16	28	70	5	110
3	0	19	90	5.7	184
4	−16	10	70	5	110
5	16	10	120	7.2	391

The total power of the heat source is constant ($Q = 1130$ W) and the average heat flux (power density) for the base wall ($q_{avg} = 38.75$ W·cm^{-2}) are identical for both heat flux settings, as indicated in Eqs. (3.22) and (3.23). The difference between Q and $\sum_i Q_i$ is due to the truncation effect of the Gaussian on the limited extent plate. The maximum peak values for the two cases are slightly different, i.e. 130 W·cm^{-2} at (x_1, y_1) for two-peak heat flux and 120 W·cm^{-2} at (x_1, y_1) and (x_5, y_5) for five-peak heat flux, respectively.

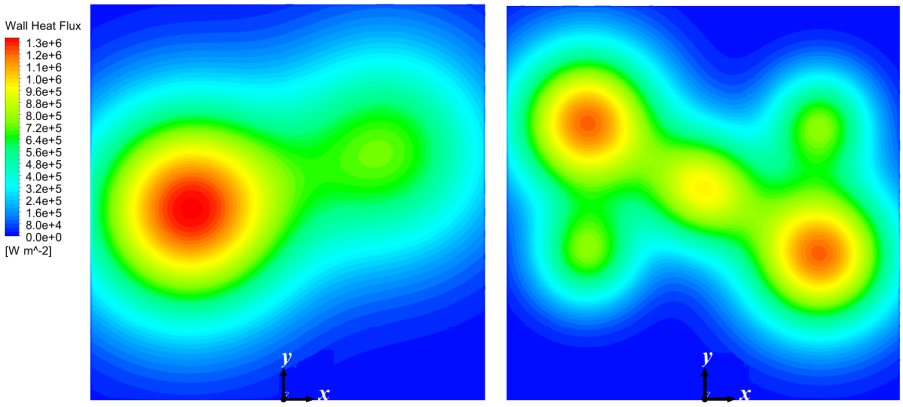

Figure 3.3 Two-peak and five-peak heat flux at the base wall.

$$Q = \iint_A q(x,y)\, dA = 1130 \text{ (W)} \tag{3.22}$$

$$q_{avg} = \frac{Q}{A} = \frac{1}{A}\iint_A q(x,y)\, dA = 38.75 \text{ (W·cm}^{-2}\text{)} \tag{3.23}$$

Different from other non-uniform heat sources e.g., several squares with uniform heat flux in each specific area [71,167], the Gaussian-shaped heat flux has been chosen in this study considering the gradient of real heat flux generated by the electronic components [29][30]. Note that it can be replaced by other heat flux profiles without much influencing the effectiveness of the algorithm. The two-peak case represents the asymmetry heat flux profile, while the five-peak case considers the centrosymmetric heat flux condition.

In this study, 3D fluid flow simulations were performed under steady-state with heat transfer, using a commercial code Fluent (version 18.2). The gravity effect was also considered. *k-ε* RNG model was used to simulate the turbulent flow, providing better accuracy for rapidly strained flows and swirling flows at relatively low Reynolds number conditions. For the pressure-velocity coupling, the SIMPLE method was used. For discretization, the second-order spatial discretization scheme was chosen for pressure and second-order upwind differentiation for momentum, turbulent kinetic energy, and turbulent dissipation rate. The solution was considered to be converged when (i) the maximum temperature of the heating surface and the pressure drop was constant from one iteration to the next (less than 0.5% variation), and (ii) the normalized residuals were lower than 10^{-8} for the energy equation and 10^{-5} for other governing equations.

For each iteration step of the optimization algorithm, MATLAB R2016b was used for data post-processing of the computed flow and temperature profiles from Fluent, to calculate the size variation of each channel inlet according to Eq. (3.5) and to pass the renewed geometric coordinates to Ansys Workbench for a new CFD simulation.

A grid independence study was conducted with the increasing number of total elements from 0.28 million to 2.27 million. Table 3.3 shows the values of pressure drop and maximum solid temperature obtained with different grids under an inlet mass flow rate of 0.011731 kg·s-

[1] (v_{in}=0.6 m·s^{-1}). A pressure drop variation within 1% and a maximum solid temperature within 0.7 K could be achieved with the grid elements higher than 1.14 million. Comparisons were also made on the fluid velocity profiles at the centerline of the outlet surface (x-direction). Again, there is no obvious difference for grids with elements number higher than 1.14 million. As a result, this grid with 1.14 million elements (0.5 million elements for the fluid zone and 0.64 elements for the solid zone) has been chosen for the present study considering a tradeoff between the computation cost and accuracy. The calculation was carried out in a workstation with Intel (R) processor Xeon (R) CPU E5-2620 and 32 GB memory. Two hours were needed for each optimization step.

Table 3.3. Comparison of the pressure drop, the maximum temperature, and the velocity profile for different tested grids

Grid (million elements)	0.28	0.52	0.75	1.14	1.76	2.27
Pressure drop (Pa)	1231.3	1216.6	1206.4	1196.7	1191.4	1185.4
The maximum temperature at the heating surface (K)	384.8	383.9	384.2	383.8	384.0	384.4
Velocity profile at the centerline of the outlet surface	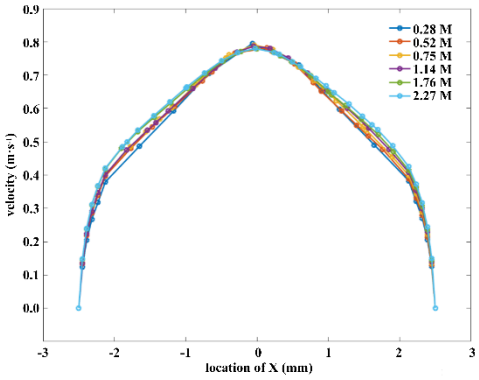					

3.2.4 Performance indicators

The performance of the heat sink was evaluated by the maximum temperature of the base wall, the global thermal resistance, and the pressure drop. The global thermal resistance (R_{th}) of the heat sink is calculated by Eq. (3.24):

$$R_{th} = \frac{T_{base}^{max} - T_{in}}{Q} \text{ (K·W}^{-1}\text{)} \tag{3.24}$$

Where $T_{base}^{\max}$ is the maximum temperature at the heating surface (base wall) of the heat sink, T_{in} is the inlet fluid temperature (293 K), and Q is the total heating power (1130 W).

The pressure drop in different sections of the fluid domain is also monitored:

$$\Delta P_{tot} = \Delta P_{dis} + \Delta P_{ch} + \Delta P_{col} \text{ (Pa)} \tag{3.25}$$

Where ΔP_{dis}, ΔP_{ch} and ΔP_{col} stands for the pressure drop in the distributor section, the parallel channels section (including the channel inlets with variable widths), and the collector section, respectively.

The inlet Reynolds number and the mean Reynolds number in the mini-channels are calculated by Eqs. (3.26) and (3.27), respectively.

$$Re_{in} = \frac{\rho_f v_{in} D_{in}}{\mu_f} = \frac{4m_{in}}{\pi \mu_f D_{in}} \tag{3.26}$$

$$Re_{ch} = \frac{\rho_f \bar{v}_{ch} D_{ch}}{\mu_f} = \frac{m_{in}}{4\pi \mu_f D_{ch}} \tag{3.27}$$

Where v_{in} and $\bar{v}_{ch}$ (m·s^{-1}) are the inlet and mean channel velocities, respectively. D_{in} and D_{ch} (m) are the hydraulic diameters of the global inlet port and the mini channel, respectively.

Non-dimensional parameters m^* and w^* are defined as follows.

$$m^* = \frac{m_i}{\bar{m}} \tag{3.28}$$

$$w^* = \frac{w_i}{\bar{w}} \tag{3.29}$$

Where $\bar{m}$ and $\bar{w}$ are the mean channel mass flow rate and the mean width of channel inlets, respectively.

3.3 Results and discussions

In this section, the flow distribution and thermal characteristics of the straight mini-channel heat sink with optimized channel inlets are shown and compared with the conventional heat sink with equal channel inlets. In addition, a parametric study and a robustness test on the relationship between the tailored flow distribution, the overall thermal resistance, and the total pressure drop are reported.

Figure 3.4 shows that the value of $MF_{T^{max}}$ (Eq. 3.4) evolves along with the increasing step number. It took the two-peak heat flux case 14 iteration steps to achieve the convergence ($MF_{T^{max}}$<0.003), and for the case of five-peak heat flux, 10 iteration steps were needed.

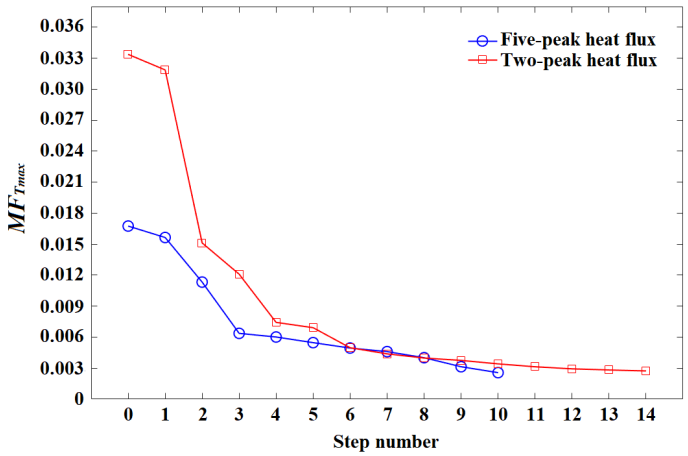

Figure 3.4. Evolution of *MF* value along with the optimization step for two and five-peak heat flux cases

3.3.1 Flow distribution characteristics

Figures 3.5 (a) and (b) present the widths of channel inlets and the flow distribution characteristics of cooling fluid among mini-channels as a function of the optimization step for the two-peak heat flux case. From Figure 3.5 (a), it can be seen that the largest channel inlet is located at the position where peak temperature appears for all steps (except for step 0). As the iteration step proceeds, the widths of the channel inlet for channel number 1-6 gradually enlarge, much broader than those for channel number 7-16 due to the location of the larger hot spot with higher temperatures. With the constraint of constant passage ratio, the inlet widths of channels 8-16 have all been narrowed, despite a (smaller) heat flux peak located in this region.

This variation of the channel inlet widths results in the evolution of the fluid flow distribution characteristics, as shown in Figure 3.5 (b). For the starting step 0 (equal channel inlet widths), the shape of the mass flow distribution curve is almost symmetric concerning the centerline. Middle channels (No. 8 and 9) receive the highest mass flow rate, and it gradually decreases for the channels located closer to the edges (No. 1 and 16). This is because of the middle location of inlet/outlet tubes (U-type flow arrangement). The unmatched flow rate distribution to the heat flux peaks causes inevitably temperature hot spots (as shown in Figure 3.7). Generally speaking, the evolution of the flow distribution curve shows a similar tendency as the evolution of the inlet widths curve, indicating an effective control of the channel mass flow rate by adjusting the inlet widths. Under the constraint of a constant total mass flow rate, a large proportion of the cooling fluid has been guided to channels 1-8, where the larger heat flux peak is located.

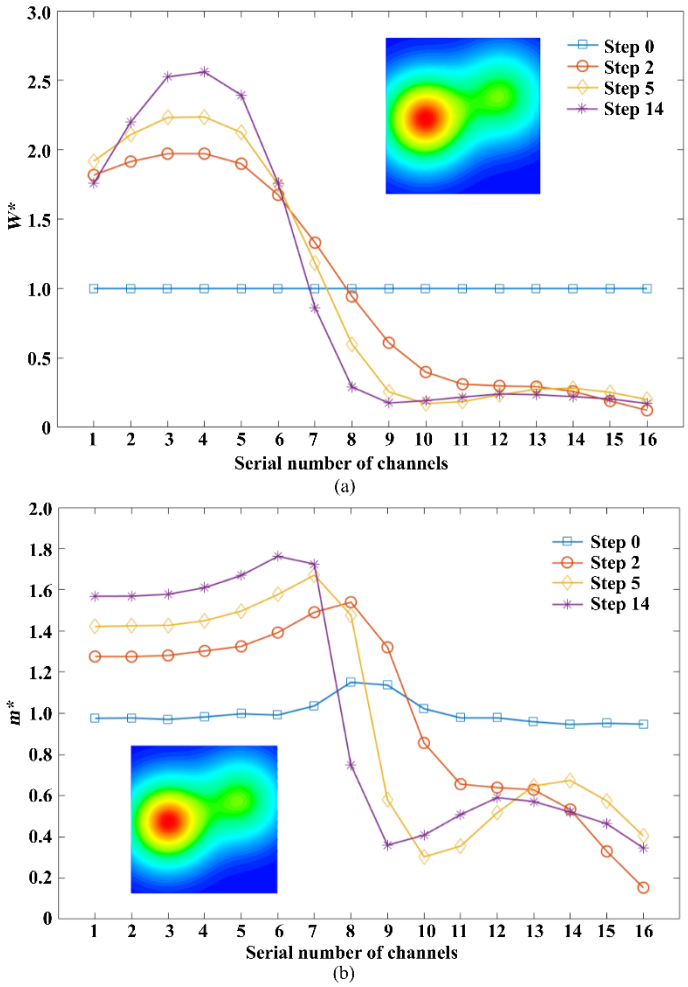

Figure 3.5. Channel inlet width evolution (a) and flow distribution (b) among mini-channels for step 0, step 2, step 5 and step 14 of the two-peak heat flux case

Figures. 3.6 (a) and (b), analogous to Figure 3.5, are for the five-peak heat flux case. The channel inlet widths curve firstly tends to form the bathtub shape in step 2, and then gradually generates the three peaks shape at the middle and two edge sides in step 10. This is in line with the fact that the channel inlet widths in channels are modified in each step according to the temperature of hot spots on the heating surface. Even if the heat flux is centrosymmetric, one of the two highest heat flux peaks close to the distributing manifold has a lower temperature hot spot than the other near the collecting manifold. Before the coolant passes through the highest heat flux point close to the global outlet tube, it has already absorbed some quantity of heat in the straight channels. As a result, the inlet widths of the channels corresponding to the highest heat flux peak close to the outlet become the largest at the final step, as clearly shown in Figure 3.6 (a).

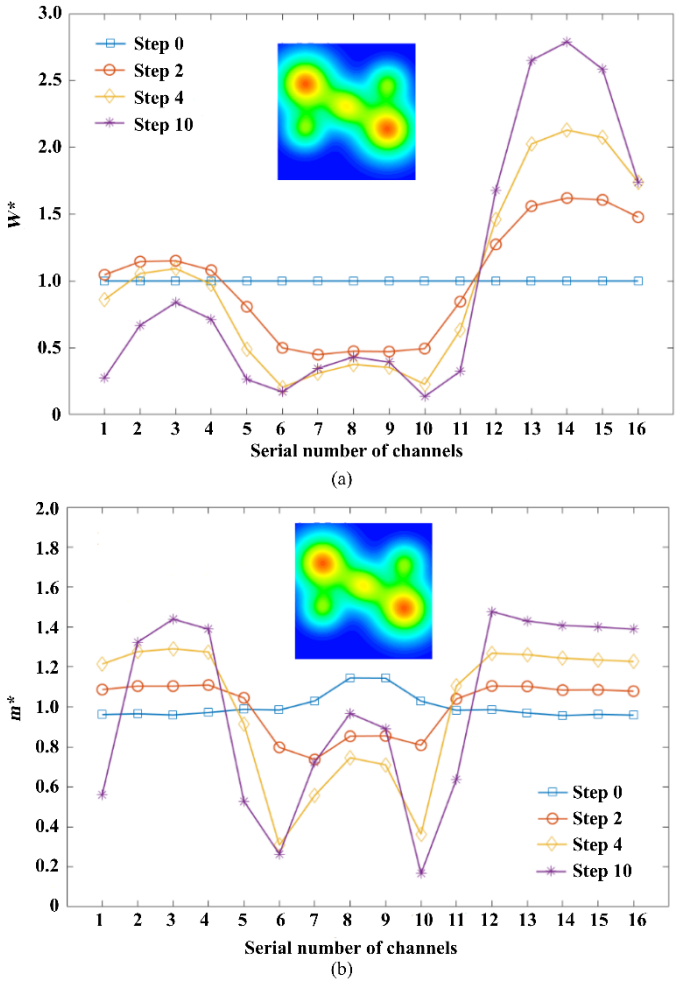

Figure 3.6. Channel inlet width evolution (a) and flow distribution (b) among mini-channels for step 0, step 2, step 4 and step 10 of the five-peak heat flux case

Regarding the flow distribution shown in Figure 3.6 (b), the mass of cooling fluid is guided towards the edges, and a more mass flow rate should be delivered to the location situated with the highest heat flux (channels No. 13-15). The sum of mass flow rates allocated to channels No. 12-16 is higher than that allocated to channels No. 1-5 at step 10, mainly due to the cooling capacity difference of coolant as discussed above.

3.3.2 Temperature fields

Figure 3.7 shows the evolution of temperature cartography on the heating surface along with the optimization steps for the two-peak heat flux case. For step 0, the maximum temperature occurs in monitoring planes 3 and 4 where the larger heat flux peak is located. By running the optimization algorithm, the higher amount of heat in this area is absorbed and efficiently evacuated owing to the broadened channel inlets and the increased mass flow rate of cooling fluid. Step by step, the hot spots largely disappear and the maximum temperatures of the 16 monitoring planes are (almost) equalized.

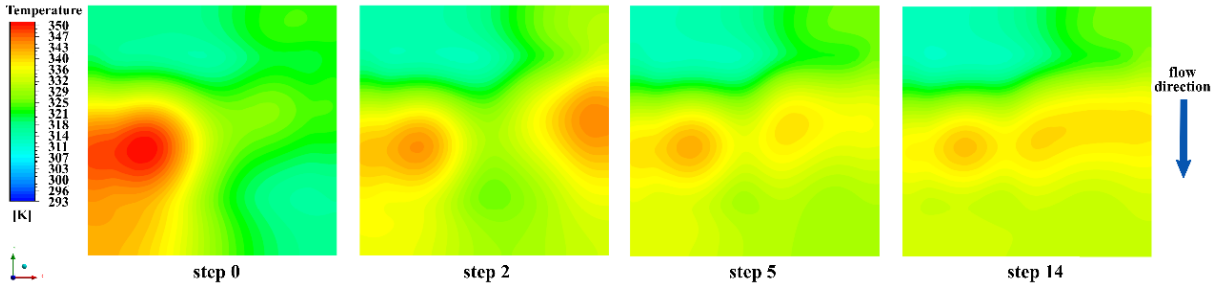

Figure 3.7 Temperature cartography on the base wall of the heat sink at optimization step 0, step 2, step 5 and step 14 for the two-peak heat flux case (q_{avg}=38.75 W·cm^{-2}; v_{in}=0.6 m·s^{-1})

Similarly, Figure 3.8 depicts the temperature cartography evolution for the five-peak heat flux case. For equal channel inlet condition, the diagonal arrangement of five heat flux peaks does not result in 5 diagonal temperature hot spots because the heat generated near the distributing manifold could be more efficiently absorbed by the cooling fluid at the lower temperature. In contrast, the temperature hot spot close to the collecting manifold is rather obvious, the maximum temperature being 347.44 K. With the optimization algorithm proceeds, the hot spot occurring in monitoring planes 12-16 begins to decrease and diagonally extends to the middle and left parts of the base wall. At the final step 10, the maximum temperatures of the 16 monitoring planes are (almost) equalized and the peak temperature of the base wall can be reduced to 341.5 K.

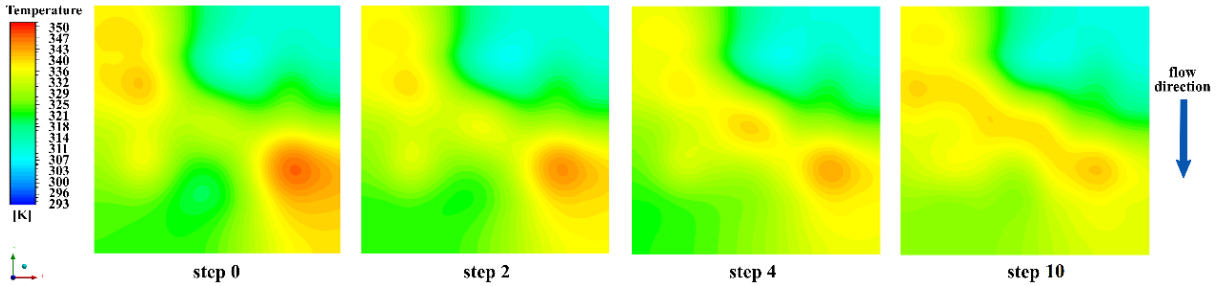

Figure 3.8. Temperature cartography on the base wall of the heat sink at optimization step 0, step 2, step 4 and step 10 for the five-peak heat flux case (q_{avg}=38.75 W·cm^{-2}; v_{in}=0.6 m·s^{-1})

T_i^{max} values of the monitoring planes are shown in Figure 3.9. For the two-peak heat flux case, the largest difference between the maximum temperatures of the monitoring planes is about 27 K at step 0 (equal channel inlet widths). This temperature difference becomes smaller as the optimization iteration proceeds and finally reaches 3.4 K at step 14. It may be observed that the evolution of the T_i^{max} curve shown in Figure 3.9 (a) follows the reverse trend of the channel inlet widths curve shown in Figure 3.5 (a). The initially equal channel inlet widths are adjusted by our algorithm step by step to flatten the T_i^{max} curve, indicating the effectiveness of the variation rule as proposed in Eq. (3.5). Similarly, Figure 3.9 (b) shows the evolution of the T_i^{max} values of the monitoring planes for the five-peak heat flux case. The difference between the maximum temperatures is reduced from about 15 K at step 0 to smaller than 3 K at step 10. Compared to the two-peak heat flux case with the same area-weighted average power density, the five-peak case with more heat flux peaks shows a relatively more uniform temperature distribution. As a result, it costs fewer iteration steps to reach the optimization criterion.

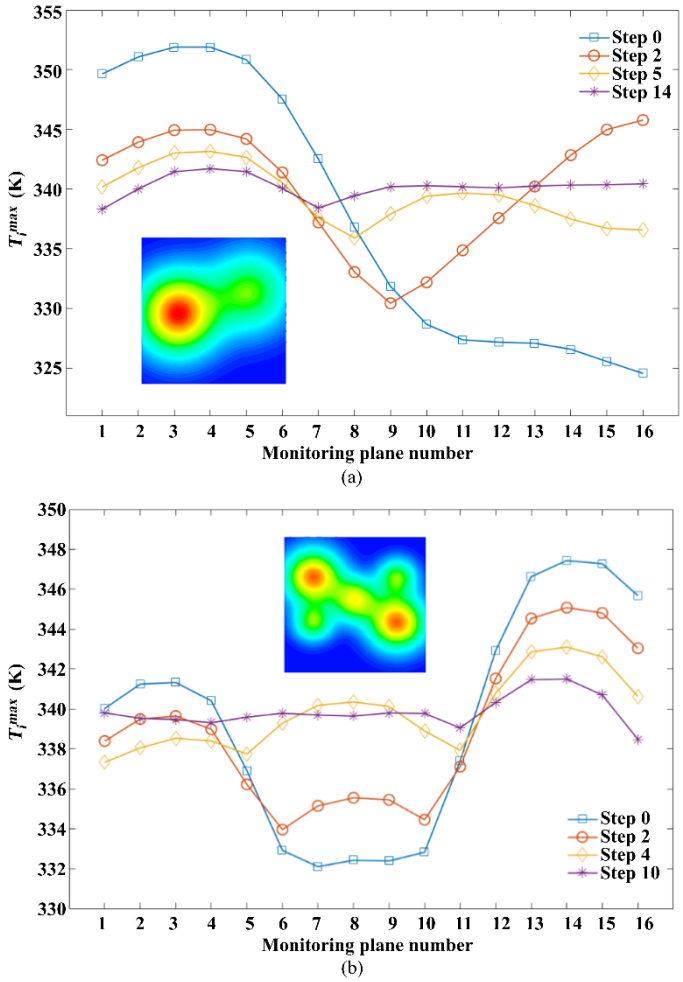

Figure 3.9. T_i^{max} in each monitoring plane as a function of the optimization step for (a) two-peak heat flux case and (b) five-peak heat flux case

The maximum temperature at the base wall as a function of the optimization step is plotted in Figure 3.10 for both the two-peak and five-peak cases. The reduction of maximum temperature is significant, reaching 10 K and 7 K for two-peak and five-peak cases, respectively. Recall that every 10 K reduction of maximum junction temperature could double the service time of the electronic devices [33]. It may be observed that the maximum temperature of the base wall decreases sharply for the first four optimization steps, mainly because of the large difference between the T_i^{max} and the average value $\bar{T}^{max}$. The slope of the maximum temperature curve becomes smaller for the rest steps (about 2-3 K reduction) and finally stabilizes at the value of 341.7 K (two-peak case) and 341.5 K (five-peak case), respectively.

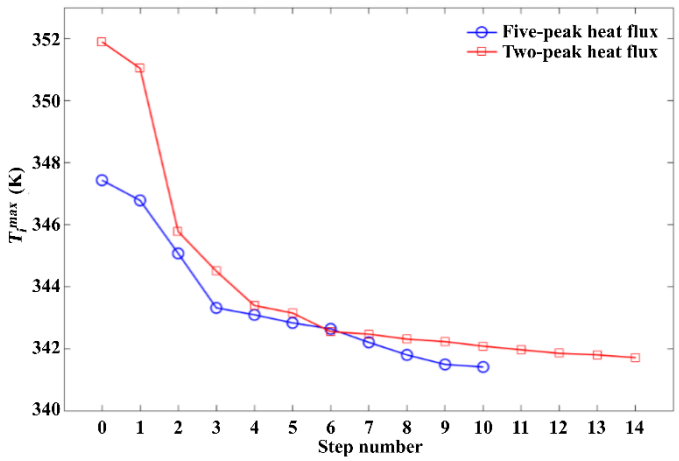

Figure 3.10. Maximum temperature evolution for two and five peaks heat flux cases

3.3.3 Pressure drop characteristics

Figure 3.11 shows the evolution of pressure drops of the heat sink versus the optimization step. Different values of pressure drop are plotted, including the total pressure drop (Δp_{tot}) and sectional pressure drops (Δp_{dis}, Δp_{ch}, Δp_{col}), for the two-peak heat flux case (Figure 3.11 (a)) and the five-peak heat flux case (Figure 3.11 (b)). For both cases, the total pressure drop as well as the sectional pressure drop increase with the optimization steps, because the adjustment of channel inlet widths for tailoring the flow distribution adds supplemental hydraulic resistance. The pressure drop of the parallel mini-channels section (Δp_{ch}) makes the largest contribution to the total pressure drop and continues to grow faster than others (Δp_{dis}; Δp_{col}) along with the optimization step. This is because of the changing velocities in channels and the unequal channel inlet widths. The pressure drops in the distributing and collecting manifolds, accounting for a small portion of the total pressure drop, slightly increase with the optimization step for both testing cases.

The pressure drop increase in the parallel channels section is difficult to avoid because of some narrowed channel inlets and tailored non-uniform flow distribution, for more efficient cooling. Nevertheless, for the pressure drops in distributing and collecting manifolds, some better header designs [86] may be considered to reduce the total pressure drop. Note that the proposed optimization method in this study is compatible with other manifold shapes.

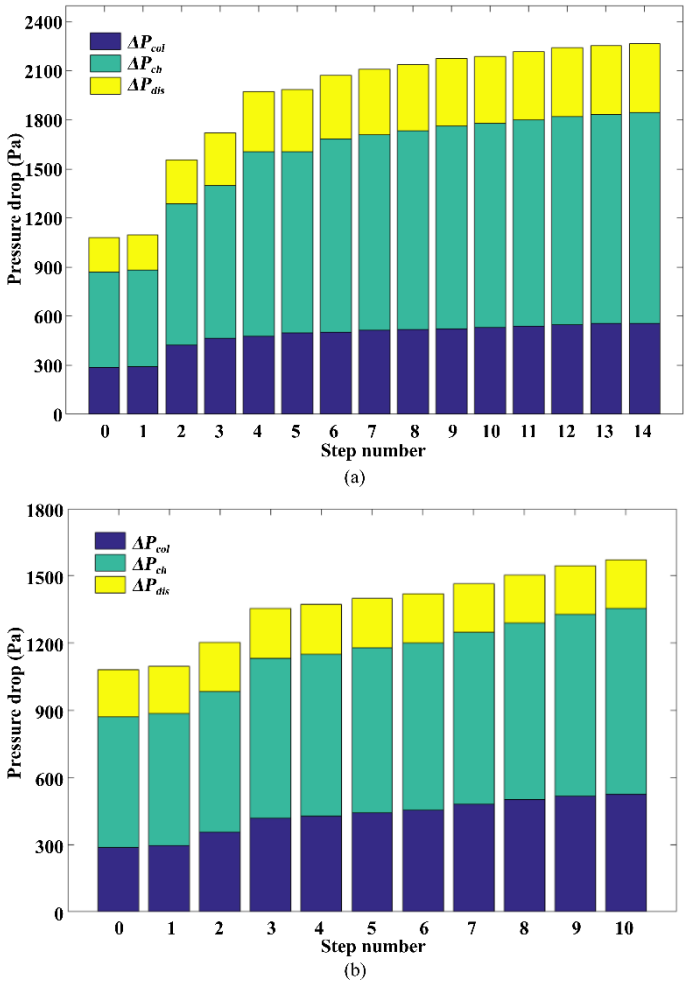

Figure 3.11. Evolution of the total and sectional pressure drops of the heat sink as a function of the optimization step for (a) two-peak heat flux case and (b) five-peak heat flux case

3.4 Effective range of optimized channel inlet widths-a robustness study

In the above section, it has been demonstrated that under the design heat flux and flow rate conditions, the proposed optimization algorithm is effective in reducing the maximum temperature of the base wall. But for actual use, it will be interesting and of practical significance to further test the optimization method when the workload (heat flux, inlet velocity, etc.) deviates from its design point. The conventional parallel straight channels heat sink with equal channel inlets (step 0) is introduced as a reference for comparison.

3.4.1. Effect of inlet velocity

The optimized heat sink configuration (five-peak heat flux, v_{in} = 0.6 m·s^{-1}, q_{avg} = 38.75 W·cm^{-2}) was tested under other four inlet velocities (heat flux profile remains unchanged), i.e. v_{in} = 0.5 m·s^{-1}; 0.55 m·s^{-1}; 0.65 m·s^{-1} and 0.7 m·s^{-1}. The thermal resistance R_{th} (as defined in Eq. (3.24)) values of the optimized heat sink obtained under different v_{in} conditions are plotted in the red line in Figure 3.12. Note that the blue line shows the R_{th} value of the heat sink with equal channel inlet widths (step 0). In general, the R_{th} decreases with the increasing mean Re_{ch}

for both heat sink configurations because of the higher cooling capacity of the coolant at the higher flow rate. The heat sink with channel inlets optimized under v_{in} = 0.6 m·s^{-1} (mean Re_{ch} = 487), when operated under other inlet velocities (mass flow rate) conditions, always shows a lower R_{th} (about 14%) than that of the conventional heat sink with equal channel inlet widths.

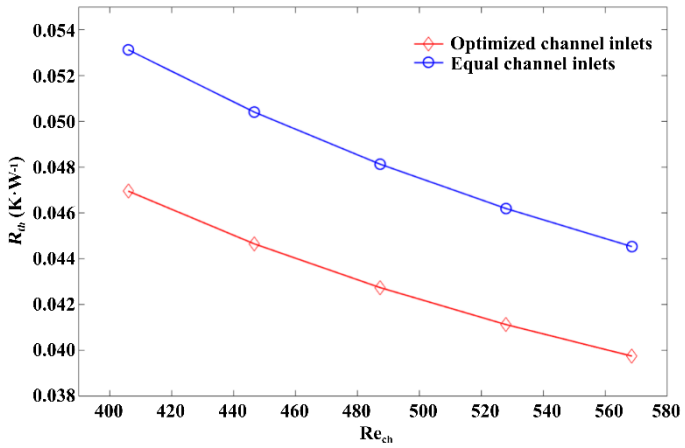

Figure 3.12. Thermal resistance as a function of mean channel Reynolds number for the optimized heat sink configuration (five-peak heat flux, v_{in} = 0.6 m·s^{-1}, q_{avg} = 38.75 W·cm^{-2}) and for the conventional heat sink configuration with equal channel inlets

3.4.2 Effect of pressure drop increase

Another option to reduce the thermal resistance and the maximum temperature of the heat sink without optimization is to simply increase the mass flow rate (cooling capacity) of the coolant. But similar to any other heat transfer enhancement technique, higher mass flow rate results in an increased pressure drop (pumping power consumption). It is therefore interesting to compare different cooling enhancement measures considering both the thermal resistance and the pressure drop.

Figure 3.13 presents the thermal resistance of the heat sink as a function of the pressure drop, comparing the two cooling enhancements. Note that the blue line shows the performance of the conventional heat sink configuration (equal channel inlet widths) with increasing mass flow rate (v_{in}=0.6 m·s^{-1}, 0.65 m·s^{-1}, 0.7 m·s^{-1}, 0.75 m·s^{-1}) whereas the red line represents different optimization steps of the heat sink with varied channel inlet widths (v_{in} = 0.6 m·s^{-1}). In general, the thermal resistance decreases with the increasing mass flow rate and the pressure drop. An encouraging result is that to reach the same thermal resistance, tailoring the flow distribution of the cooling fluid using the proposed optimization method always costs a smaller pressure drop (up to 6.5%) than simply increasing the total coolant mass flow rate for conventional parallel straight channels heat sink. The consumed pumping power is better "utilized" for the cooling purpose to reduce the maximum temperature of the heat sink.

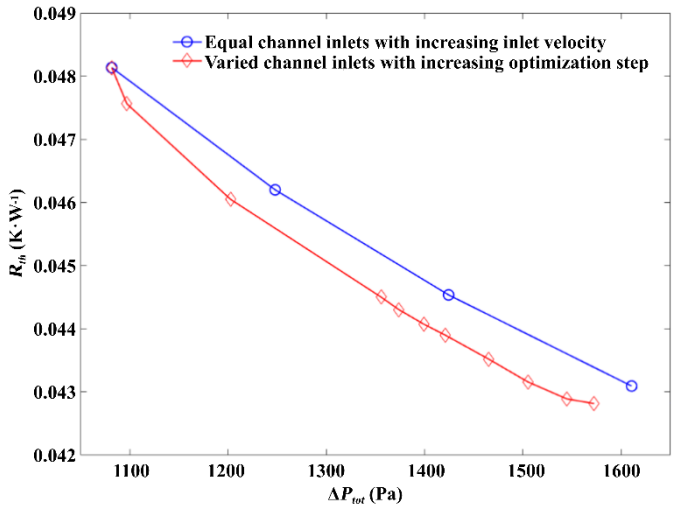

Figure 3.13. Thermal resistance as a function of the total pressure drop of the heat sink by optimizing the channel inlet widths and by increasing the total mass flow rate of cooling fluid

3.4.3 Effect of average heat flux

The power dissipation of electronic devices (e.g. CPU) is often dynamic in actual operation due to the varied frequency and the switched load capacitance. Therefore, testing the optimized heat sink under a certain range of heat flux is necessary. The following test aims to investigate the efficiency and robustness of the optimized heat sink under various average heat fluxes but with a similar pattern since the position of power dissipation elements is often fixed.

Figure 3.14 shows the influence of the heat flux variation (q_{avg} = 24-45 W·cm^{-2}) on the thermal performances of the heat sink. The red line marks the thermal resistance value of the optimized heat sink configuration (under five-peak heat flux, v_{in} = 0.6 m·s^{-1}, q_{avg} = 38.75 W·cm^{-2}) while the blue line is for the equal channel inlets configuration. The trend of thermal resistance for both heat sink configurations firstly goes down and then gradually climbs. For equal channel inlets configuration, the lowest thermal resistance is achieved at q_{avg} =30 W·cm^{-2}, while for optimized channel inlets configuration the lowest thermal resistance value is obtained logically under its nominal design condition at q_{avg} = 38.75 W·cm^{-2}. But even not being operated under its nominal design point, the optimized channel inlets configuration can maintain the thermal resistance at a low level, about 9.4% lower than that of the equal channel inlets configuration. The thermal performance robustness of the optimized channel inlets configuration under variable average heat flux conditions is thereby highlighted.

The green square marker presents the thermal resistance of the heat sink with its channel inlets optimized under the corresponding area-weighted average heat flux. The difference of R_{th} between the nominal design point (green square) and pseudo design point (red star) reduces as the area-weighted average heat flux increases, and the maximum difference of R_{th} is 0.0014 K·W^{-1} at q_{avg} = 30 W·cm^{-2}, indicating that the channel inlets optimized under one nominal design heat flux could be considered as pseudo optimal with an acceptable tolerance (<3%) when the average heat flux varies within a certain range.

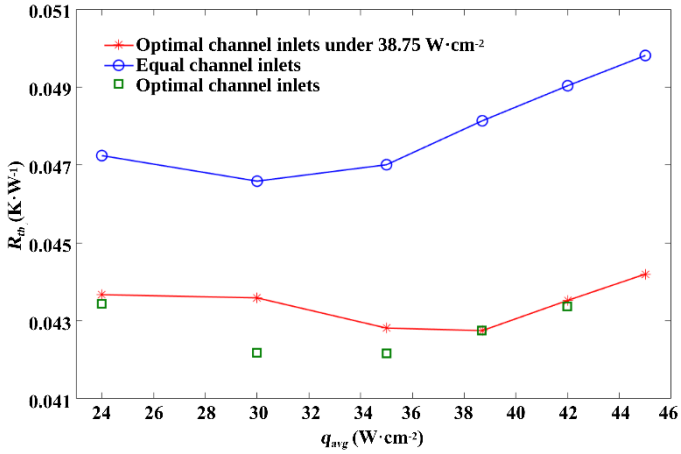

Figure 3.14. Thermal resistance under different average heat flux conditions for optimized heat sink configuration under q_{avg} = 38.75 W·cm^{-2}, for optimized heat sink under corresponding area-weighted average heat flux (q_{avg} = 24-45 W·cm^{-2}) and for the equal channel inlet widths configuration

3.5 Conclusion and the following work

In this chapter, a parallel straight mini-channels heat sink subjected to a non-uniform multiple-peak heat flux has been studied, to minimize the maximum temperature on the base wall. The flow distribution of the cooling fluid among the parallel channels is tailored by adjusting the channel inlet widths using an iterative optimization algorithm. The working condition applicability of the optimized channel inlet configuration has also been tested and compared to the equal channel inlet widths heat sink configuration. The main findings obtained may be summarized as follows.

- The maximum temperature can be reduced by 10 K using the proposed optimization method, under the area-weighted average heat flux of 38.75 W·cm^{-2} for the two-peak heat flux case. For the five-peak heat flux case, the maximum temperature can be decreased by 4 K to 7 K for the average heat flux ranging from 24-45 W·cm^{-2}, respectively.
- The heat sink configuration with optimized channel inlets could always provide smaller thermal resistance than that of the equal channel inlet configuration (reference straight channel heat sink) under different average heat flux or total mass flow-rate conditions.
- At the same pressure drop, tailoring the flow distribution of the cooling fluid is more efficient in reducing the thermal resistance than simply increasing the mass flow rate of the cooling liquid. The consumed pumping power is better utilized for cooling purposes to reduce the maximum temperature of the heat sink.
- The effectiveness and robustness of the optimization algorithm have been illustrated by that the channel inlet widths configuration optimized under one certain average heat flux could be considered as pseudo-optimal with an acceptable tolerance when the average heat flux varies within a certain range.

It should be noted that the proposed optimization method depends largely on the correctness of CFD simulation. The validation of fluid flow and temperature profiles by testing a laboratory heat sink prototype has been done and would be presented in the later Chapter 5.

This size/shape optimization method, though relatively straightforward, has still its limitations. It has been developed for the conventional straight channel-type heat sink so that only the flow distribution property can be tailored or optimized while the global flow path configuration can by no means be modified. In this regard, the other originally proposed topology optimization approaches with more degrees of freedom than the predefined parallel straight channel geometry would be interesting to be investigated, which will be the main subject of the next chapter 4. Both optimized heat sinks' performances would be compared numerically and experimentally in Chapter 5.

Appendix 3.A

The flow chart of the size optimization on straight channel heat sink is shown in Figure 3.A.

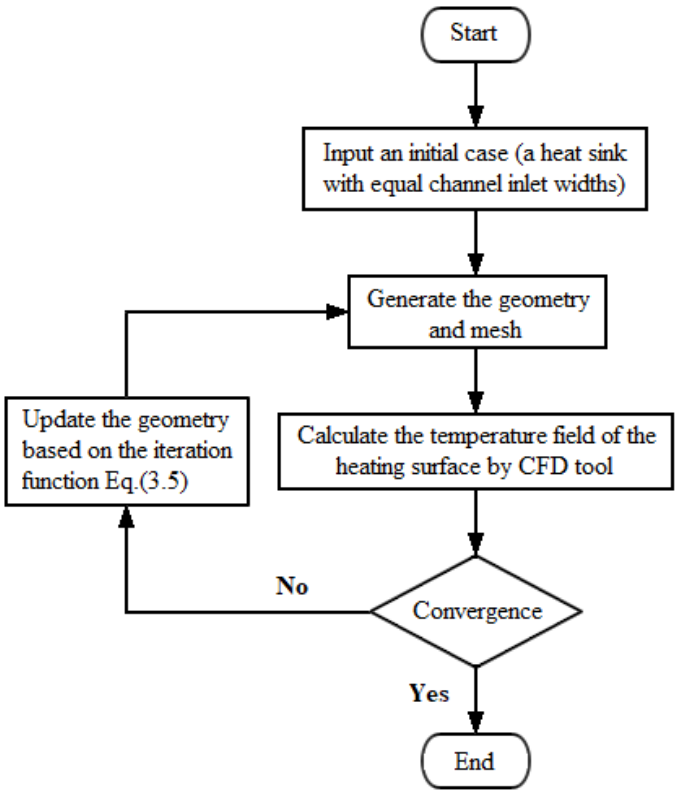

Figure 3.A Flow chart of the size optimization for tailoring mass flow distribution in straight channel heat sink.

Chapter 4: A genetic algorithm-based topology optimization (GATO) method for convective cooling of a heating surface with multiple heat sources

Chapter Summary

To achieve the highest degree of freedom of heat sink design, this chapter presents the development of a genetic algorithm-based topology optimization (GATO) method for convective cooling of a heating surface under multiple-peak heat flux. In more detail, the middle area of the heat sink receiving heat flux is treated as the design domain and represented as a $M_{row \times column}$ binary matrix. Each element in the matrix is considered either as fluid or as solid, and their allocation is optimized to minimize the peak temperature (T_{peak}) at the heating surface of the heat sink under the constraint of constant void volume for the fully-connected fluid domain. For each optimization step, the fluid flow and temperature characteristics are obtained by CFD simulation using OpenFoam and the GA operations (selection, crossover, mutation, etc.) are applied. The impacts of design and operation parameters on the flow channel configuration optimized are evaluated, including the heat flux shape, the fluid void fraction, the inlet velocity, and the resolution of the design domain. The cooling performance of the GATO heat sink is also compared to the reference straight channel heat sink (RSC) under the same conditions.

The results obtained show that (1) the proposed GATO method could successfully determine the optimal flow channel configuration of the heat sink, decreasing the T_{peak} at the heating surface; (2) The optimized flow channel configuration depends on the design and operating parameters, of the effectiveness and robustness of the GATO method is clearly shown; (3) Compared to conventional RSC heat sink, the GATO heat sink provides a better cooling performance, with a reasonable increase of the pressure drop.

Keywords of the Chapter:

Heat sink design, Multiple-peak heat flux, Genetic algorithm (GA), Topology optimization (TO), Flow channel configuration, Cooling performance

4.1 Introduction

In Chapter 3, a size optimization method for channel inlets has been developed for adjusting the flow distribution among the parallel straight channel of a heat sink. Nevertheless, such optimization methods are based on a predefined initial geometry. Topology optimization (TO) treats this problem differently by acting directly on the global spatial distribution of fluid and solid materials and their connectivity within a certain domain [168]. It has the highest degrees of freedom, capable of proposing complex but highly efficient designs without being limited to the prescribed geometry.

Currently, the mainstream of TO works on a heat sink (exchanger) structural optimization combines the density-based method, the FEM (finite element method), and the gradient-based optimizer [131], as has been discussed in chapter 2.4. It has shown good efficiency in handling optimization problems with a high number of design variables [169]. Nevertheless, this TO strategy has some difficulties in handling numerical artifacts or descriptions of clear interfaces, such that thresholding is an indispensable post-treatment to eliminate the intermediate value of the design variable (density). More importantly, it can be easily trapped into the local optimum [138], necessitating the development of some gradient-free approaches, like genetic algorithm (GA) and Bayesian optimization, to overcome these deficiencies and to converge towards a global optimum [139].

The GA is a stochastic evolutionary algorithm (EA) that mimicries the biological evolution of species based on chromosomes and genes [170]. Merited by its robustness to the global optimum and good fitness to multi-objective optimization, it has been developed and used by many researchers for the optimization of heat transfer, including both conduction and convection problems [171,172]. A limited number of attempts [144–148] have been made in recent years, as reviewed in chapter 2.4, but none of them addresses the TO of global flow channel configuration in heat sinks. Moreover, the majority of the TO studies deal with the simplified 2D design domain (only with several exceptions [142]), obviously insufficient to handle problems involving more complex heating boundaries with multiple heat sources.

Being motivated by the remaining research gaps to fill, we develop in this work a *GA-based TO (GATO) method to optimize the global flow channel configuration of the heat sink for the forced-convection cooling of a heating surface under multiple-peak heat flux*. Different from other studies existing in the literature, the pseudo-3D design domain of the heat sink is represented by a binary matrix in a direct explicit way, each element being either solid (0) or fluid (1). Consequently, the TO problem of flow channel configuration in the design domain becomes then the search for the best allocation of 0 and 1 cells in the matrix. A 3D finite volume method (FVM) solver is used for the modeling of conjugate heat transfer and fluid flow for each design, showing its robustness and stability in handling complex CFD problems. An in-house coded GA is used as the optimizer to renew the design variables (matrices) to minimize the peak temperature of the heating surface (T_{peak}) under specific constraints of constant void fraction for the fully connected fluid phase. In more detail, the local features (genes) that

contribute to the lowered T_{peak} value would be maintained in successive generations while those that bring about worse results would be discarded, a procedure analogizing the mechanism of natural selection as the "*survival of the fittest*". One generation after another will converge to the optimized flow channel configuration that has the lowest T_{peak} on the heating surface. This TO method combining direct explicit parametrization, FVM, and GA, inspired and developed from the pioneering works of Boichot et al. [6,173] on the pure conduction optimization problem, has never been used for the convection cooling of a heating surface under multiple heat sources to the best of our knowledge.

The remaining parts of this chapter are organized as follows. Section 4.2 introduces the methodology, in which each step of the GATO algorithm is presented in detail. In section 4.3, the optimization results of a heat sink design under multiple-peak heat flux are discussed. A comprehensive parametric study evaluating the influences of different design variables is reported in section 4.4, demonstrating the robustness, effectiveness, and flexibility of the developed GATO method. Section 4.5 provides further discussions on some interesting issues to better highlight the advantages and limitations of this method. Finally, the main conclusions and following work are summarized in section 4.6.

4.2 Methodology

4.2.1 Heat sink model

Figure 4.1 shows a representative schematic view of the heat sink geometry for this study. It has a single inlet (and outlet) straight channel of w_{in} (w_{out}) in width and L_{in} (L_{out}) in length, both aligned with the center line of the heat sink. In between the inlet/outlet tubes is a rectangular cuboid having overall dimensions of L_{middle} in length (y direction), w_{design} in width (x direction), and e in depth (z-direction). This core part of the heat sink consists of 3 sections: the inlet manifold ($w_{design} \times L_{dis}$), the middle flow channel domain ($w_{design} \times L_{design}$), and the outlet manifold ($w_{design} \times L_{col}$). Note that all the flow channels are coplanar with the same channel depth of e, rendering it a pseudo-3D fluid domain adapted for design parametrization. Only the upper surface of the flow channel domain (heating surface with a surface area of A_{design}) receives a non-uniform multiple-peak heat flux while all other surfaces enclosing the heat sink are considered adiabatic walls. In that way, the total amount of heat generated will be transferred and absorbed by the cooling fluid. The middle flow channel domain, also named the design domain, is constituted by both fluid and solid (cubic) elements at a given void fraction (Φ), each element having $w_{element}$ in width and $L_{element}$ in length. Their spatial distribution determines consequently the topology of the flow path and the cooling performance that should be optimized by GATO. One special case is the conventional straight channel configuration, with a channel width of w_{ch} and a separating wall thickness of w_{sw} between two neighboring channels, which is shown in Figure 4.1 (a) and considered as the reference design (abbreviated as "RSC" hereafter) for performance comparison.

The following assumptions and simplifications have been made for this study:

- Steady-state, in-compressible Newtonian and viscous fluid flow;
- Negligible radiation heat transfer; negligible heat loss to the environment;
- No phase change for the working fluid.

Equations for mass and energy conservation could then be written as:

$$m_{in} = m_{out} \tag{4.1}$$

$$Q = \iint q dA_{design} = m_{in}\left(Cp_{f,out}T_{f,out} - Cp_{f,in}T_{f,in}\right) \tag{4.2}$$

Where m_{in} or m_{out} is the inlet or outlet mass flow rate of the cooling fluid, respectively. Q is the total input power (W); q is the heat flux at the heating surface; Cp_f is the specific heat of cooling fluid; $T_{f,in}$ or $T_{f,out}$ is the inlet or outlet fluid temperature, respectively.

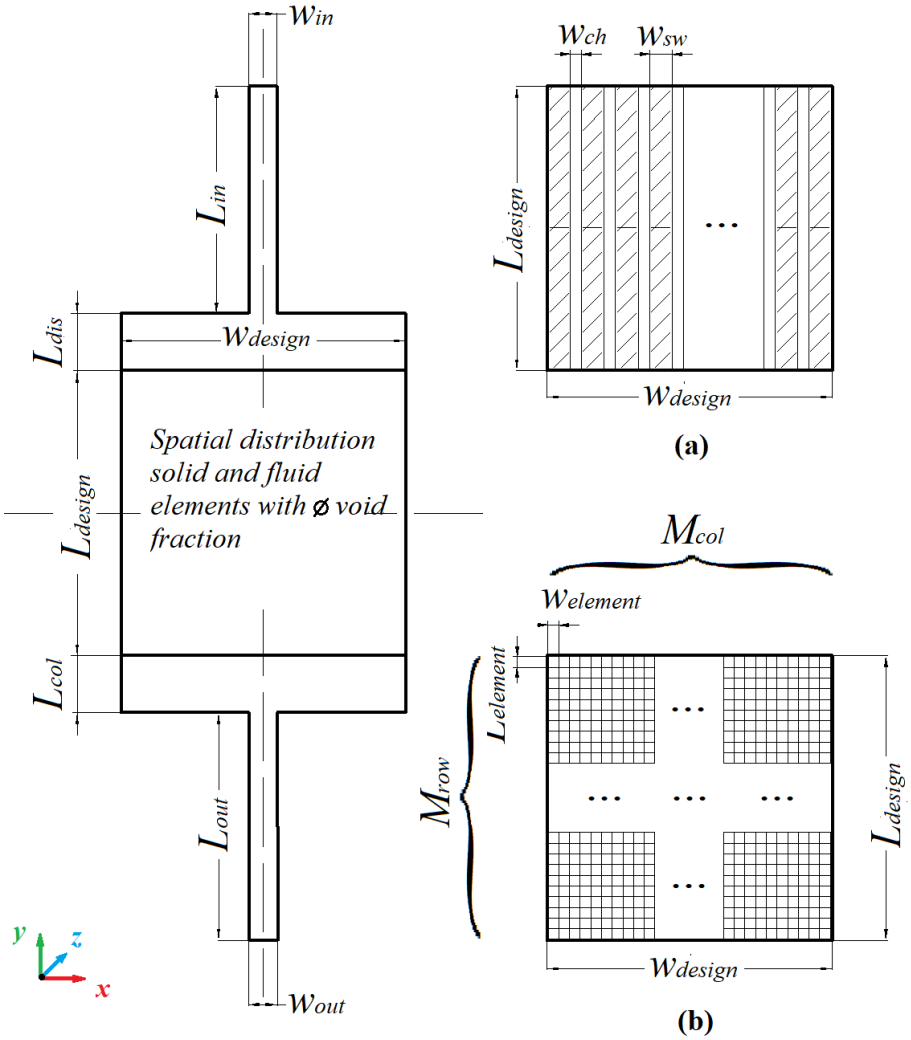

Figure 4.1. Schematic view of the heat sink model for GATO and RSC: (a) special case of a parallel straight channel heat sink (RSC) and (b) design domain of the GATO heat sink represented by fluid or solid (cubic) elements.

4.2.2 GA procedure

A GA procedure is developed to determine the best spatial distribution of the fluid and solid elements in the design domain to minimize the peak temperature of the heating surface (T_{peak}) (it is also the fitness function in this optimization) under the constraint of constant void fraction (Φ) for the fully connected fluid phase. The reason for this fully connected fluid domain constraint is to prevent the existence of isolated fluid element(s) enclosed by solids, which may cause the boiling of fluid due to local overheating. To do this, the design domain is gridded into *r* rows and *c* columns and expressed by a binary matrix $M_{(r\times c)}$, each element in *M* representing either solid (0) or fluid (1) as shown in Figure 4.1 (b). the TO problem can then be formulated as Eq. (4.3).

$$Find\ M_{(r\times c)} \tag{4.3}$$

$$Minimize\ T_{peak}$$

$$s.t.$$

$$\begin{cases} \Phi = constant \\ Connectivity = 1 \end{cases}$$

The general principle of GA is to assess the configurations among a starting random population, keep the best ones that meet the objective function (or fitness), and then cross and mutate them to get a new child population of the same size, and so on. One generation after another, the best design is expected to be determined. The main procedure of GA in this study is shown in the flow chart (Figure 4.2) and described in detail below.

- ***Initial generation***: several $M_{(r\times c)}$ matrices (100 in this study) are generated by random allocation of 0 and 1 elements at fixed Φ. The repeatability and connectivity are checked to guarantee that only the non-repeated *M* with a fully connected fluid domain is included in every generation. Each *M* is treated as an individual in this generation to be evaluated in the next steps.
- ***Geometry transformation***: all the matrices in the generation would be transformed into real geometry models (such as shown in Figure 4.3) by writing all the dimensions and 0 & 1 distribution information into a coded script as an executable file for the CFD tool.
- ***Performance evaluation of individuals***: the fluid flow and heat transfer characteristics of each configuration are calculated by the CFD method. Especially, the objective function (T_{peak} in this study) values of individuals are obtained and extracted.
- ***Ranking, selection, and elites keeping***: all the tested configurations are ranked according to fitness (objective function). A certain amount of well-evaluated configurations (50 in this study, ranked from 2 to 51) with a higher ranking are selected as future parents to create the individuals of the next generation while others are eliminated from reproduction. Note that the top-ranked individual(s) are considered elite(s) (1 in this study) and would be maintained in the next generation, preventing the loss of the most fitted "genes" [174].

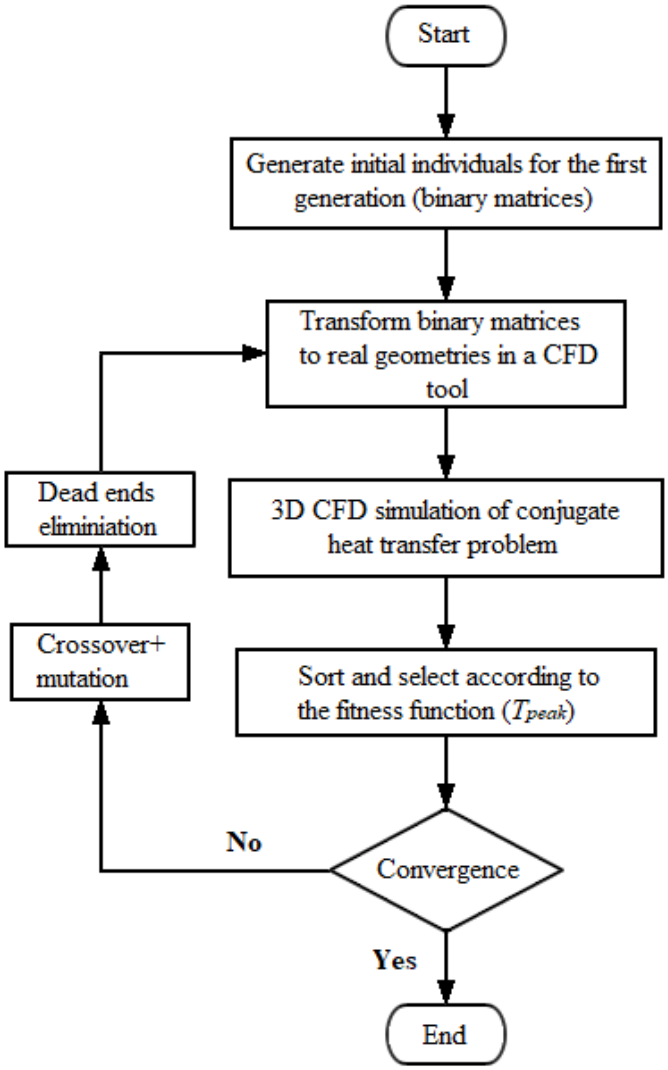

Figure 4.2. Flow chart of the GATO algorithm for global flow channel optimization in heat sinks

- ***Crossover and Mutation***: Crossover operation is firstly performed on two neighboring individuals between the top 2 to the top 51 in the ranking list (top one as elite) to produce two children. One-point crossover is used in the current study, i.e., based on a randomly selected element in the matrix either horizontal or vertical crossover is performed with equal probability. Then, each produced child is set to have a 20% probability to mutate, by either horizontal or vertical string swapping with equal probability. In that way, better genes (regarding fitness) would be inherited while in the meantime good diversity could be ensured. 100 children are generated and at the same time, the constant void fraction and connectivity constraints are obeyed. More detailed information about the crossover and mutation operations is given in Appendix 4.A of this chapter.
- ***Dead ends elimination***: In case one fluid element is surrounded on three sides by solid cells, the flow velocity is usually near zero thus the cooling effect at these ends might be low. Therefore, an additional step is to eliminate these fluid elements, considered dead ends, by randomly exchanging their locations with some solid cells, keeping always the constant Φ and full connectivity. More explanation about this step may be found in

Appendix 4.B. All the matrices in this new generation will then be transferred to the geometry transformation step for recurrence following the above-explained procedure.

- ***Termination criterion:*** the GATO is considered to be completed when the variation of the median value of the objective function (T_{peak}) from one generation to the next is smaller than 1×10^{-4} for at least 10 generations (Eq. 4.4). The flow channel configuration and the thermo-hydraulic characteristics of the optimum topology will be exported.

$$\left(\sum_{k=n-9}^{n} \left|\frac{T_k^{median} - T_{k-1}^{median}}{T_{k-1}^{median}}\right|\right) < 1 \times 10^{-3} \tag{4.4}$$

4.2.3 Calculation of flow and temperature fields by CFD method

The fluid flow and heat transfer characteristics of each flow channel configuration are calculated by CFD simulation. The governing Navier-Stokes equations and heat transfer equations under steady-state are the same as those presented in chapter 3, Eqs. 3.9 - 3.12, thus will not be repeated here. Detailed simulation parameters used in this study are presented in section 4.3.1.

4.2.4 Performance indicators and non-dimensional parameters

Various parameters are used as performance indicators, introduced below. The overall thermal resistance of heat sink R_{th} is defined in Chapter 3, Equation (3.24). The overall pressure drop of the heat sink is calculated as the pressure difference between the inlet and outlet ports:

$$\Delta P = P_{in} - P_{out} \tag{4.5}$$

The Nusselt number (Nu) of the heat sink and the Reynolds number (Re) at the inlet channel are calculated by Eqs. (4.6) and (4.7):

$$Nu = \frac{h_{avg} \cdot D_{h,design}}{\lambda_f} \tag{4.6}$$

$$Re_{in} = \frac{\rho_f \cdot v_{in} \cdot D_{h,in}}{\mu_f} \tag{4.7}$$

Where λ_f, ρ_f and μ_f are the thermal conductivity, density, and dynamic viscosity of the fluid, respectively. v_{in} is the inlet flow velocity and $D_{h,in}$ is the hydraulic diameter of the inlet channel. The hydraulic diameter $D_{h,design}$ of the flow channels in the design domain are calculated as follows [175]:

$$D_{h,design} = \frac{4Volume_{ch}}{S_w} \tag{4.8}$$

Where $Volume_{ch}$ and S_w are the total wetted volume and the total wetted surface area of the flow channels in the design domain, respectively. The average heat transfer coefficient h_{avg} is calculated by Eq. (4.9):

$$h_{avg} = \frac{Q}{A_{eff}(T_{w,avg} - T_{f,avg})} \tag{4.9}$$

Where A_{eff} is the effective solid-fluid interface area, $T_{w,avg}$ is the average channel wall temperature, and $T_{f,avg}$ is the average fluid temperature calculated by:

$$T_{f,avg} = \frac{T_{f,in} + T_{f,out}}{2} \tag{4.10}$$

The standard deviation of temperature (STD_T) at the heating surface is calculated as:

$$STD_T = \sqrt{\frac{1}{n-1}\sum_{Pix=1}^{n}(T_{Pix} - \bar{T})^2} \tag{4.11}$$

Where n is the total number of points with temperature value at the heating surface; Pix is the No.Pix point and $\bar{T}$ is the average temperature at the heating surface.

Velocity, temperature, and pressure parameters are normalized as below:

$$v^* = \frac{v}{v_{in}} \tag{4.12}$$

$$T^* = \frac{T - T_{f,in}}{T_{f,out} - T_{f,in}} \tag{4.13}$$

$$P^* = \frac{P}{P_0} \tag{4.14}$$

Where P_0 is pressure drop when the design void fraction (Φ) is equal to 1.

4.3 Benchmark case and optimization results

In this section, the optimization results of a benchmark heat sink case are presented to show the feasibility and effectiveness of the proposed GATO method.

4.3.1 Benchmark case and numerical parameters

Figure 4.3 shows the 3-D CFD model for the studied benchmark case of the heat sink subjected to GATO. The dimension and operation details are listed in Table 4.1. The middle design domain has a square shape of 50 mm × 50 mm, represented by a binary matrix of $M_{50\times50}$. The fluid void fraction (Φ) for this benchmark case is set as 0.50, i.e. equal solid and fluid elements, and their distribution is subjected to optimization. Recall that for the convenience of simulation and optimization, the entire fluidic circuit has an identical channel depth of e=1 mm,

making every fluid or solid element as a cubic form to morph and for the simplification of the geometry model and CFD calculation. The channel thickness could also be a parameter for a 3D TO of the fluid domain, but not considered in this study.

Table 4.1 Dimensions of the benchmark case

Geometric parameter (mm)	w_{in}& w_{out}	w_{design}&L_{design}	L_{in}& L_{out}	L_{dis}& L_{col}	$w_{element}$&$L_{element}$
Dimensions (in mm)	5	50	40	10	1

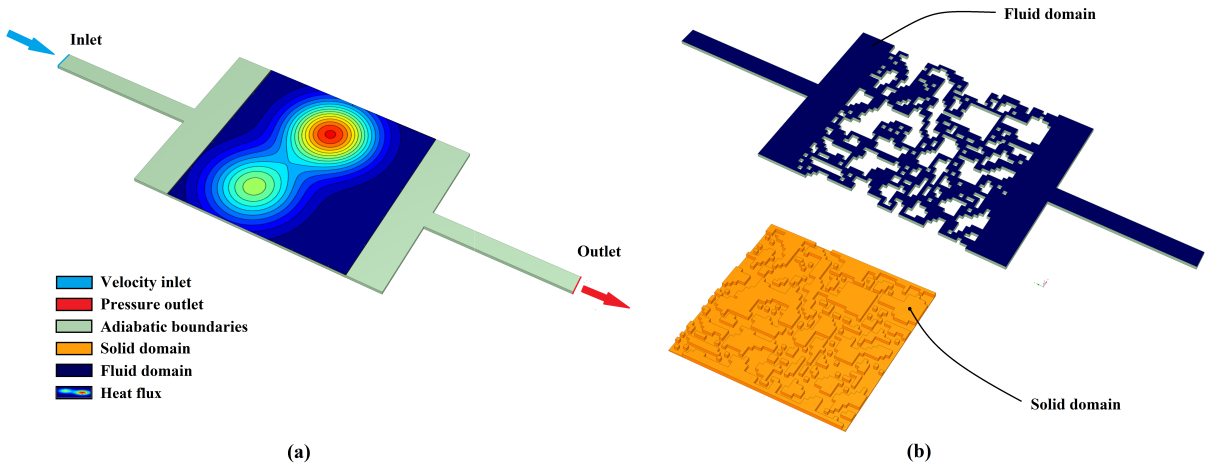

Figure 4.3. Heat sink model for the benchmark study. (a) Geometry and boundary conditions; (b) example of solid and fluid domains.

Water and aluminum are used as the fluid phase and the solid phase, respectively. Their physical properties are considered as constant and values are listed in Table 4.2.

Table 4.2. Physical properties of the fluid and solid used for simulations

Material	Density ($kg \cdot m^{-3}$)	Thermal conductivity ($W \cdot m^{-1} \cdot K^{-1}$)	Specific heat capacity ($J \cdot kg^{-1} \cdot K^{-1}$)	Viscosity ($Kg \cdot m^{-1} \cdot s^{-1}$)
Water	998.2	0.6	4182	1.003×10^{-3}
Aluminum	2719	202.4	871	-

3D CFD simulations were performed to calculate the fluid flow and heat transfer characteristics of each design. Fluid velocity inlet (v_{in}=0.1 $m \cdot s^{-1}$) normal to the inlet boundary surface is set, with a temperature of 293 K. The corresponding inlet Reynolds number Re_{in} is calculated to be 166 to make sure the whole flow region is under laminar. The pressure outlet boundary is set for the outlet surface with zero-gauge pressure. All walls are considered non-slip and adiabatic, except for the upper surface of the design domain (heating surface of the heat sink). For the latter, a Gaussian-shape two-peak heat flux (HF) distribution is defined, given by the following Eq. (4.15).

$$q(x,y) = \sum_{i=1}^{2} B_i e^{-\frac{(x-x_i)^2+(y-y_i)^2}{2\sigma_i^2}} \quad (4.15)$$

The heat flux peak located at the position (x_i, y_i) has a maximum value of B_i and σ_i indicates the spatial spread. The total power of the heat sources is equal to 90 W (due to the lower inlet *Re* number to avoid the phase-change of fluid), corresponding to an average heat flux (power density) for the heating surface of $q_{ave} = 3.6$ W·cm^{-2}. Detailed values of parameters in Eq. 4.15 and the shape of the heat fluxes are given in Table 4.3.

Table 4.3. Gaussian-shape two-peak heat flux

	x_i (mm)	y_i (mm)	B_i $(W \cdot cm^{-2})$	σ_i (mm)	
Heat flux (HF) 1:					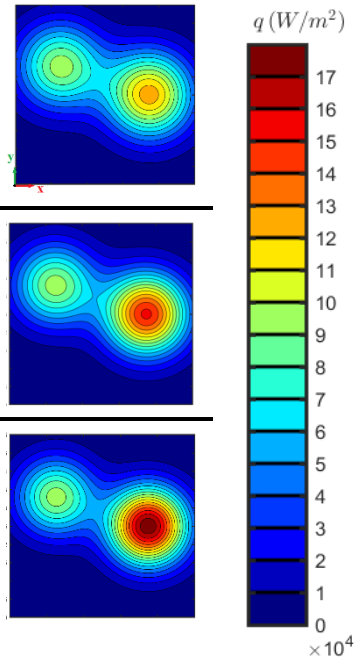
1	37.5	25	12.5	8.45	
2	12.5	33	9.5	8.45	
Heat flux (HF) 2:					
1	37.5	25	15.2	7.91	
2	12.5	33	9.5	7.91	
Heat flux (HF) 3:					
1	37.5	25	17.7	7.45	
2	12.5	33	9.5	7.45	

In this study, an open-source FVM code OpenFoam (version 7) was used to solve the governing equations presented in section 3.2.3. Note that the gravity and viscous heating effects were not considered for simplification. The multi-physics conjugate heat transfer solver "chtMultiRegionFoam" in OpenFoam has been used for both solid and fluid domains [176]. No re-meshing is needed when updating the individuals from one generation to the next in the GATO procedure, thereby saving computational time and data storage. The laminar model was used for fluid flow due to the small *Re* numbers in the fluid domain. The widely used SIMPLE algorithm was employed for the velocity-pressure coupling. Geometric-Algebraic Multi-Grid (GAMG) solver with diagonal incomplete-Cholesky with Gauss-Seidel (DICGaussSeidel) smoother was used to solve the pressure equations for a faster iteration. Stabilized Precondition Conjugate Gradient (PBiCGStab) with Diagonal incomplete-LU (DILU) was used to solve the energy and momentum equations. The solution was considered to be converged when (i) the maximum temperature of the heated surface and the inlet-outlet pressure drop were constant

from one iteration to the next (less than 0.5% variation), and (ii) the normalized residuals were lower than 10^{-5} for the energy equation and 10^{-4} for other governing equations.

Structured cube shape meshes with equal edge lengths were generated. The grid used in the study had 129 k elements in total, with 71 k elements for the fluid zone and 56 k elements for the solid zone. A grid independence study (a randomly chosen topological individual in the initial generation of the benchmark study) was conducted to guarantee that the current mesh density used was appropriate and sufficient regarding both accuracy and calculation time. More details of the mesh independence study can be found in Appendix 4.C of this chapter. The CFD simulations using OpenFoam were performed with the help of a High-performance computing (HPC) cluster CCIPL (Le Centre de Calcul Intensif des Pays de la Loire) [177]. Matlab (version: R2020 a) was used for the matrix generation and updating, data processing, and GA procedure.

4.3.2 Optimization results of the benchmark case

Figure 4.4 depicts the evolution of T_{peak}^{min} and T_{peak}^{median} amongst the 100 individuals along with the increasing number of GA generations. More precisely, T_{peak}^{min} stands for the smallest value of 100 T_{peak} in a generation while T_{peak}^{median} stands for the average value between the 50th and 51st of T_{peak} values in a generation. It took 170 generations to meet the defined convergence criterion (Eq. 4.4), the value of T_{peak}^{median} being decreased from 365.1 K to 348.6 K. Correspondingly, the T_{peak}^{min} value also decreased continuously from 358.6 K (generation 1) to 348.6 K (generation 170), indicating the effectiveness of the proposed GATO method in attaining the defined optimization objective. Note that some stairs appeared in the T_{peak}^{min} curve especially during the first half of the convergence, which is mainly due to the elite keeping in GA: the crossover and mutation process cannot give birth to a better individual that underscores the top-ranked one in the previous generation. Also note that at the convergence, the T_{peak}^{min} and T_{peak}^{median} values are very close (but not the same), indicating that the fitness difference between the top 50 individuals is very small.

Figure 4.5 shows the flow channel configuration of the design domain (a), the corresponding velocity fields (b) at the middle channel depth (z^*=-0.5), and the temperature field (c) on the heating surface for the top-ranked individual of generation 1, 10, 25, 45, 74 and 170. It is clearly illustrated that the flow topology evolves during the GA optimization to meet the objective function. In more detail, fluid elements tend to join together and form larger channels near the inlet and outlet manifolds. In contrast, pin-fin structures and small bifurcations and confluences are more likely to appear in the middle area where two heat flux peaks are located. Such a trend increases the fluid-solid contacting surface area and interrupts the formation of boundary layers, and enhances the cooling. The global structure of the flow paths is more or less established at generation 45 (e.g., a big cluster of solid elements downstream of the left heat flux peak) and inherited in the following generations. From then on, local details (small transversal flow paths) are still generated and adjusted along with the GA optimization.

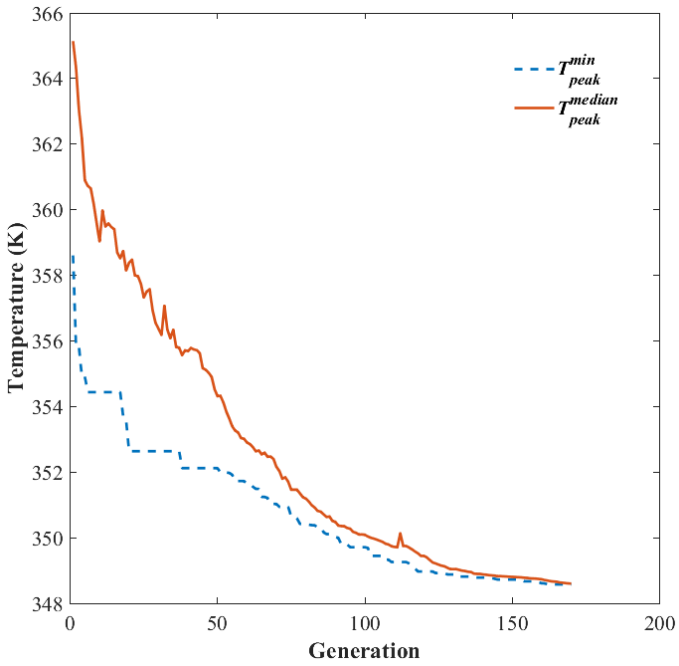

Figure 4.4. Evolution of T_{peak}^{min} and T_{peak}^{median} amongst the 100 individuals along with the increasing number of GA generations

At the end of generation 170, a higher proportion of cooling fluid mass is guided from the inlet to the right part of the design domain. This is because the larger heat flux peak is located in this area and closer to the outlet manifold, higher cooling capacity (higher mass and lower temperature of coolant) is thereby needed to remove the temperature hot spots. The evolution of the temperature field on the heating surface along with GA steps (Figure. 4.5 (c)) shows clearly the better cooling performance of the heat sink by optimization of the flow path topology. The temperature hot spots gradually disappear and the isotherms become more parallel to the line connecting the two hot spots. perpendicular to the global flow direction (from the inlet to the outlet) along with better temperature uniformity.

The results of this benchmark case indicate that at the constraint of constant void fraction (Φ), the fluid elements have been arranged more efficiently to form an adapted flow configuration corresponding to the power and location of heat sources. In this way, the T_{peak} (objective) can be decreased generation by generation by the GATO method, achieving the best cooling of the heating-generating surface.

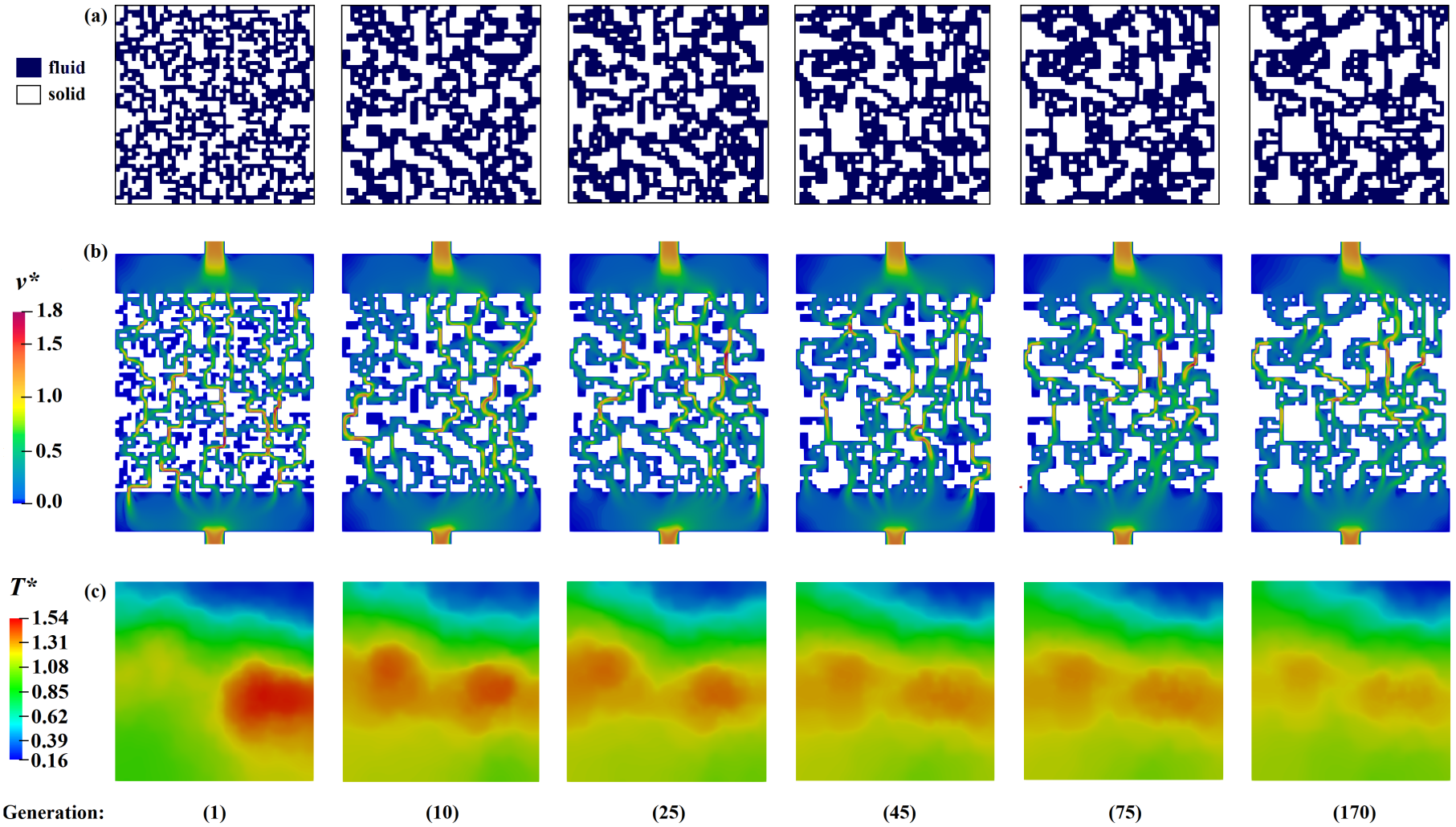

Figure 4.5. Top-ranked flow path configuration for the benchmark case at generation 1, 10, 25, 45, 74, and 170. (a) Fluid/solid elements distribution in the design domain; (b) Corresponding velocity field at mid-channel depth (z^*=-0.5); (c) Temperature field at the heating surface.

4.4 Effects of design variables of GATO on the optimized channel configuration: a parametric study

In section 4.3, the GATO has been successfully applied to obtain the optimal flow configuration (heat sink geometry) for the benchmark case. Here the optimized channel configuration as a function of the key design variables is investigated, including the heat flux shape (q), the void fraction (Φ), the inlet flow velocity (v_{in}), and the design domain resolution ($M_r \times_c$). Note that other parameters are kept the same as the benchmark except for the variable being evaluated. The conventional RCS heat sink as shown in Figure 4.1 (a) has also been introduced for testing. To make it comparable, the geometrical parameters of the RSC heat sinks may be different based on the various parameters we investigate in this section, as presented in Table 4.4. Their cooling performances under the same design variables and operating conditions are compared and reported below.

Table 4.4 The geometrical information of the RSC heat sinks introduced for performance comparison with GATO heat sinks.

Void fraction (Φ)	w_{ch} (mm)	w_{sw} (mm)	Number of channels	L_{design} (mm)	Geometry
0.40	1	1.5	20	50	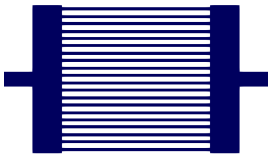
0.50 (Benchmark)	1	1	25	50	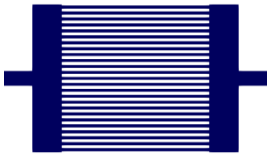
0.65	1	0.5	32	50	
0.80	1	0.25	40	50	

Resolution	w_{ch} (mm)	w_{sw} (mm)	Number of channels	L_{design} (mm)	Geometry
$M_{25\times25}$	2	1	12	50	
$M_{100\times100}$	0.5	0.5	50	50	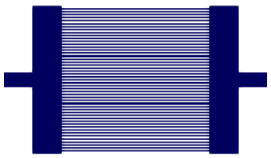

4.4.1 Influences of peak heat flux difference

Three heat fluxes shown in Table 4.3 have been used as input for the heating surface. They have the same total power (Q=90 W; q_{avg} = 3.6 W·m^{-2}) but differentiate between them by the increasing value of the higher heat flux peak. The GATO has been executed for each and the obtained optimization results are shown in Figure 4.6.

Shown in Figures 4.6 (a) and 4.6 (b) are the optimal channel configurations of the design domain, and the normalized velocity field, respectively. A similar general pattern may be observed, i.e., more fractionated small solid islands at the location of two heat flux peaks while bigger solid blocks in other regions. The more difference between the two peak values of the heat flux (e.g., heat flux 3 (HF 3)), the more fluid elements are allocated at the right part of the design domain to deliver more mass of the cooling fluid to the higher temperature hot spot (cf. Figure 4.6 (b)).

The temperature contours at the heating surface of GATO and RSC heat sinks are shown in Figure 4.6 (c) and Figure 4.6 (d), respectively. Temperature hot spots can be observed for the RSC heat sink, while they are by and large eliminated in the GATO heat sink with clearly improved temperature uniformity. The T_{peak} value for the GATO heat sink is 345.5 K (HF 1), 348.6 K (HF 2), and 351.3 K (HF 3), respectively, smaller than that of the RSC heat sink (351.3 K, 356.5 K, and 361.0 K, respectively). The greater the difference between two peaks (e.g., HF 3), the more reduction of T_{peak} could be achieved by GATO compared to RSC. As already shown in chapter 3, the RCS as a basic (conventional) configuration is logically less performant in handling highly heterogeneous heating surfaces, for which the benefits of the GATO method are more significant.

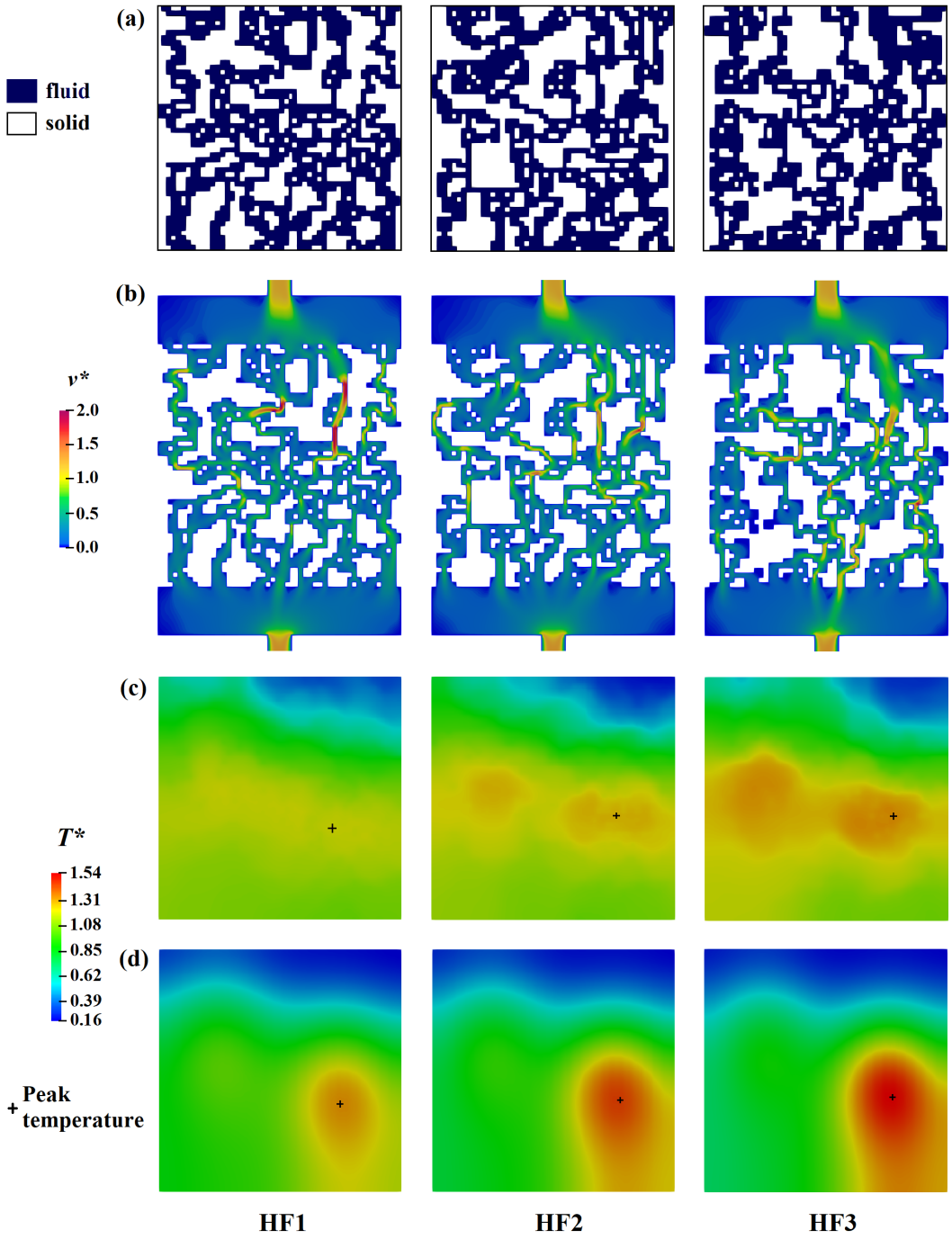

Figure 4.6 Influence of heat flux shape on the performance of GATO and RSC heat sinks. (a) optimized flow channel configuration; (b) velocity field (z^*=-0.5) of the GATO heat sink; (c) temperature field at the heating surface of the GATO heat sink; (d) temperature field at the heating surface of the RSC heat sink.

Table 4.5 lists the performance indicators of GATO and RSC heat sinks subjected to different heat fluxes. Generally, the *Nu* number of the GATO heat sink is about 40%-50% higher than that of the RSC heat sink, owing to the complex flow path configuration obtained that breaks the thermal boundary layer of fluid and therefore enhances the convection heat transfer. Nevertheless, the pressure drop is inevitably boosted due to the geometry complexity, and the P^* value of GATO is significantly higher than that of RSC, However, the global pressure drop of the GATO heat sink (< 220 Pa) is still small at this low flow rate condition.

The R_{th} values follow the same tendency as T_{peak} discussed above. The values of STD_T increase with the rising difference of two heat flux peaks, but the temperature distribution is more uniform at the heating surface of the GATO heat sink than that of the RSC heat sink.

Table 4.5 Performance comparison between GATO and RSC heat sinks under different heat fluxes.

Heat flux	*Nu* (GATO)	*Nu* (RSC)	R_{th} ($K \cdot W^{-1}$) (GATO)	R_{th} ($K \cdot W^{-1}$) (RSC)	*P** (GATO)	*P** (RSC)	T_{peak} (K) (GATO)	T_{peak} (K) (RSC)	STD_T (K) (GATO)	STD_T (K) (RSC)
HF1	5.7	3.8	0.58	0.64	1.88	1.15	345.5	351.3	10.3	13.0
HF2	5.7	3.9	0.61	0.70	1.82	1.15	348.5	356.8	11.4	14.3
HF3	5.3	3.9	0.64	0.75	1.92	1.15	351.3	361.0	11.7	15.5

4.4.2 Void fraction (Φ) of the design domain

The influence of void fraction on the cooling performance of the heat sink optimized by GATO has been evaluated, by varying the Φ value from 0.40 to 0.80. The obtained results (optimal flow path configuration, velocity field, and temperature contour) are depicted in Figure 4.7.

At a low void fraction (Φ=0.4), the limited amount of fluid elements is organized by GATO into a mesh-type flow circuit with relatively clear splitting or merging junctions. Fluid with higher velocity magnitude is guided by the main flow paths to cool down the temperature hotspots. In contrast, at a high void fraction (Φ=0.8), the excessive fluid elements are arranged like a porous medium in which the velocity magnitude is much lower. The numerous small solid islands work as pin-fin structures surrounded by the cooling fluid calmly flowing, the contacting surface area is thereby higher. Nevertheless, it can be seen from Figure 4.7 (b) that some fluid elements have near-zero velocity, implying that the void fraction is not all efficiently used. The sharping of the flow path could be done by eliminating these fluid elements considered as dead volume, which will be presented in later section 4.5.1.

By examining Figure 4.7 (c), it is worth noting that the lowest T_{peak} value (346.4 K) is reached at Φ=0.65 after GATO optimization. Higher or lower values of Φ render higher T_{peak} of the GATO heat sink, and also the higher R_{th} values as reported in Table 4.6. Recall that Φ is treated as a constraint in the algorithm, i.e., constant Φ of all the individuals to be evaluated in the GATO. Such constraints may need to be revisited to achieve a more general optimum.

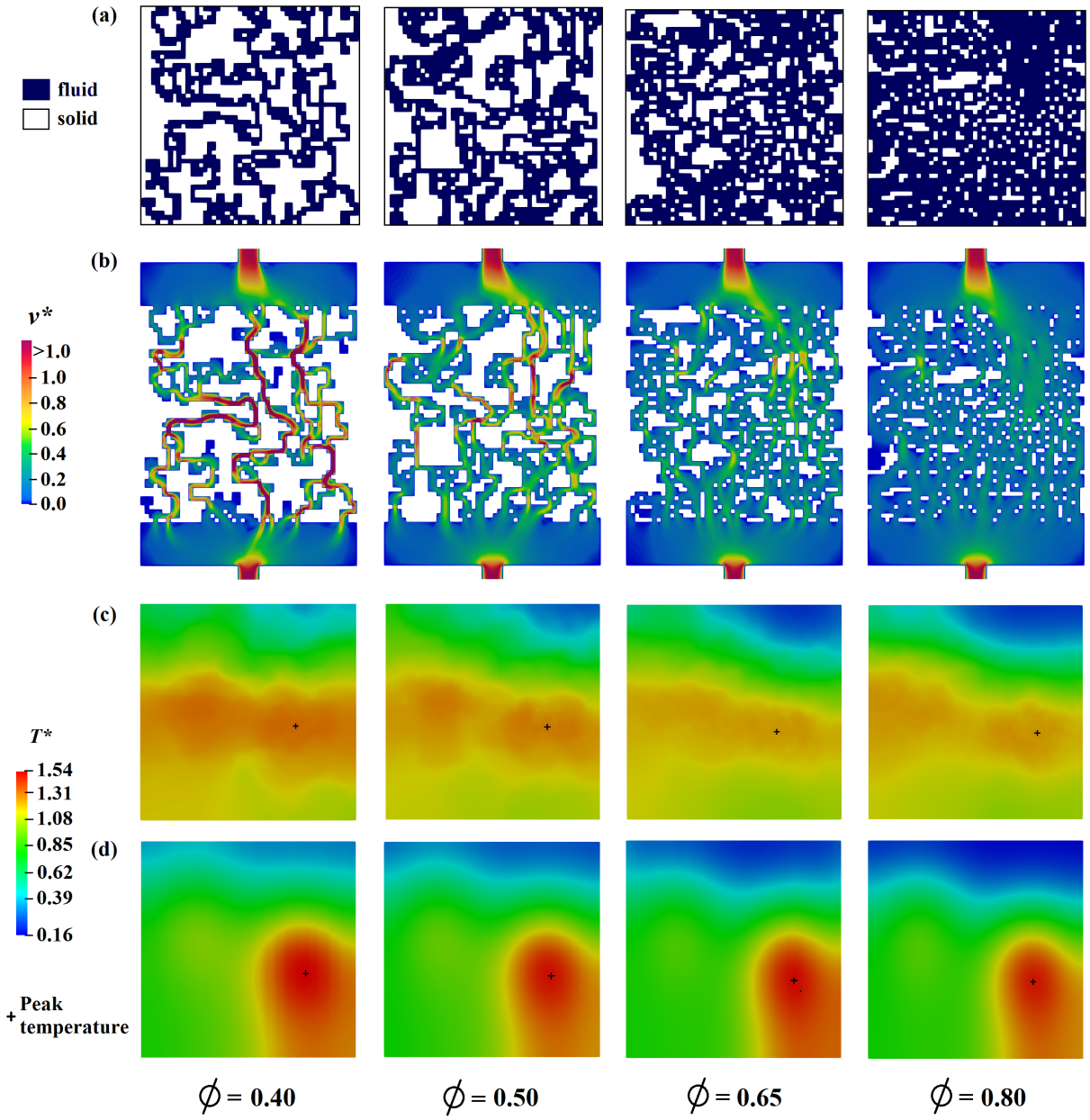

Figure 4.7 Influence of fluid void fraction (Φ) on the performance of GATO and RSC heat sinks. (a) optimized flow channel configuration; (b) velocity field (z^*=-0.5) of the GATO heat sink; (c) temperature field at the heating surface of the GATO heat sink; (d) temperature field at the heating surface of the RSC heat sink.

The performance comparison between the GATO and RSC heat sinks at different Φ values is presented in Figure 4.7 (c & d), and in Table 4.6 as well. The *Nu* numbers of GATO heat sinks are very close, but all higher than those of parallel straight channels with the same Φ, indicating better cooling performance. Regarding the RSC heat sink, the *Nu* number significantly decreases with the increasing Φ, mainly due to an increase of the effective heat transfer surface area (higher number of channels as shown in Table 4.4) between fluid and solid under the same input power, which reduces heat transfer coefficient. Moreover, STD_T values for both GATO and RSC are larger at a high void fraction, this is because of the low-temperature region at the entrance of the design domain, closer to the fluid inlet temperature. But the GATO heat sink has a more uniform temperature distribution at the heating surface than

that of the RSC heat sink for the same Φ value, owing to the dispersed hot spots by the optimized flow path configuration.

The pressure drop of the GATO heat sink significantly increases with the decreasing Φ value, i.e., P^* reaches 3.89 (429.4 Pa) at Φ=0.4. In addition to the higher velocity magnitude in the main flow paths, the numerous splitting/merging junctions also create additional singular losses [178]. Regarding the RSC, the pressure drop increase is relatively small, i.e., P^* ranging from 1.08 to 1.20.

Table 4.6 Performance comparison between GATO and RSC heat sinks for different void fraction values.

Φ	Nu (GATO)	Nu (RSC)	R_{th} (K · W^{-1}) (GATO)	R_{th} (K · W^{-1}) (RSC)	P^* (GATO)	P^* (RSC)	T_{peak} (K) (GATO)	T_{peak} (K) (RSC)	STD_T (K) (GATO)	STD_T (K) (RSC)
0.40	5.6	4.4	0.63	0.72	3.89	1.20	350.0	358.0	10.6	13.6
0.50	5.7	3.9	0.61	0.70	1.82	1.15	348.5	356.8	11.4	14.3
0.65	5.3	3.3	0.59	0.71	1.30	1.10	346.4	357.3	12.9	15.5
0.80	5.6	2.1	0.59	0.70	1.13	1.08	346.8	356.2	13.7	16.3

4.4.3 Inlet velocity

The benchmark heat sink has been optimized by GATO under different inlet velocities (v_{in}=0.1, 0.2, and 0.4 m·s^{-1}) to investigate the influence of increasing fluid flow rate (or Re_{in}) on the optimized flow path configuration and its cooling performance. The optimization results as well as the performance comparison with the RSC heat sink are reported in Figure 4.8 and Table 4.7.

It can be observed from Figure 4.8 (a &b) that for all three tested inlet velocities, the main mass flow is delivered to the location of heat flux peaks, and more fluid flow is guided towards the higher peak than the smaller heat flux peak. With v_{in} increases, the main flow structure in the entrance manifold tends to be fractioned into more small streams to compensate the stronger inertial effect. Lower T_{peak} can be reached at high v_{in} due to the higher cooling capacity, i.e., 348.6 K (v_{in}=0.1 m·s^{-1}), 329.7 K (v_{in}=0.2 m·s^{-1}) and 321.5 K (v_{in}=0.4 m·s^{-1}) respectively. Nevertheless, the normalized value (T^*_{peak}) increases with the increasing v_{in} due to the smaller ($T_{f,out} - T_{f,in}$).

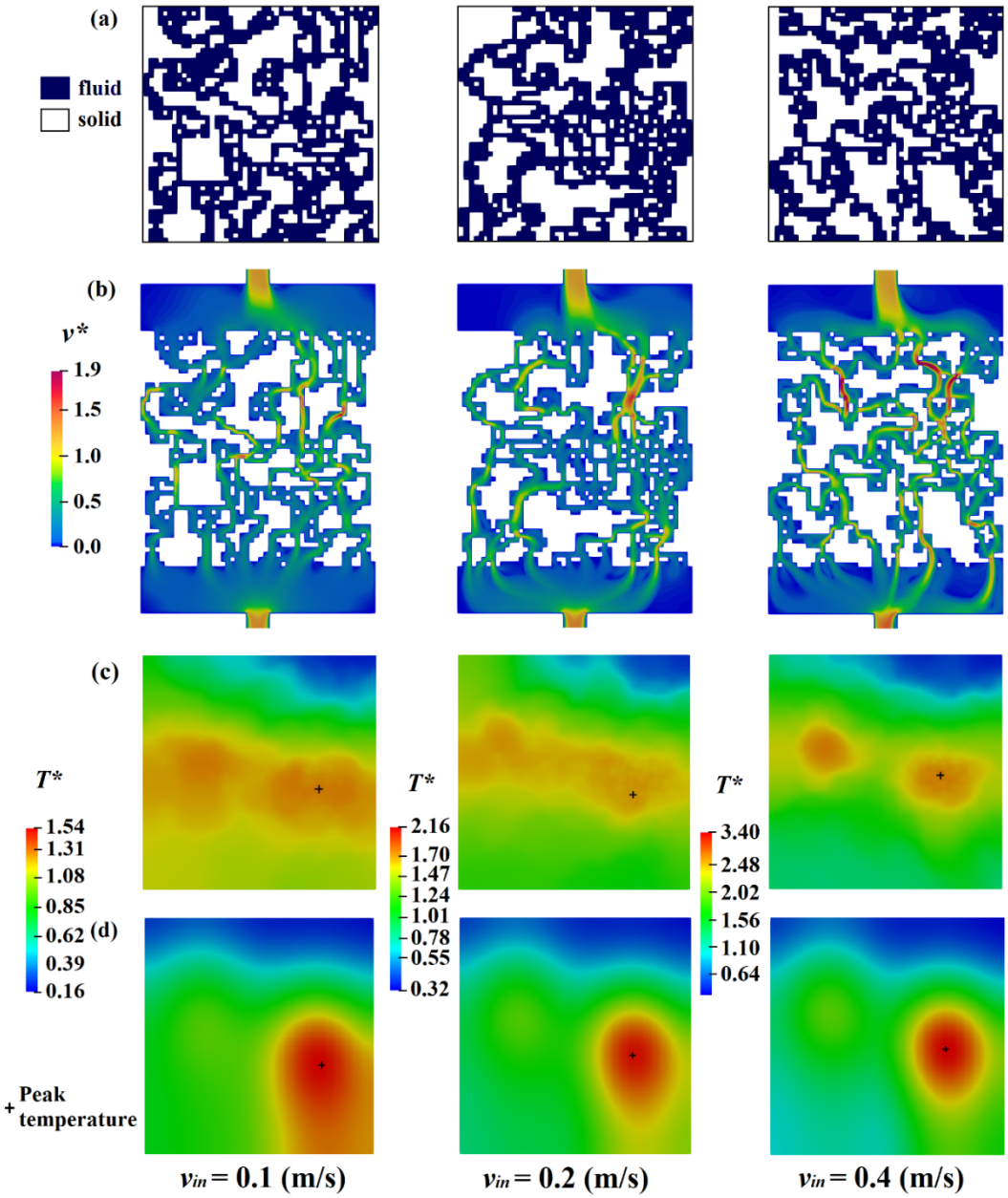

Figure 4.8 Influence of inlet fluid velocity (v_{in}) on the performance of GATO and RSC heat sinks. (a) optimized flow channel configuration; (b) velocity field (z^*=-0.5) of the GATO heat sink; (c) temperature field at the heating surface of the GATO heat sink; (d) temperature field at the heating surface of the RSC heat sink.

Table 4.7 lists the global thermal and hydraulic performances of GATO and RSC under different v_{in} values for comparison. The increasing v_{in} (Re_{in}) results in reduced R_{th}, $T_{peak,}$ and STD_T but increased Nu and P^*. The higher cooling capacity at a high fluid mass flow rate enhances the convection heat transfer and temperature uniformity at the heating surface while at the same time raising the pressure drop. The augmentation of Nu number by applying the GATO method (compared to RSC heat sink) is more significant at a high flow rate, i.e., 46% at v_{in}=0.1 m·s^{-1} whereas 80% at v_{in}=0.4 m·s^{-1}. However, this enhancement is achieved at the cost of higher pressure drop (pumping power consumption) since in the current optimization algorithm, no hydraulic criterion is considered in the objective function nor as constraints. This

issue will be further addressed in Chapter 6 of this thesis. Furthermore, the GATO heat sinks optimized under three v_{in} values show better temperature uniformity than corresponding RSC heat sinks. With the increase of inlet velocity, the difference in temperature uniformity tends to be smaller, which indicates that the GATO heat sink could more obviously provide a better temperature uniformity than the RSC heat sink under a low inlet mass flow.

Table 4.7 Performance comparison between GATO and RSC heat sinks under different inlet velocities.

V_{in} (Re_{in})	Nu (GATO)	Nu (RSC)	R_{th} ($K \cdot W^{-1}$) (GATO)	R_{th} ($K \cdot W^{-1}$) (RSC)	P^* (GATO)	P^* (RSC)	T_{peak} (K) (GATO)	T_{peak} (K) (RSC)	STD_T (K) (GATO)	STD_T (K) (RSC)
0.1 m·s^{-1} (166)	5.7	3.9	0.61	0.70	1.82	1.15	348.5	356.8	11.4	14.3
0.2 m·s^{-1} (332)	7.8	5.1	0.40	0.48	2.09	1.14	329.7	336.3	6.9	9.2
0.4 m·s^{-1} (663)	10.6	5.9	0.31	0.36	4.21	1.12	321.5	326.1	5.8	6.7

4.4.4 Design domain resolution

The matrix resolution of the design domain ($M_{r\times c}$) determines directly the number of fluid and solid elements that can be allocated during the GA, thereby playing an important role in the optimization. To explore the influence of this structure fineness, the GATO has been executed under different matrix resolutions (M25×25; M50×50 and M100×100), with the void fraction (Φ=0.50), inlet velocity (v_{in}=0.1 m·s^{-1}) and heat flux (HF2) as the same as the benchmark case. The optimization results are shown in Figure 4.9.

Although a similar pattern of mass flow delivery at a global level is proposed by GATO as has been discussed above, the flow path details are rather different at a local level, i.e., more local complex structures can be formed at the higher matrix resolution as shown in Figure 4.9 (a & b). The higher number of elements to morph brings highly diversified individuals during optimization, capable of constructing thin and dense channels with split and recombine flow paths. Moreover, the solid-fluid interface area could be largely increased, leading to the lowered T_{peak} of the optimized flow channel geometry, i.e., 356.1 K at $M_{25\times25}$ and 341.3 K at $M_{100\times100}$.

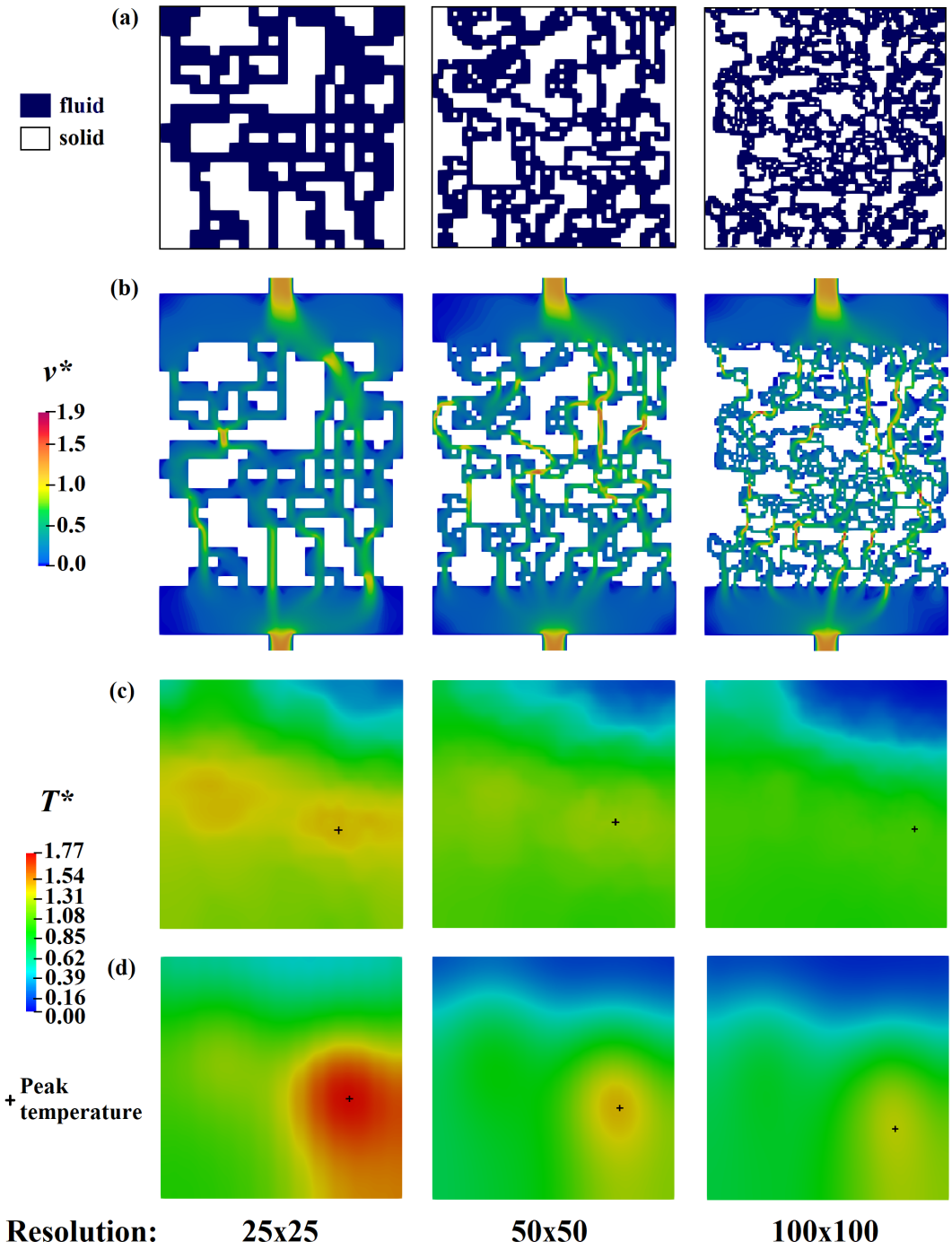

Figure 4.9 Influence of matrix resolution ($M_{r\times c}$) on the performance of GATO and RSC heat sinks. (a) optimized flow channel configuration; (b) velocity field (z^*=-0.5) of the GATO heat sink; (c) temperature field at the heating surface of the GATO heat sink; (d) temperature field at the heating surface of the RSC heat sink.

Table 4.8 presents the influence of $M_{r\times c}$ on the global thermal and hydraulic performances of the GATO heat sink. RSC heat sinks with the channel width equaling the element width (w_{ch}=$w_{element}$, cf. Figure 4.1) are also introduced for comparison. Again, both the *Nu* number and the P^* of the GATO heat sink are higher than those of the RSC heat sink due to the above-explained reasons. *Nu* number for both types of heat sinks gradually declines with the increasing design resolution. This is because of the smaller hydraulic diameter (D_h) of the

flow circuit on the hand, and the lowered average heat transfer coefficient (h_{avg}) on the other hand. In particular, the relatively small *Nu* number of RSC at $M_{100\times100}$ (w_{ch}=0.5 mm) could be the heat conduction takes the dominant effect over the heat convection due to the small channel width. The temperature distribution at the heating surface is the most uniform at w_{ch}=1 mm and $M_{50\times50}$ for both RSC and GATO heat sinks. Further increasing the mesh resolution (smaller channel size) will reduce the temperature uniformity due to the existence of a low-temperature region at the entrance of the design domain, as discussed above. Higher pressure drop is resulted in high $M_{r\times c}$, mainly due to the increased flow path complexity (thereby more singular losses).

Table 4.8 Performance comparison between GATO and RSC heat sinks under different matrix resolutions of the design domain.

Matrix resolution	*Nu* (GATO)	*Nu* (RSC)	R_{th} ($K \cdot W^{-1}$) (GATO)	R_{th} ($K \cdot W^{-1}$) (RSC)	*P** (GATO)	*P** (RSC)	T_{peak} (K) (GATO)	T_{peak} (K) (RSC)	STD_T (K) (GATO)	STD_T (K) (RSC)
$M_{25\times25}$	7.8	5.3	0.69	0.87	1.30	1.10	356.1	372.1	12.1	15.0
$M_{50\times50}$	5.7	3.9	0.61	0.70	1.82	1.15	348.5	356.8	11.4	14.3
$M_{100\times100}$	4.9	1.7	0.53	0.63	2.33	1.34	341.3	350.6	12.6	15.2

The results discussed in Table 4.8 also show that higher matrix resolution in GATO has the advantage of decreasing the R_{th} at a certain inlet velocity but at the cost of higher pressure drop. Moreover, a higher number of GA generations is needed to reach the convergence due to the increased number of design variables and also the individual diversity, requiring more calculation time. Once optimized, the obtained flow circuit complexity with fine structures also put place higher demands on the level of manufacturing precision for its realization. Therefore, in practice, the appropriate design resolution should be decided by considering both the available computing resources and the fabrication capacity.

4.5 Further discussions

Further discussions are made on some issues raised above, to revisit and understand the effectiveness as well as the limitations of the proposed GATO method.

4.5.1 Post-treatment for deal volume elimination

Despite the dead-end elimination step in the optimization algorithm (cf. Figure 4.2), fluid elements with low-velocity magnitude are still numerous in the optimized GATO flow configuration, especially at a high void fraction (cf. Figure 4.7). These fluid elements bring about unclear and ineffective fluid paths, which could be further eliminated by a post-treatment of the optimized flow geometry. As an example, a threshold value of $v^*_{threshold} = 0.0055$ has been applied for this purpose, i.e., all fluid elements having a velocity magnitude smaller than 5.5% of v_{in} are considered dead volume and thus will be eliminated. The flow path configuration

and the velocity field at different Φ values before and after this post-treatment are shown in Figure 4.10.

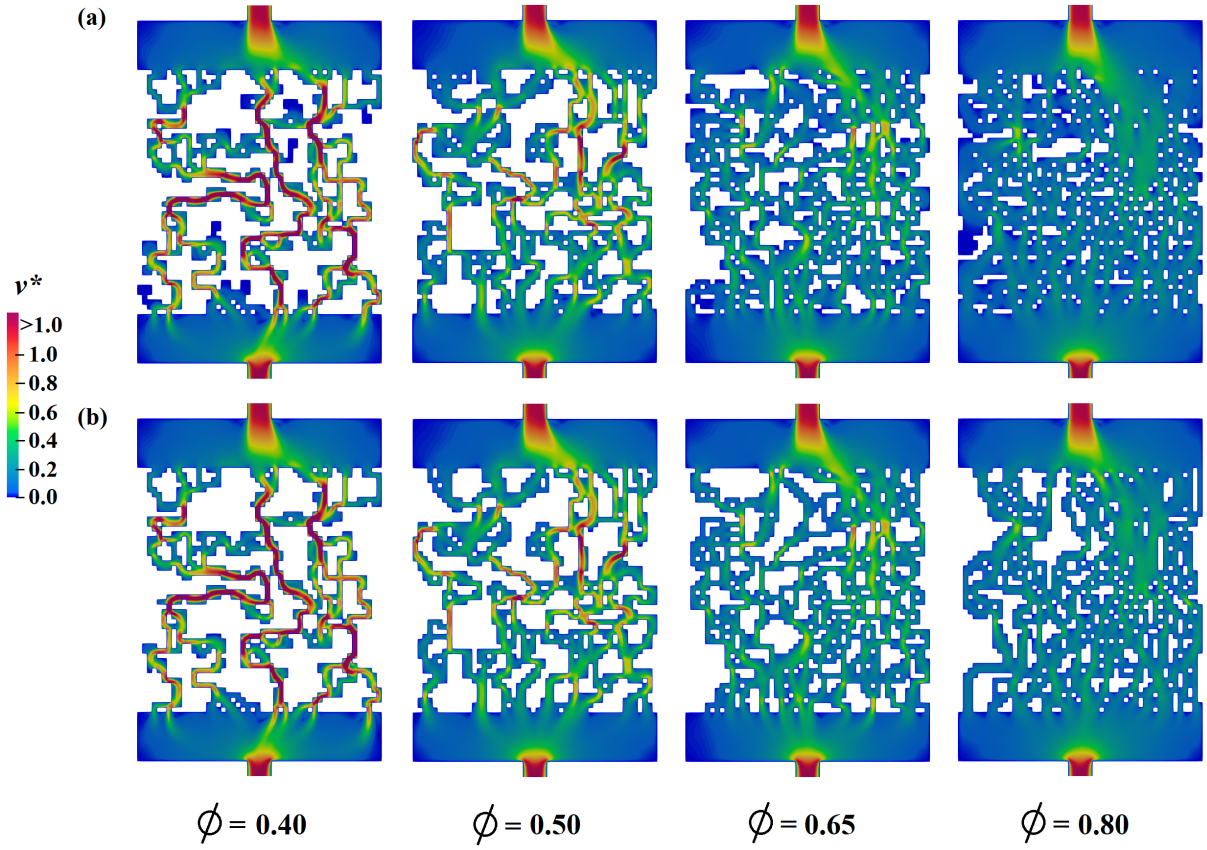

Figure 4.10 Post-treatment of the optimal flow configuration for dead volume elimination. (a) Original flow circuit; (b) flow circuit after post-treatment

It can be observed that the fluid paths become clearer, beneficial for the actual fabrication of the optimized heat sink in practice. The effective void fraction (Φ) declines after post-treatment but has a negligible impact on the thermal and hydraulic performances of the heat sink (Table 4.9). Note that a higher threshold value may result in smoother flow structures, but this aspect has not been further explored in this study.

Table 4.9 Φ, T^* and P^* of the GATO heat sink before and after post-treatment for dead volume elimination

Φ (before)	Φ (after)	T^* (before)	T^* (after)	P^* (before)	P^* (after)
0.40	0.36	1.31	1.31	3.90	3.90
0.50	0.44	1.28	1.27	1.83	1.84
0.65	0.56	1.22	1.22	1.31	1.32
0.80	0.65	1.24	1.24	1.15	1.16

4.5.2 Repeatability

The optimization algorithm has been executed another two times with the same settings for the benchmark case (chapter 4.3.1), to test the reproducibility of flow configuration at convergence. The convergence curves are shown in Figure 4.11. It can be observed that the T_{peak}^{median} values of the three runs at the convergence are very close (348.6 K, 348.9 K, and 349.3 K), with only a 1.26% difference. The final T_{peak}^{min} values are also quite close with a difference smaller than 0.7% (348.6 K, 348.8 K, and 349.0 K), indicating the good robustness of the GATO in achieving the defined optimization objective. This difference should still be reduced by setting a more stringent convergence criterion (Eq. 4.4) but will be rather time-consuming due to the GA's nature.

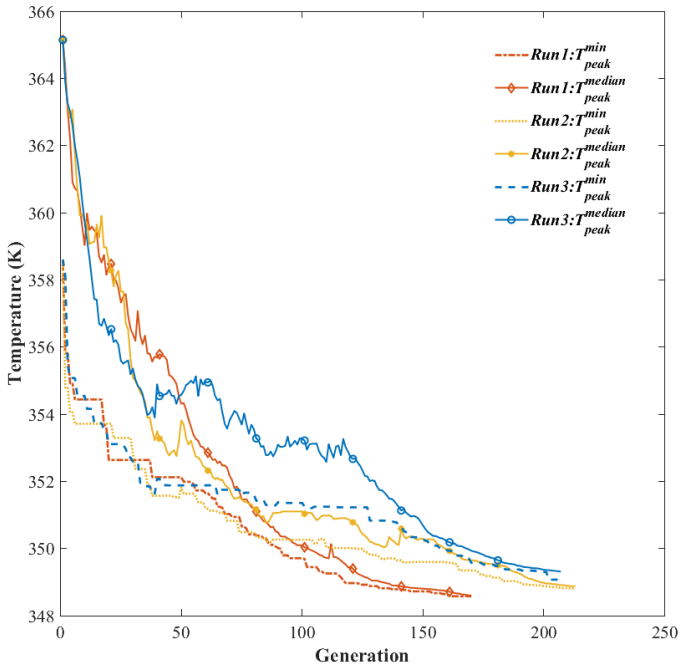

Figure 4.11 The convergence curve of T_{peak}^{median} and T_{peak}^{min} for three runs of the GATO for the benchmark case.

Nevertheless, a diversified flow configuration has been obtained each time by running the GATO (Figure 4.12), indicating the random feature during the crossover and mutation steps of the GA. Since they all provide the same cooling performance, several solutions may all be considered as very close to the global optimum, i. e., the objective function (T_{peak}) is rather flat near the global optimal point regarding the variation of the fluid/solid elements distribution.

Figure 4.12 (c) compares the temperature contour on the heating surface obtained by 3 runs of GATO. While the global pattern is quite similar (a small angle between isotherms and global flow direction due to the heat flux peak asymmetry), a slight difference at a local level can still be observed, especially in the position of the T_{peak}.

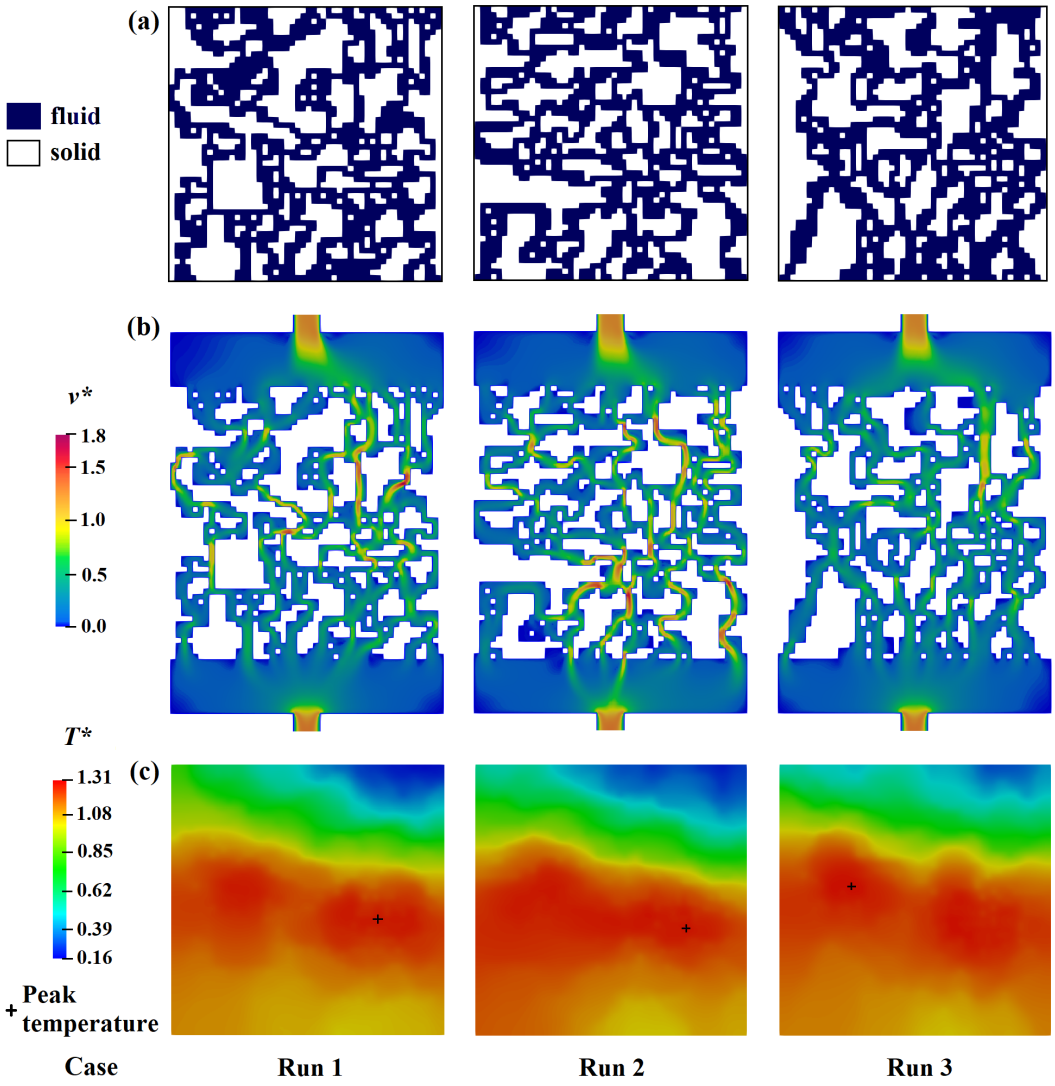

Figure 4.12 Comparison of the three runs of the GATO for the benchmark case. (a) optimized flow configuration; (b) velocity field (z^*=-0.5); (c) temperature field at the heating surface.

Additionally, the $\log_{10}$ value of the variation of the difference of the last two generations divided by the difference of the first two generations of the first run (benchmark case) has been plotted and shown as Figure 4.13. Evidently, at the end, the value of the convergence curve still has the tendency to decrease, even the difference of last two generations has already reached 1% of the difference of the first two generations. This may demonstrate that the convergence curve seems not to achieve the strict convergence from the mathematics point of view. However, the variation of objective function (T_{peak}) was only 0.002 K, which could be considered as largely sufficient (on the base of the convergence criterion in Eq.4.4) in real engineering practice.

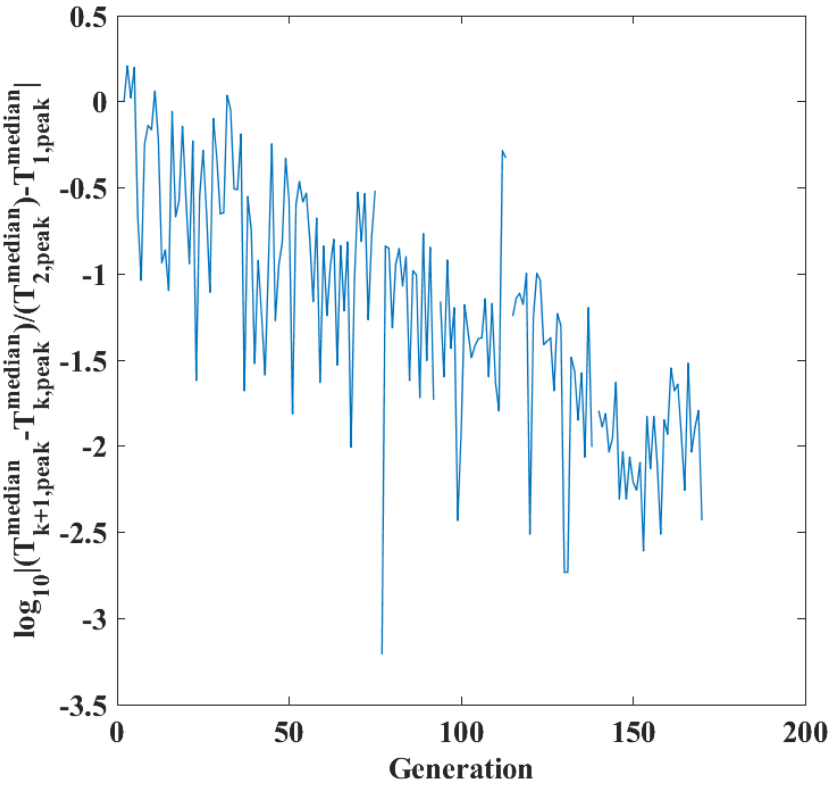

Figure 4.13 Convergence curve about $\log_{10}$ value of the variation of the difference of the last two generations divided by the difference of the first two generations.

4.5.3 Simplifications in CFD model

Some simplifications have been made in the CFD calculation to save computational time, including the negligible gravity and viscous heating effects (eligible for small channel depth and small total pressure drop), negligible heat loss to the ambient, and the temperature-independent physical properties for both fluid and solid phases. The fluid viscosity could vary a lot within the operation temperature range, i.e., from $\mu = 1 \times 10^{-3}$ Pa·s at 293.15 K to 3.54×10^{-4} Pa·s at 353.15 K. Moreover, heat loss may also need to be considered when an adiabatic boundary cannot be provided. These factors will be further considered in GATO for our following work in chapter 5 regarding the experimental validation.

Careful readers may also notice that the operating conditions for the benchmark heat sink (this chapter) are slightly different from the one tested in chapter 3: smaller flow rate, smaller power input, and lower number of heat flux peaks. This is also to simplify the CFD calculation so that the laminar model can be used for the fluid flow. Theoretically, the GATO method developed here can also be used for turbulent flow patterns under a higher power input with multiple heat sources. But the CFD computation step will be more complicated and time-consuming. Moreover, the current GATO method may also be extended to real 3D by dividing the design domain into a 3D matrix, the channel thickness being another optimization parameter. But it is beyond the scope of this Ph.D. thesis.

4.5.4 Effectiveness vs. limitations

Based on the results and discussions presented above, the advantages of the present GATO method (especially compared with the conventional FEM+density-based method) could be summarized as follows: (1) a clear fluid-solid boundary owing to the explicit parametrization of design variables, avoiding non-physical gray scales; (2) direct CFD analysis of designs without re-meshing by the FVM solver, ensuring the conservativeness/accuracy, and with excellent parallelism; and (3) robustness of GA optimizer to approach global optima subjected to complex heat boundaries (non-uniform heating with multiple-peak heat flux).

The parameter study in chapter 4.4 indicates the effectiveness and robustness of the proposed GATO method by proposing optimized flow path configurations with better cooling performance than the reference straight channel heat sink. Nevertheless, some limitations of the optimized designs are also shown, such as the higher pressure drop, the existence of dead volumes, and the existence of numerous possible optimal configurations close to the global minimum point. These problems may be treated by the post-treatment (section 4.5.1), or by revisiting the objective function (e.g., multi-criteria optimization) and constraints (void fraction-free). Further investigations have been done and will be presented in Chapter 6 of this thesis.

Another obvious limitation of this method is the high computation cost, i.e., with the current simplifications of the CFD model, two or three weeks are still needed to obtain a GATO-optimized configuration. This is mainly due to the sequencing & queuing of the HPC (free user account of CCIPL) as well as the cluster-local data exchange: GA algorithm written by local Matlab code while CFD simulations are performed in HPC. The “effective” calculation time is about 72 hours for one GATO run, which is not prohibitive at all. A significant reduction of computational time is thereby feasible by executing the GA algorithm directly in the HPC, or by using some local workstations instead of the HPC.

Parameters of GA play an important role on the efficiency and rapidness of this algorithm. In this study, the CFD computation of the heat sink has not been simplified into 2D for the purpose of performing the GA parameter study. That is mainly due to the concerns that the identified parameters for GA by a 2D model may not be applicable in the real 3D heat sink study. Instead, some GA parameters were selected based on general knowledge [109], including the crossover type, the mutation rate, the elite number, the number of individuals in each generation, etc. A detailed parametric study [e.g., [147] could be useful to evaluate the separate effect of each parameter on the GA diversity and the convergence speed, to determine the appropriate parameter settings within an acceptable computational cost. This could be a direction for our following work.

4.6 Conclusion and perspectives

In this chapter, a GATO method has been developed and tested to obtain the optimal global flow channel configuration of the heat sink for cooling a non-uniform heating surface with multiple heat sources. Minimizing the peak temperature at the heating surface (T_{peak}) is defined as the optimization objective under the constraint of constant void fraction for a fully-connected fluid domain. Effects of design variables, like heat flux peak intensity, the void fraction, the inlet velocity, and the matrix resolution on the effectiveness of the GATO method have been investigated. The thermal and hydraulic performances of the optimized GATO heat sink have been compared with those of conventional straight channel (RSC) heat sink under the same conditions. The main conclusions could be drawn as followed:

- The proposed GATO method could successfully determine the optimal spatial distribution of the fluid/solid elements in the design domain. The resulted meshed channel circuits intentionally guide the cooling fluid to the overheating positions, leading to the minimized T_{peak} of the heating surface.
- The optimized flow configurations depend strongly on the values of design and operating parameters. The robustness and the reproducibility tests also imply that many "close-to-the-optima" solutions can be proposed by GATO because of the insensitivity of the objective function to the global optimum at the fixed stopping criterion.
- Compared with conventional RSC heat sinks, the GATO heat sinks always achieve a better thermal performance, indicated by the higher Nu number, the lower $R_{th,}$ and the better temperature uniformity at the heating surface, but at the cost of the higher pressure drop. The performance improvement is more significant under more heterogeneous heating conditions (higher intensity difference between heat flux peaks), highlighting the strong adaptability of the developed optimization method owing to the more morphologic freedom offered by GA to address unspecified problems.
- A higher matrix resolution of the design area leads to lowered T_{peak} at convergence, owing to the generation of finer and more complex structures at a local level. Nevertheless, a larger number of GA generations is needed thus time-consuming. Regarding engineering application, the appropriate design resolution (size of the element to morph) should be decided by considering both the available computing resources and the fabrication capacity.

This CFD-based optimization method relies on the accuracy of numerical simulation while the experimental validation of the proposed method is indispensable. This involves the simulation, optimization, fabrication, experimental testing, and performance comparison of different heat sink prototypes (RSC, OSC, and GATO), which will be presented in the next chapter 5. Meanwhile, different objective functions considering both thermal and hydraulic indicators and other constraints for GATO are also investigated and results will be presented in Chapter 6 of this thesis.

Appendix 4.A: Crossover and mutation operations

After sorting in an ascending way of T_{peak} values of 100 individuals, the top 2 to the top 51 individuals (the top one kept as elite) in the ranking list are chosen to run the crossover operation. One parent pair will give birth to 2 children, in this way, 100 individuals are created for the next generation. The crossover parent pair for each individual is the previous and next ranking individuals. The last-ranked individual (top 51) would crossover with the second-ranked individual (top 2).

In this study, the crossover operation for the binary matrix follows the study of [179], presented below in Figure 4.A1. Crossover can be done either horizontally (A1a) or vertically (A1b). Firstly, a random element inside the matrices of parents would be chosen; then for horizontal crossover, the matrices of parents would be separated into two parts (part one includes those whose row number is smaller than the chosen element and the rest for part 2. For the row where the chosen element is located, the elements whose column number is smaller than the selected element belongs to part one, and the rest belong to part two. After that, child 1 would be created by combining part one from parent 1 and part two from parent 2. The vertical crossover has similar procedures. They are clearly shown in Figure 4.A1. The probability of either horizontal crossover or vertical crossover is 50%.

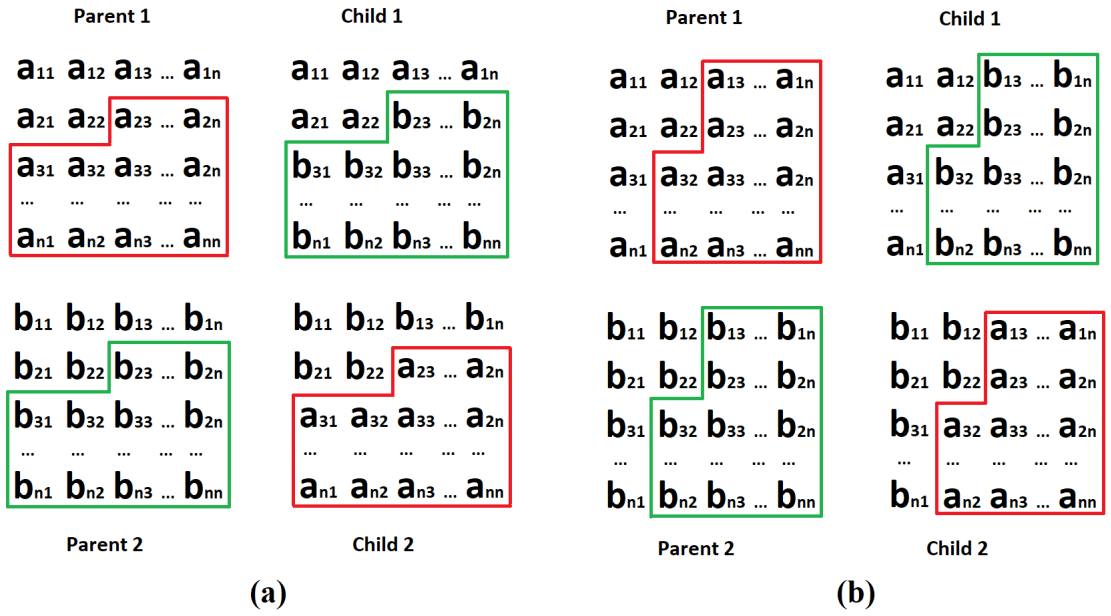

Figure 4.A1 (a) Horizontal crossover and (b) vertical crossover [179].

Each child is set to have a 20% probability to mutate. The mutation operation includes horizontal string or vertical string swapping mutation as shown in Figure 4.A2. To do that, two different rows (or columns) within the matrix would be randomly chosen, and their positions will be swapped to create new individuals. The probability of horizontal string swapping or vertical string swapping is set as 50%.

It should be noted that the crossover and mutation operations would be repeated such that the full connectivity of the flow domain is satisfied.

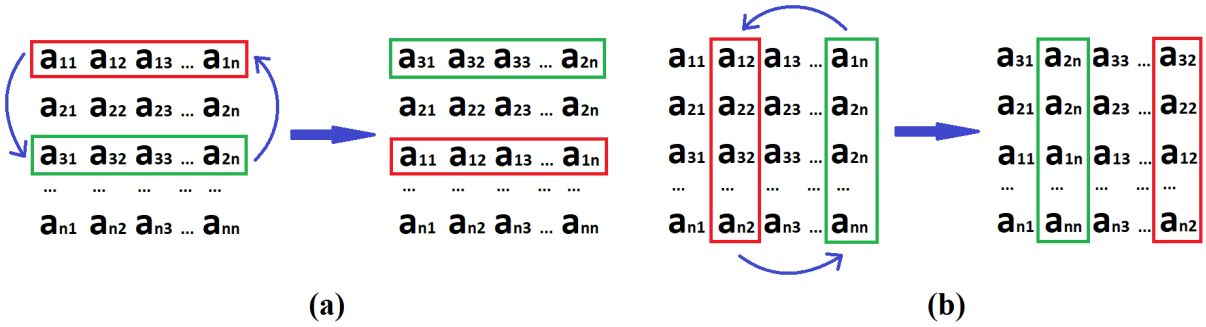

Figure 4.A2 (a) Horizontal string swapping mutation and (b) vertical string swapping mutation [179].

Appendix 4.B: Dead ends elimination

The dead ends are defined as the fluid elements which have almost no mass flow passing by. The elimination of those fluid dead ends is helpful to establish the main flow paths while at the same time, increasing individual diversity. From the binary matrix point of view, they can be easily identified when the fluid element (1) is surrounded on three sides by solid elements (0), as shown in Figure 4.B. These eliminated fluid elements will be randomly allocated to the locations of solid elements as shown in Figure 4.B(b), keeping the void fraction (Φ) constant.

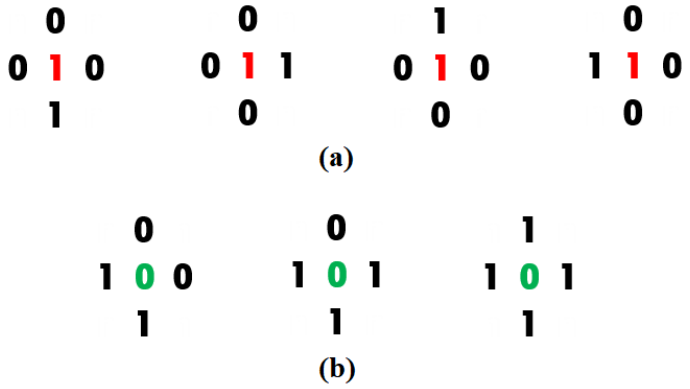

Figure 4.B Dead end elimination step in the GATO. (a) the fluid elements to be eliminated and (b) the solid elements where to put the eliminated fluid elements.

Appendix 4.C: Mesh independency study for CFD simulation in OpenFoam

Figure 4.C presents the mesh independency study of a randomly chosen individual from the first generation of GATO. T^*_{peak} (the objective function) is chosen as the indicator for the mesh independency study. It can be seen that when the grid number is higher than 127 k, the variation of T^*_{peak} becomes rather small (<0.72%). Therefore, the mesh size of 127 k (marked in a black circle in Figure 4.C) was chosen considering both the calculation accuracy and time consumption.

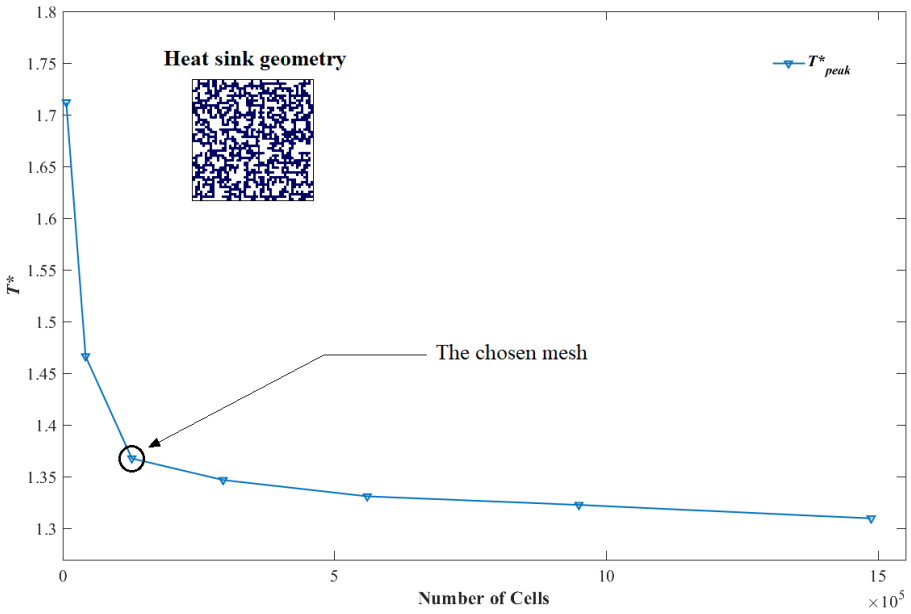

Figure 4.C Mesh convergence study for the CFD simulation in OpenFoam.

Chapter 5: Performance evaluation and comparison of heat sinks under multiple heat sources: an experimental and numerical study

Chapter Summary

This chapter presents experimental and numerical to evaluate and compare the performances of different heat sinks under multiple heat sources. Different heat sink prototypes are optimized, machined, instrumented, and tested, including uniform straight channel heat sink (RSC heat sink), optimized straight channel heat sink (OSC heat sink), and genetic algorithm-based topology optimization heat sink (GATO heat sink). The PIV method has been used to measure the velocity field of the RSC heat sink, while IR thermography has been applied to measure the temperature fields of the cooling fluid in three heat sinks. The visualization results obtained are compared with the CFD calculation, showing good agreements between each other.

A systematic numerical study has then been performed to test three heat sinks under a wide range of operating conditions. The numerical results showed that the GATO heat sink can always achieve the best hydrodynamic and thermal performances among the three heat sinks. The effectiveness and robustness of the GATO approach for heat sink optimization have then been proven.

Keywords of the Chapter:

Heat sink; Multiple heat sources; Performance evaluation; Particle Image Velocimetry (PIV); Infrared thermography; Computation Fluid Dynamics (CFD).

5.1 Introduction

In the previous chapters 3 and 4, two optimization methods have been proposed and developed for optimizing the geometry of heat sink under multiple-peak heat flux: channel inlet size optimization for tailoring the fluid flow distribution among the parallel channels (chapter 3) and genetic algorithm-based topology optimization (GATO) for global flow channel configuration optimization (chapter 4). The results obtained on the benchmark case have all shown that both methods could successively achieve the defined optimization objective (min T^*_{peak}). Further numerical study on the influences of different design and operating parameters also demonstrated that the heat sink optimized by the GATO method (named GATO heat sink hereafter) and the one with optimized distribution (named OSC heat sink hereafter) both had better thermal performance compared to the reference straight channel (RSC) heat sink, at the cost of a reasonable pressure drop increase.

Despite all these encouraging results obtained, additional work is still required in various aspects, listed as below.

- The heat sink model used for GATO (Figure 4.3) has a simplified geometry (e.g., zero wall thickness) and boundary condition (e.g., adiabatic wall), to save computational time. A detailed simulation study of the GATO heat sink with realistic geometry and operating conditions is thereby necessary for its performance evaluation.
- The performance comparison between the optimized heat sinks by different methods (OSC and GATO) and the reference case (RSC) under a wide range of operating conditions is extremely useful. The analysis of different performance evaluation criteria will showcase the effectiveness and robustness of the two optimization methods developed in this thesis, as well as their limitations.
- And most important of all, chapters 3 and 4 devoted to the development of optimization methods relied only on the CFD simulation results while the experimental work consists of an indispensable step for the numerical model validation and also for the performance characterization.

These listed aspects constitute then the main motivations for the work performed and presented in this chapter. *The main objective of this part of the work is to evaluate and compare the performances of different heat sinks under multiple heat sources, by using numerical, experimental, and optimization approaches*. In more detail regarding the methodology, OSC and GATO heat sinks have been optimized by the optimization methods developed in earlier chapters. CFD simulations of the heat models using Ansys Fluent code have been performed to evaluate and compare their thermal and hydraulic performances under a wide range of operating conditions. Experimental testing of different heat sink prototypes fabricated in-house has been performed to obtain detailed information on the flow and temperature fields, which are essential for the validation of the numerical model. Optical-based measuring techniques, for which the research team in LTEN has strong expertise and experience [162,180], have been selected,

developed, and implemented for this purpose, including the particle image velocimetry (PIV) for velocity field measurement and infrared thermography for temperature field measurement.

The novelty and uniqueness of this work lie in the experimental testing of heat sinks with TO-optimized geometry, under multiple heating source conditions, which has never been done in the literature (as summarized in chapter 2.5). The main contribution of the present study is the employment of optical-based techniques for measuring the flow and temperature fields in the heat sink. Especially for the temperature field measurement by IR thermography, a few researchers [153,154,159] have used such a technique for characterizing the TO-optimized heat sinks (as listed in Table 2.1), but only the temperature distribution on the upper solid cover has been measured. This is relatively simple to perform in practice, but the measuring surface is far from the heating surface thus neither representative nor enough sensitive to the geometry of flow configurations. Differentiating from all of the others, our work goes a step further by *measuring the near-wall fluid temperature distribution at the fluid-solid interface*, which is closer to the heating surface, permitting a better observation and characterization. The technical difficulty lies in the IR transparent optical access to the target fluid domain. This has been solved in our study by introducing and installing a sapphire window, ensuring most of the IR radiation emitted by fluid would be captured by the IR camera (will be further explained in section 5.3).

The rest of the chapter is organized as follows. Section 5.2 presents the PIV study on a transparent RSC prototype under isothermal conditions. Section 5.3 presents the IR thermography measurement for three heat sink prototypes (RSC, OSC, and GATO) under multiple heating sources. In each section, the test rig, the machined prototype, the measuring principle the data processing will be presented in detail, and the experimental results obtained are compared with CFD simulation results given model validation. Furthermore, further analysis and discussion on the local flow and heat transfer characteristics of three heat sinks based on the numerical results are given in section 5.4. Their thermal and hydraulic performances under a wide range of operating conditions are compared as well. Finally, in section 5.5, the main conclusions drawn are summarized.

5.2 Velocity distribution measurement of RSC heat sink under isothermal condition

This section presents the experimental work on the measurement of velocity distribution inside an RSC heat sink prototype under isothermal conditions, using the PIV technique. The results of PIV measurements are mainly used to validate the CFD model under a laminar flow pattern.

5.2.1 Test-rig

Figure 5.1 shows the schematic diagram of the test rig in LTEN for PIV measurement. It includes the fluid circuit (in blue) including the test section, and the PIV measurement facility

(in green). The fluid circuit is composed of a water tank (10 L), a pump and valves, a flowmeter (0 to 2×10^{-6} $m^3 \cdot s^{-1}$; accuracy: 4.6%) and the test section (RSC). Water was used as the working fluid, its flow rate was controlled by a precision pump (REGLO-*z*, 32–3200 mL min^{-1}, instrumental error less than 0.1%). Hollow Glass Spheres (HGS, supplier: Dantec) with a diameter of 10 μm were used as seeding particles in our study.

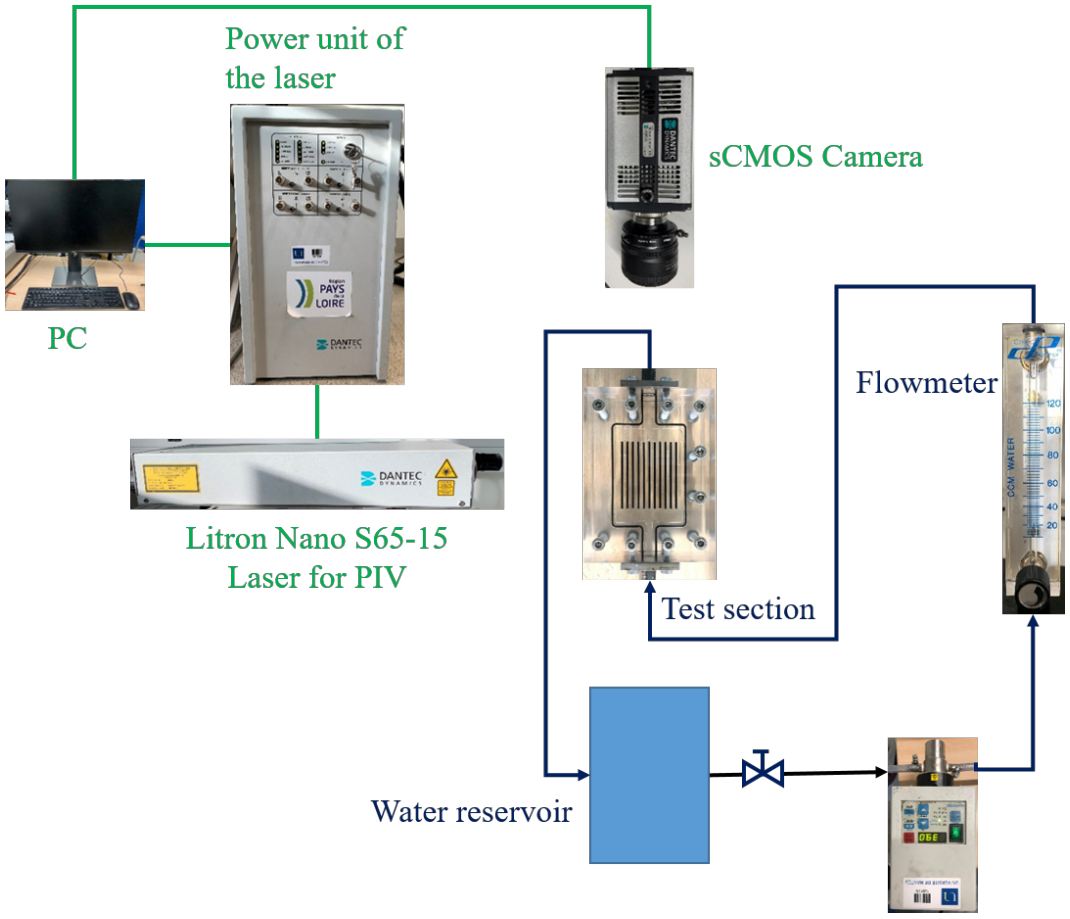

(a)

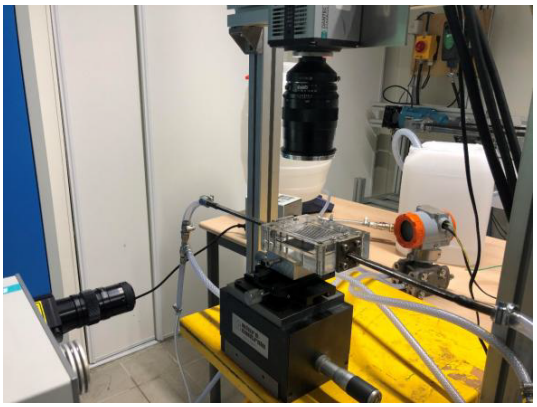

(b)

Figure 5.1 The test-rig in LTEN for PIV measurement in this study. (a) schematic view; (b) photo view

5.2.2. Test section

A transparent prototype based on RSC configuration has been specially designed, fabricated, and tested for the velocity field measurement. The overall dimension of this prototype is 120 mm in length and 90 mm in width. The prototype made of PMMA is composed of two parts: a base block and a cover as shown in Figure 5.2 (a) left and right, respectively. The flow channel with an identical depth of 2 mm was carved by digital machining at the surface of the base block. Grooves were reserved on the cover plate to embed sealing strips at the edge of the fluid domain and in between the channels to prevent leakage. The cover and base plates were assembled by 10 bolts as shown in Figure 5.2 (b).

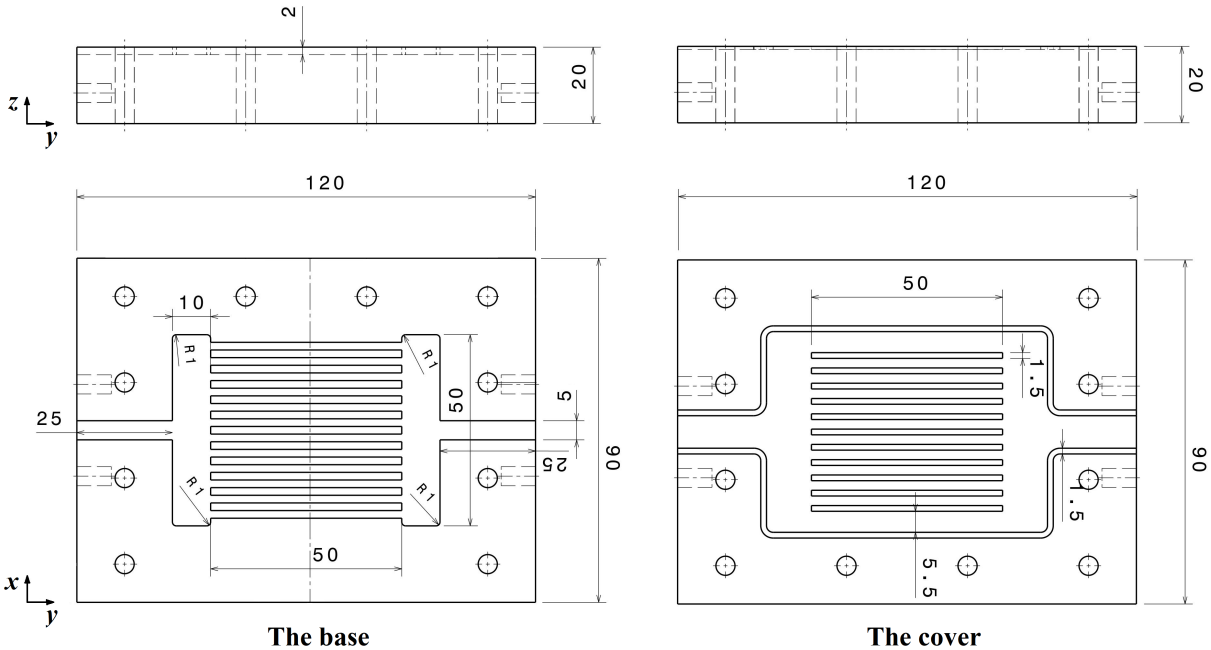

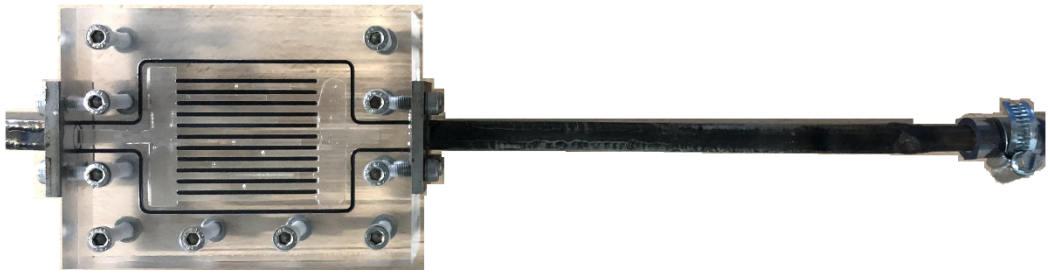

(b)

Figure 5.2 RSC prototype used for velocity field measurement. (a) schematic drawing and (b) a photo of the fabricated prototype with an extended entrance tube.

The fluid domain is composed of one inlet channel (5 mm in width and 25 mm in length) and distributing manifold (50 mm in width and 10 mm in length), one outlet channel and collecting manifold of the same dimensions as the inlet, and 12 parallel straight channels in the middle. Each channel has the dimension of 2 mm in width, 2 mm in depth, and 50 mm in length, uniformly spacing one another by separating walls of 2 mm in thickness.

A stainless steel tube with a rectangular cross-section of 5 mm × 2 mm has been connected to the inlet channel of the RSC prototype having the same dimension, providing additional entrance length for the development of the velocity profile. The length of this stainless steel tube is 130 mm, sufficient to achieve a fully-developed laminar flow (L>$0.0575 \cdot Re_{in} \cdot D_{h,in}$ [181]) in the current study ($D_{h,in} = 2.86$ mm and maximum $Re_{in} = 569$).

5.2.3 PIV facility, measuring parameters, and data processing

The PIV facility usually contains an illumination unit (Laser), an imaging unit (camera), a power supply, a data processing unit, and a synchronizer for the camera and laser pulse. Figure 5.3 displays the basic principle of PIV measurement [182]. Firstly, tracer particles are distributed uniformly in the target flow domain for measurement. Then, the laser forms a 2-D light sheet in the target domain where the velocity field is going to be measured. After, the high-resolution camera records two frames at a different time to observe the motion of particles by the Eulerian approach and calculate the local velocity.

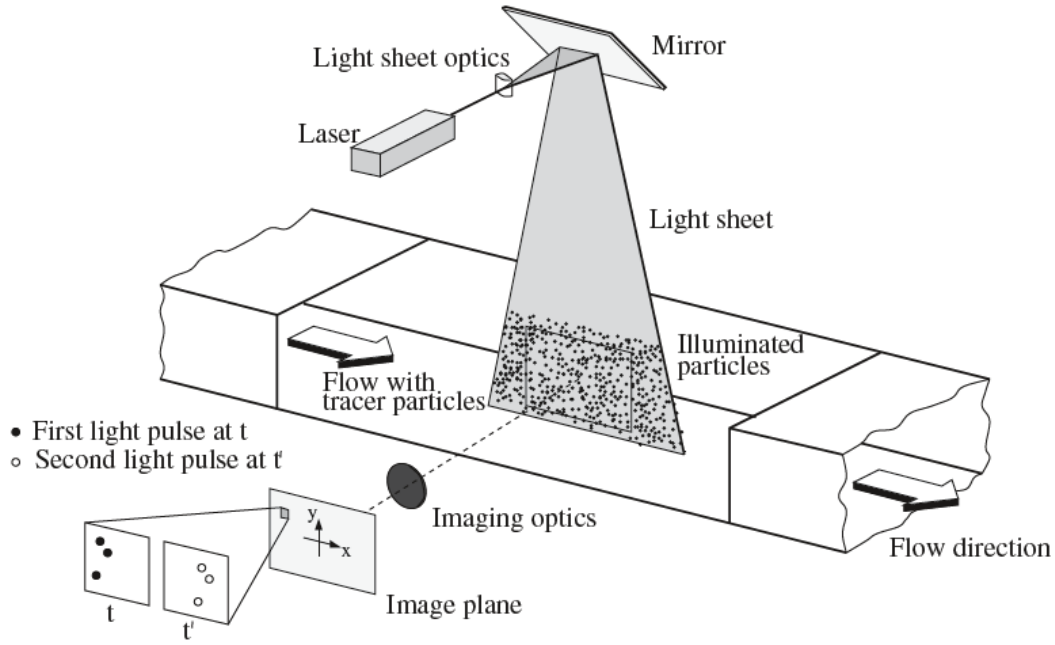

Figure 5.3 The basic principle of PIV measurement for velocity field [182]**.**

The instruments used in this study are as follows. A commercial laser model Litron Nano S65-15 PIV was used as the light source, forming a laser sheet at the middle plane (z=1 mm) of the fluid channels. The light scattered by the seeding particles was caught by a scientific Complementary Metal–Oxide–Semiconductor (sCMOS) camera ($z$yla 5.5) with a resolution of 2560×2160 pixels. A synchronizer was applied to ensure the laser and sCMOS camera would cooperate accordingly. A commercial software DANTEC Dynamic Studio 7.2 was used to set the parameters of image taking, data acquisition, and post-processing.

The PIV recording would start when the fluid flow reaches the steady state laminar flow. After the acquisition of 2000 images with double frame/single exposure under the frequency of

10 Hz, the pre-processing would be performed, including spatial calibration, defining, and applying the mask for background removal. In more detail, the positions and coordinates of the vector field would be firstly calibrated and then the mask would be defined and applied to the images to cover the domain of no interest (e.g., solid parts). After that, the cross-correlation method by Fast Fourier Transform (FFT) algorithm was applied to determine the local displacement vector between two illuminations through an interrogation area grid set to be 16 × 16. PIV data validation by median filtering was utilized to remove spurious noise. Finally, the average vector fields and standard deviations would be obtained. An example of the final validated velocity vectors and normalized standard deviations is shown in Figures 5.4 and 5.5, respectively.

Figure 5.4 shows the validated pixel number in the measuring field among 2000 images. In most of the measuring fields, the validated pixel number is between 1900 – 2000, showing a credible measurement. The spots with a lower number appear at the entrance of distributing manifold and the inlets of parallel channels, which are coherent with the values of the standard deviation of velocity vectors described below.

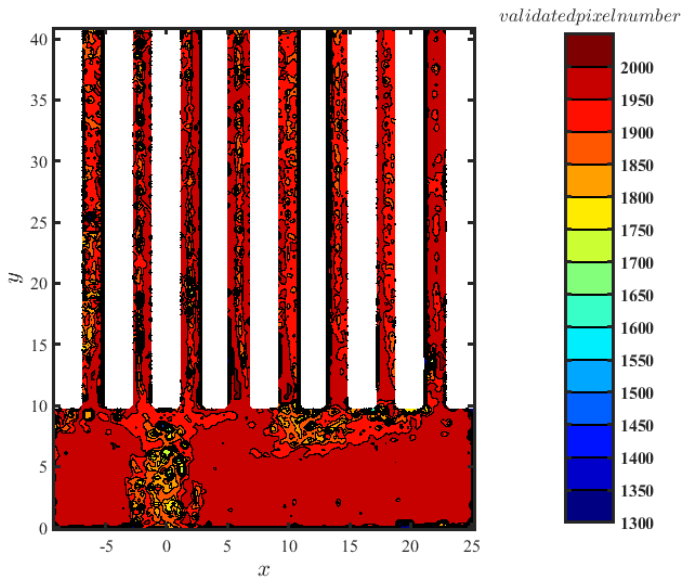

Figure 5.4 Example of the validated pixel number in the testing field among 2000 images.

Figure 5.5 shows the normalized standard deviation of velocity vectors (U^* and V^* normalized by the inlet velocity) of 2000 images in every measured pixel. It can be observed that the U^* values (x-component) do not show a large deviation (Figure 5.5 (a)). For V^* values (y-component), however, a quite big difference could be observed in the distributing manifold and at the enhancement of two middle channels (Figure 5.5 (b)). The reason could be the secondary flow and high-velocity magnitude at these regions which increase the probability of random particle motions. Another possible reason is particle aggregation: during the acquisition of 2000 images (200 seconds), the particles following the main fluid streams stagnate and accumulate in these areas. Therefore, the image of velocity vectors taken at a different time would be influenced by different amounts of particles, bringing the higher values of *StdDev V**.

In brief, 2000 images are sufficient to capture the velocity field under a steady state based on the validated pixel number and statistic of standard deviation shown in Figure 5.4 and Figure 5.5. Some high standard deviation values in the region of the distributor near the inlet still exist, which is caused by the aggregation of particles. The longer time it takes, the more chance this phenomenon of particle aggregation would appear.

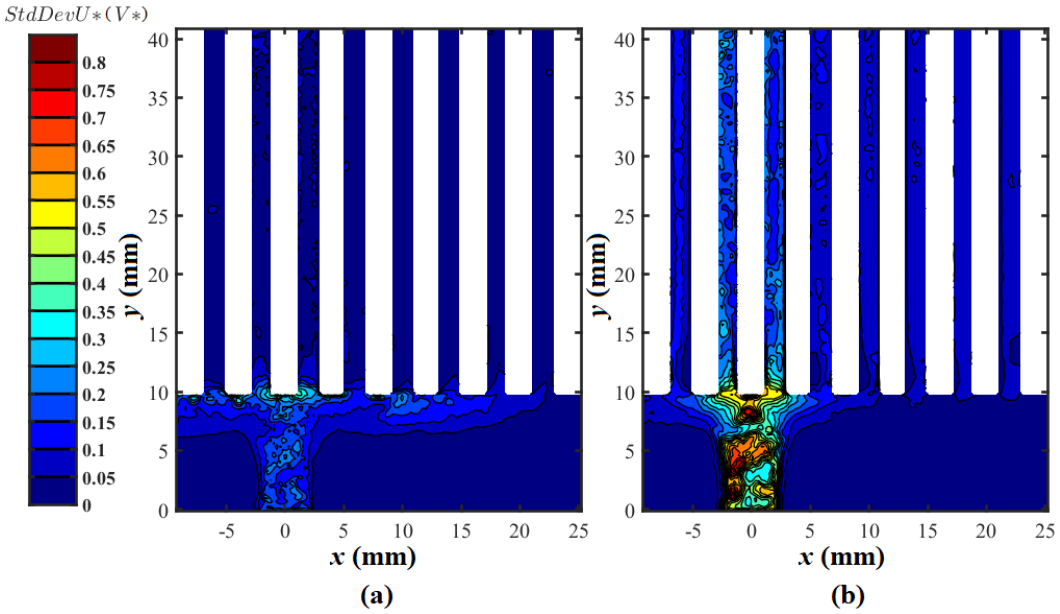

Figure 5.5 The standard deviation of the velocity vectors depending on *x* component (a) and *y* component (b).

5.2.4 Parameters for CFD simulation

To compare with the PIV measurements, 3D CFD simulations were performed in parallel to calculate the velocity field inside the flow circuit, using the same geometrical characteristics as the RSC prototype presented in section 5.2.2 (long inlet channel included). Water was used as the working fluid with constant physical properties (density: 998.2 kg m^{-3}, viscosity: 0.001003 kg m^{-1} $s^{-1,}$ and heat capacity: 4182 J kg^{-1} K^{-1}). The inlet velocity was set to be constant and equal to the experimental condition. The operational pressure was fixed at 101,325 Pa. Simulations were performed under steady-state, incompressible, and isothermal condition. The gravity effect at –*z* direction was also taken into account.

Navier–Stokes equations as shown in chapter 3.2.3 were solved by Ansys Fluent code (version R19.1), using the SIMPLE method for pressure-velocity coupling, and second-order upwind differential scheme for discretization of momentum, the second-order method for pressure and Green-Gauss node based approach for the gradient. The Laminar flow model was given the small flow rate tested (inlet *Re* number around 400). Constant velocity inlet at inlet surface was given and the boundary condition of the outlet was set as pressure-outlet with zero static pressure. Channel walls were considered as no slip.

The structured mesh was generated to build up the geometry model, including about 0.4 million elements in total. The solutions were considered to be converged when (1) the sums of normalized residuals for control equations are all less than 1×10^{-5}, and (2) the global pressure drop is constant from one iteration to the next (less than 0.05 Pa).

5.2.5 Comparison between PIV and CFD results on the velocity fields

To capture more details of the fluid motion, the PIV visualization window covers three fourth of the channels with 134 × 159 vectors, as marked in the green frame shown in Figure 5.6 (a). The velocity magnitude in this area, obtained by PIV measurement and by CFD calculation, is shown in Figures 5.6 (b) and 5.6 (c), respectively. Note that the tested volume flow rate at the inlet is 1.42×10^{-6} $m^3 \cdot s^{-1}$, corresponding to an inlet Re_{in}=404 and average channel Re_{ch}=34. Generally, a good agreement can be observed between the PIV and CFD results, i.e., the maximum velocity appears at the middle of distributing manifold facing the inlet port. Two middle channels receive a large amount of the mass flow while the proportion for the rest of the channels is relatively small. This symmetric feature can be globally seen in the PIV velocity field, but irregular iso-velocity lines and some singular points are also visible, especially at high-velocity magnitude areas. This is due to the sticking and crusting of the seeding particles at the channel walls during the, disturbing the PIV measurement at a certain level as has been explained in the above section.

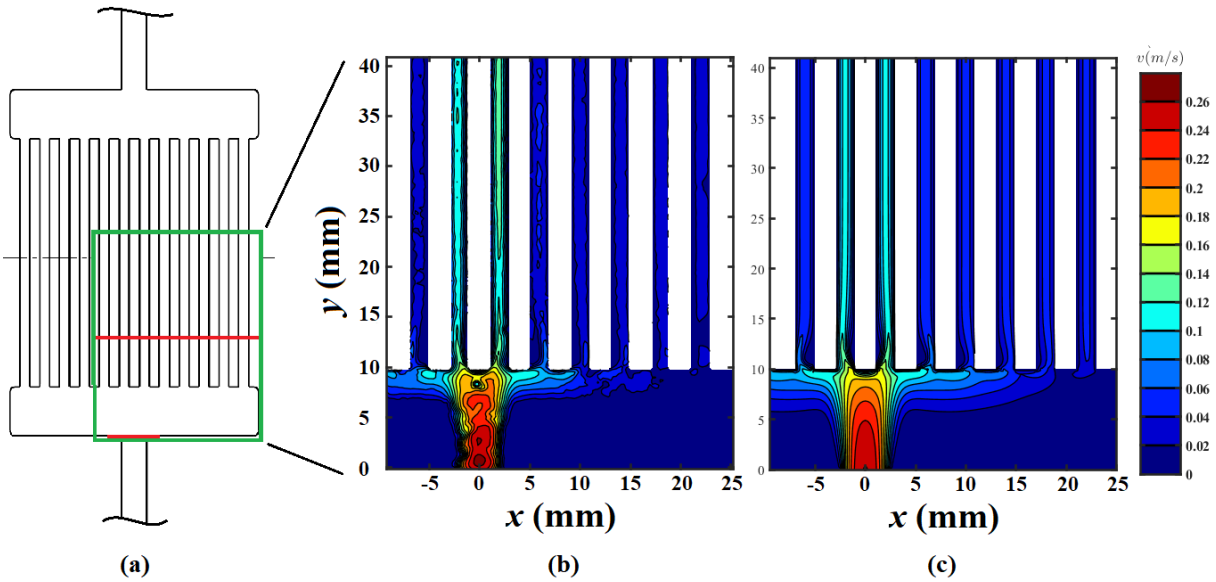

Figure 5.6 Comparison of the velocity magnitude at the mid-depth of the channels. (a) the visualization window; (b) PIV results and (c) CFD results. (unit: $m \cdot s^{-1}$)

Furthermore, to compare more details of PIV results with CFD calculations, the fluid velocity profiles at local positions marked in red in Figure 5.6 (a) are shown in Figure 5.7 (a) and (b). Various curved are plotted for comparison, including:

- The experimental curve (blue) obtained by PIV measurement;

- The CFD curve (orange) obtained by the numerical model under isothermal condition (section 5.2.4);
- The CFD curve (purple) was obtained by a more detailed numerical model built for thermal calculation (would be presented in section 5.3 thermal measurement), with the boundary conditions of 120 W multiple-peak heat flux input and temperature-dependent physical properties.
- And an analytical expression of velocity profile (green) for fully-developed laminar flow in a rectangular channel (Purday's model) [183].

$$\frac{v}{v_{max}} = \left[1 - \left(\frac{x}{a}\right)^{b}\right] \tag{5.1}$$

where v_{max} is the peak value of the velocity profile; a is the half channel width (in x direction), and b is the correcting factor based on the aspect ratio (b=3.5 is calculated based on this study[183]).

Figure 5.7 (a) plots the velocity magnitudes at the entrance of the distributing manifold (the first pixel of the PIV image). Both isotherm CFD model calculations and PIV measurement capture rather similar velocity magnitude profiles, and they are generally in good agreement with the theoretical calculation. The peak of velocity magnitude obtained by the CFD-thermal model is slightly lower than others. This is because the rise of global temperature results in a decreased fluid viscosity, bringing about a lower velocity gradient in the x-axis compared to the one under isothermal condition.

Figure 5.7 (b) shows the velocity magnitude profiles in the parallel channels (y=21.95 mm as the red line marked in Figure 5.6a). It can be observed from both CFD and PIV results that the two middle channels have the highest velocity peak due to their position facing the inlet port. The velocity peaks in the rest of the channels are much smaller. These observations are in echo with the velocity magnitude contours shown in Figure 5.6.

Nevertheless, some differences between the CFD calculations and PIV measurements are still noticeable, especially the peak of velocity profiles in channels 1-5 (counting from right to left). The underestimation of the flow rate by PIV measurement could be due to the deviation of the laser sheet from the middle plane. The thickness of the laser sheet is 1.5 mm while the channel thickness is 2 mm, there could be a great chance that the particles captured by the camera did not position in the middle plane. The statistical calculation of the velocity magnitude by including these participles would thereby be lower than that of CFD calculations. The flow distribution obtained by PIV seems not symmetrical, while a symmetrical fluid flow distribution is supposed to be obtained due to the symmetry feature of the flow circuit (and it is the case of CFD calculations). The reason could be due to the location of the laser source at the right side of the testing field and more particles detected in the region closer to the laser source; or due to a small inclination of the laser sheet (or prototype) along the x direction.

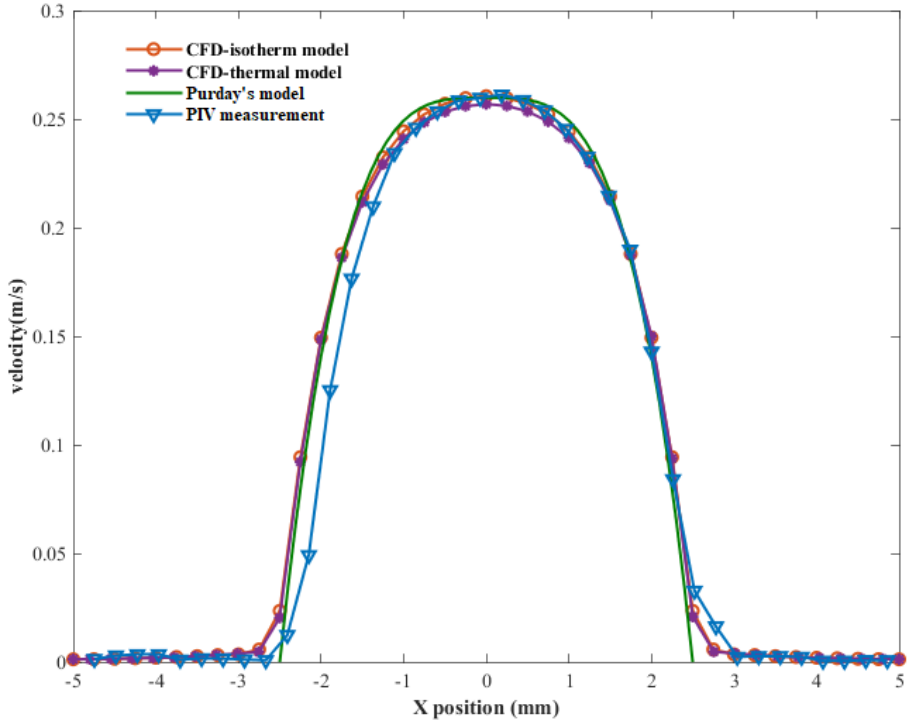

(a)

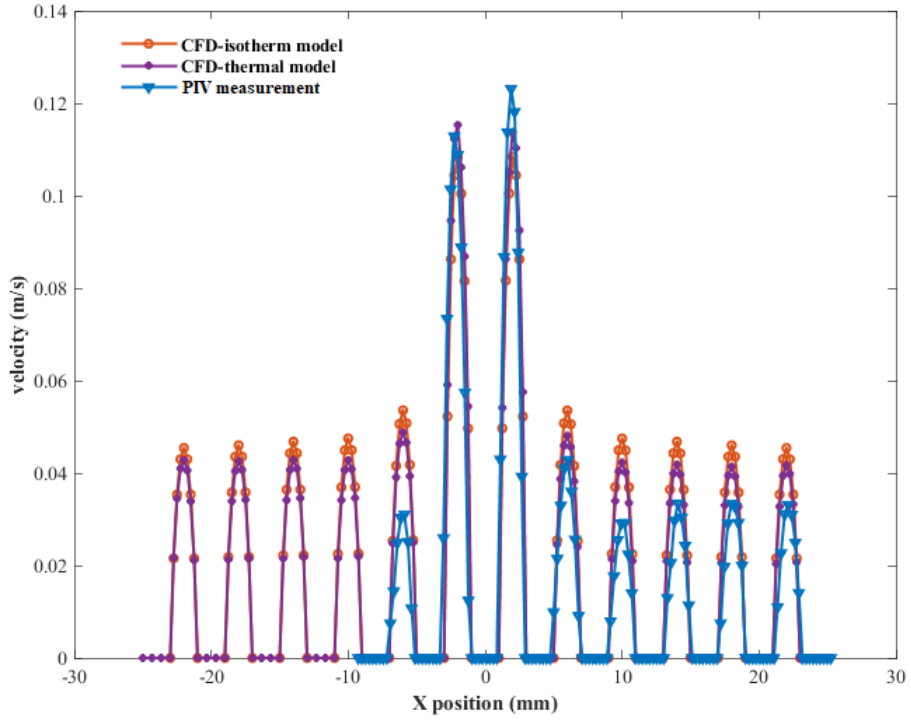

(b)

Figure 5.7 Comparison of the velocity profiles at the entrance of distributing manifold (a) and among the parallel channels (b).

5.2.6 Summary

In general, the results of CFD computations and PIV measurements show good consistency. The fully-developed laminar flow pattern is achieved at the entrance of the distributing manifold, and the choice of laminar flow model in the CFD calculation could be validated. The velocity fields don't change much by considering the heating effect in the CFD-thermal model. This part of work under isothermal condition helps establish a good basis for the following testing and performance comparison of heat sinks with multiple heat sources.

Similar flow behaviors could be present in the OSC prototype, which has been shown in our earlier study with a similar geometry [162]. The Ansys Fluent with proper simulation parameters has shown its calculation accuracy for such parallel straight channel flow circuit, thereby PIV measurement for OSC structure has not been repeated in this thesis work. Regarding the GATO flow circuit with a much more complex geometry, several technical difficulties still exist, some of which have already been mentioned above, including particle stagnation and agglomeration due to the secondary flow, the laser sheet transmission, calibration, etc. These technical difficulties remain to be solved for a credible PIV testing of the GATO prototype, which is certainly interesting but unfortunately not performed in this thesis work. Our effects have then been devoted to the testing of three heat sinks prototypes under heating condition and their performance evaluation, which will be presented in the next section.

It should be noted that the pressure drop has not been measured in this experimental study. It is mainly due to the low pressure drop value of the heat sinks caused by small inlet Re_{in} number (about 300 Pa). Such low pressure value is difficult to be detected and would not be a limiting factor in real practice.

5.3. Temperature characteristics of heat sinks under multiple heating condition

This section presents the experimental work on the measurement of temperature distribution at the fluid-solid interface inside the RSC, OSC, and GATO heat sinks. The experimental results are mainly used to validate the CFD model of the three heat sinks under multiple heating sources.

The experimental technique used in this study for such purpose is optical-based IR thermography. Compared with conventional temperature measurements technique like thermocouples or temperature sensors which can only obtain temperature information at certain points, the non-intrusive feature of IR thermography could obtain the temperature distribution of a surface of interest (pixels in the frame of data) with ensured accuracy.

5.3.1 Experimental set-up

Figure 5.8 shows the schematic diagram of the test rig in LTEN for the thermal measurement of heat sinks. It consists of a flow circuit, the heat supply unit, and the IR

thermography facility. Pure water was used as the coolant, initially stored in a water reservoir (at ambient temperature and pressure) located at a high position. It was charged into the test section (heat sink) by the gravity effect, and its flow rate could be adjusted and controlled by a valve and a flowmeter. After absorbing the heat in the test section, the water at a higher temperature was discharged to another water tank. Two K-type thermocouples (estimated uncertainty: ±0.2 K) were installed at the inlet and the outlet tube of the test section to measure the inlet and outlet water temperature, respectively. The measured data of thermocouples were monitored and recorded by a K-type thermocouple thermal meter (HI935002, uncertainty: ±0.2%). A power supply (model: Rohde & Schwarz, HMP4040, 384 W) was used to offer heat for three cartridge heaters (ARCELI, 24 V, 40W) at a set heating power. An IR camera (X-series) has been used to monitor and record the temperature distribution at the target surface of interest.

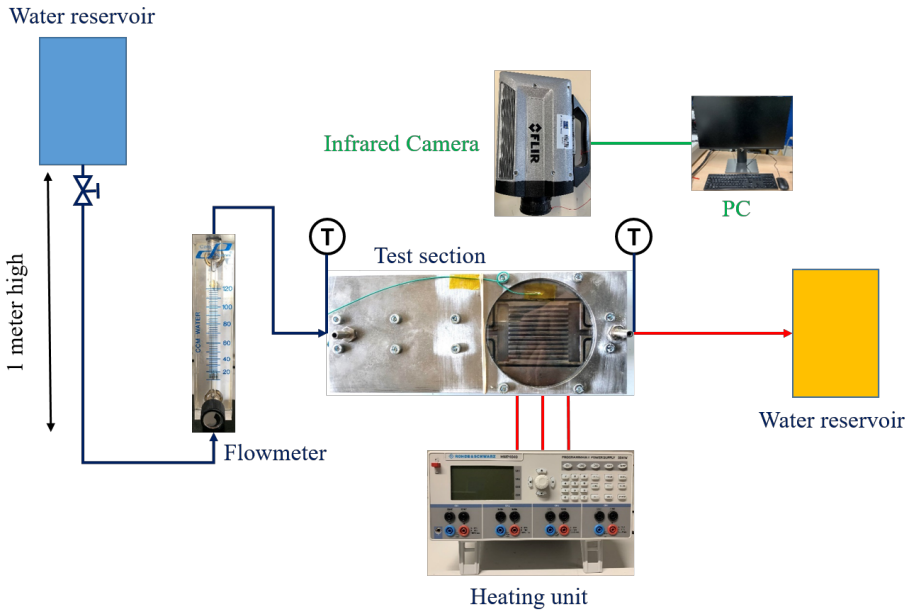

(a)

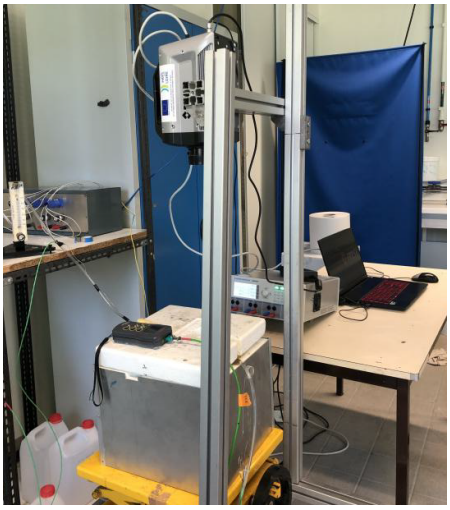

(b)

Figure 5.8 The test rig in LTEN for IR thermography measurement. (a) schematic view; (b) photo view.

5.3.2 Heat sink prototypes

A test section has been designed and fabricated for the thermal test of different heat sinks (RSC, OSC, GATO). It has an overall dimension of 250 mm × 110 mm × 20 mm (excluding the heater jackets), with a sandwich concept consisting of a base plate, a sapphire disk in the middle, and a cover plate, as shown in Figure 5.9 (a). The base plate is made of stainless steel 304, with the fluid channels machined on it, as shown in Figure 5.9 (b). The sapphire disk with a diameter of 100 mm is fixed in the circular groove of the cover plate (also made of stainless steel), providing optical access to the IR camera for measuring the temperature distribution (Figure 5.9 (a)). The thickness of the base, sapphire disk, and cover plate is 10 mm, 4 mm, and 10 mm, respectively. Three cylindrical heaters (with diameters: 6 mm, 8 mm, and 10 mm, respectively) were installed inside the three heater jackets (with total diameters: 10 mm, 12 mm and 15 mm and 46 mm in length), embedded at the bottom of the base at 6 mm depth. Their locations and shapes are indicated in Figure 5.9 (b) and also in Figure 5.11 (a), the distance between the heaters' head and the bottom wall of the flow channels being 2 mm. Sealing strips were installed around the edges of the fluid domain to prevent leakage and bolts were used for further sealing (e.g., Figure 5.9 (d)). The tightness of the assembled test section has been checked and ensured before each series of tests.

Three flow channel configurations have been tested, representing RSC, OSC, and GATO heat sink. All three configurations have a long inlet tube of 130 mm, providing sufficient length for the establishment of a fully-developed laminar flow at the entrance of the distributing manifold (Figure 5.9).

The flow channel configuration of the RSC heat sink has the same geometry and dimensions as those of the transparent prototype used for PIV measurement. Detailed information can be found in section 5.2.2 and Fig. 5.2 of this chapter thus will not be repeated here.

The ORS flow channel is mainly based on the RSC, but with the width distribution of the channel inlets optimized by the method developed in former Chapter 3 for tailoring the flow distribution according to the locations of the heat flux. The optimization has been done using Ansys Fluent code, under a total input power of 120 W (40 W for each heater) and with an inlet water volume flow rate of 1.667×10^{-6} $m^3\cdot s^{-1}$ (100 $mL\cdot min^{-1}$; Re_{in}= 474). More details about the optimization procedure for the OSC heat sink can be found in Chapter 3. In practice, a mini orifice baffle of 2 mm thickness has been fabricated and installed at the end of the distributing manifold, as shown in Figure 5.10. The orifice width for each channel corresponds then its optimized inlet width, as listed in Table 5.1, to properly distribute the inlet flow.

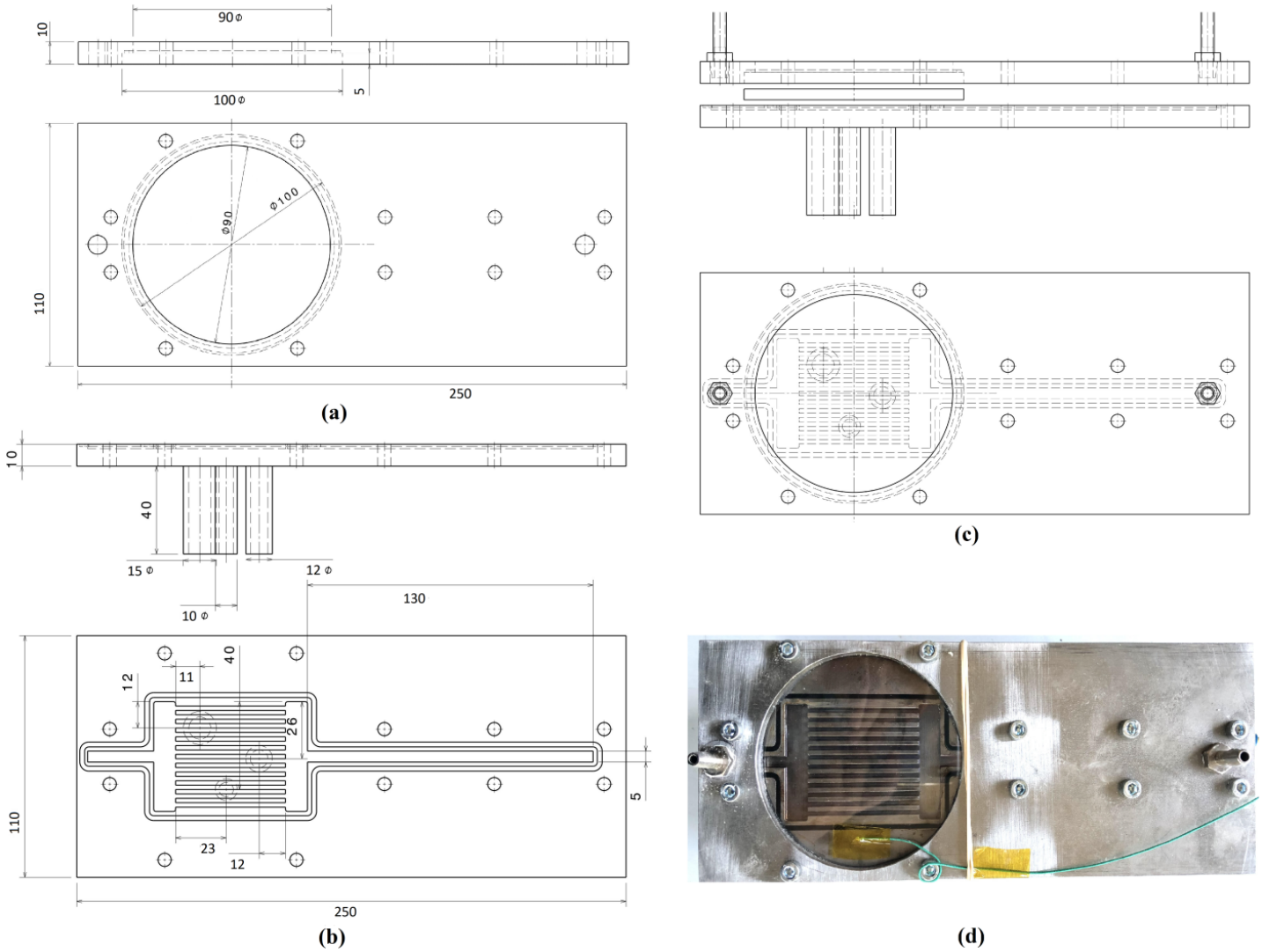

Figure 5.9 Geometry and dimensions of the sandwiched-type test section for thermal measurement. (a) cover plate; (b) base plate; (c) assembled heat sink (d) Photo view of the RSC heat sink.

Table 5.1 Optimized widths of channel inlets of the OSC heat sink for thermal test

Channel number	1	2	3	4	5	6	7	8	9	10	11	12
Size (mm)	0.64	1.46	1.63	1.59	1.17	0.87	1.31	1.34	3.57	4.01	3.91	2.51

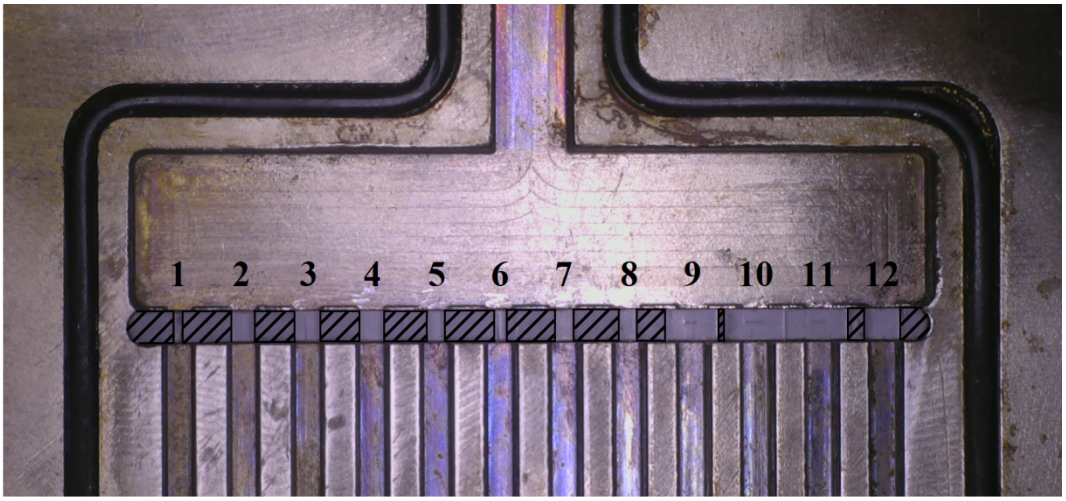

Figure 5.10 Photo of the mini orifice baffle installed for the OSC heat sink

The GATO heat sink has been optimized following the approach presented in the former chapter 4, under the same operating conditions as the OSC heat sink (120 W; Re_{in}= 474), The matrix resolution for the design domain is set as $M_{25\times25}$, indicating the dimension of each cubic element of 2 mm at the side. The void fraction for the fluid is set at Φ=0.48, identical to that for RSC and OSC heat sink for a fair comparison. More details on the optimization procedure are presented in Chapter 4), and the optimized geometry is shown in Figure 5.11 (a). The GATO flow channel has been machined by digital milling in LTEN, a photo view of the assembled test section for the thermal test is shown in Figure 5.11 (b).

To prevent the test section from heat loss, the three heater jackets were inlaid inside three layers of rectangular refractory bricks stacked together (Figure 5.12 (a)), and the whole test section was wrapped by an insulating foam box filled with glass (Figure 5.12 (b)). In this way, the whole test section is well-insulated, except the surface of the sapphire window for IR thermography.

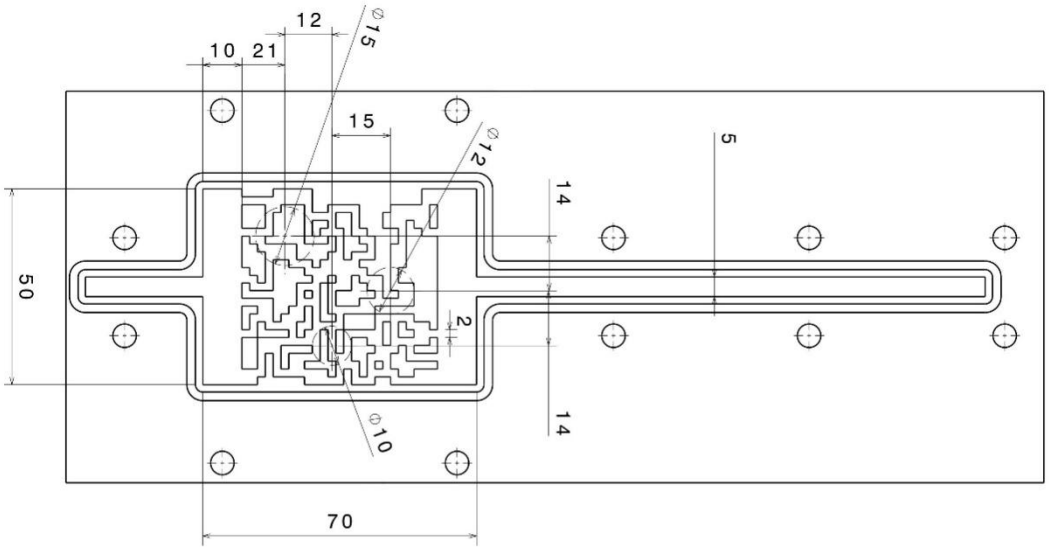

(a)

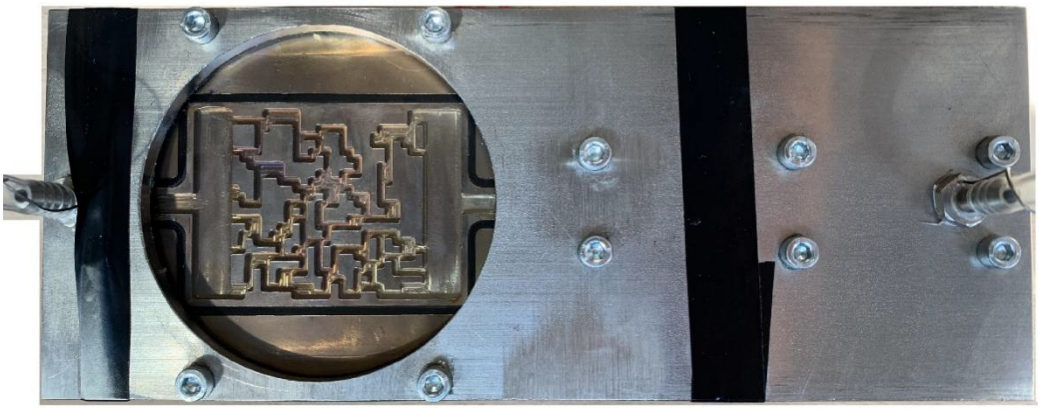

(b)

Figure 5.11 Geometry and dimensions of the GATO heat sink for thermal measurement. (a) Schematic view and (b) photo view.

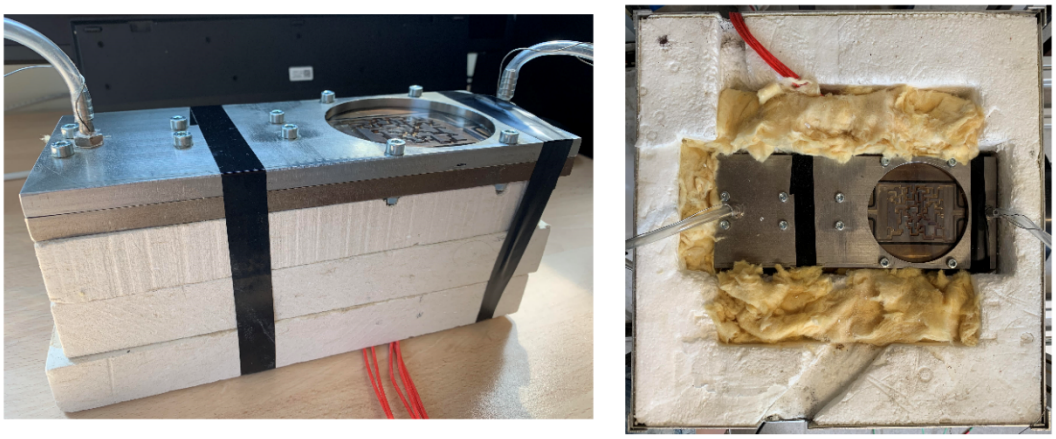

(a) (b)

Figure 5.12 The insulation of the test section for the thermal test.

5.3.3 InfraRed Thermography measurement

The basic principle of IR thermography is that the IR radiation emitted by an object could be detected by the lens of an IR, which is then converted to an electrical signal proportionally. After amplification and data processing, the signal could be transformed and displayed as a temperature value. Most of the currently used IR cameras for temperature detection are sensitive in either the middle or the long wavelength spectral bands [184]. For our study, the broadband of the IR camera (X-series) ranges from $1.5\ \mu m - 5\ \mu m$. Under this range of wavelength, the emissivity of water is 0.92 – 0.96, while the transmission percentage is less than 10% [185]. For the sapphire window with 4 mm thickness, the transmission percentage is over 65% [186]. Therefore, the thermal radiation emitted by water could be detected by the IR camera through the sapphire window. It should be noted that *the fluid-solid interface temperature between the sapphire disk and the water in contact* has been measured by IR thermography, which has never been done for the experimental characterization of TO heat sinks in the literature.

Three heat sinks have been tested under different operating conditions, with total input power values ranging from 60 W to 120 W (identical power for the three heaters) and inlet flow rates ranging from $1.333\times10^{-6}\ m^3\cdot s^{-1}$ (80 $mL\cdot min^{-1}$; Re_{in}=379) to $2\times10^{-6}\ m^3\cdot s^{-1}$ (120 $mL\cdot min^{-1}$; Re_{in}=569). For each test, the measurements were performed after the thermal balance at steady-state has been reached, i.e., the fluid outlet temperature is stable and the ratio of heat absorbed by the fluid to the total input power is higher than 95% (an example of heat balance check is shown in Appendix 5.A). Once the steady state was reached, a synchronized image recording was executed by the commercial software FLIR ResearchIR Max under the frame frequency of 30 Hz. The final measured temperature field with a resolution of 512×640 pixels was calculated by averaging the temperature values of 300 images at each pixel.

5.3.4 CFD simulation parameters

To compare with the IR thermography measurements, a full 3D CFD simulations for fluid flow and heat transfer were performed for three heat sinks under the same heating conditions as in the experiments. Water was used as the working fluid with temperature-dependent physical properties (cf. Table 3.1). The physical properties of the solid parts (stainless steel and sapphire) were considered constant and their values are listed in Table 5.2. The operational pressure was fixed at 101325 Pa. Simulations were performed under a steady-state, incompressible, and laminar flow regime with heat transfer. The viscous heating was neglected while the gravity effect at the *z* direction was considered.

Navier–Stokes equations as shown in chapter 3.2.3 were solved by Ansys Fluent code (version R19.1). Least squares cell-based, second order upwind differential, and second order scheme were used for discretization of gradient, momentum, and pressure. The inlet velocity and temperature of fluid were set to be constant and equal to experimental conditions. The boundary condition of the outlet was set as pressure-outlet with zero static pressure. Three heaters are simplified as thermal boundary conditions of the surface heat flux of three cylinders.

Each surface heat flux has the same input power but a different surface area, which generates various heat fluxes. Channel walls for the fluid domain were considered as no slip. The external walls were set as adiabatic, except for the external sapphire window for which a heat transfer coefficient (7 $W \cdot m^{-2} \cdot K^{-1}$) with the ambient has been set. Figure 5.13 presents (a) the GATO heat sink CFD model and (b) the thermal boundary condition of input power equal to 120 W.

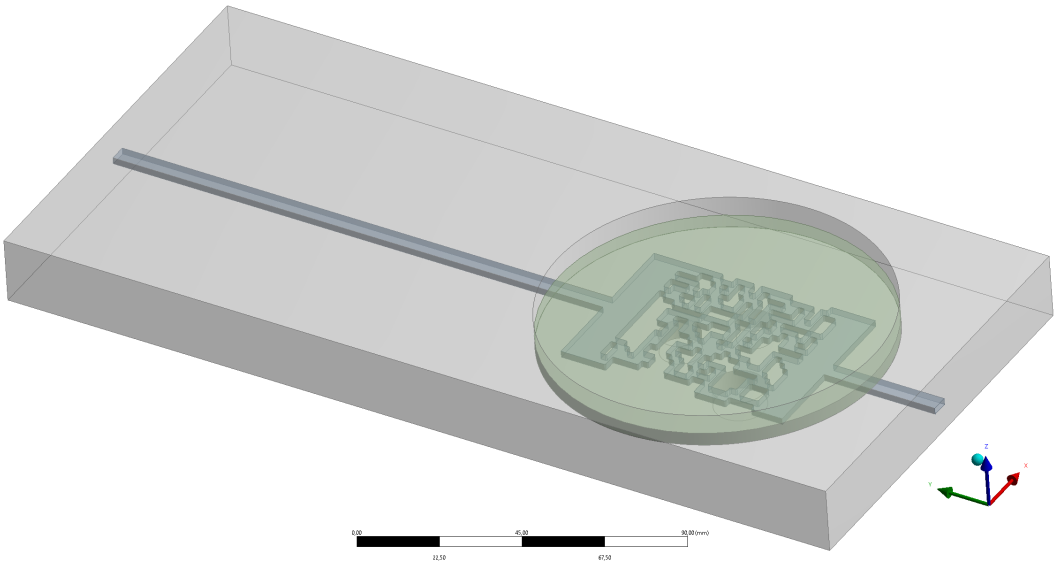

(a)

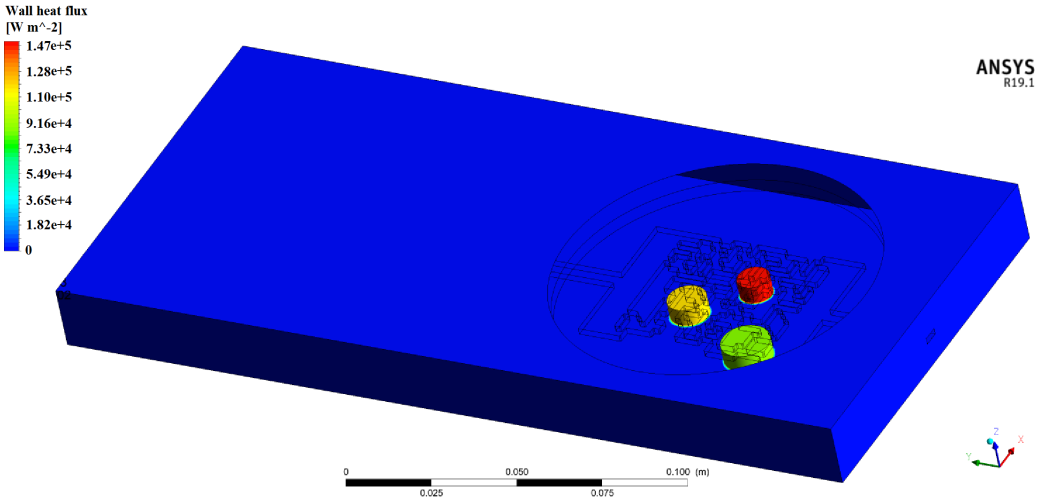

(b)

Figure 5.13 GATO heat sink CFD model and thermal boundary condition of input power = 120 W.

The structured mesh was generated to build up the geometry model, including about 0.17 million elements for the fluid, and 14.4 million elements for the solid parts. The solutions were considered to be converged when (1) the sums of normalized residuals for control equations are all less than 1×10^{-5}, and (2) the global pressure drop is constant from one iteration to the next (less than 0.05 Pa).

Table 5.2 Thermal-physical properties of solid materials used in CFD simulation [187][188]

Property	Value	
Stainless steel 304		
Thermal conductivity ($W \cdot m^{-1} \cdot K^{-1}$)	$\lambda_s = 16.27$	(5.2)
Specific heat ($J \cdot kg^{-1} \cdot K^{-1}$)	$Cp_s = 502.48$	(5.3)
Density ($kg \cdot m^{-3}$)	$\rho_s = 8030$	(5.4)
Sapphire		
Thermal conductivity ($W \cdot m^{-1} \cdot K^{-1}$)	$\lambda_{sa} = 38.2$	(5.5)
Specific heat ($J \cdot kg^{-1} \cdot K^{-1}$)	$Cp_{sa} = 700$	(5.6)
Density ($kg \cdot m^{-3}$)	$\rho_{sa} = 3980$	(5.7)

5.3.6 Comparison between IR measurements and CFD results

- Temperature contours at the measuring surface

Figure 5.14 presents the normalized temperature (T^* defined in Eq. 4.13) field at the fluid-solid interface (inner surface of the sapphire disk) obtained by IR measurements and CFD simulations under the total input power of Q_{tot}=120 W and volume flow rate of 1.667×10^{-6} $m^3 \cdot s^{-1}$ (100 $mL \cdot min^{-1}$; Re_{in}=474). For the RSC heat sink, the IR and CFD isotherms of the match well in the global trend, with the center hot spot facing the inlet port cooled down. The temperature isotherms are generally perpendicular to the flow direction in the first half of the design domain whereas two hot spots are visible near the collecting manifold. Some slight differences exist at the manifold entrance and the position of the largest heater (upper-left corner). The maximum temperature of the testing interface at 322.7 K (IR) and 325.2 K (CFD), respectively.

Good agreement between IR and CFD results on the temperature field can also be observed for the OSC heat sink, the maximum temperature being 324.3 K (IR) and 325.4 K (CFD), respectively. One slight difference is that the isotherms of the experimental result tend to move more forward to the positive *y* direction, and the isotherm curves valued at 1.3 in two middle channels are sharper than those of the CFD results. In global, the shape of isotherms is rather similar to those of the RSC heat sink.

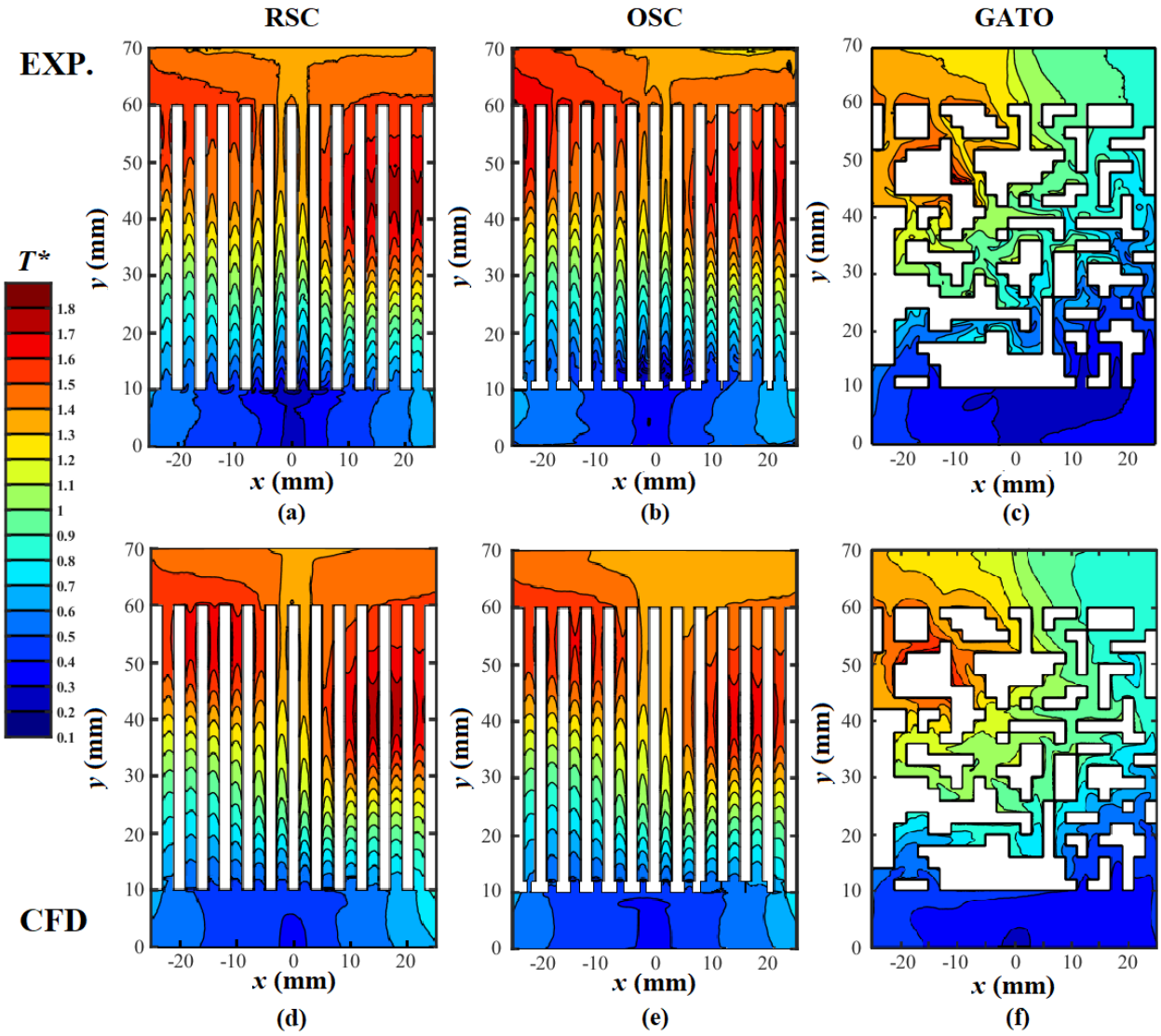

Figure 5.14 Comparison of the normalized fluid temperature contours obtained by IR thermography measurement result (a-c) and CFD simulations (d-f) for RSC, OSC, and GATO heat sinks, respectively. Condition: total input power of Q_{tot}=120 W; volume flow rate of 1.667×10^{-6} $m^3 \cdot s^{-1}$(100 mL·min^{-1}; Re_{in}=474)

Regarding the GATO heat sink, the experiment and CFD results show again a good consistency. Different from the temperature contours of RSC and OSC heat sinks, the highest temperature region no longer appears at the middle-right position of the design domain, but instead at the upper-left corner where the largest heater is located. Distinguished from the trend observed for RSC and OSC heat sinks, the temperature isotherms decrease diagonally from the upper-left corner to the bottom-right corner. The coolant is guided to cool down the temperature hot spot by the topologically-optimized fluid channel configuration, implying the effectiveness of the GATO method. The maximum temperatures are very close, i.e., 328.52 K and 329.14 K for IR measurement and CFD calculation, respectively.

A statistical analysis of Fig. 5.14 shows that the surface area of hotspots (e.g., T^*>1.75) on the measuring surface reaches 8.79 mm^2 (RSC), 1.32 mm^2 (OSC) and 0.56 mm^2 (GATO), respectively, implying better temperature uniformity at the heating surface through enhanced

cooling by applying the two optimization methods. Further performance evaluation and comparison between the three heat sinks will be presented in chapter 5.4.

- Temperature profiles along the sampling lines

For a more detailed comparison between the IR measurement and CFD simulations, the T^* profile along three sampling lines is plotted for the RSC heat sink (in Figure 5.15) and for the OSC heat sink (Figure 5.16), respectively (channel NO.1, NO.6 and NO.11, with the position of x = -22 mm, -2 mm and = 18 mm, respectively, and y ranges from 10 mm to 60 mm). The results are discussed below.

From Figure 5.15 (RSC heat sink), it can be observed the IR and CFD T^* curves are generally matched, especially for channel No.1 (orange). Nevertheless, a relatively higher departure may be observed for I channel NO. 6 (purple), especially at the entrance region where the ΔT^* could reach 0.146. For the plot of channel NO.11 which goes through the hot spot, the maximum ΔT^* between IR and CFD results is about 0.07. The maximum T^* reaches 1.75 at y=42 mm based on the CFD calculation, while for the IR measurement, it is about 1.73 at y=43 mm, again showing good consistency.

T^* profiles at the same channel locations are plotted in Figure 5.16 for the OSC heat sink. A similar global trend of IR and CFD curves may be observed, but the departure between them is more noticeable compared to that of the RSC heat sink. In more detail, the largest value of ΔT^* reaches 0.13, 0.23, and 0.15 for channels No.1, No.6, and No.11, respectively. This larger discrepancy could be due to the limitation of fabrication precision in realizing the mini orifice baffle for the OSC. The machining accuracy cannot achieve the precision of the optimized channel inlet widths (orifice sizes) as indicated in Table 5.1., which may influence the flow distribution properties among the parallel channels. Since the cooling effect of each channel relies strongly on the mass flow rate passing through, a small departure from the desired flow rate may result in a noticeable difference in the fluid temperature profiles in the channel, as shown in Figure 5.16. This also indicates that the size optimization method acting on the channel inlet width, really pragmatic and simple to implement, may be limited more by the fabrication/realization precision to achieve the optimized flow distribution among the parallel channels of the ORC heat sink.

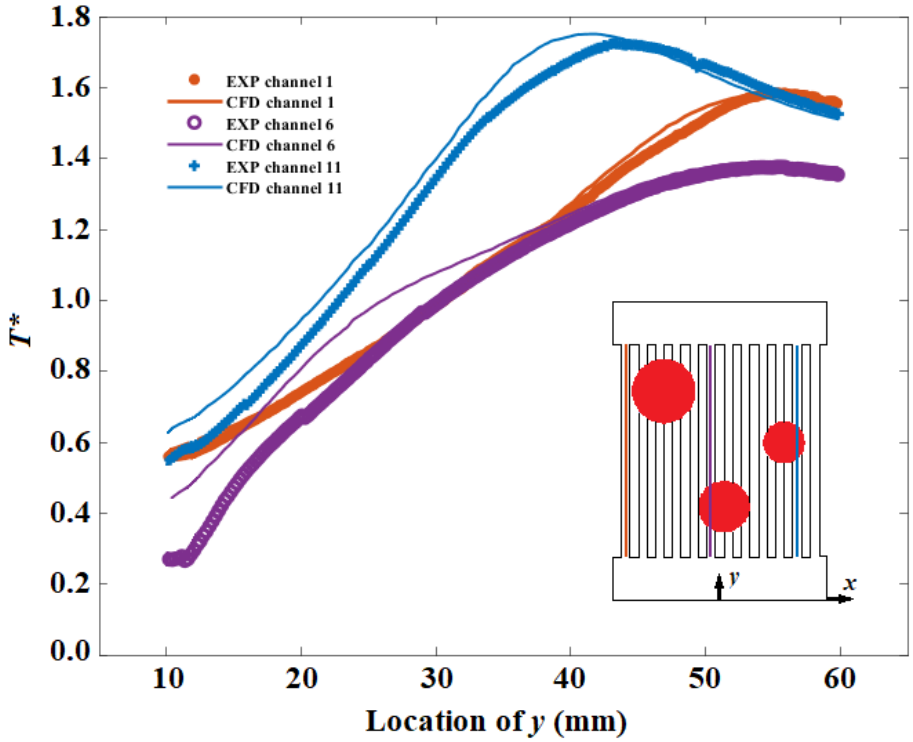

Figure 5.15 Comparison of temperature profiles in different channels of RSC heat sink. Condition: total input power of Q_{tot}=120 W; volume flow rate of 1.667×10^{-6} $m^3 \cdot s^{-1}$(100 mL·min^{-1}; Re_{in}=474)

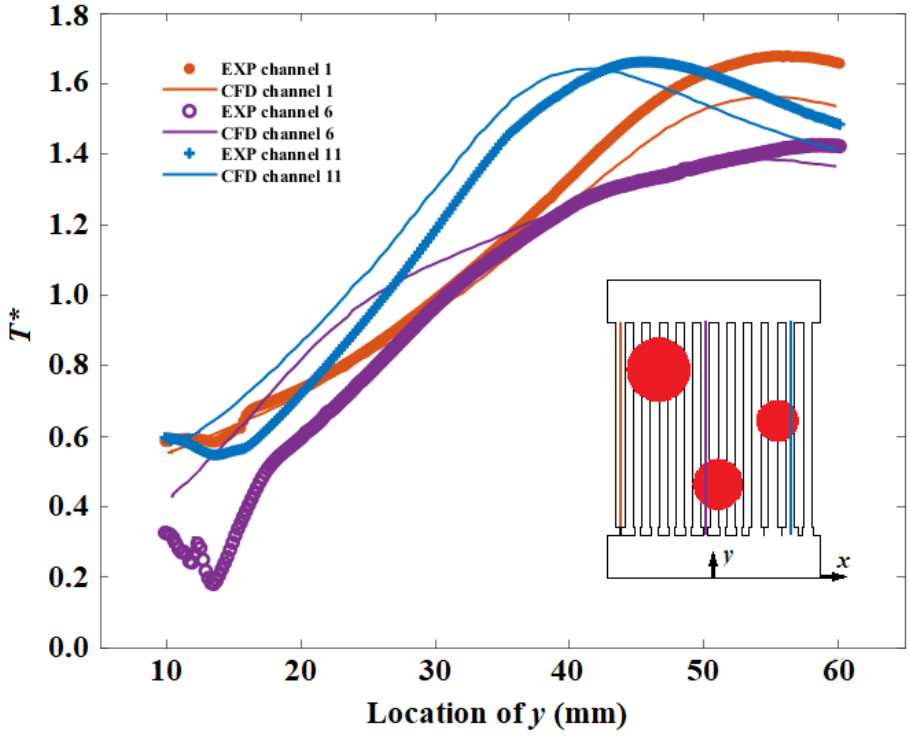

Figure 5.16 Comparison of temperature profiles in different channels of OSC heat sink. Condition: total input power of Q_{tot}=120 W; volume flow rate of 1.667×10^{-6} $m^3 \cdot s^{-1}$(100 mL·min^{-1}; Re_{in}=474)

- Average temperature and temperature uniformity of the measuring surface

Figure 5.17 presents the CFD prediction and the IR measurement of the area-weighted average temperature (T_{avg}^*) and the standard deviation STD_{T*} for the measuring surface of three heat sinks under various input power (Q_{tot}: 60 to 120 W) and inlet flow rate ($1.333\times10^{-6}$to 2×10^{-6} $m^3\cdot s^{-1}$) conditions. The STD_{T*} value is calculated by Eq. 5.8:

$$STD_{T*} = \sqrt{\frac{1}{n-1}\sum_{Pix=1}^{n}(T_{Pix}^* - \bar{T}^*)^2} \tag{5.8}$$

In experimental data, where n is the total number of pixels of the measuring surface.T_{Pix}^* is the normalized temperature at pixel Pix and $\bar{T}^*$ is the average value of all T_{Pix}^*. And in numerical results, n is the total number of mesh nodes of the measuring surface.

From Figure 5.17 (a), it can be observed that the largest STD_T^* difference is 8.6% for the OSC heat sink (120 W input power and 2×10^{-6} $m^3\cdot s^{-1}$(Re_{in}=569) inlet volume flow rate), due to the reason explained above. The maximum STD_{T*} error for the RSC heat sink and GATO heat sink is within 3.7% and 5.7%, respectively, showing good agreement between the IR and CFD results. A similar observation can be made for T_{avg}^* shown in Figure 5.17 (b). Good agreement between IR and CFD results can be drawn, the maximum error being 8.2% (RSC), 2.9% (OSC), and 6.7% (GATO), respectively.

In conclusion, the CFD model used for the thermal test can be validated by the IR measuring results. It is worth noting that among the three tested heat sinks, the GATO heat sink has the lowest values of STD_{T*} and T_{avg}^* for the measuring surface (inner sapphire wall in contact with the fluid). This implies that the GATO heat sink could have the best cooling performance, which will be further discussed in the next section.

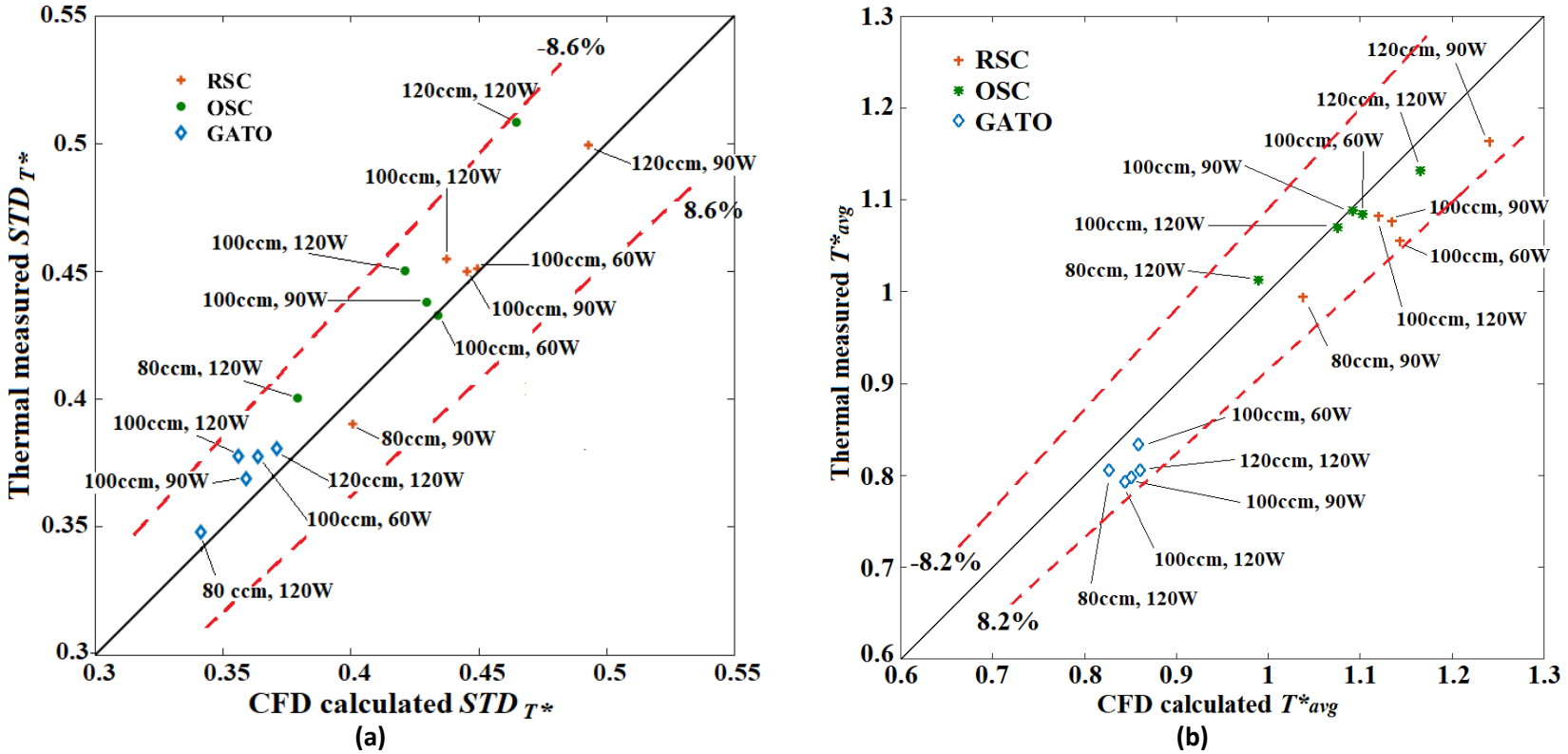

Figure 5.17 The CFD calculated and IR measured values of STD_{T*} (a) and T^*_{avg} (b) for three heat sinks. Conditions: input power Q_{tot}: 60 to 120 W; inlet flow rate: 1.333×10^{-6} to 2×10^{-6} $m^3\cdot s^{-1}$ (the unit: ccm is $mL\cdot min^{-1}$).

5.4 Performance evaluation and comparison between three heat sinks: further analysis of the CFD results

In the previous section, the IR measurements on the fluid-solid interface have been used to validate the CFD models. Further analysis of the CFD results will be rather beneficial to gain more information on the local fluid flow and heat transfer characteristics of the three tested heat sinks as well as their global thermal and hydraulic performance evaluation under a wide range of operating conditions.

5.4.1 Local fluid flow and heat transfer characteristics of three heat sinks

Figure 5.18 shows the T^* cartography on the heating surface (2 mm below the bottom wall of the fluid channels) of the three heat sinks, extracted from the obtained CFD results. The temperature hots pots due to the power input from the three heaters are visible.

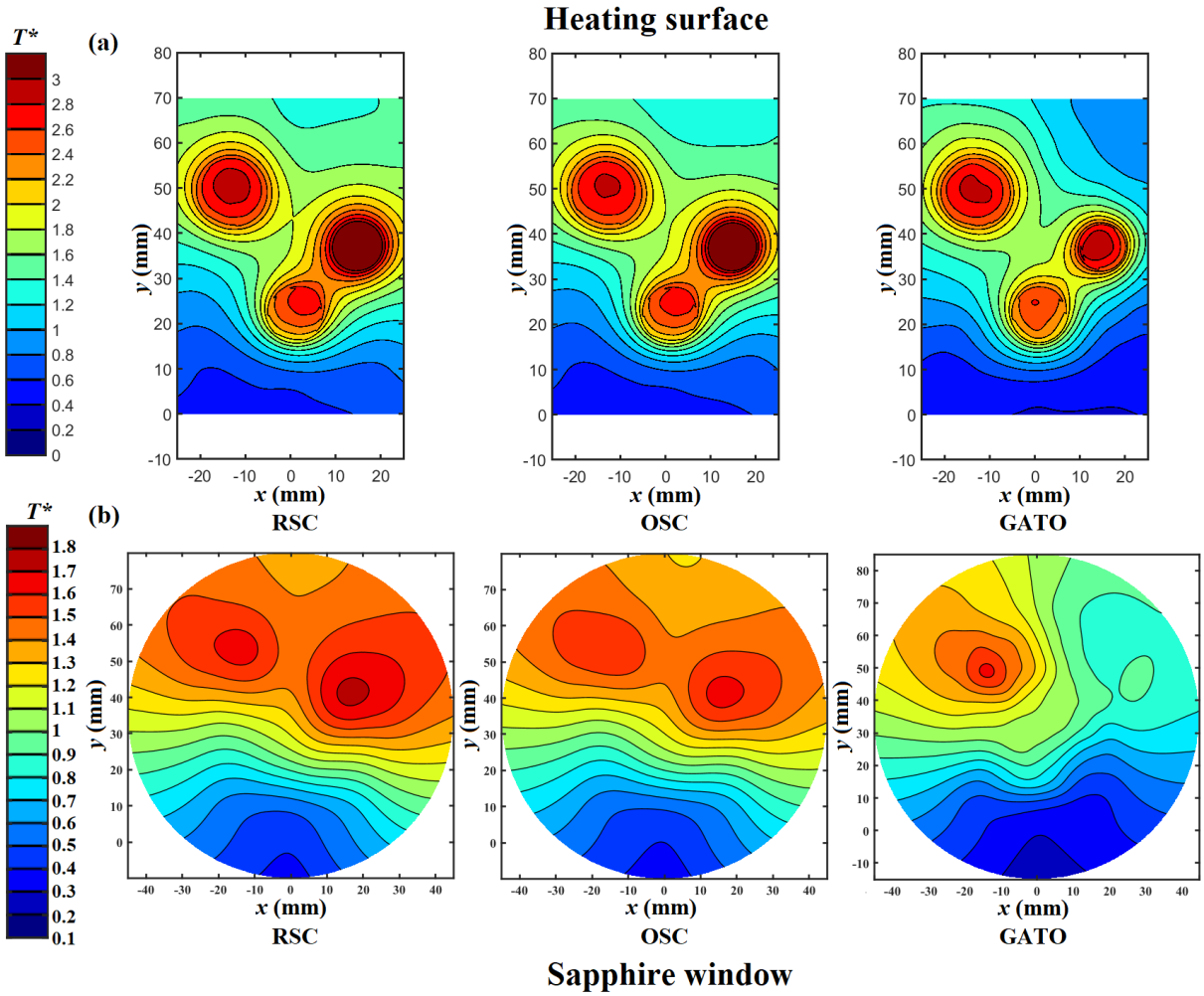

Figure 5.18 Comparison of the normalized temperature distribution on the heating surface (a) and outer sapphire window (b) of three heat sinks. Condition: total input power of Q_{tot}=120 W; volume flow rate of 1.667×10^{-6} $m^3\cdot s^{-1}$(100 mL·min^{-1}; Re_{in}=474).

For the RSC heat sink, the $T^*_{peak} = 3.73$ (356.8 K) is found at the middle-right position of the heating surface. This is because given the same power input (40 W), the heat flux is the highest for the heater with the smallest heating surface area (d=6 mm). The temperature field on the heating surface of the OSC heat sink follows a similar trend, with overheated areas shrinking a bit owing to the tailored flow distribution realized by the optimized channel inlet widths. The peak temperature $T^*_{peak} = 3.64$ (355.4 K) is still located at the position that receives the highest heat flux. For the GATO heat sink, the peak temperature of the heating surface has been significantly decreased to $T^*_{peak} = 2.94$ (343.8 K), 13.1 K, and 11.6 K smaller than that of the RSC and OSC heat sink, respectively. The temperature cartography also shows that the three uneven hot spots tend to be dissipated uniformly with the help of GATO.

Besides, the temperature distributions at the outer wall of the sapphire disc (circle surface area) are also shown in Figure 5.18. The T^* scale was set to be the same as Figure 5.14 for a better comparison. It is obvious that the temperature differences on outer wall of sapphire window (cover plate) are smaller than those at the testing surface (fluid-solid interface) in Figure 5.14 of three heat sinks. This illustrates the reason why the temperature field of the fluid-solid interface has been chosen for IR thermography. Because it is nearer to the heating surface thus more sensitive to the temperature uniformity improvement due to applying the optimization methods.

The thermal performance of a single-phase cooling heat sink is greatly related to the fluid flow behaviors for heat convection. Therefore, a detailed analysis of the fluid domain in the three heat sinks has been made. The numerical results are shown in Figures 5.19 - 5.21 and commented on below. presents the velocity contours in the x-y plane, velocity vectors of cross sections in the x-z plane, and the zoom-in figures from the previous cross-section of the CFD thermal model of three heat sinks.

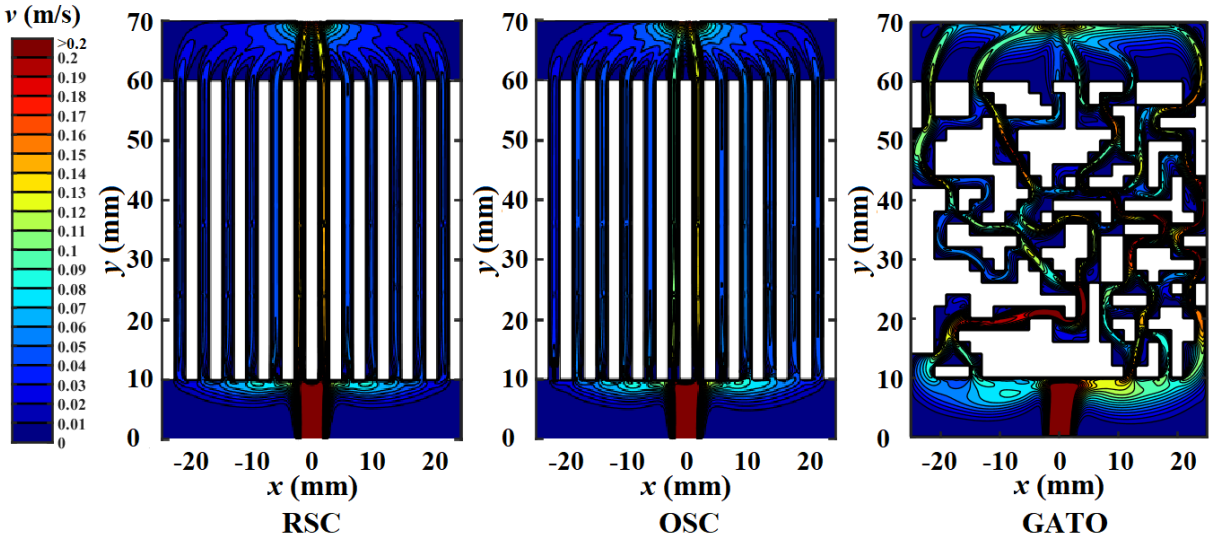

Figure 5.19 Contour of velocity magnitude at the mid-depth of the fluid channels (z=1 mm) for three studied heat sinks. Condition: total input power of Q_{tot}=120 W; volume flow rate of 1.667×10^{-6} m^3·s^{-1}(100 mL·min^{-1}; Re_{in}=474)

Figure 5.19 presents the contour of velocity magnitude (*x*-*y* plane) at the mid-depth of the fluid channels (*z*=1 mm) for three studied heat sinks. For the RSC heat sink, the fluid flow distribution behavior has already been discussed in detail in section 5.2 devoted to the PIV test (Figure 5.7). Regardless of the location and heat flux of the three heaters, the geometry and dimension specificities of RSC render always the highest amount of cooling fluid passing through the two middle channels, while other channels are less supplied. This is the intrinsic drawback of the RSC heat sink, which may not be of sufficient concern for cooling a uniformly heated surface, but certainly not enough performant to treat localized multiple heat sources. For the OSC heat sink, more fluid is guided to the side (e.g., *x*>0) where the higher heat flux is located. Nevertheless, the cooling performance improvement is limited concerning the RSC heat sink. This is because the optimization method works only on the adjustment of flow distribution among parallel channels, while in each channel the flow direction is the same (*y* direction). This approach has shown its effectiveness for cooling a heating surface with multiple Gaussian-shape heat fluxes (chapter 3). But for the case of localized multiple heat sources but each with uniform heat flux, the limitation of this optimization method due to the lack of design freedom can be seen. This happens to be the distinguished advantage of the GATO approach, which needs no geometry presetting but has the highest degree of freedom to morph. The channel turnings, bifurcations, and intersections shown in Figure 5.19 can only be proposed by the TO method. Rather complex and non-established flow patterns can be generated, including divergent/confluence flows, transversal flows, and secondary flows, to enhance the forced heat convection, especially near the heat sources. As a result, the reduction of T^*_{peak} at the heated surface is more significant by applying the GATO method (compared to the flow distribution optimization).

Figure 5.20 compares the velocity vectors in the channel cross sections (*x*-*z* plane) at the channel mid-length (*y*=35 mm) of the three heat sinks. For better observation, the scale factor is set to 5 for magnification. It is rather obvious that the velocity vectors in the *x*-*z* plane of the GATO heat sink far exceed the amount in RSC and OSC heat sinks.

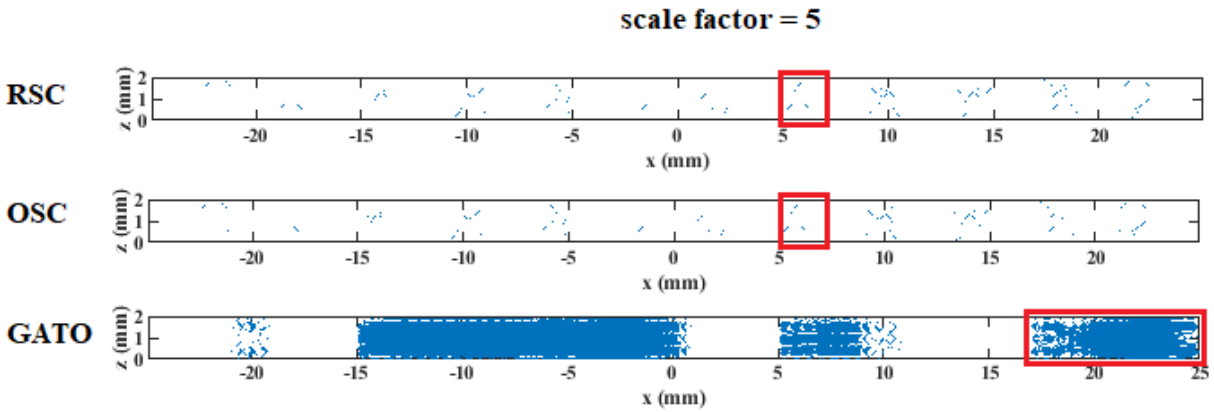

Figure 5.20 Comparison of the velocity vectors at the channel cross sections of RSC, OSC, and GATO heat sinks (Channel mid-length at *y*=35 mm).

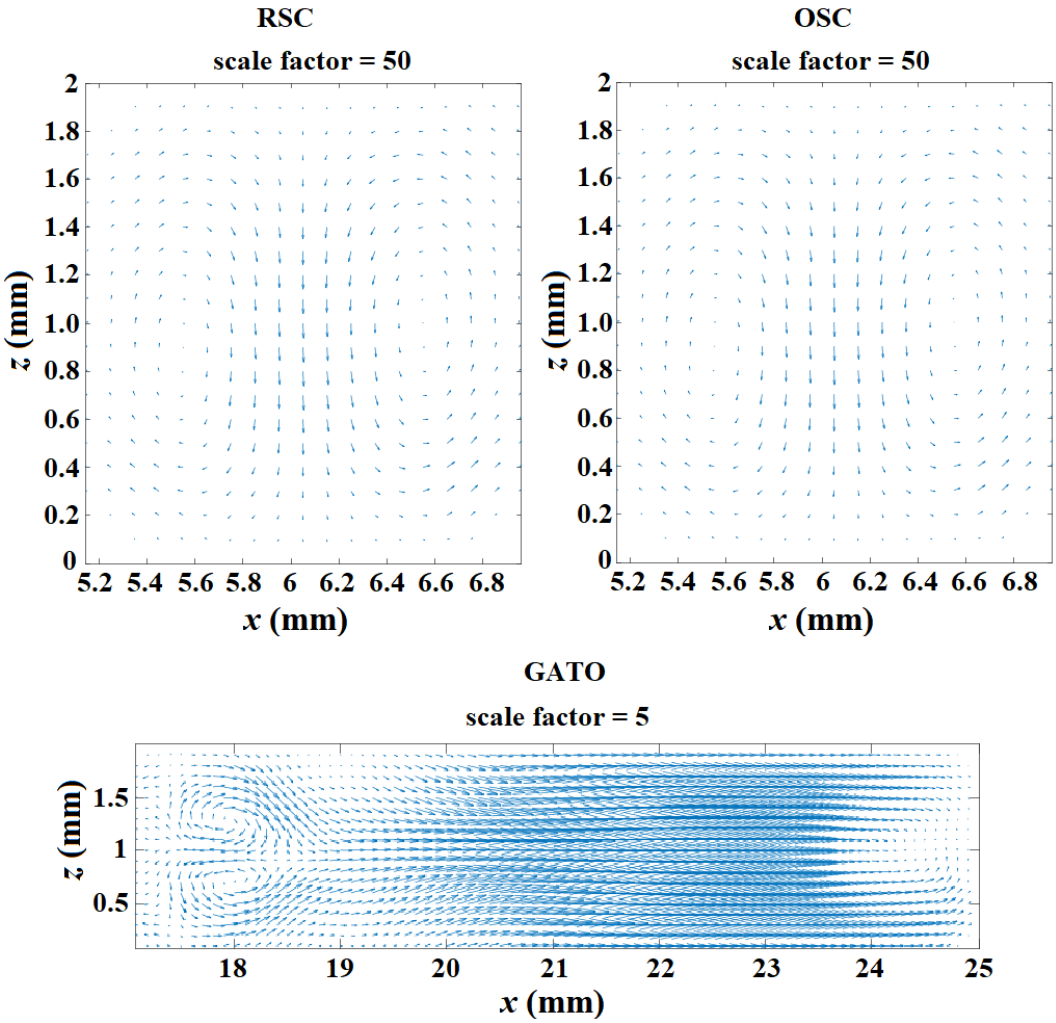

Figure 5.21 Zoom-in images for the velocity vectors in the cross sections.

The zoom-in images of some sampling positions are shown in Figure 5.21 with different scale factors. The distribution and directions of velocity vectors in the cross-section of RSC and OSC heat sinks are quite similar. Two small vortices are formed with descending velocity vectors (z-direction) in the middle of the cross-section and ascending velocity vectors (z-direction) at each side wall. This is because of the higher temperature of the bottom and side walls (close to the heaters) than the upper wall (inner surface of the sapphire disk). The buoyancy effect due to the fluid temperature difference (thus the density difference) results in the appearance of such vortices. Vortices and secondary flows are much more obvious for the GATO case shown in Figure 5.21, which is mainly due to the flow confluence and diverging at that intersection.

5.4.2 Comparison of the global thermal and hydraulic performances of three heat sinks

Local fluid flow and heat transfer characteristics have been discussed in the previous chapter 5.4.1, showing that the GATO heat sink has the lowest T^*_{peak} in the heating surface, which is following the defined objective function for the optimization methods. In this section, attention is focused on the evaluation and comparison of the global thermal and hydraulic

performances of three heat sinks. For this purpose, more CFD simulations (using the thermal model) have been performed for three heat sinks. The testing condition covers a wide range, with the inlet fluid flow rate ranging from 0.667×10^{-6} to 2.33×10^{-6} $m^3\cdot s^{-1}$ (40 to 140 $mL\cdot min^{-1}$; Re_{in}: 237 to 663) and total input power increasing from 30 W to 180 W (identical input for three heaters). Other operating parameters are kept the same (inlet fluid temperature at 20 °C; environment temperature at 17 °C and convection heat transfer coefficient at the outer sapphire disk at 7 $W\cdot m^{-2}\cdot K^{-1}$). The obtained numerical results are used to calculate several global indicators for heat sink performance evaluation, including the Nusselt number (*Nu*), the performance evaluation criterion (*PEC*) number, and the *Po/Nu* ratio, introduced below.

The calculation of the *Nu* number for the heat sink follows Eq. (4.6) explained in chapter 4. The *PEC* for OSC and GATO heat sink is calculated based on Eq. (5.9) [189].

$$PEC = \frac{Nu/Nu_{reference}}{\sqrt[3]{\Delta P/\Delta P_{reference}}} \tag{5.9}$$

where the RSC heat sink is considered as the reference case. ΔP (Pa) is the global inlet-outlet pressure drop of the heat sink. The Poiseuille number (*Po*) is calculated by Eq. (5.10)

$$Po = f \cdot Re_{avg} \tag{5.10}$$

Where Re_{avg} and f is the average *Re* number of the fluid domain, and the Darcy friction factor, calculated by Eq. (5.11) and Eq. (5.12), respectively.

$$Re_{avg} = \frac{\rho_{f,avg} v_{avg} D_h}{\mu_{avg}} \tag{5.11}$$

Where $\rho_{f,avg}$ and μ_{avg} are the average fluid density ($kg\cdot m^{-3}$) and average fluid dynamic viscosity ($kg\cdot m^{-1}\cdot s^{-1}$). v_{avg} the volume-weighted average velocity of the fluid domain ($m\cdot s^{-1}$). D_h is the hydraulic diameter of the fluid circuit (m) expressed by Eq. (4.8) in Chapter 4.

$$f = \frac{\Delta P}{L} \cdot \frac{2\cdot D_h}{\rho_{f,avg}\cdot v_{avg}^2} \tag{5.12}$$

Where L is the distance (m) between the inlet and outlet.

The numerical results obtained are analyzed and discussed as follows.

5.4.2.1 Nusselt number

Figure 5.22 (a) presents the *Nu* number of three heat sinks as a function of the inlet *Re* number. It can be observed that RSC and OSC heat sinks have similar *Nu* numbers (*Nu*=6 for RSC and 6.3 for OSC), and vary little with the Re_{in}. In contrast, a much higher *Nu* number can be achieved for the GATO heat sink, ranging from 9.1 to 14.8 when Re_{in} increases from 284 to 663. The boosting of *Nu* number for GATO heat sink is mainly attributed to the geometry

complexity of GATO heat sink. Secondary flows and transversal flows were frequently generated under this kind of complex geometry, which prevented the establishment of thermal boundary layers and therefore enhanced the convective heat transfer as shown in section 5.4.1. Compared to RSC and OSC heat sinks, the thermal performance enhancement in terms of *Nu* by GATO is rather significant, especially at high Re_{in}. At the section of higher Re_{in} between around 550 - 660, the slope of the *Nu* number curve of GATO heat sink seemed to be increased, and this may be caused by local turbulence flow (more details could be found in Appendix 5.B of this chapter). However, the existence of some local turbulences would further bring benefits for the cooling performance by enhanced forced heat convection. Whereas for RSC and OSC, developed laminar flow dominates the heat transfer in the parallel channels (except for the inlet region), resulting in a relatively stable *Nu* value under the tested Re_{in} conditions. Therefore, the enhancement brought by the GATO heat sink compared to RSC or OSC heat sinks, indicated by the *Nu* increase, is more significant owing to the combined effects of geometry complexity and the local turbulences.

Figure 5.22 (b) shows the *Nu* number for three heat sinks as a function of total input power Q_{tot}. All three *Nu* curves show a slight increase when Q_{tot} increases from 30 W to 180 W. This is mainly because of the slightly lower water thermal conductivity at a higher temperature due to the higher power input. The *Nu* numbers between RSC and OSC heat sinks are rather close, ranging from 5.6 to 6.4 and 6.0 to 7.1, respectively. Again, the GATO heat sink shows a much higher *Nu* number, ranging from 11.1 to 12.0 under the tested Q_{tot} conditions. This indicates that the GATO heat sink, though optimized for minimizing the T_{peak} of the heating surface, has the best global thermal performance in terms of the *Nu* number.

Figure 5.23 shows a comparison of *Nu* numbers of three tested heat sinks as a function of the pressure drop (ΔP). It may be observed that RSC and OSC heat sinks have relatively low *Nu* numbers, about 6.3 – 6.4 for the RSC heat sink, and 6.5 - 6.7 for the OSC heat sink, respectively. On the other hand, the *Nu* number of the GATO heat sink varies between 9.1 and 17.5 when ΔP increases from 128 Pa to 518 Pa. from the overlapped ΔP range, it can be seen that the *Nu* number of the GATO is much higher than that of RSC and OSC heat sinks at the same ΔP. This implies that with the same pumping power consumption/cost, the GATO heat sink always provides a much better thermal performance than RSC and OSC heat sinks. More evidence on this point will be given when discussing other performance indicators in the following sub-sections.

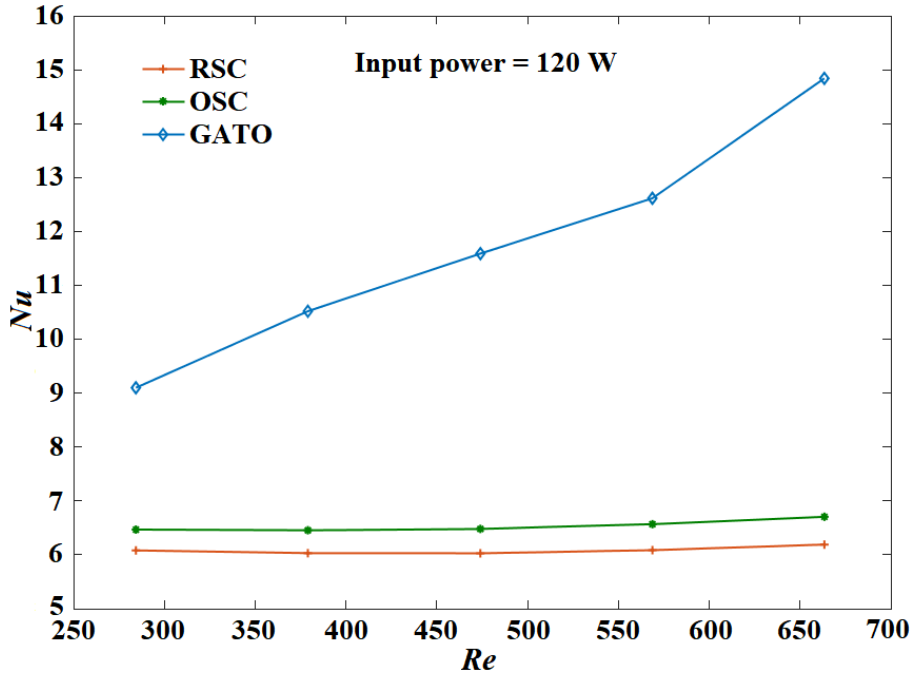

(a)

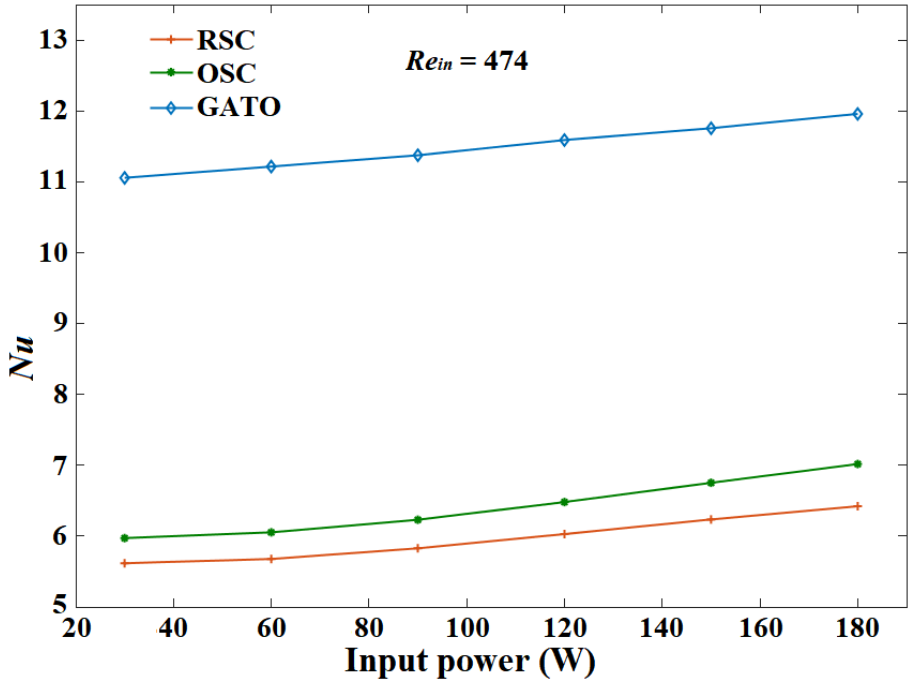

(b)

Figure 5.22 Comparison of the *Nu* numbers of three tested heat sinks (a) *Nu* vs. Re_{in}; (b) *Nu* vs. Q_{tot}.

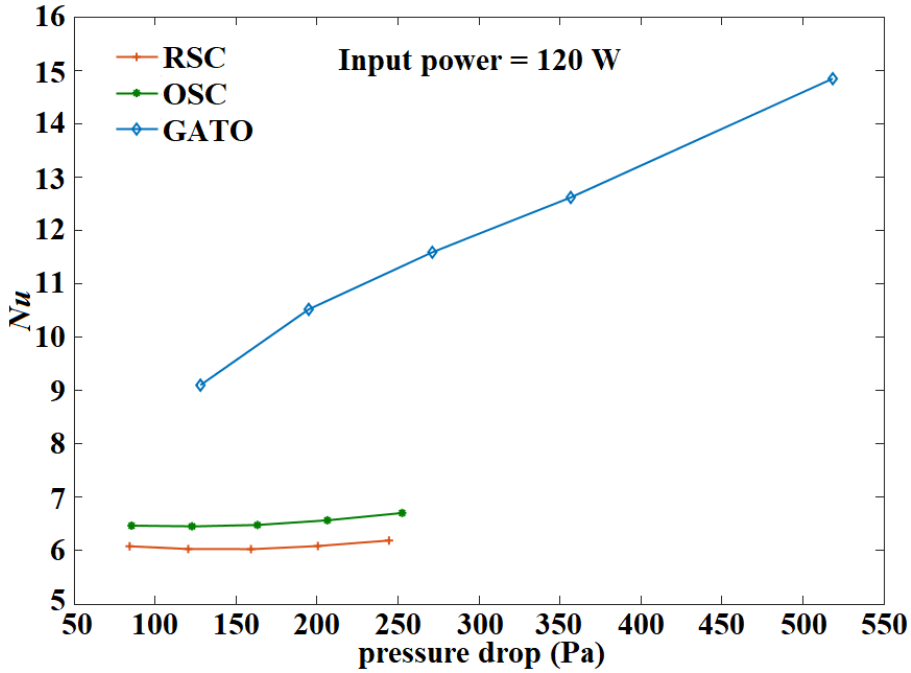

Figure 5.23 *Nu* number as a function of pressure drop for RSC, OSC and GATO heat sinks.

5.4.2.2 PEC number

The *PEC* number evaluates the heat sink performance considering both thermal and hydrodynamic aspects. It indicates the possible performance enhancement that can be achieved by a novel design of a heat sink concerning a reference case (here the RSC). The *PEC* value greater than 1 implies that the enhancement of thermal performance is beneficial at the cost of the pressure drop increase, and this is the case for both OSC and GATO heat sinks as shown in Figure 5.24. Among them, the *PEC* values (about 1.05) remain almost unchanged under the tested Re_{in} conditions. While for the GATO heat sink, it rises from 1.30 up to 1.87, the performance enhancement is rather significant. This is rather encouraging since pressure drop has not been considered in the GATO method developed in chapter 4, neither as an objective nor as a constraint.

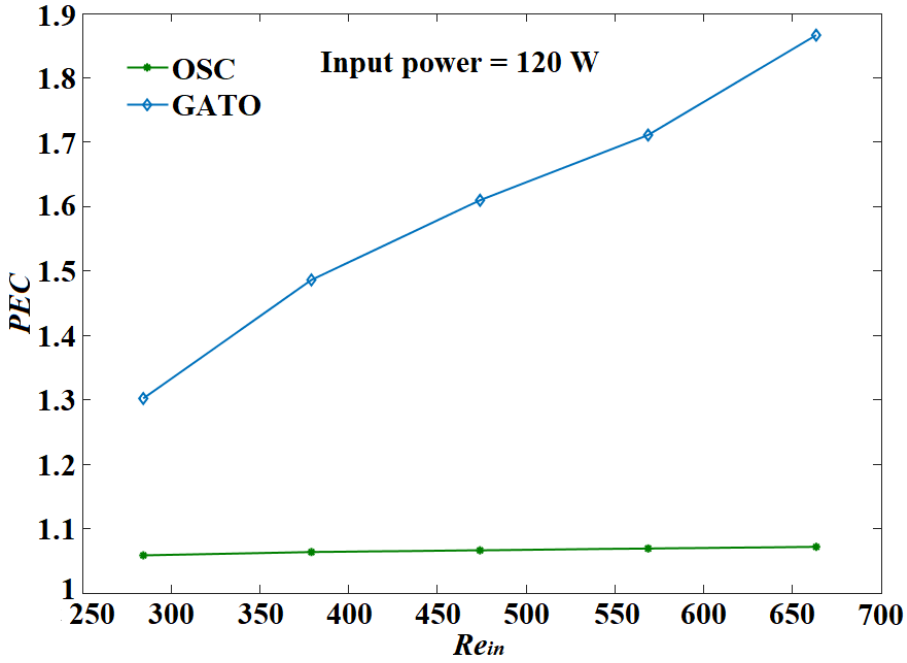

Figure 5.24 *PEC* values of OSC and GATO heat sinks under various inlet *Re* numbers.

5.4.2.3 Po/Nu ratio

The *Po/Nu* ratio considers also both the hydraulic and thermal performances of a heat sink, with the smaller ratio indicating better performance. Figure 5.25 (a) shows the values of *Po/Nu* for three tested heat sinks as a function of total power input. All three curves descend with the increasing Q_{tot}. While *Nu* values remain almost constant with the increasing Q_{tot} (as shown in Figure 5.22 (b)), the decreased *Po/Nu* ratio is mainly due to the decreased *Po* number at a higher Q_{tot}. The higher Q_{tot} raises the fluid temperature in general, thereby a smaller fluid viscosity and smaller ΔP. Among the three tested heat sinks, the GATO heat sink has always the lowest *Po*/*Nu* ratio at a given Q_{tot}, at least 13.7% and 7.5% lower than those of RSC and OSC heat sinks.

Figure 5.25 (b) presents the *Po*/*Nu* ratio vs. Re_{in} for three tested heat sinks. The curves for RSC and OSC heat sinks gradually rise with the increasing Re_{in} number. This is due to the boosted *Po* number but a rather stable *Nu* number at a higher Re_{in} number, indicating that increasing the flow rate of coolant is not beneficial in terms of thermal & hydraulic performances of RSC and OSC heat sinks. As for the GATO heat sink, the *Po*/*Nu* ratio is rather stable under the tested Re_{in} range. The slight rise of *Po*/*Nu* ratio at two extremes of the tested Re_{in} range is mainly because the GATO heat sink has been optimized under Re_{in}=474. Nevertheless, the effectiveness and robustness of the method considering both the thermal and hydraulic performances can still be seen under the tested Re_{in} range.

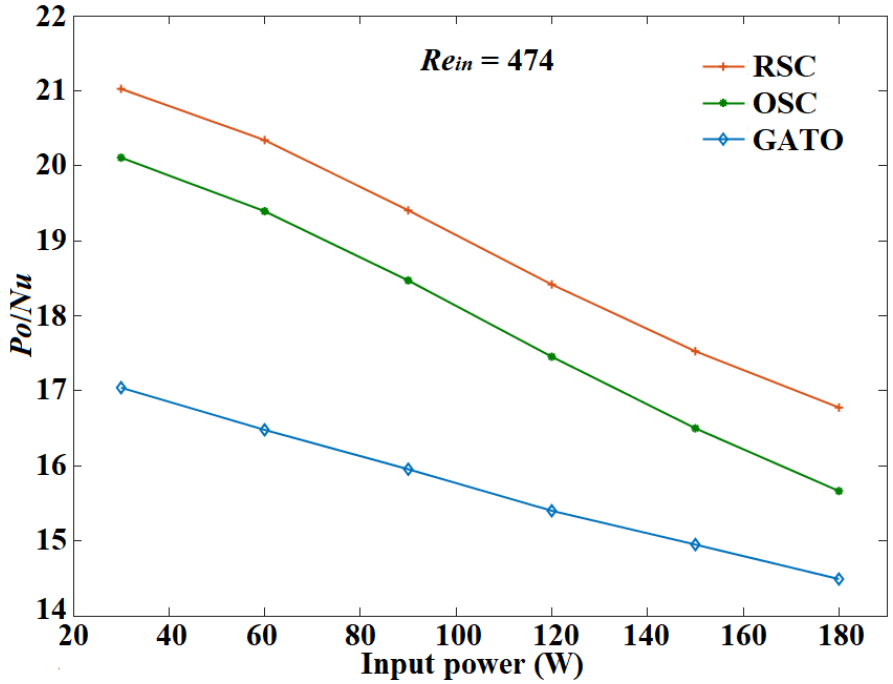

(a)

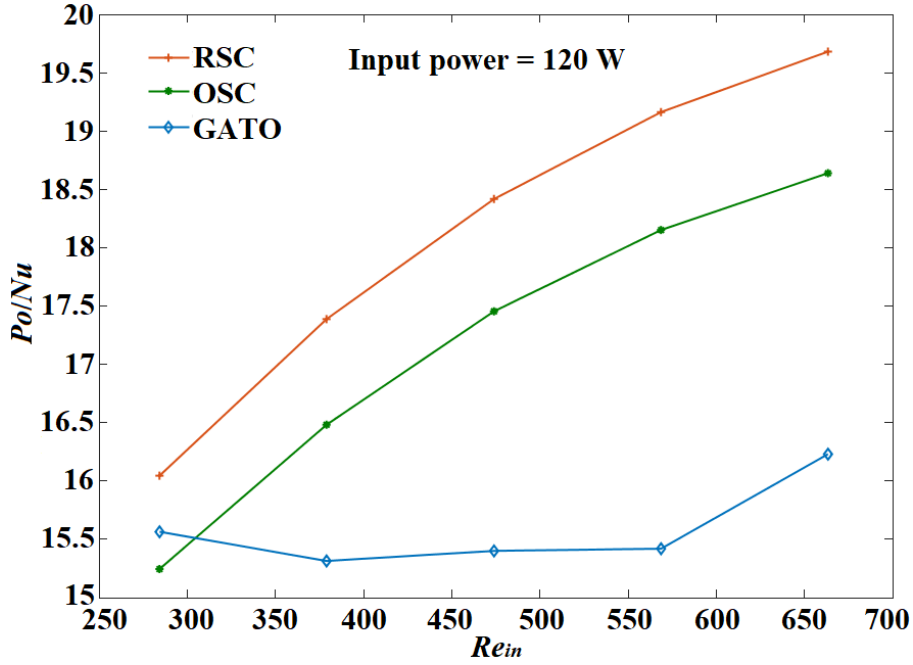

(b)

Figure 5.25 Comparison of the *Po/Nu* ratio for the three tested heat sinks. (a) *Po/Nu* vs. Q_{tot}; and (b) *Po/Nu* vs. Re_{in}.

5.5 Conclusion

This chapter has been devoted to the performance comparison and evaluation of different heat sinks using both experimental and numerical approaches. Three heat sinks have been tested, including the RSC, OSC, and GATO, under a wide range of operating conditions. The PIV method has been used to measure the velocity field at the mid-depth of the fluid domain while

IR thermography has been applied to measure the temperature distribution at the fluid-solid interface. The main conclusions could be drawn as followed:

- The velocity profiles of the RSC prototype captured by PIV show good agreement with the CFD calculations, so s to validate the numerical model (laminar) for fluid flow;
- IR measurements and CFD calculations on the temperature distribution at the fluid-solid interface of three heat sinks are in good agreement, validating thereby the CFD model for the simulation of three heat sinks.
- Amongst the three tested heat sinks, the GATO heat sink shows the smallest T^*_{peak} at the fluid-solid interface as well as at the heating surface, showing the good effect of the GATO method in removing the temperature hotspots under multiple heat sources. The enhancement of convection heat transfer is mainly achieved by the non-established, transversal, and secondary flows in the GATO heat sink with numerous channel turnings, bifurcations, and intersections.
- The performance comparison based on different performance indicators also shows that the GATO heat sink has the best thermal and hydraulic performances under a wide range of operating conditions. The performance enhancement is rather significant compared to RSC or OSC heat sinks.

All the above conclusions showcase that the GATO approach is a rather effective and robust method due to its highest degree of design freedom. It is worth mentioning that the good performances GATO heat sink are based on the single optimization objective of minimization of the T_{peak} at the heating surface. Testing different optimization criteria for the GATO method would be the goal for the next chapter 6.

Appendix 5.A: An example of steady state establishment

The heat sink models were optimized under a steady state, therefore, the thermal measurement should be performed after the fluid flow and heat transfer reach the steady state. Figure 5.A1 shows an example of the thermal transient (OSC heat sink) from the beginning of the system heating up to the time when it reached a constant outlet fluid temperature. The power absorbed by the working fluid was then calculated. This record was based on the boundary conditions of 120 W total input power and 1.667×10^{-6} $m^3 \cdot s^{-1}$ volume flow rate (100 mL·min^{-1}; Re_{in}=474). The ambient temperature and the inlet temperature at the moment were 296.55 K and 294.85 K, respectively. Q' stands for the heat absorbed by the coolant, which was calculated by the difference between inlet and outlet temperature and the flow rate, and Q is the total input power (from the heaters). It took about 25 minutes to reach the steady state of the system. The ratio was about 98.1% and the estimated heat loss was about 2.3 W.

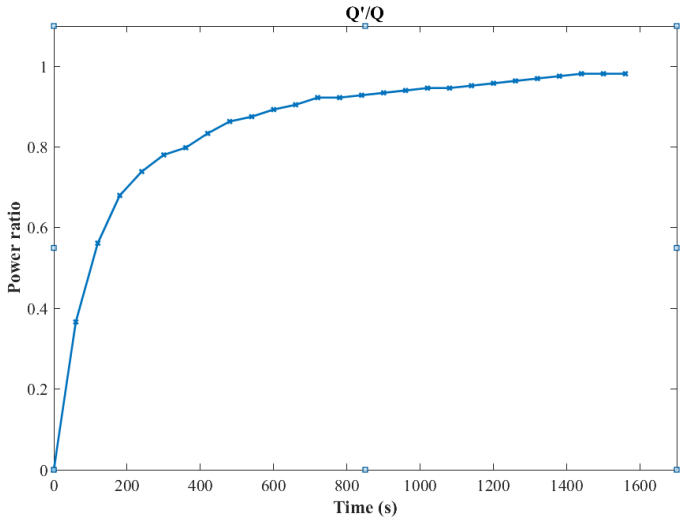

Figure 5.A1 The thermal transient state of the system under the boundary condition of 120 W input power and 1.667×10^{-6} $m^3 \cdot s^{-1}$ volume flow rate (100 mL·min^{-1}; Re_{in}=474) of OSC heat sink.

Appendix 5.B: CFD results obtained from a $k-\varepsilon$ RNG turbulence model for the GATO heat sink

A $k-\varepsilon$ RNG turbulence model was applied to capture the fluid domain in the GATO heat sink for the observation of the fluid flow. Figure 5.B1 (a) and (b) present the turbulent intensity and turbulent kinetic energy of at the middle plane of fluid domain. The whole fluid domain is covered by a low turbulent intensity value, which is less than 5%. The turbulent intensity of most area is between 0% to 3.5%, which indicates a rather low turbulence level. Similarly, Figure 5.B1 (b) also displays a rather low turbulent kinetic energy globally, which is smaller than 0.002 at most of region. Those results indicate that while local turbulences are present in certain locations of the fluid domain, the flow is globally under laminar condition.

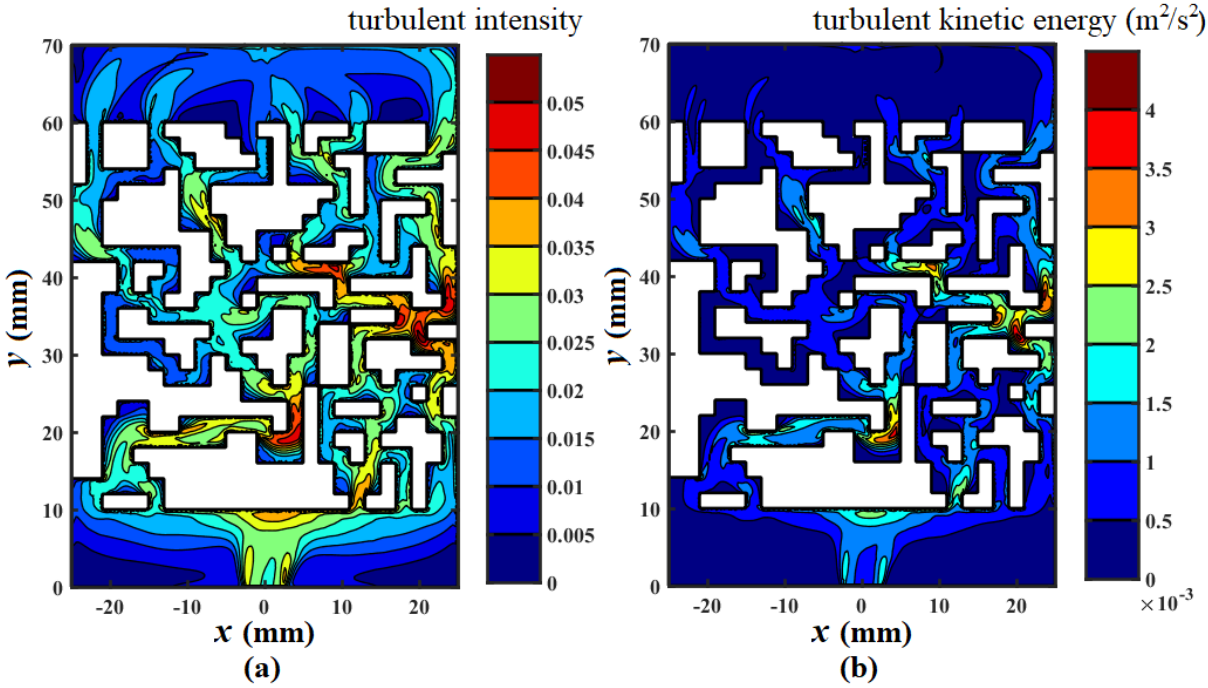

Figure 5.B1 Turbulent intensity (a) and turbulent kinetic energy (b) at the middle plane of the fluid domain under the boundary condition of 120 W input power and 1.667×10^{-6} $m^3 \cdot s^{-1}$ volume flow rate (100 mL·min^{-1}; Re_{in}=474) of GATO heat sink (k-ε RNG turbulence model).

Additionally, the velocity fields at the middle plane captured by CFD laminar model and $k-\varepsilon$ RNG turbulence model are shown as Figure 5.B2 (a) and (b). By comparison, both velocity fields have the similar profile at the same location and the same variation tendency in different places. This indicates that either applying laminar model or turbulence model would not much influence the global fluid flow pattern in the GATO heat sink. Therefore, in this study, the laminar flow model used in the CFD calculations is reasonable.

Furthermore, the temperature distributions obtained by CFD laminar model, IR thermography and CFD turbulence model are compared in Figure 5.B3 (a-c). In the cold region (the distributor), the non-dimensional temperature ranging from 0.1 to 0.2 was better captured by turbulence model compared with the experimental result. Regarding the hot region which is more crucial to indicate the existence of hotspots, obviously, the surface of high temperature region in turbulence model was smaller than that of the experimental result. This hot area of interest could be better identified by the laminar model than the turbulence model. In whole region, the consistency between numerical and experimental results is better by using the laminar flow model.

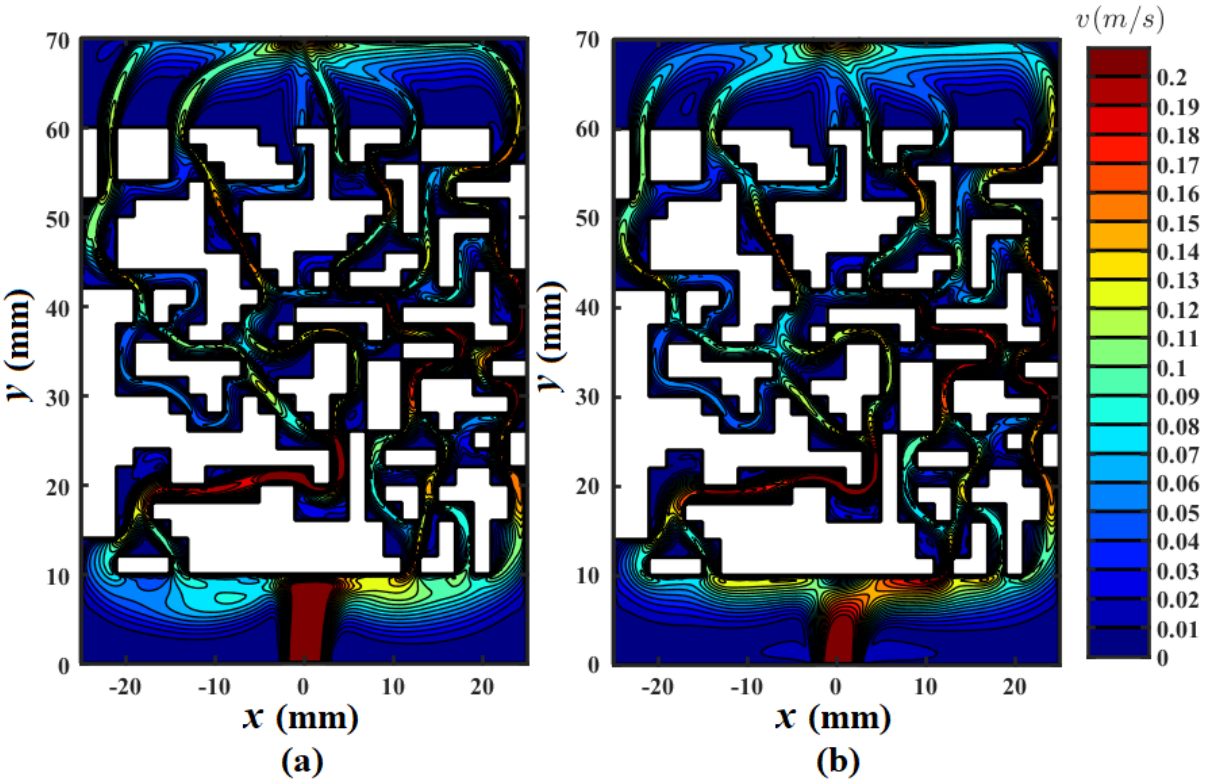

Figure 5.B2 Velocity fields at the middle plane of the fluid domain of GATO heat sink, obtained by using a laminar model (a) and a $k-\varepsilon$ RNG turbulent model (b) under the boundary condition of 120 W input power and 1.667×10^{-6} $m^3 \cdot s^{-1}$ volume flow rate (100 mL·min^{-1}; Re_{in}=474).

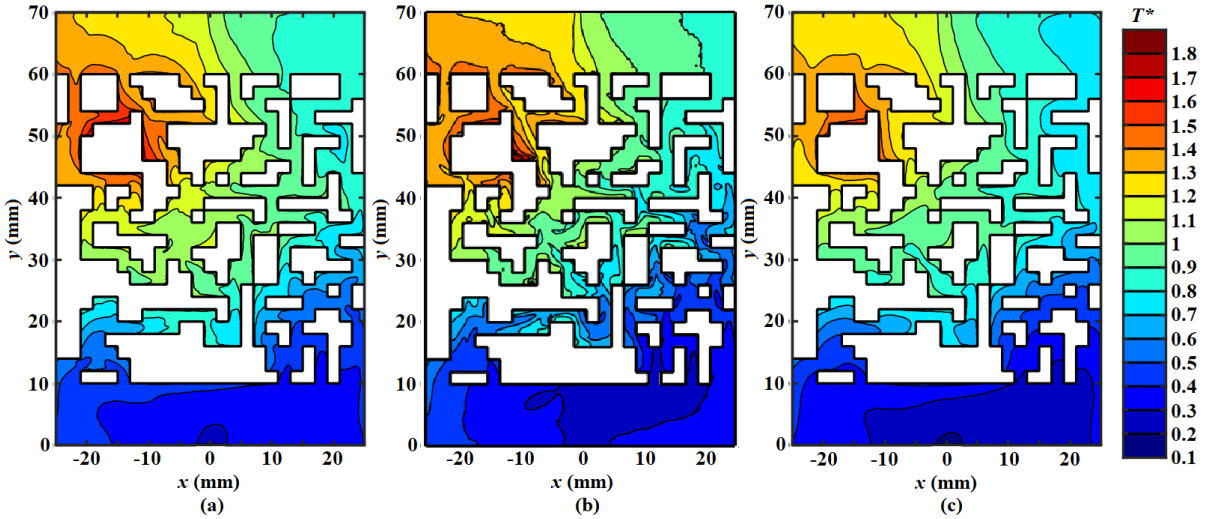

Figure 5.B3 Temperature fields at the testing surface of GATO heat sink, obtained by using a laminar model (a), experimental measurement (b) and a $k-\varepsilon$ RNG turbulent model (c) under the boundary condition of 120 W input power and 1.667×10^{-6} $m^3 \cdot s^{-1}$ volume flow rate (100 mL·min^{-1}; Re_{in}=474).

Chapter 6: Comparison of different objective functions for the GATO approach

Chapter summary:

This chapter will explore the influence of different objective functions that concern both hydrodynamic and thermal performance on the optimal flow path configurations obtained by our GATO approach. In particular, three different objectives, i.e., the root mean square deviation (RMSD) of the temperature field at the heating surface, the ratio between the heat sink's global Poiseuille number and Nusselt number, and the weighted-sum function of peak temperature at the heating surface and the global pressure drop, will be examined. It illustrates the evolution of heat sink geometry, flow channel configuration, and temperature distributions at the heating surface for three different optimizations. The results of the optimal heat sinks will be compared and evaluated in terms of different performance indicators. The results show that the proposed GATO method is effective and robust in handling complex objective functions. However, minimizing global performance indicators such as RMSD or Po/Nu may not necessarily result in lower peak temperatures or pressure drops. Minimizing the weighted-sum objective function that considers both the peak temperature and pressure drop not only achieves lower peak temperatures and pressure drops but also results in higher Nusselt numbers and lower Poiseuille numbers than other objective functions.

Keywords of the Chapter:

Objective functions, Weighted-sum objective function, Thermo-hydraulic performance, GATO

6.1 Introduction

In the literature on TO for heat exchangers and heat sinks, the objective functions are mainly focused on thermal and/or hydrodynamic performance. Therefore, the commonly used objective functions can be broadly classified into those that indicate thermal performance and those that indicate hydrodynamic performance. Objective functions that reflect thermal performance mainly include the average temperature of a heating surface or solid parts of heat sinks, exchanged heat, thermal resistance, temperature rise, temperature difference, root mean square temperature, heat transfer rate, thermal compliance, recoverable thermal power, maximum temperature, and heat dissipation. Objective functions that embody hydrodynamic performance include pressure drop and energy dissipation. According to the review paper [131], Figure 6.1 summarizes the objective functions used in 86 articles on TO for heat exchangers and heat sinks. From the statistical data of Figure 6.1 (a), the objective functions of average temperature, exchanged heat, and pressure drop are preferred. Moreover, most articles (55%) focus on optimizing thermal performance using a single objective function, while a significant portion (40%) consider both thermal and hydrodynamic performance using a duo-objective function. Only a small number of studies (5%) use a triple-objective function, which not only considers thermal performance but also includes multiple indicators such as average temperature and temperature difference.

Chapter 4 presents a GATO approach and conducts various parameter studies using a single objective function (maximizing peak temperature at the heating surface) while maintaining a stable void fraction of fluid and ensuring connectivity when generating new individuals during optimization. The peak temperature at the heating surface is a crucial criterion for the thermal performance of a heat sink, as it ensures that the electronics can function properly. However, using only the maximum temperature value as a single point data only provides local information about the entire heating surface, it is important to consider global statistical values such as mean and standard deviation. Additionally, optimizing only for thermal performance may not be sufficient for the overall design of a heat sink, as it also needs to consider hydraulic performance.

This chapter aims to fill the gaps in previous studies by choosing the Root Mean Square Deviation (RMSD) of the temperature field at the heating surface as an additional objective function. This considers the entire temperature field instead of just a single point of data. The optimization will also include a multi-objective function that takes into account both hydrodynamic and thermal performance using the ratio between the Poiseuille number (Po) and Nusselt number (Nu). Additionally, an objective function that combines normalized peak temperature and normalized pressure drop will be minimized using weighting factors. The results of these optimizations will be compared and evaluated.

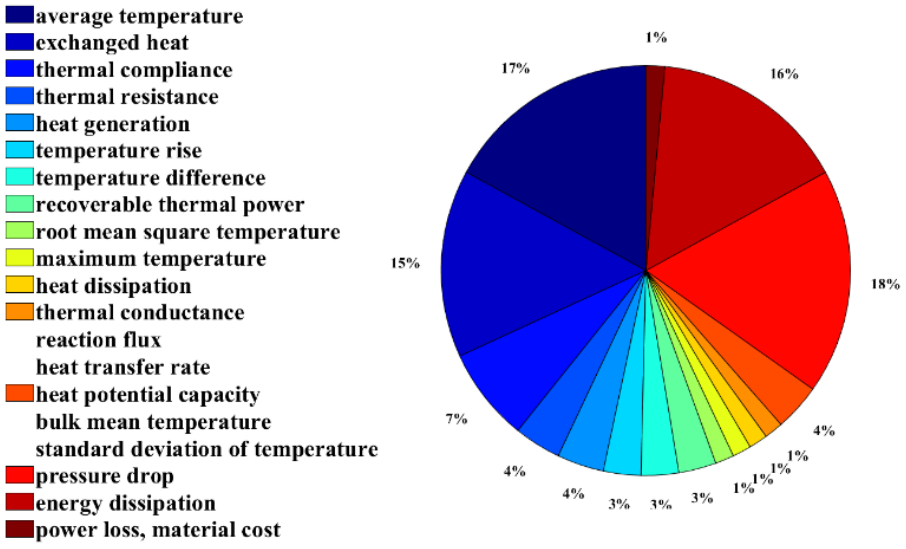

Figure 6.1 (a) The percentage of objective functions used in the TO heat changers (b) and the percentage of the objective number concerned in one TO of heat exchangers.

It's worth noting that the boundary conditions and constraints used in this chapter's optimization are the same as the benchmark case presented in section 4.3.1.

6.2 Root mean square deviation (RMSD) minimization

Temperature uniformity at the heating surface is a very important criterion for heat sink thermal performance. It reflects the uneven heating degree of the heated surface of an electronic. In the literature, the applied objective functions indicating temperature uniformity are the temperature difference and root mean square temperature. Here, the RMSD of a normalized temperature would be considered an objective function as described as follows:

$$f_{oj1} = RMSD_{T^*} = \sqrt{\frac{\sum_1^{P_{tot}} (T^*)^2}{P_{tot}}} \tag{6.1}$$

Where P_{tot} and T^* are the total number of cells/points of the heat sink heating surface in CFD mesh, and the normalized temperature is defined by the equation (4.13) in Chapter 4.

The minimization of $RMSD_{T^*}$ not only considers the temperature uniformity of the heating surface but also tends to optimize the temperature of all the cells towards the inlet temperature (based on the definition of T^*). After 172 iterations, the optimization of minimizing $RMSD_{T^*}$ has been converged based on the convergence criterion (Eq. 4.4) and its convergence history is presented in the following Figure 6.2, i.e., the value of $RMSD_{T^*}$decreases from 1.052 to 0.899.

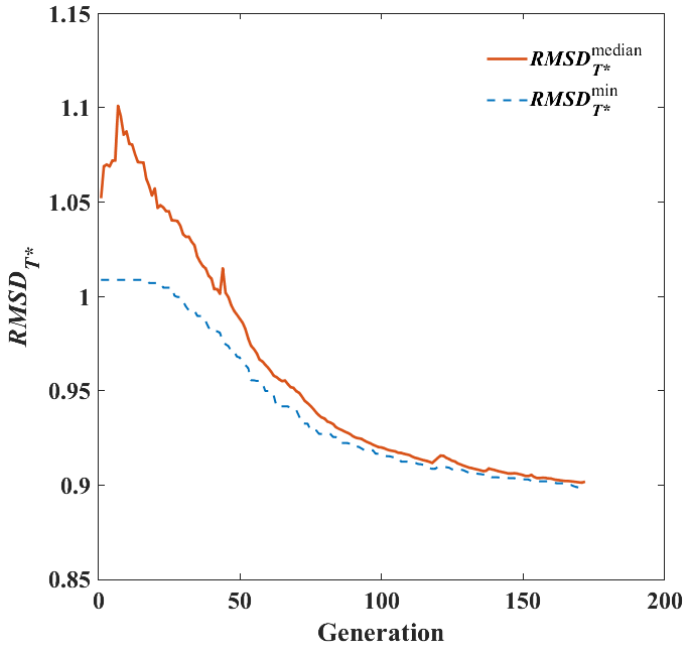

Figure 6.2 Iteration curve and the evolution of minimum value in every generation for $RMSD_{T^*}$ minimization.

More details on the geometry, velocity field, and temperature distribution evolution in the iterative process are presented in Figure 6.3. The most evident evolution in the temperature distribution along with the iteration is that the surface area between $0.85<T^*<1.08$ (in green) becomes larger and occupies the largest area in the heating surface. The objective of minimizing $RMSD_{T^*}$ tends to decrease the temperature in every cell of the heating surface with the same weighting factor to the target value ($T_{f,in}$=293 K). For this purpose, the main flow paths during iteration in Figure 6.3 (b) are formed to guide the inlet flow firstly to the side where the lower heat flux peak is located to ensure a lower temperature area, which is easier to realize because the location of lower heat flux peak is near the inlet, and then the main flow with a higher temperature than inlet temperature goes to the location of temperature hot spot to cool the highest temperature, which explains the existence of temperature hot spot. In general, this indicates that the GATO approach is effective in obtaining an optimal TO geometry for the minimization of $RMSD_{T^*}$.

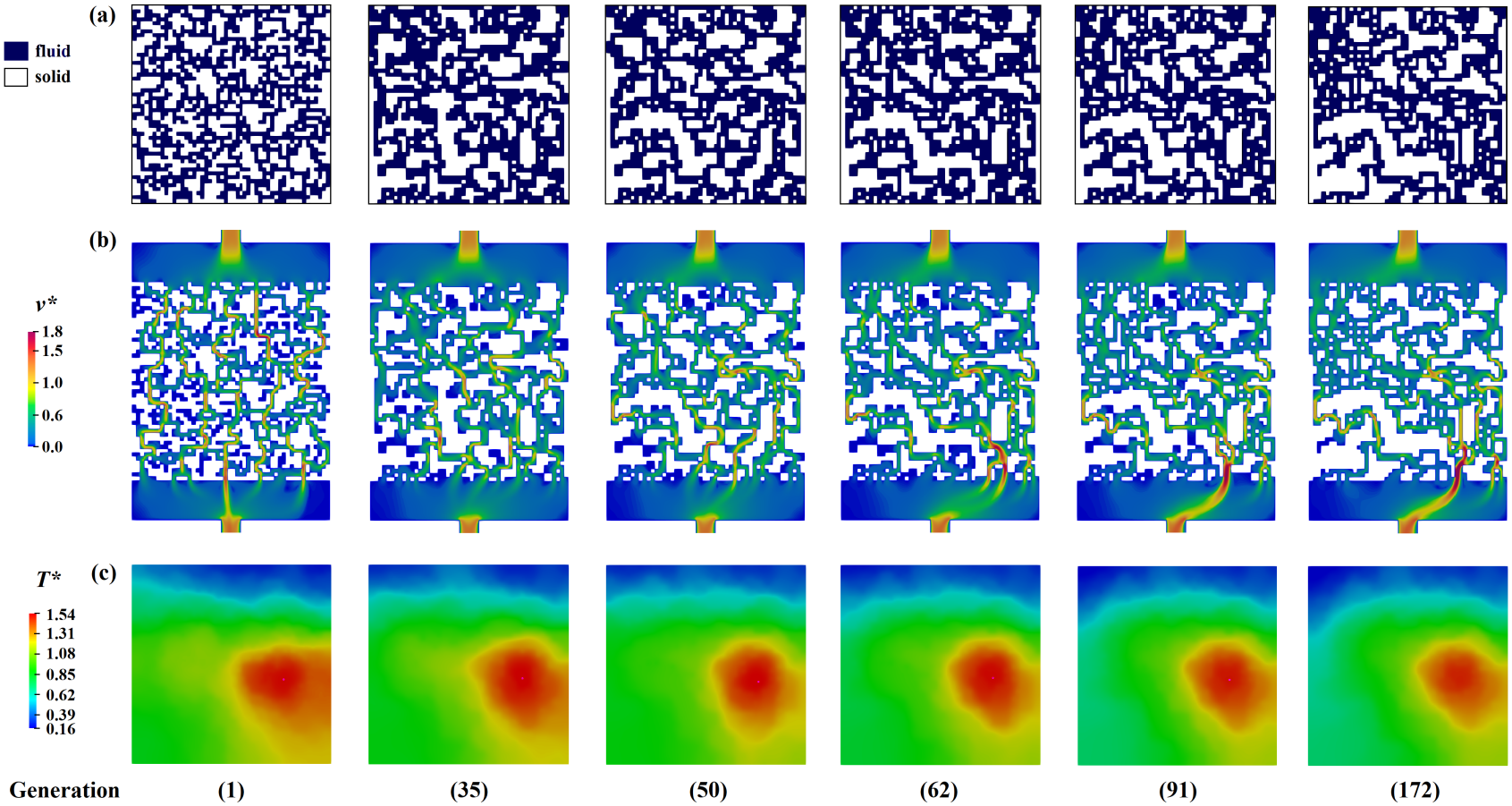

Figure 6.3 Top-ranked flow path configuration for $RMSD_{T^*}$ minimization at generation 1, 35, 50, 62, 91, and 172. (a) Fluid/solid elements distribution in the design domain; (b) Corresponding velocity field at mid-channel depth; (c) Temperature field at the heating surface.

6.3 *Po*/*Nu* minimization

In addition to thermal performance, it is important to evaluate the hydrodynamic performance of a heat sink. Two non-dimensional indicators, the *Po* number, and *Nu* number evaluate hydrodynamic and thermal performance through friction factor and convective heat transfer coefficient. Therefore, in this section, the *Po/Nu* ratio (Eq. 6.2) will be used as the objective function in this optimization. The expressions of *Nu* number and *Po* number are presented as Eq.4.6 in Chapter 4 and Eq.5.10 in Chapter 5.

$$f_{oj2} = \frac{Po}{Nu} \tag{6.2}$$

It should be noted that the *Po* number and the *Nu* number are calculated based on some global parameters, such as the global hydraulic diameter, the area-weighted average temperature at the solid and fluid interface, etc. It may not affect much on a local value, like peak temperature. It took 151 iterations to achieve the convergence recorded in Figure 6.4. The value of *Po*/*Nu* reduces from 17.23 to 5.25.

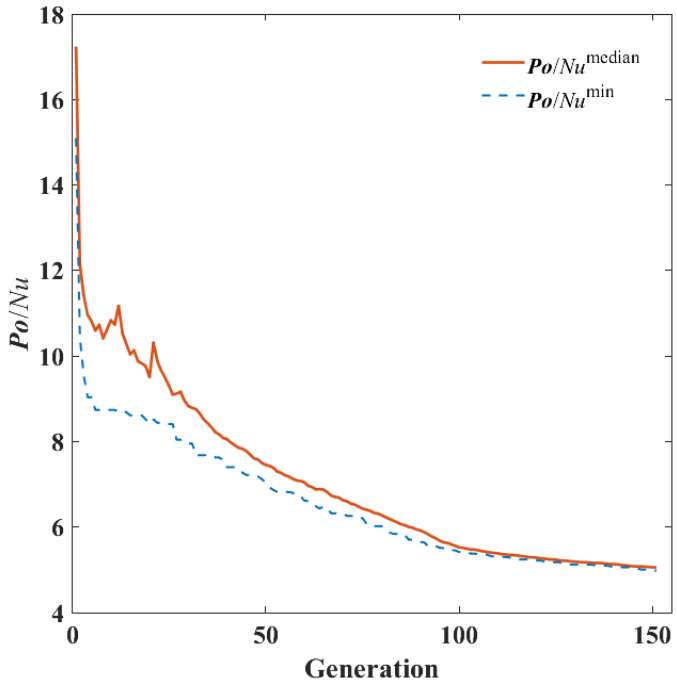

Figure 6.4 Iteration curve and the evolution of minimum value in every generation for *Po*/*Nu* minimization.

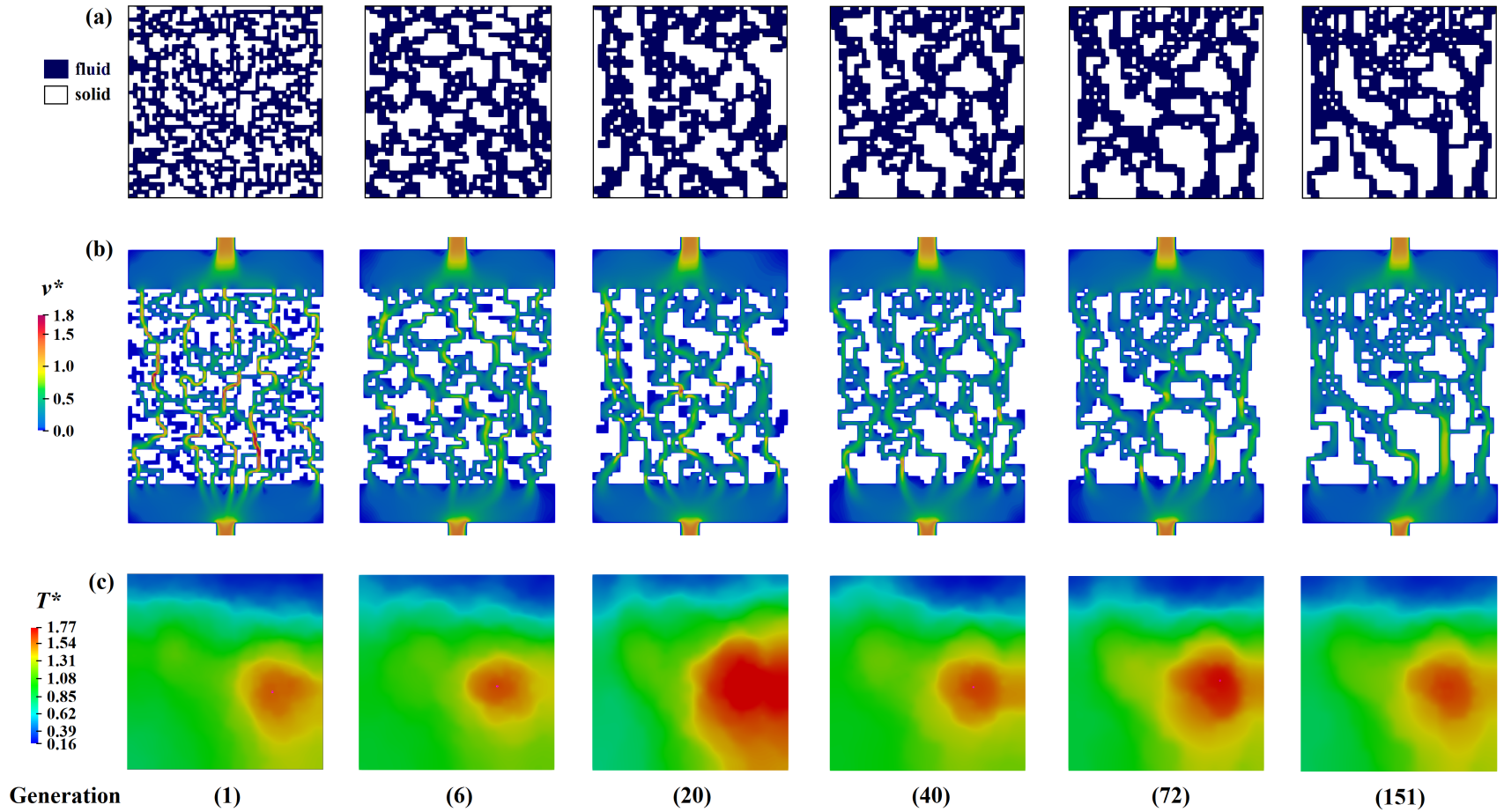

Figure 6.5 Top-ranked flow path configuration for *Po*/*Nu* minimization at generation 1, 6, 20, 40, 72, and 151. (a) Fluid/solid elements distribution in the design domain; (b) Corresponding velocity field at mid-channel depth; (c) Temperature field at the heating surface.

Figure 6.5 records the optimization progress of top-ranked flow path configuration, velocity field at mid-channel depth, and temperature distribution at the heating surface of generation for 1, 6, 20, 40, 72, and 151. Minimizing *Po*/*Nu* aims to decrease pressure drop and increase the heat transfer coefficient. This is related to the area-weighted average temperature of fluid and solid interface, and the global hydraulic diameter of the heat sink design area. With a constant void fraction (0.50), a higher *Nu* number is achieved by a shorter wetted perimeter and a lower solid-fluid wall area-weighted average temperature. Thus, the optimal geometry in Figure 6.5 (a) would have larger solid islands, indicating a shorter wetted perimeter.

6.4 Weighted-sum objective function of peak temperature and pressure drop

In this section, the objective function is a combination of important thermal performance indicator, the peak temperature at the heating surface (in normalized form), and the normalized pressure drop, as expressed below:

$$f_{oj3} = \omega_1 T^*_{peak} + \omega_2 P^* \tag{6.3}$$

Where ω_1 and ω_2 are two weighting factors that indicate the importance of the optimized objective. Here $\omega_1 = \omega_2 = 0.5$ shows the equal importance of the two indicators. The optimization has converged after 222 iterations as shown in Figure 6.6. The best result in 100 individuals of objective decreases from 1.91 to 1.26. The actual peak temperature decreased from 358.6 K to 350.3 K, and the pressure drop reduce from 240.05 Pa to 132.85 Pa.

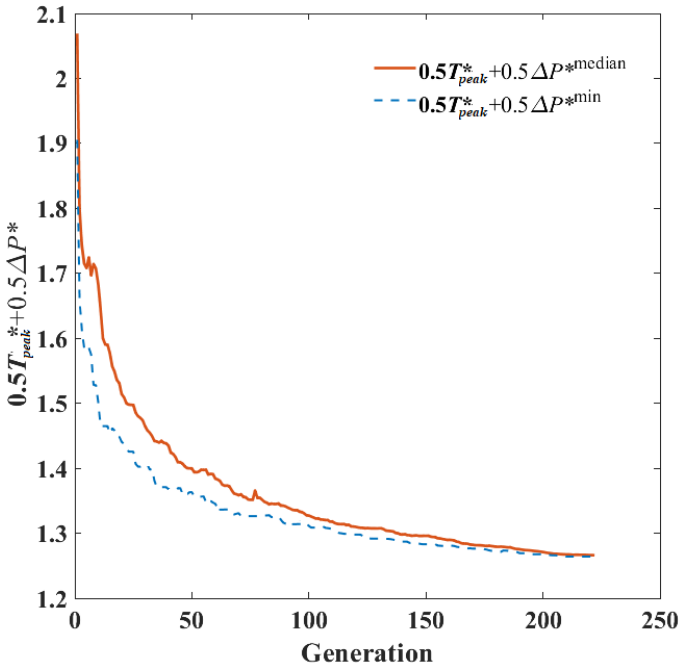

Figure 6.6 Iteration curve and the evolution of minimum value for $0.5T^*_{peak} + 0.5P^*$ minimization.

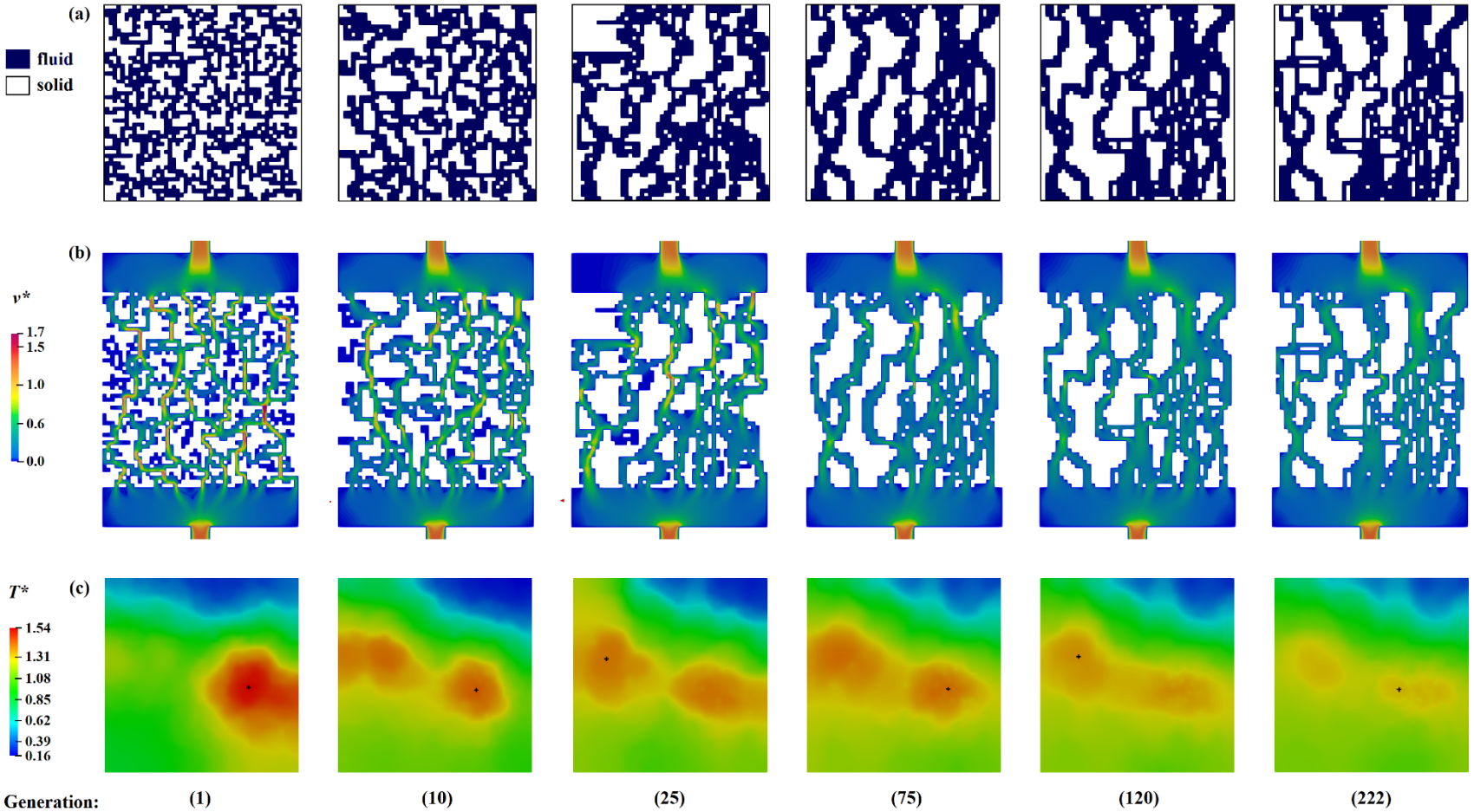

Figure 6.7 Top-ranked flow path configuration for peak temperature and pressure drop minimization at generation 1, 10, 25, 75, 120, and 222. (a) Fluid/solid elements distribution in the design domain; (b) Corresponding velocity field at mid-channel depth; (c) Temperature field at the heating surface.

Figure 6.7 presents the evolution of the geometries, velocity fields at the mid-depth of fluid domains, and temperature contours at the heating surfaces of top-ranked individuals in generations 1, 10, 25, 75, 120, and 222. From the temperature contour of generation 1 to generation 10, the hot spot has diverged into two hot spots with lower temperatures and the maximum temperature point keeps on the same side. Not until generation 25, the maximum temperature point moves to the other side where the lower heat flux peak is located, and the global fluid paths have been formed. More fluid elements are arranged on the right side where the highest heat flux peak exists. Compared with the flow paths in generation 75, more horizontal flow paths are generated in the TO geometries of generation 120 and 222 due to the objective of minimizing the peak temperature. But compared to the benchmark case (section 4.3.1) for minimizing only the T^*_{peak}, fewer transversal flow paths are generated in this current due to considering the pressure drop at the same time.

6.5 Comparison of optimizations of different objectives

Figure 6.8 records all the pressure drop and peak temperature values of individuals in 222 generations in $0.5T^*_{peak} + 0.5P^*$ minimization, with color change indicating the evolutionary direction of GA. The optimal choices based on other objective functions are also plotted for comparison. It can be observed that with the increase of GA generation, the color changes from blue to red, forming a sharp corner that points in the direction of lower pressure drop and temperature. This indicates that the GATO could satisfy both the minimization of temperature and pressure drop (the yellow point) at the same time. The green point in Figure 6.8 is the optimal point for minimizing only the T^*_{peak} at the heating surface (benchmark case in chapter 4). It is evident that the peak temperature of this optimal point is the lowest compared to others, but at the cost of a higher pressure drop. It is reasonable because there is no constraint of pressure drop when performing T^*_{peak} minimization. The temperature difference between the green and yellow points is not so high (about 1.5 K), which indicates that the objective function considering both peak temperature and pressure drop would reach a low temperature close to the single objective optimization of minimization of only the peak temperature.

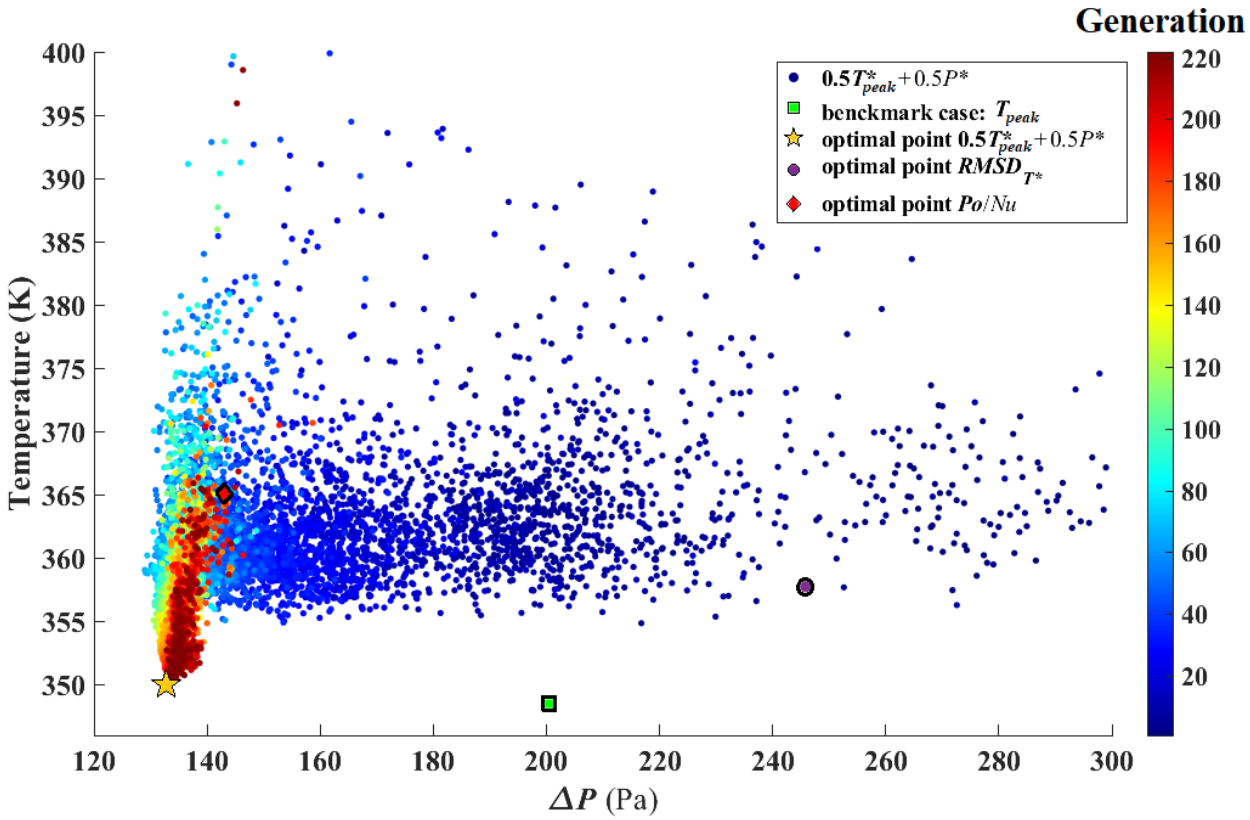

Figure 6.8 The temperature and pressure drop plot of all the calculated individuals in $0.5T^*_{peak} + 0.5P^*$ minimization optimization (blue points), the optimal points of minimization of $0.5T^*_{peak} + 0.5P^*$ (yellow point), $RMSD_{T^*}$ (purple point), Po/Nu (redpoint), and T_{peak} (benchmark case in Chapter 4) (green point).

Since the objectives of $RMSD_{T^*}$ (purple point) and Po/Nu (redpoint) are global or averaged values, it is difficult to observe from the indicator of peak temperature. As for the pressure drop for the optimal point of Po/Nu, it can be seen that the optimal point of Po/Nu can reach a low-pressure drop than both green and purple points. Nevertheless, the T_{peak} value achieved with this optimization objective function is the highest.

Table 6.1 presents different performance indicators for optimal heat sinks based on various optimization objectives. It is obvious that when the indicator is the optimization objective itself, the indicator reaches its minimum value. This again reflects the effectiveness and robustness of the GATO approach developed in this study, which can handle different and complicated optimization problems. From the table, we may see, as an objective indicating the global performance, the minimization of f_{oj2} (Po/Nu) brings the largest Nu and a rather low Po. And minimization of f_{oj1} ($RMSD_{T^*}$) can bring neither a lower peak temperature nor a lower pressure drop. The weighted-sum objective function like f_{oj3}, which would bring both lower peak temperature and pressure drop, at the same time have better Nu and Po numbers than those of the single objective of T^*_{peak} minimization. In real practice, it should be a good choice as an optimization objective function with adjustable values of ω_1 and ω_2.

Table 6.1 Different indicators of optimal heat sinks based on various optimization objectives

	T^*_{peak}	P^*	Nu	Po	$RMSD_{T^*}$
T_{peak} (Benchmark in Chapter 4)	1.28	1.82	5.7	62.7	1,042
$f_{oj1} = RMSD_{T^*}$	1.49	2.23	8.1	66.5	0.899
$f_{oj2} = \frac{Po}{Nu}$	1.66	1.30	9.6	51.0	1.048
$f_{oj3} = \omega_1 T^*_{peak} + \omega_2 P^*$	1.31	1.21	6.5	50.4	1.075

6.5 Conclusions

In this chapter, the minimization of three objectives: $f_{oj1} = RMSD_{T^*}$, $f_{oj2} = \frac{Po}{Nu}$ and $f_{oj3} = \omega_1 T^*_{peak} + \omega_2 P^*$ has been performed. The evolution of TO heat sink geometry, fluid flow configuration, and temperature distributions at the heating surface of three optimizations are shown. All the heat sink performance indicators of the obtained optimal TO heat sinks are presented and compared. The main conclusions can be drawn as follows:

- The GATO approach is robust and effective to solve the optimization problem with the complicated expression of objective functions;
- Minimizing an objective function indicating the global performance of a heat sink, like f_{oj1} and f_{oj2} may give neither a lower peak temperature nor a lower pressure drop.
- The optimization of f_{oj3} brought both a lower temperature and a lower pressure drop with better *Nu* and *Po* numbers than optimizing an objective function only considering the peak temperature.

Furthermore, to well combine the physic law with GATO approach, the minimization of the local entropy generation for a better heat transfer enhancement could be performed in the future study, which is also practical by applying this GATO method.

Chapter 7: General conclusions and perspectives

7.1 Conclusions

This thesis focuses on the design and optimization of high-performance heat sinks for effective convective cooling of a heat-generating surface with multiple-peak heat flux. A size optimization approach based on conventional straight channel heat sink optimization and a genetic algorithm-based topology optimization (GATO) approach have been developed, tested, and compared. Experimental validations of the optimized numerical models have been performed. The influence of different objective functions for the GATO approach has been studied. The main conclusions of each chapter could be drawn as follows:

In **chapter 2**, a survey on electronics indicates that non-uniform multiple heat sources widely exist in electronics. Under this circumstance, overheating issues slowing down the working efficiency, irreversible deterioration, and reduction of the electronics in a lifetime turn more serious. Among various thermal management methods, single-phase liquid cooling using heat sinks is found to be a compact, simple, low-cost, and safer solution. Geometry optimization of heat sinks has been intensively attempted to improve their performance. For a conventional straight channel heat sink, no research has systematically studied the optimal (tailored) flow distribution inside a heat sink under uneven heating conditions for thermal performance improvement. For a TO heat sink, most topology approaches are based on gradient methods, which might be easily trapped into a local optimum and have difficulties to define the fluid-solid interface. Only a few researchers experimentally test TO heat sinks; no research so far has measured the temperature distribution of the cooling fluid inside the TO heat sinks.

In **chapter 3**, based on a conventional parallel straight mini-channel heat sink (RSC) subjected to a non-uniform multiple-peak heat flux, a size optimization method has been developed to adjust the channel inlet widths. The flow distribution among the parallel channels could thereby be optimized to minimize the peak temperature (T_{peak}) on the heating surface. It was found that the proposed size optimization method was able to reduce the T_{peak} by 10 K under an area-weighted average heat flux of 38.75 $W \cdot cm^{-2}$ in the two-peak heat flux case. The heat sink configuration featuring optimized channel inlets (OSC) consistently demonstrated lower thermal resistance compared to the RSC heat sink under various average heat flux and total mass flow rate conditions. Furthermore, at the same pressure drop, optimizing the flow distribution of the cooling fluid was found to be more effective in reducing the thermal resistance than simply increasing the mass flow rate of the cooling liquid. The effectiveness and robustness of the optimization algorithm were demonstrated when the average heat flux varied within a certain range.

In **chapter 4**, the GATO method has been developed and tested to determine the optimal global flow channel configuration of a heat sink, again under a non-uniform heating surface with multiple heat sources. The optimization objective is to minimize the peak temperature at

the heating surface (T_{peak}) under the constraint of a constant void fraction in the fully-connected fluid domain. The proposed GATO method was able to successfully determine the optimal spatial distribution of the fluid/solid elements in the design domain. The optimized flow configurations were found to depend strongly on the values of the design and operating parameters. Robustness and reproducibility tests also showed that the GATO method can produce many "close-to-the-optima" solutions due to the insensitivity of the objective function to the global optimum at the fixed stopping criterion. Compared to conventional RSC heat sinks, GATO heat sinks consistently showed better thermal performance, as indicated by higher *Nu* numbers, lower R_{th} values, and better temperature uniformity at the heating surface. However, these improvements came at the cost of a higher pressure drop. Increasing the matrix resolution of the design area resulted in a lower T_{peak} at convergence due to the generation of finer and more complex structures at the local level. But this requires higher computational resources and sets higher requirements on the fabrication technology for its realization.

In **chapter 5**, RSC, OSC, and GATO heat sinks have been tested both experimentally and numerically. The velocity fields obtained by PIV measurement for the RSC prototype have been compared with the CFD calculation for laminar flow model validation. The temperature fields at the fluid-solid interface, obtained by IR measurements, have also been compared with the CFD calculation results, showing good agreement between each other. The GATO heat sink provided smaller areas of temperature hotspots and better temperature uniformity than RSC and OSC heat sinks at both the fluid-solid interface and the heating surface. GATO heat sink has shown at least 49.6% and 40.6% higher *Nu* numbers than that of the RSC and OSC heat sinks under a wide range of inlet *Re* numbers, and more significant performance improvement could be achieved under different input powers. The GATO heat sink has shown the lowest *Po*/*Nu* ratio within the testing input power and *Re* number range, more than 12% and 7.1% lower than those of RSC and OSC heat sinks.

In **chapter 6**, various objective functions ($RMSD_{T^*}$, *Po/Nu* and $\omega_1 T^*_{peak} + \omega_2 P^*$) have been introduced to the GATO approach. The thermal and hydraulic performances of the obtained optimal TO heat sinks are presented and compared. The GATO approach has shown its robustness and effectiveness in handling complicated expressions of objective functions. The optimization by minimizing a weighted sum of $\omega_1 T^*_{peak} + \omega_2 P^*$ could be brought both a lower temperature and a lower pressure drop with better *Nu* and *Po* numbers than optimizing an objective function only considering the peak temperature.

7.2 Perspectives

The newly proposed GATO approach has been first developed in this thesis, therefore, there are still lots of details that can be improved. Due to the limitation of computational resources, the proposed method hasn't been put into some extension usage during the thesis. Based on the results obtained in this thesis, several perspectives are proposed for short term or for long run:

The future works in the short term:

- **The way to create new generations**

In this thesis, the necessary condition to generate a new individual is that the new individual resulting from the cross-over operation should have only one connectivity of all fluid elements, which would neglect a large number of diverse individuals. A method to improve this disadvantage is that first allow the creation of a binary matrix with more than one connectivity after cross-over, and then, replace the solid islands of less solid elements with fluid elements.

- **The GA parameter study**

To save time, the GA parameters in this thesis are referred to by other articles with similar optimization cases. The GA optimizations are different, and their parameters should be studied and defined before applying the approach on obtaining better optimal results or saving computation time. The parameters mentioned here include the individual number in one generation, the point number of cross-over, the probability of vertical and horizontal cross-over and mutation rate, the number of elite-keeping individuals, etc.

- **The post-processing of TO geometries with a filter**

Since the topological geometries are built based on binary matrices, the 90° corners of square-shaped fluid/solid elements are unavoidable. Therefore, for better looking and smoother boundaries to decrease pressure drop of the topological geometries. The solution could be a filter or an intermediate step between fluid and solid during the optimization process for the optimal geometry as a post-processing procedure.

- **The automation of the whole process**

In this study, the scripts to run GATO is coded in Matlab, which is commercial software. Therefore, it could not be applied in this HPC (CCIPL). As a result, the computation time is about two to three weeks for one optimization. While, this is not necessary if applying a script from an open-source software like python, it would cost about three days to complete a GATO case. Still, the time could be decreased if there are more cores and nodes available in an HPC.

- **GATO without the constraint of the constant void fraction**

All the previous GATOs were performed under the constraint of the constant void fraction during optimization. However, from the parameter study of void fraction, it was found that there was a lowest T_{peak} at certain void fraction and Φ=1.0 will not lead to the best result. Therefore, a void fraction-free optimization could be concerned to explore the optimal void fraction to obtain the lowest T_{peak} at a global level.

- **The improvement of straight channel size optimization on the optimization constrain and objective function**

In chapter 3, the channel inlets were optimized under the constraint of the constant inlet porosity. Nevertheless, if this constraint has been released, the optimal result could be better. Furthermore, the work of the multi-objective thermal-hydrodynamic performance can be also performed for the optimization of the inlet/outlet or header manifolds of a straight channel heat sink.

The future works in the long run:

- **The extension of 3-D optimization with the GATO approach**

To simplify the model and due to the limitation of computation resources, the TOs in this thesis are performed based on a 2-D matrix. However, when increasing the thickness of the fluid domain in a heat sink, the geometry variation in the z direction cannot be ignored in optimization. Therefore, the 3-D TO should be applied in this case.

- **Turbulence flow with the GATO approach**

The CFD model applied in this thesis for the TO heat sink is under a laminar region. In reality, to achieve a better performance, turbulence flow can be encountered. Therefore, the interest of future work could be the TO heat sink with turbulent flow, which would be more difficult to choose a suitable turbulence model to capture in such complicated TO geometry, and with a more refined mesh, it will be a more time-consuming task.

- **Two fluid flows exchanger**

Unlike a single fluid heat sink, two or multiple fluids flows exchanger transfer the heat from one fluid to the other/another. The solid geometry separating two fluids plays an important role in heat transfer efficiency. The proposed GATO approach in this thesis could be a good choice to optimize the geometry of the exchanger.

- **Machine learning enhanced GATO**

A huge amount of computation time could be saved if machine learning (ML) is applied. The optimal TO geometries obtained in this study could be used as the training database for the ML optimizer. Suitable geometries (matrix) are expected to be proposed by the ML optimizer for varied boundary conditions such as heat flux, inlet mass flow rate etc.

- **Comparison of gradient-based TO with GATO by experimental and numerical study**

To compare the performance of heat sinks optimized by gradient-based and non-gradient-based TO approaches, experimental and numerical studies could be conducted in the future. Firstly, numerical optimizations using both approaches would need to be performed under the same objective, constraints and boundary conditions. Following this, the optimized heat sinks should be fabricated and tested under identical conditions. Finally, the performance of both heat sinks could be calculated and compared.

- **IR thermography of all the fluid-solid interface**

In this thesis, we only measured one fluid-solid interface's temperature. In the future, a heat sink could be fabricated with Infrared transparent material to measure the entire fluid-solid interface's temperature to obtain more global thermal information about the heat sink by IR camera.

List of references

[1] G.E. Moore, Cramming more components onto integrated circuits, Reprinted from Electronics, volume 38, number 8, April 19, 1965, pp.114 ff., IEEE Solid-State Circuits Soc. Newsl. 11 (2006) 33–35. https://doi.org/10.1109/N-SSC.2006.4785860.

[2] Z. Zhang, X. Wang, Y. Yan, A review of the state-of-the-art in electronic cooling, E-Prime. (2021) 100009. https://doi.org/10.1016/j.prime.2021.100009.

[3] S. Zeng, B. Kanargi, P.S. Lee, Experimental and numerical investigation of a mini channel forced air heat sink designed by topology optimization, Int. J. Heat Mass Transf. 121 (2018) 663–679. https://doi.org/10.1016/j.ijheatmasstransfer.2018.01.039.

[4] M. Wei, Y. Fan, L. Luo, G. Flamant, CFD-based evolutionary algorithm for the realization of target fluid flow distribution among parallel channels, Chem. Eng. Res. Des. 100 (2015) 341–352. https://doi.org/10.1016/j.cherd.2015.05.031.

[5] M. Wei, Y. Fan, L. Luo, G. Flamant, Design and optimization of baffled fluid distributor for realizing target flow distribution in a tubular solar receiver, Energy. (2015). https://doi.org/10.1016/j.energy.2016.04.016.

[6] R. Boichot, L. Wang, L. Luo, Y. Fan, Cellular automaton methods for heat and mass transfer intensification, 2013. https://doi.org/10.1007/978-1-4471-4742-8_6.

[7] R. Boichot, Y. Fan, A genetic algorithm for topology optimization of area-to-point heat conduction problem, Int. J. Therm. Sci. 108 (2016) 209–217. https://doi.org/10.1016/j.ijthermalsci.2016.05.015.

[8] S. Basu, K.S. Hariharan, S.M. Kolake, T. Song, D.K. Sohn, T. Yeo, Coupled electrochemical thermal modelling of a novel Li-ion battery pack thermal management system, Appl. Energy. 181 (2016) 1–13. https://doi.org/10.1016/j.apenergy.2016.08.049.

[9] Z. Shang, H. Qi, X. Liu, C. Ouyang, Y. Wang, Structural optimization of lithium-ion battery for improving thermal performance based on a liquid cooling system, Int. J. Heat Mass Transf. 130 (2019) 33–41. https://doi.org/10.1016/j.ijheatmasstransfer.2018.10.074.

[10] S. Goutam, A. Nikolian, J. Jaguemont, J. Smekens, N. Omar, P. Van Dan Bossche, J. Van Mierlo, Three-dimensional electro-thermal model of li-ion pouch cell: Analysis and comparison of cell design factors and model assumptions, Appl. Therm. Eng. 126 (2017) 796–808. https://doi.org/10.1016/j.applthermaleng.2017.07.206.

[11] S. Ma, M. Jiang, P. Tao, C. Song, J. Wu, J. Wang, T. Deng, W. Shang, Temperature effect and thermal impact in lithium-ion batteries: A review, Prog. Nat. Sci. Mater. Int. 28 (2018) 653–666. https://doi.org/10.1016/j.pnsc.2018.11.002.

[12] G. M. Ehrlich, Handbook of Batteries, 3rd ed., McGraw-Hill, New York, 2002.

[13] issues that Lithium-ion battery under overheating, (n.d.). https://news.asu.edu/20171227-solutions-asu-expert-lithium-ion-battery-overheating-danger#:~:text=A%3A When a LIB overheats,more heat and gaseous products.

[14] R. Zhao, Overheating Prediction and Management of Lithium-Ion Batteries, Carleton University, 2018. https://doi.org/10.22215/etd/2018-13187.

[15] What happens when lithium-ion batteries overheat and explode, (n.d.). https://www.ucl.ac.uk/chemical-engineering/news/2015/apr/what-happens-when-lithium-ion-batteries-overheat-and-explode.

[16] Y. Tang, Y. Luo, P. Du, H. Wang, H. Ma, Y. Qin, P. Bai, G. Zhou, Experimental investigation on active heat sink with heat pipe assistance for high-power automotive LED headlights, Case Stud. Therm. Eng. 28 (2021) 101503. https://doi.org/10.1016/j.csite.2021.101503.

[17] E.Y. Gatapova, G. Sahu, S. Khandekar, R. Hu, Thermal management of high-power LED module with single-phase liquid jet array, Appl. Therm. Eng. 184 (2021) 116270. https://doi.org/10.1016/j.applthermaleng.2020.116270.

[18] X. Zhang, R.-C. Li, Q. Zheng, Analysis and simulation of high-power LED array with microchannel heat sink, Adv. Manuf. 1 (2013) 191–195. https://doi.org/10.1007/s40436-013-0027-0.

[19] J. Hu, L. Yang, M. Whan Shin, Mechanism and thermal effect of delamination in light-emitting diode

packages, Microelectronics J. 38 (2007) 157–163. https://doi.org/10.1016/j.mejo.2006.08.001.

[20] LED temperature limit, (n.d.). https://ledlightsunlimited.net/2020/09/15/effects-of-temperature-on-led-lights/.

[21] Bimal K. Bose, Power Electronics and Variable Frequency Drives: Technology and Applications, Wiley-IEEE Press, New York, 1997. https://ieeexplore.ieee.org/servlet/opac?bknumber=5263964.

[22] U. Schlapbach, M. Rahimo, C. von Arx, A. Mukhitdinov, S. Linder, 1200V IGBTs operating at 200°C? An investigation on the potentials and the design constraints, in: Proc. 19th Int. Symp. Power Semicond. Devices IC's, IEEE, 2007: pp. 9–12. https://doi.org/10.1109/ISPSD.2007.4294919.

[23] Z. Hu, X. Ge, D. Xie, Y. Zhang, B. Yao, J. Dai, F. Yang, An Aging-Degree Evaluation Method for IGBT Bond Wire with Online Multivariate Monitoring, Energies. 12 (2019) 3962. https://doi.org/10.3390/en12203962.

[24] N. An, M. Du, Z. Hu, K. Wei, A High-Precision Adaptive Thermal Network Model for Monitoring of Temperature Variations in Insulated Gate Bipolar Transistor (IGBT) Modules, Energies. 11 (2018) 595. https://doi.org/10.3390/en11030595.

[25] A. Yahyaee, A. Bahman, F. Blaabjerg, A Modification of Offset Strip Fin Heatsink with High-Performance Cooling for IGBT Modules, Appl. Sci. 10 (2020) 1112. https://doi.org/10.3390/app10031112.

[26] U.-M. Choi, F. Blaabjerg, K.-B. Lee, Study and Handling Methods of Power IGBT Module Failures in Power Electronic Converter Systems, IEEE Trans. Power Electron. 30 (2015) 2517–2533. https://doi.org/10.1109/TPEL.2014.2373390.

[27] X.Z. Qiu, G.R. Zhang, W.J. Chen, T. Yu, X.M. Hou, Q.Z. Zhang, G.Q. Xu, Review of IGBT Junction Temperature Extraction and Estimation Methods, IOP Conf. Ser. Mater. Sci. Eng. 774 (2020) 012091. https://doi.org/10.1088/1757-899X/774/1/012091.

[28] J. Wei, Challenges in cooling design of CPU packages for high-performance servers, in: Heat Transf. Eng., 2008: pp. 178–187. https://doi.org/10.1080/01457630701686727.

[29] R. Mahajan, Chia-pin Chiu, G. Chrysler, Cooling a Microprocessor Chip, Proc. IEEE. 94 (2006) 1476–1486. https://doi.org/10.1109/JPROC.2006.879800.

[30] Thomas Brunschwiler, Interlayer thermal management of high-performance microprocessor chip stacks, 1. Aufl, Cuvillier, Göttingen, 2012.

[31] E. Beyne, C.J.M. Lasance, J. Berghmans, eds., Thermal Management of Electronic Systems II, Springer Netherlands, Dordrecht, 1997. https://doi.org/10.1007/978-94-011-5506-9.

[32] What is the safe CPU temperature range?, (n.d.). https://levvvel.com/what-is-the-safe-cpu-temperature-range/.

[33] V. Manoj Siva, A. Pattamatta, S.K. Das, Effect of flow maldistribution on the thermal performance of parallel microchannel cooling systems, Int. J. Heat Mass Transf. 73 (2014) 424–428. https://doi.org/10.1016/j.ijheatmasstransfer.2014.02.017.

[34] CPU temperture limit, (n.d.). https://www.pcgamer.com/cpu-temperature-overheat/#:~:text=Overclocking temperatures could in theory,°C at the most.

[35] IEA, Renewable electricity growth is accelerating faster than ever worldwide, supporting the emergence of the new global energy economy, (2021).

[36] M. Yamaguchi, F. Dimroth, J.F. Geisz, N.J. Ekins-Daukes, Multi-junction solar cells paving the way for super high-efficiency, J. Appl. Phys. 129 (2021) 240901. https://doi.org/10.1063/5.0048653.

[37] high-efficiency multi-junction solar cell has better performance, (n.d.). https://www.energy.gov/eere/solar/multijunction-iii-v-photovoltaics-research.

[38] S.P. Philipps, A.W. Bett, III-V Multi-junction solar cells and concentrating photovoltaic (CPV) systems, Adv. Opt. Technol. 3 (2014) 469–478. https://doi.org/10.1515/aot-2014-0051.

[39] A. Braun, B. Hirsch, A. Vossier, E.A. Katz, J.M. Gordon, Temperature dynamics of multijunction concentrator solar cells up to ultra-high irradiance, Prog. Photovoltaics Res. Appl. 21 (2013) 202–208. https://doi.org/10.1002/pip.1179.

[40] C. Min, C. Nuofu, Y. Xiaoli, W. Yu, B. Yiming, Z. Xingwang, Thermal analysis and test for single

concentrator solar cells, J. Semicond. 30 (2009) 044011. https://doi.org/10.1088/1674-4926/30/4/044011.

[41] extreme temperature for CPS, (n.d.). https://www.science.org.au/curious/technology-future/concentrating-solar-thermal.

[42] W.-C. Tan, K.-K. Chong, M.-H. Tan, Performance study of water-cooled multiple-channel heat sinks in the application of ultra-high concentrator photovoltaic system, Sol. Energy. 147 (2017) 314–327. https://doi.org/10.1016/j.solener.2017.03.040.

[43] M. V Pukhovoy, K.A. Kunts, S.E. Spesivtsev, O.A. Kabov, Maximum heat fluxes and features of heat transfer mechanisms with boiling during jet impingement cooling of electronics, J. Phys. Conf. Ser. 1867 (2021) 012036. https://doi.org/10.1088/1742-6596/1867/1/012036.

[44] I. Mudawar, Recent Advances in High-Flux, Two-Phase Thermal Management, in: Vol. 2 Heat Transf. Enhanc. Pract. Appl. Heat Mass Transf. Fire Combust. Heat Transf. Multiph. Syst. Heat Mass Transf. Biotechnol., American Society of Mechanical Engineers, 2013. https://doi.org/10.1115/HT2013-17046.

[45] J.S. Hyung Hee Cho, Kyung Min Kim, Applications of impingement jet cooling systems, Nova Science Publishers, Inc., 2011.

[46] J. Kim, Spray cooling heat transfer: The state of the art, Int. J. Heat Fluid Flow. 28 (2007) 753–767. https://doi.org/10.1016/j.ijheatfluidflow.2006.09.003.

[47] R. J., Multiphase Spray Cooling Technology in Industry, in: Adv. Technol., InTech, 2009. https://doi.org/10.5772/8217.

[48] C. Roe, X. Feng, G. White, R. Li, H. Wang, X. Rui, C. Li, F. Zhang, V. Null, M. Parkes, Y. Patel, Y. Wang, H. Wang, M. Ouyang, G. Offer, B. Wu, Immersion cooling for lithium-ion batteries – A review, J. Power Sources. 525 (2022) 231094. https://doi.org/10.1016/j.jpowsour.2022.231094.

[49] W. Wu, S. Wang, W. Wu, K. Chen, S. Hong, Y. Lai, A critical review of battery thermal performance and liquid based battery thermal management, Energy Convers. Manag. 182 (2019) 262–281. https://doi.org/10.1016/j.enconman.2018.12.051.

[50] Y. Deng, C. Feng, J. E, H. Zhu, J. Chen, M. Wen, H. Yin, Effects of different coolants and cooling strategies on the cooling performance of the power lithium ion battery system: A review, Appl. Therm. Eng. 142 (2018) 10–29. https://doi.org/10.1016/j.applthermaleng.2018.06.043.

[51] a fan, (n.d.). https://www.idcooling.com/Product/detail/id/318/name/SE-224-XTS.

[52] phase change cooling system, (n.d.). https://fr.wikipedia.org/wiki/Phase-change_cooling.

[53] phase change cooling shortcomings, (n.d.). https://www.grcooling.com/blog/two-phase-versus-single-phase-immersion-cooling/.

[54] Z. Duan, H. Ma, B. He, L. Su, X. Zhang, Pressure Drop of Microchannel Plate Fin Heat Sinks, Micromachines. 10 (2019) 80. https://doi.org/10.3390/mi10020080.

[55] pin-fin, (n.d.). https://premioinc.com/blogs/blog/what-makes-up-a-rugged-industrial-pc.

[56] A.A. Amoako, J.J. Doom, Optimization of heat sinks in a range of configurations, in: 2018 Jt. Thermophys. Heat Transf. Conf., American Institute of Aeronautics and Astronautics, Reston, Virginia, 2018. https://doi.org/10.2514/6.2018-2945.

[57] W. Khan, A., J. Culham, R., M. Yovanovich, M., The Role of Fin Geometry in Heat Sink Performance, J. Electron. Packag. 128 (2006) 324–330. https://doi.org/10.1115/1.2351896.

[58] C.H. Hoang, N. Fallahtafti, S. Rangarajan, A. Gharaibeh, Y. Hadad, C. Arvin, K. Sikka, S.N. Schiffres, B. Sammakia, Impact of fin geometry and surface roughness on performance of an impingement two-phase cooling heat sink, Appl. Therm. Eng. 198 (2021) 117453. https://doi.org/10.1016/j.applthermaleng.2021.117453.

[59] A. Cano-Banda, Fernando; Gonzalez-Valle, Ulises C.; Tarazona-Cardenas, Sindy; Hernandez-Guerrero, Effect of different geometry flow pattern on heat sink performance, in: the 12th International Conference on Heat Transfer, Fluid Mechanics and Thermodynamics, Costa de Sol, Spain, 2016. http://hdl.handle.net/2263/62070.

[60] P. Cui, Z. Liu, Enhanced flow boiling of HFE-7100 in picosecond laser fabricated copper microchannel heat sink, Int. J. Heat Mass Transf. 175 (2021) 121387. https://doi.org/10.1016/j.ijheatmasstransfer.2021.121387.

[61] H.E. Ahmed, B.H. Salman, A.S. Kherbeet, M.I. Ahmed, Optimization of thermal design of heat sinks: A review, Int. J. Heat Mass Transf. 118 (2018) 129–153. https://doi.org/10.1016/j.ijheatmasstransfer.2017.10.099.

[62] D.D.. Palande, D.N. Ghuge, G. Katale, A Comprehensive Review on Plate Heat Sink, SSRN Electron. J. (2022). https://doi.org/10.2139/ssrn.4043284.

[63] S. Tang, Y. Zhao, Y. Diao, Z. Quan, Effects of various inlet/outlet positions and header forms on flow distribution and thermal performance in microchannel heat sink, Microsyst. Technol. 24 (2018) 2485–2497. https://doi.org/10.1007/s00542-017-3688-y.

[64] M. Saeed, M.-H. Kim, Header design approaches for mini-channel heatsinks using analytical and numerical methods, Appl. Therm. Eng. 110 (2017) 1500–1510. https://doi.org/10.1016/j.applthermaleng.2016.09.069.

[65] A. Abdoli, G. Jimenez, G.S. Dulikravich, Thermo-fluid analysis of micro pin-fin array cooling configurations for high heat fluxes with a hot spot, Int. J. Therm. Sci. 90 (2015) 290–297. https://doi.org/10.1016/j.ijthermalsci.2014.12.021.

[66] Y.F. Li, G.D. Xia, D.D. Ma, Y.T. Jia, J. Wang, Characteristics of laminar flow and heat transfer in microchannel heat sink with triangular cavities and rectangular ribs, Int. J. Heat Mass Transf. 98 (2016) 17–28. https://doi.org/10.1016/j.ijheatmasstransfer.2016.03.022.

[67] P. Promvonge, T. Chompookham, S. Kwankaomeng, C. Thianpong, Enhanced heat transfer in a triangular ribbed channel with longitudinal vortex generators, Energy Convers. Manag. 51 (2010) 1242–1249. https://doi.org/10.1016/j.enconman.2009.12.035.

[68] G. Wang, D. Niu, F. Xie, Y. Wang, X. Zhao, G. Ding, Experimental and numerical investigation of a microchannel heat sink (MCHS) with micro-scale ribs and grooves for chip cooling, Appl. Therm. Eng. 85 (2015) 61–70. https://doi.org/10.1016/j.applthermaleng.2015.04.009.

[69] M. Paknezhad, A.M. Rashidi, T. Yousefi, Z. Saghir, Effect of aluminum-foam heat sink on inclined hot surface temperature in the case of free convection heat transfer, Case Stud. Therm. Eng. 10 (2017) 199–206. https://doi.org/10.1016/j.csite.2017.06.007.

[70] G.D. Xia, J. Jiang, J. Wang, Y.L. Zhai, D.D. Ma, Effects of different geometric structures on fluid flow and heat transfer performance in microchannel heat sinks, Int. J. Heat Mass Transf. 80 (2015) 439–447. https://doi.org/10.1016/j.ijheatmasstransfer.2014.08.095.

[71] S. Kumar, P.K. Singh, A novel approach to manage temperature non-uniformity in minichannel heat sink by using intentional flow maldistribution, Appl. Therm. Eng. 163 (2019) 114403. https://doi.org/10.1016/j.applthermaleng.2019.114403.

[72] Y. Li, S. Roux, C. Castelain, L. Luo, Y. Fan, Tailoring the fluid flow distribution in a parallel mini-channel heat sink under multiple-peak heat flux, Therm. Sci. Eng. Prog. 29 (2022) 101182. https://doi.org/10.1016/j.tsep.2021.101182.

[73] S. Kumar, P.K. Singh, Effects of flow inlet angle on flow maldistribution and thermal performance of water cooled mini-channel heat sink, Int. J. Therm. Sci. 138 (2019) 504–511. https://doi.org/10.1016/j.ijthermalsci.2019.01.014.

[74] R. Manikanda Kumaran, G. Kumaraguruparan, T. Sornakumar, Experimental and numerical studies of header design and inlet/outlet configurations on flow mal-distribution in parallel micro-channels, Appl. Therm. Eng. 58 (2013) 205–216. https://doi.org/10.1016/j.applthermaleng.2013.04.026.

[75] R. Chein, J. Chen, Numerical study of the inlet/outlet arrangement effect on microchannel heat sink performance, Int. J. Therm. Sci. 48 (2009) 1627–1638. https://doi.org/10.1016/j.ijthermalsci.2008.12.019.

[76] K. Chen, W. Wu, F. Yuan, L. Chen, S. Wang, Cooling efficiency improvement of air-cooled battery thermal management system through designing the flow pattern, Energy. 167 (2019) 781–790. https://doi.org/10.1016/j.energy.2018.11.011.

[77] P. Dąbrowski, Mitigation of Flow Maldistribution in Minichannel and Minigap Heat Exchangers by Introducing Threshold in Manifolds, J. Appl. Fluid Mech. 13 (2020) 815–826. https://doi.org/10.29252/jafm.13.03.30454.

[78] H. Liu, P. Li, J. Van Lew, D. Juarez-Robles, Experimental study of the flow distribution uniformity in flow distributors having novel flow channel bifurcation structures, Exp. Therm. Fluid Sci. 37 (2012) 142–153. https://doi.org/10.1016/j.expthermflusci.2011.10.015.

[79] C. Pistoresi, Y. Fan, L. Luo, Numerical study on the improvement of flow distribution uniformity among parallel mini-channels, Chem. Eng. Process. Process Intensif. 95 (2015) 63–71. https://doi.org/10.1016/j.cep.2015.05.014.

[80] J. Zhou, M. Ding, H. Bian, Y. Zhang, Z. Sun, Characteristics of flow distribution in central-type compact parallel flow heat exchangers with modified inlet and header, Appl. Therm. Eng. 166 (2020) 114636. https://doi.org/10.1016/j.applthermaleng.2019.114636.

[81] I.A. Ghani, N.A. Che Sidik, N. Kamaruzzaman, W. Jazair Yahya, O. Mahian, The effect of manifold zone parameters on hydrothermal performance of micro-channel HeatSink: A review, Int. J. Heat Mass Transf. 109 (2017) 1143–1161. https://doi.org/10.1016/j.ijheatmasstransfer.2017.03.007.

[82] J.-Y. Song, S. Hah, D. Kim, S.-M. Kim, Enhanced flow uniformity in parallel mini-channels with pin-finned inlet header, Appl. Therm. Eng. 152 (2019) 718–733. https://doi.org/10.1016/j.applthermaleng.2019.02.069.

[83] X. Liu, J. Yu, Numerical study on performances of mini-channel heat sinks with non-uniform inlets, Appl. Therm. Eng. 93 (2016) 856–864. https://doi.org/10.1016/j.applthermaleng.2015.09.032.

[84] Q. Hou, Y. Xuan, W. Lian, Y. Xu, Y. Ma, A novel approach for suppressing flow maldistribution in mini-channel heat exchangers, Int. J. Therm. Sci. 184 (2023) 108020. https://doi.org/10.1016/j.ijthermalsci.2022.108020.

[85] H. Fatahian, N.F. Jouybari, M.E. Nimvari, E. Fatahian, W. Zhang, Improving the flow uniformity in compact parallel-flow heat exchangers manifold using porous distributors, J. Therm. Anal. Calorim. 147 (2022) 12919–12931. https://doi.org/10.1007/s10973-022-11451-z.

[86] N. Gilmore, A. Hassanzadeh-Barforoushi, V. Timchenko, C. Menictas, Manifold configurations for uniform flow via topology optimisation and flow visualisation, Appl. Therm. Eng. (2021). https://doi.org/10.1016/j.applthermaleng.2020.116227.

[87] H.A. Dhahad, E.M. Alfayydh, K.H. Fahim, Effect of flow field design and channel/header ratio on velocity distribution: An experimental approach, Therm. Sci. Eng. Prog. 8 (2018) 118–129. https://doi.org/10.1016/j.tsep.2018.08.013.

[88] Y.-T. Mu, L. Chen, Y.-L. He, W.-Q. Tao, Numerical study on temperature uniformity in a novel mini-channel heat sink with different flow field configurations, Int. J. Heat Mass Transf. 85 (2015) 147–157. https://doi.org/10.1016/j.ijheatmasstransfer.2015.01.093.

[89] X. Hao, Z. Wu, X. Chen, G. Xie, Numerical Analysis and Optimization on Flow Distribution and Heat Transfer of a U-Type Parallel Channel Heat Sink, Adv. Mech. Eng. 7 (2015) 672451. https://doi.org/10.1155/2014/672451.

[90] I. Mitra, I. Ghosh, Mini-channel heat sink parameter sensitivity based on precise heat flux re-distribution, Therm. Sci. Eng. Prog. 20 (2020) 100717. https://doi.org/10.1016/j.tsep.2020.100717.

[91] S. Annapurna, S. Varughese, A. Niranjanappa, H.R. K, A Design of Experiments Approach Towards Desired Flow Distribution Through Manifolds in Electronics Cooling, Def. Sci. J. 72 (2022) 516–525. https://doi.org/10.14429/dsj.72.17883.

[92] J.-Y. Song, S. Senguttuvan, W.-W. Choi, S.-M. Kim, Effects of manifold design parameters on flow uniformity in parallel mini-channels, Int. J. Mech. Sci. 234 (2022) 107694. https://doi.org/10.1016/j.ijmecsci.2022.107694.

[93] G. Narendran, N. Gnanasekaran, Investigation on novel inertial minichannel to mitigate maldistribution induced high temperature zones, Energy Convers. Manag. 271 (2022) 116300. https://doi.org/10.1016/j.enconman.2022.116300.

[94] W. Lou, Y. Fan, L. Luo, Single-tank thermal energy storage systems for concentrated solar power: Flow distribution optimization for thermocline evolution management, J. Energy Storage. 32 (2020) 101749. https://doi.org/10.1016/j.est.2020.101749.

[95] O.O. Milman, D.B. Spalding, V.A. Fedorov, Steam condensation in parallel channels with nonuniform heat removal in different zones of heat-exchange surface, Int. J. Heat Mass Transf. 55 (2012) 6054–6059. https://doi.org/10.1016/j.ijheatmasstransfer.2012.06.016.

[96] M. Wei, Y. Fan, L. Luo, G. Flamant, Fluid flow distribution optimization for minimizing the peak temperature of a tubular solar receiver, Energy. 91 (2015) 663–677. https://doi.org/10.1016/j.energy.2015.08.072.

[97] S. Baodong, W. Lifeng, L. Jianyun, C. Heming, Multi-objective optimization design of a micro-channel heat sink using adaptive genetic algorithm, Int. J. Numer. Methods Heat Fluid Flow. 21 (2011) 353–364. https://doi.org/10.1108/09615531111108512.

[98] I.K. Karathanassis, E. Papanicolaou, V. Belessiotis, G.C. Bergeles, Multi-objective design optimization of a micro heat sink for Concentrating Photovoltaic/Thermal (CPVT) systems using a genetic algorithm, Appl. Therm. Eng. 59 (2013) 733–744. https://doi.org/10.1016/j.applthermaleng.2012.06.034.

[99] G.-M. Normah, J.-T. Oh, N.B. Chien, K.-I. Choi, A. Robiah, Comparison of the optimized thermal performance of square and circular ammonia-cooled microchannel heat sink with genetic algorithm, Energy Convers. Manag. 102 (2015) 59–65. https://doi.org/10.1016/j.enconman.2015.02.008.

[100] S. Halelfadl, A.M. Adham, N. Mohd-Ghazali, T. Maré, P. Estellé, R. Ahmad, Optimization of thermal performances and pressure drop of rectangular microchannel heat sink using aqueous carbon nanotubes based nanofluid, Appl. Therm. Eng. 62 (2014) 492–499. https://doi.org/10.1016/j.applthermaleng.2013.08.005.

[101] D. Lin, C.-H. Kang, S.-C. Chen, Optimization of the Micro Channel Heat Sink by Combing Genetic Algorithm with the Finite Element Method, Inventions. 3 (2018) 32. https://doi.org/10.3390/inventions3020032.

[102] T.-C. Hung, W.-M. Yan, X.-D. Wang, Y.-X. Huang, Optimal design of geometric parameters of double-layered microchannel heat sinks, Int. J. Heat Mass Transf. 55 (2012) 3262–3272. https://doi.org/10.1016/j.ijheatmasstransfer.2012.02.059.

[103] X.-D. Wang, Bin An, J.-L. Xu, Optimal geometric structure for nanofluid-cooled microchannel heat sink under various constraint conditions, Energy Convers. Manag. 65 (2013) 528–538. https://doi.org/10.1016/j.enconman.2012.08.018.

[104] X.-D. Wang, B. An, L. Lin, D.-J. Lee, Inverse geometric optimization for geometry of nanofluid-cooled microchannel heat sink, Appl. Therm. Eng. 55 (2013) 87–94. https://doi.org/10.1016/j.applthermaleng.2013.03.010.

[105] C. Leng, X.-D. Wang, T.-H. Wang, W.-M. Yan, Optimization of thermal resistance and bottom wall temperature uniformity for double-layered microchannel heat sink, Energy Convers. Manag. 93 (2015) 141–150. https://doi.org/10.1016/j.enconman.2015.01.004.

[106] R.V. Rao, K.C. More, J. Taler, P. Ocłoń, Dimensional optimization of a micro-channel heat sink using Jaya algorithm, Appl. Therm. Eng. 103 (2016) 572–582. https://doi.org/10.1016/j.applthermaleng.2016.04.135.

[107] H. Yin, R. Ooka, Shape optimization of water-to-water plate-fin heat exchanger using computational fluid dynamics and genetic algorithm, Appl. Therm. Eng. 80 (2015) 310–318. https://doi.org/10.1016/j.applthermaleng.2015.01.068.

[108] K. Foli, T. Okabe, M. Olhofer, Y. Jin, B. Sendhoff, Optimization of micro heat exchanger: CFD, analytical approach and multi-objective evolutionary algorithms, Int. J. Heat Mass Transf. 49 (2006) 1090–1099. https://doi.org/10.1016/j.ijheatmasstransfer.2005.08.032.

[109] Y. Ge, S. Wang, Z. Liu, W. Liu, Optimal shape design of a minichannel heat sink applying multi-objective optimization algorithm and three-dimensional numerical method, Appl. Therm. Eng. 148 (2019) 120–128. https://doi.org/10.1016/j.applthermaleng.2018.11.038.

[110] C.B. Dokken, B.M. Fronk, Optimization of 3D printed liquid cooled heat sink designs using a micro-genetic algorithm with bit array representation, Appl. Therm. Eng. 143 (2018) 316–325. https://doi.org/10.1016/j.applthermaleng.2018.07.113.

[111] W.A. Khan, M.B. Kadri, Q. Ali, Optimization of Microchannel Heat Sinks Using Genetic Algorithm, Heat Transf. Eng. 34 (2013) 279–287. https://doi.org/10.1080/01457632.2013.694758.

[112] A. Husain, K.-Y. Kim, Optimization of a microchannel heat sink with temperature dependent fluid properties, Appl. Therm. Eng. 28 (2008) 1101–1107. https://doi.org/10.1016/j.applthermaleng.2007.12.001.

[113] K. Kulkarni, A. Afzal, K.-Y. Kim, Multi-objective optimization of a double-layered microchannel heat sink with temperature-dependent fluid properties, Appl. Therm. Eng. 99 (2016) 262–272. https://doi.org/10.1016/j.applthermaleng.2016.01.039.

[114] Y. Alperen, C. Sertac, Multi objective optimization of a micro-channel heat sink through genetic algorithm,

Int. J. Heat Mass Transf. 146 (2020) 118847. https://doi.org/10.1016/j.ijheatmasstransfer.2019.118847.

[115] W.T. L. Piegl, The NURBS Book, second ed., Springer, 1997.

[116] G. Lee, I. Lee, S.J. Kim, Topology optimization of a heat sink with an axially uniform cross-section cooled by forced convection, Int. J. Heat Mass Transf. 168 (2021) 120732. https://doi.org/10.1016/j.ijheatmasstransfer.2020.120732.

[117] Y. T. Yang; H. S. Peng; H. T. Hsu, Numerical Optimization of Pin-Fin Heat Sink with Forced Cooling, Int. J. Electron. Commun. Eng. 7(7) (2013) 884–891. https://doi.org/doi.org/10.5281/zenodo.1087203.

[118] H. Keramati, F. Hamdullahpur, M. Barzegari, Deep reinforcement learning for heat exchanger shape optimization, Int. J. Heat Mass Transf. 194 (2022) 123112. https://doi.org/10.1016/j.ijheatmasstransfer.2022.123112.

[119] A. Ghasemi, A. Elham, Multi-objective topology optimization of pin-fin heat exchangers using spectral and finite-element methods, Struct. Multidiscip. Optim. 64 (2021) 2075–2095. https://doi.org/10.1007/s00158-021-02964-6.

[120] M. Ahmadian-Elmi, A. Mashayekhi, S.S. Nourazar, K. Vafai, A comprehensive study on parametric optimization of the pin-fin heat sink to improve its thermal and hydraulic characteristics, Int. J. Heat Mass Transf. 180 (2021) 121797. https://doi.org/10.1016/j.ijheatmasstransfer.2021.121797.

[121] C.-H. Huang, Y.-H. Chen, An optimal design problem in determining non-uniform fin heights and widths for an impingement heat sink module, Appl. Therm. Eng. 63 (2014) 481–494. https://doi.org/10.1016/j.applthermaleng.2013.11.008.

[122] Y.-T. Yang, S.-C. Lin, Y.-H. Wang, J.-C. Hsu, Numerical simulation and optimization of impingement cooling for rotating and stationary pin–fin heat sinks, Int. J. Heat Fluid Flow. 44 (2013) 383–393. https://doi.org/10.1016/j.ijheatfluidflow.2013.07.008.

[123] C.-T. Chen, H.-I. Chen, Multi-objective optimization design of plate-fin heat sinks using a direction-based genetic algorithm, J. Taiwan Inst. Chem. Eng. 44 (2013) 257–265. https://doi.org/10.1016/j.jtice.2012.11.012.

[124] J. Zhao, S. Huang, L. Gong, Z. Huang, Numerical study and optimizing on micro square pin-fin heat sink for electronic cooling, Appl. Therm. Eng. 93 (2016) 1347–1359. https://doi.org/10.1016/j.applthermaleng.2015.08.105.

[125] H. Nemati, M.A. Moghimi, P. Sapin, C.N. Markides, Shape optimisation of air-cooled finned-tube heat exchangers, Int. J. Therm. Sci. 150 (2020) 106233. https://doi.org/10.1016/j.ijthermalsci.2019.106233.

[126] M.E. Polat, F. Ulger, S. Cadirci, Multi-objective optimization and performance assessment of microchannel heat sinks with micro pin-fins, Int. J. Therm. Sci. 174 (2022) 107432. https://doi.org/10.1016/j.ijthermalsci.2021.107432.

[127] Y. Wang, Y. Li, D. Liu, The application of genetic algorithm for pin-fin heat sink optimization design, in: 2009 4th IEEE Conf. Ind. Electron. Appl., IEEE, 2009: pp. 2816–2821. https://doi.org/10.1109/ICIEA.2009.5138723.

[128] W. Yang, J.K. Mills, Optimization of Pin Arrangement and Geometry in EV and HEV Heat Sink Using Genetic Algorithm Coupled With CFD, in: 2021 IEEE Int. Conf. Mechatronics Autom., IEEE, 2021: pp. 332–337. https://doi.org/10.1109/ICMA52036.2021.9512837.

[129] F. Ismayilov, A. Akturk, Y. Peles, Systematic micro heat sink optimization based on hydrofoil shape pin fins, Case Stud. Therm. Eng. 26 (2021) 101028. https://doi.org/10.1016/j.csite.2021.101028.

[130] Y. Huang, M. Xu, H. Li, S. Shen, X. Song, H. Liu, A. Waili, L. Zhao, W. Wei, Novel thermal design of micro-bream-fin heat sink using contour-extraction-based (CEB) method, Int. J. Therm. Sci. 165 (2021) 106952. https://doi.org/10.1016/j.ijthermalsci.2021.106952.

[131] A. Fawaz, Y. Hua, S. Le Corre, Y. Fan, L. Luo, Topology optimization of heat exchangers: A review, Energy. 252 (2022) 124053. https://doi.org/10.1016/j.energy.2022.124053.

[132] G.H. Yoon, Topological design of heat dissipating structure with forced convective heat transfer, J. Mech. Sci. Technol. 24 (2010) 1225–1233. https://doi.org/10.1007/s12206-010-0328-1.

[133] X. Dong, X. Liu, Multi-objective optimal design of microchannel cooling heat sink using topology optimization method, Numer. Heat Transf. Part A Appl. 77 (2020) 90–104.

https://doi.org/10.1080/10407782.2019.1682872.

[134] V. Subramaniam, T. Dbouk, J.-L. Harion, Topology optimization of conjugate heat transfer systems: A competition between heat transfer enhancement and pressure drop reduction, Int. J. Heat Fluid Flow. 75 (2019) 165–184. https://doi.org/10.1016/j.ijheatfluidflow.2019.01.002.

[135] K. Yaji, T. Yamada, M. Yoshino, T. Matsumoto, K. Izui, S. Nishiwaki, Topology optimization in thermal-fluid flow using the lattice Boltzmann method, J. Comput. Phys. 307 (2016) 355–377. https://doi.org/10.1016/j.jcp.2015.12.008.

[136] S. Sun, P. Liebersbach, X. Qian, Large Scale 3D Topology Optimization of Conjugate Heat Transfer, in: 2019 18th IEEE Intersoc. Conf. Therm. Thermomechanical Phenom. Electron. Syst., IEEE, 2019: pp. 1–6. https://doi.org/10.1109/ITHERM.2019.8757230.

[137] J. Alexandersen, Efficient topology optimisation of multiscale and multiphysics problems., 2016. https://doi.org/https://doi.org/10.13140/RG.2.2.15890.45761.

[138] O. Sigmund, J. Petersson, Numerical instabilities in topology optimization: A survey on procedures dealing with checkerboards, mesh-dependencies and local minima, Struct. Optim. 16 (1998) 68–75. https://doi.org/10.1007/BF01214002.

[139] Gao Wei, An improved fast-convergent genetic algorithm, in: IEEE Int. Conf. Robot. Intell. Syst. Signal Process. 2003. Proceedings. 2003, IEEE, n.d.: pp. 1197–1202. https://doi.org/10.1109/RISSP.2003.1285761.

[140] Y. Joo, I. Lee, S.J. Kim, Topology optimization of heat sinks in natural convection considering the effect of shape-dependent heat transfer coefficient, Int. J. Heat Mass Transf. 109 (2017) 123–133. https://doi.org/10.1016/j.ijheatmasstransfer.2017.01.099.

[141] S.B. Dilgen, C.B. Dilgen, D.R. Fuhrman, O. Sigmund, B.S. Lazarov, Density based topology optimization of turbulent flow heat transfer systems, Struct. Multidiscip. Optim. 57 (2018) 1905–1918. https://doi.org/10.1007/s00158-018-1967-6.

[142] S. Sun, P. Liebersbach, X. Qian, 3D topology optimization of heat sinks for liquid cooling, Appl. Therm. Eng. 178 (2020) 115540. https://doi.org/10.1016/j.applthermaleng.2020.115540.

[143] M. Yu, X. Wang, J. Gu, S. Ruan, Z. Li, S. Qian, J. Zhang, C. Shen, A synergic topology optimization approach on distribution of cooling channels and diverse-intensity heat sources for liquid-cooled heat sink, Struct. Multidiscip. Optim. 65 (2022) 48. https://doi.org/10.1007/s00158-021-03113-9.

[144] M. Yoshimura, K. Shimoyama, T. Misaka, S. Obayashi, Topology optimization of fluid problems using genetic algorithm assisted by the Kriging model, Int. J. Numer. Methods Eng. 109 (2017) 514–532. https://doi.org/10.1002/nme.5295.

[145] K. Shimoyama, A. Komiya, Multi-objective Bayesian topology optimization of a lattice-structured heat sink in natural convection, Struct. Multidiscip. Optim. 65 (2022) 1. https://doi.org/10.1007/s00158-021-03092-x.

[146] B.S. Mekki, S.P. Lynch, Voxel-Based Topology Optimization of Heat Exchanger Fins, in: AIAA SCITECH 2022 Forum, American Institute of Aeronautics and Astronautics, Reston, Virginia, 2022. https://doi.org/10.2514/6.2022-2445.

[147] B.S. Mekki, J. Langer, S. Lynch, Genetic algorithm based topology optimization of heat exchanger fins used in aerospace applications, Int. J. Heat Mass Transf. 170 (2021) 121002. https://doi.org/10.1016/j.ijheatmasstransfer.2021.121002.

[148] K. Yaji, S. Yamasaki, K. Fujita, Data-driven multifidelity topology design using a deep generative model: Application to forced convection heat transfer problems, Comput. Methods Appl. Mech. Eng. 388 (2022) 114284. https://doi.org/10.1016/j.cma.2021.114284.

[149] E.M. Dede, Y. Liu, Experimental and numerical investigation of a multi-pass branching microchannel heat sink, Appl. Therm. Eng. 55 (2013) 51–60. https://doi.org/10.1016/j.applthermaleng.2013.02.038.

[150] X. Li, L. Zhang, B. Li, Heat transfer augmentation in microchannel heat sink based on isogeometric topology optimization framework, Appl. Math. Model. 104 (2022) 163–187. https://doi.org/10.1016/j.apm.2021.11.021.

[151] J.S. Lee, S.Y. Yoon, B. Kim, H. Lee, M.Y. Ha, J.K. Min, A topology optimization based design of a liquid-cooled heat sink with cylindrical pin fins having varying pitch, Int. J. Heat Mass Transf. 172 (2021) 121172.

https://doi.org/10.1016/j.ijheatmasstransfer.2021.121172.

[152] S. Zeng, P.S. Lee, Topology optimization of liquid-cooled microchannel heat sinks: An experimental and numerical study, Int. J. Heat Mass Transf. 142 (2019) 118401. https://doi.org/10.1016/j.ijheatmasstransfer.2019.07.051.

[153] H. Li, X. Ding, F. Meng, D. Jing, M. Xiong, Optimal design and thermal modelling for liquid-cooled heat sink based on multi-objective topology optimization: An experimental and numerical study, Int. J. Heat Mass Transf. 144 (2019) 118638. https://doi.org/10.1016/j.ijheatmasstransfer.2019.118638.

[154] S. Qian, S. Lou, C. Ge, W. Wang, X. Tian, Y. Cai, The influence of temperature dependent fluid properties on topology optimization of conjugate heat transfer, Int. J. Therm. Sci. 173 (2022) 107424. https://doi.org/10.1016/j.ijthermalsci.2021.107424.

[155] X. Mo, H. Zhi, Y. Xiao, H. Hua, L. He, Topology optimization of cooling plates for battery thermal management, Int. J. Heat Mass Transf. 178 (2021) 121612. https://doi.org/10.1016/j.ijheatmasstransfer.2021.121612.

[156] X. Han, H. Liu, G. Xie, L. Sang, J. Zhou, Topology optimization for spider web heat sinks for electronic cooling, Appl. Therm. Eng. 195 (2021) 117154. https://doi.org/10.1016/j.applthermaleng.2021.117154.

[157] T. Zhou, C. Guo, X. Shao, A Novel Mini-Channel Heat Sink Design with Arc-Type Design Domain by Topology Optimization, Micromachines. 13 (2022) 180. https://doi.org/10.3390/mi13020180.

[158] J. Zhou, M. Lu, Q. Zhao, D. Hu, H. Qin, X. Chen, Thermal design of microchannel heat sinks using a contour extraction based on topology optimization (CEBTO) method, Int. J. Heat Mass Transf. 189 (2022) 122703. https://doi.org/10.1016/j.ijheatmasstransfer.2022.122703.

[159] C. Ri, Z. Huifen, M. Yixin, Z. Shengxian, Design and Numerical Study of Liquid Cooling Radiator Based on Topology Optimization Method, SSRN Electron. J. (2022). https://doi.org/10.2139/ssrn.4085333.

[160] J.C.K. Tong, E.M. Sparrow, J.P. Abraham, Attainment of Flowrate Uniformity in the Channels That Link a Distribution Manifold to a Collection Manifold, J. Fluids Eng. 129 (2007) 1186–1192. https://doi.org/10.1115/1.2754319.

[161] M. Wei, Y. Fan, L. Luo, G. Flamant, Design and optimization of baffled fluid distributor for realizing target flow distribution in a tubular solar receiver, Energy. 136 (2017) 126–134. https://doi.org/10.1016/j.energy.2016.04.016.

[162] M. Wei, G. Boutin, Y. Fan, L. Luo, Numerical and experimental investigation on the realization of target flow distribution among parallel mini-channels, Chem. Eng. Res. Des. 113 (2016) 74–84. https://doi.org/10.1016/j.cherd.2016.06.026.

[163] M. Wei, Nouvelles méthodes pour l'optimisation de la distribution des fluides et leurs applications dans les systèmes des centrales solaires à concentration (CSP), Université de Nantes, 2015.

[164] B.W. W. M. Kays, M. E. Crawford, Convective Heat and Mass Transfer, 4th Editio, Mcgraw-Hill, 2005.

[165] Engineering ToolBox, Water - Thermal Conductivity, (2018).

[166] Engineering ToolBox, Water - Density, Specific Weight and Thermal Expansion Coefficient, (2003).

[167] Y.A. Manaserh, A.R. Gharaibeh, M.I. Tradat, S. Rangarajan, B.G. Sammakia, H.A. Alissa, Multi-objective optimization of 3D printed liquid cooled heat sink with guide vanes for targeting hotspots in high heat flux electronics, Int. J. Heat Mass Transf. 184 (2022) 122287. https://doi.org/10.1016/j.ijheatmasstransfer.2021.122287.

[168] F. Dugast, Y. Favennec, C. Josset, Y. Fan, L. Luo, Topology optimization of thermal fluid flows with an adjoint Lattice Boltzmann Method, J. Comput. Phys. 365 (2018). https://doi.org/10.1016/j.jcp.2018.03.040.

[169] Joe Alexandersen, Efficient topology optimisation of multiscale and multiphysics problems, University of Southern Denmark, 2016. https://doi.org/10.13140/RG.2.2.15890.45761.

[170] J.H. Holland, Genetic Algorithms, Sci. Am. 267 (1992) 66–72. https://doi.org/10.1038/scientificamerican0792-66.

[171] L. Gosselin, M. Tye-Gingras, F. Mathieu-Potvin, Review of utilization of genetic algorithms in heat transfer problems, Int. J. Heat Mass Transf. 52 (2009) 2169–2188. https://doi.org/10.1016/j.ijheatmasstransfer.2008.11.015.

[172] J. Gao, Z. Hu, Q. Yang, X. Liang, H. Wu, Fluid flow and heat transfer in microchannel heat sinks: Modelling review and recent progress, Therm. Sci. Eng. Prog. 29 (2022) 101203. https://doi.org/10.1016/j.tsep.2022.101203.

[173] R. Boichot, Y. Fan, A genetic algorithm for topology optimization of area-To-point heat conduction problem, Int. J. Therm. Sci. 108 (2016). https://doi.org/10.1016/j.ijthermalsci.2016.05.015.

[174] D. BHANDARI, C.A. MURTHY, S.K. PAL, GENETIC ALGORITHM WITH ELITIST MODEL AND ITS CONVERGENCE, Int. J. Pattern Recognit. Artif. Intell. 10 (1996) 731–747. https://doi.org/10.1142/S0218001496000438.

[175] Chen Li, R.A. Wirtz, Development of a high performance heat Sink Based on screen-fin technology, IEEE Trans. Components Packag. Technol. 28 (2005) 80–87. https://doi.org/10.1109/TCAPT.2004.843171.

[176] OpenFoam user guide, version 7, 2019, n.d.

[177] Le Centre de Calcul Intensif des Pays de la Loire (CCIPL), (n.d.).

[178] D. Tondeur, Y. Fan, L. Luo, Constructal optimization of arborescent structures with flow singularities, Chem. Eng. Sci. 64 (2009). https://doi.org/10.1016/j.ces.2009.05.052.

[179] S. Mondal, A. Tsourdos, Optimal topology for consensus using genetic algorithm, Neurocomputing. 404 (2020) 41–49. https://doi.org/10.1016/j.neucom.2020.04.107.

[180] D. Tarlet, Y. Fan, S. Roux, L. Luo, Entropy generation analysis of a mini heat exchanger for heat transfer intensification, Exp. Therm. Fluid Sci. 53 (2014). https://doi.org/10.1016/j.expthermflusci.2013.11.016.

[181] A.S.L. Frank P. Incropera, David P. DeWitt, Theodore L. Bergman, Fundamentals of heat and mass transfer, 6th Editio, John Wiley & Sons, n.d.

[182] J. E.Willert, Markus Raffel, Christian Kompenhans, Steve T.Wereley, Particle Image Velocimetry: a practical guide, Second Edi, Springer, 2007.

[183] R.K. Shah, A.L. London, Rectangular Ducts, in: Laminar Flow Forced Convect. Ducts, Elsevier, 1978: pp. 196–222. https://doi.org/10.1016/B978-0-12-020051-1.50012-7.

[184] T. Astarita, G.M. Carlomagno, Infrared Thermography for Thermo-Fluid-Dynamics, Springer Berlin Heidelberg, Berlin, Heidelberg, 2013. https://doi.org/10.1007/978-3-642-29508-9.

[185] K.E. Kaylegian, J.M. Lynch, J.R. Fleming, D.M. Barbano, Influence of fatty acid chain length and unsaturation on mid-infrared milk analysis, J. Dairy Sci. 92 (2009) 2485–2501. https://doi.org/10.3168/jds.2008-1910.

[186] Crystran Ltd, Sapphire (Al2O3), Crystran Ltd. (2019). https://www.crystran.co.uk/optical-materials/sapphire-al2o3.

[187] Thermal physical properties of 304 Stainless Steel, (n.d.). https://www.matweb.com/search/DataSheet.aspx?MatGUID=abc4415b0f8b490387e3c922237098da&ckck=1.

[188] Thermal physical properties of sapphire, (n.d.). https://www.guildoptics.com/sapphire-properties/sapphire-properties/.

[189] L. Gong, K. Kota, W. Tao, Y. Joshi, Thermal performance of microchannels with wavy walls for electronics cooling, in: 2010 12th IEEE Intersoc. Conf. Therm. Thermomechanical Phenom. Electron. Syst., IEEE, 2010: pp. 1–6. https://doi.org/10.1109/ITHERM.2010.5501323.

COLLEGE SCIENCES
DOCTORAL DE L'INGENIERIE
PAYS DE LA LOIRE ET DES SYSTEMES

Nantes Université

Titre : Conception et optimisation topologique des dissipateurs thermiques pour le refroidissement de dispositifs électroniques avec plusieurs sources de chaleur

Mots clés : dissipateurs thermiques, refroidissement électronique, sources de chaleur multiples, distribution des fluides, optimisation topologique, algorithme génétique, thermographie infrarouge

Résumé : Les dispositifs électroniques génèrent souvent de la chaleur en différents points. Sans un refroidissement efficace, les points chauds et la surchauffe entraînent une augmentation du taux de défaillance, une détérioration des performances et des menaces pour la sécurité des composants électroniques. L'objectif principal de cette thèse est de concevoir et d'optimiser la structure des dissipateurs de chaleur par convection monophasique en minimisant la température maximale pour apporter une solution innovante à ces problèmes. Deux méthodes d'optimisation ont été développées et appliquées : l'optimisation de la taille des entrées de chaque canaux enfin de distribuer de façon optimum les fluide dans le dissipateur de chaleur à canal droit d'une part, et l'optimisation topologique de la configuration sur l'ensemble des canaux d'écoulement basée sur l'algorithme génétique (GATO). L'influence des paramètres, tels que les valeurs des pics de flux de chaleur, la vitesse d'entrée, la résolution matricielle d'un domaine de conception et la fraction de fluide a été étudiée numériquement. Ensuite, les approches d'optimisation proposées ont été validées expérimentalement en testant un dissipateur thermique à canal droit de référence (RSC), un dissipateur thermique à canal droit optimisé (OSC) et un dissipateur thermique GATO. En outre, les indicateurs de performance complets obtenus à partir des modèles validés expérimentalement des trois dissipateurs thermiques ont été comparés. Enfin, l'influence de différents objectifs d'optimisation pour la méthode GATO a été étudiée.

Title: Design and topology optimization of heat sinks for the cooling of electronic devices with multiple heat sources

Keywords: heat sink, electronic cooling, multiple heat sources, flow distribution, topology optimization, genetic algorithm, infrared thermography

Abstract: The heat-generating surface with multiple heat sources is frequently encountered in modern power electronic devices. Efficient cooling techniques are especially needed to prevent the overheating of these devices, so as to avoid consequences like performance deterioration, failure rate increase, reduced lifetime and safety threats. The main objective of this PhD thesis is to design and optimize the structure of heat sinks for single-phase convective cooling of a heat-generating surface under multiple-peak heat flux. Two optimization methods have been developed and applied in this study: one is the size optimization of channel inlets for tailoring the fluid flow distribution in straight channel heat sinks and another is the topology optimization of the global flow channel configuration based on the genetic algorithm (GATO). The impacts of design and operation parameters on the effectiveness of both optimization methods are numerically evaluated, with performance comparison to reference parallel straight channel heat sinks. After that, experimental validations of the proposed optimization approaches have been done by testing different heat sink prototypes using PIV and infrared thermography. Both the numerical and experimental results indicate that the GATO heat sink shows the best cooling performance under the tested conditions. Finally, different objective functions have been tested with the GATO method and the obtained results are further compared and discussed to showcase its effectiveness and robustness.